Aix*Marseille université
Initiative d'excellence

THÈSE DE DOCTORAT

Soutenue à Aix-Marseille Université
le 23 Septembre 2021 par

Jana Bogdanoska

Title of the thesis:
Stars and dust in the first Gyr of the Universe

Discipline
Sciences de l'Univers

Spécialité
Astrophysique et Cosmologie

École doctorale
Physique et Sciences de la Matiere ED352

Laboratoire/Partenaires de recherche
Laboratoire d'Astrophysique de Marseille (LAM)

Composition du jury

Karina CAPUTI University of Groningen (NL)	Rapportice
Hervé DOLE Université Paris-Saclay (FR)	Rapporteur
Rychard BOUWENS Leiden University (NL)	Examinateur
Daniel SCHAERER University of Geneva (CH)	Examinateur
Veronique BUAT LAM (FR)	Présidente du jury
Danis BURGARELLA LAM (FR)	Directeur de thèse

LAM LABORATOIRE D'ASTROPHYSIQUE DE MARSEILLE

cnrs dépasser les frontières

PNCG PROGRAMME NATIONAL DE COSMOLOGIE ET GALAXIES

I, undersigned, Jana Bogdanoska, hereby declare that the work presented in this manuscript is my own work, carried out under the scientific direction of Dr Denis Burgarella, in accordance with the principles of honesty, integrity and responsibility inherent to the research mission. The research work and the writing of this manuscript have been carried out in compliance with both the french national charter for Research Integrity and the Aix-Marseille University charter on the fight against plagiarism.

This work has not been submitted previously either in this country or in another country in the same or in a similar version to any other examination body.

Marseille, 28/06/2021

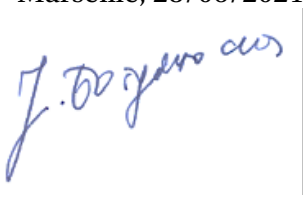

Résumé

Le sujet de ma thèse s'inscrit dans le domaine de l'astronomie extragalactique. Elle est basée sur des données multi-longueurs d'onde pour les galaxies lointaines (à haut redshift). Et mon travail a comme objectif d'estimer les principaux paramètres de ces galaxies par l'ajustement de distributions spectrales d'énergie (SED) avec un objectif central qui est l'étude de la poussière cosmique. Une revue des principaux concepts de ce travail est d'abord présentée : une brève histoire de l'Univers explique la place et l'environnement des galaxies d'intérêt. Elle continue par une explication des modèles utilisés lors de la réalisation de l'ajustement des SEDs, notamment ceux inclus dans le code CIGALE, par un aperçu des paramètres globaux des populations de galaxies dans l'Univers à haut redshift, et enfin par un résumé des propriétés physiques de la poussière, comme base pour les futurs modèles de grains de poussière de l'Univers primordial.

Cette thèse a débuté par un rappel des considérations théoriques. Ce chapitre a été écrit avec deux objectifs différents à l'esprit : S'assurer que tous ceux qui lisent cette thèse sont familiarisés avec les informations de base nécessaires pour suivre le reste du texte, et Servir de résumé des grands principes que j'ai appris tout au long de mon années en tant que doctorant.

L'introduction théorique est suivie des découvertes rapportées dans l'article que j'ai publiées au cours de ma thèse en tant que premier auteure. Ce travail relie l'atténuation de la poussière à la masse stellaire des galaxies, et à son évolution avec le redshift. Un échantillon de galaxies avec une estimation de l'atténuation de la poussière calculée à partir du paramètre IRX qui est le rapport de la luminosité de la poussière à la luminosité de l'ultraviolet lointain ($IRX = L_{dust}/L_{FUV}$) a été utilisé. Les données d'atténuation de la poussière par rapport à la masse stellaire, séparées par domaine de redshift, ont été modélisées par une fonction linéaire à paramètre unique, en supposant une atténuation de poussière apparente constante non nulle pour les galaxies de faible masse. L'origine de cet effet reste à déterminer et plusieurs possibilités sont explorées (teneur élevée en poussières réelle, variation du rapport poussières/métal, variation de la géométrie étoiles-poussières). Le paramètre estimé à partir de l'ajustement de ce modèle est utilisé pour étudier l'évolution avec le redshift de l'atténuation de la poussière cosmique et s'avère en accord avec les résultats de la littérature. Ce travail met également en évidence une évolution en redshift de la relation atténuation des poussières-masse stellaire, comme le suggèrent des travaux récents dans la plage de redshift le plus élevé.

Même s'ils servent les mêmes objectifs que ceux ci-dessus, les chapitres suivants sont plus spécifiquement consacrés à nos découvertes scientifiques. Certes, ces

découvertes ont déjà été ou seront bientôt publiées, leur inclusion dans cette thèse vise donc davantage à expliquer ma part du travail et comment je l'ai compris.

Le chapitre 3 contient le travail qui a été publié dans mon premier ouvrage en tant que premier auteure. J'ai commencé ce travail pendant ma thèse de maîtrise et il a fallu beaucoup de temps pour atteindre son état final, et toute l'histoire derrière ce projet, même les parties inédites, sont incluses dans la thèse. Le plan est légèrement différent de celui du document, car j'ai pris une section entière pour discuter de certaines des choses qui n'ont pas fonctionné, mais je ne voulais pas qu'elles soient perdues car cela détaille et contient une information importnant sur le processus scientifique qui a mené au résultat final, en incluant les impasses.

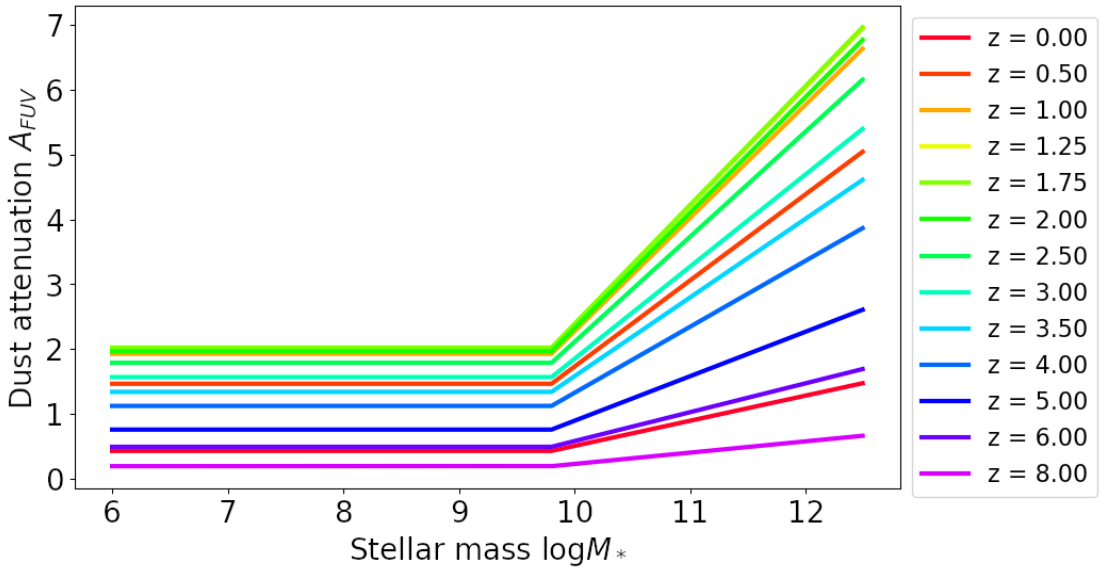

La dépendance de l'atténuation de la poussière UV sur la masse stellaire avec les paramètres dérivés par ajustement comme décrit dans la Sect. 3.2.1, montrant le modèle à différents redshifts. Les différentes lignes colorées montrent l'Eq. (3.1), pour la valeur de a calculée par Eq. (3.2) au redshift approprié.

Ainsi, au Chap. 3, nous commençons par décrire les données que nous avons utilisées : une collection de la littérature qui contient des échantillons UV sélectionnés de galaxies à différents décalages vers le rouge, pour lesquels des données UV et IR sont disponibles. Nous nous sommes assurés que les échantillons inclus étaient aussi similaires que possible, que les données sur les masses stellaires des galaxies étaient disponibles, ainsi que l'atténuation de la poussière estimée via l'IRX. Les valeurs d'IRX sont ensuite converties en atténuation de poussière dans le FUV (A_{FUV}). Ensuite, les données sont séparées en intervalles de décalage vers le rouge, et pour chaque intervalle, une relation pour la masse stellaire - atténuation de la poussière est ajustée. Les principaux résultats de nos travaux portent sur cette relation : nous montrons qu'il est raisonnable de supposer une évolution avec redshift de la dépendance $A_{FUV} - M_*$, de même que l'hypothèse d'un A_{FUV} apparent non nul pour les galaxies de faible masse donne des résultats qui sont en accord avec des résultats similaires obtenus dans la littérature.

La relation $A_{FUV} - M_*$ évoluant vers le rouge est ensuite utilisée pour calculer l'atténuation moyenne de la poussière cosmique. Ceci est fait en estimant l'atténuation moyenne de la poussière pondérée par la fonction de masse stellaire. En utilisant l'évolution du redshift de la relation $A_{FUV} - M_*$, nous reproduisons la forme de la courbe cosmique $A_{FUV} - z$ d'autres auteurs (Burgarella et al., 2013 ; Cucciati et al., 2012), une forme qui correspond au tracé SFRD classique. (Madau; Dickinson, 2014). C'est un résultat attendu, car la poussière et la formation d'étoiles se trouvent généralement ensemble dans l'Univers.

Le chapitre suivant résume le travail qui sera prochainement publié dont je serai la deuxième auteure. Nous poursuivons les travaux de Burgarella et al. (2020) en utilisant des méthodes similaires sur l'échantillon de galaxies ALPINE, qui fournit une mesure de la raie [CII]158μm de $4,5 < z < 6,5$ galaxies. Cet échantillon a été observé par diverses études, et un grand catalogue de données auxiliaires multi-longueurs d'onde est disponible. Nous effectuons un ajustement des SEDs sur les galaxies ALPINE avec CIGALE, visant à déterminer les paramètres de ces galaxies, à savoir la masse stellaire, SFR, âges stellaires, masse de poussière, pente UV, etc. En utilisant les résultats de l'ajustement des SEDs, nous étendons les résultats de Burgarella et al. sur plusieurs diagrammes diagnostiques clés, qui seront utilisés pour étudier l'évolution des galaxies et l'accumulation de poussière à travers les temps cosmiques.

Le chapitre suivant (Chap. 4) décrit l'ouvrage que nous sommes en train de publier. Le sujet est légèrement différent de celui du Chap. 3, bien que le thème de l'ajustement SED soit toujours prédominant. Dans ce travail, les galaxies à grand redshift sont étudiées, en se concentrant sur le relevé ALPINE. Les méthodes utilisées sont basées sur Burgarella et al. (2020), qui travaillent avec des galaxies avec un redshift $z > 6$ qu'ils comparent à un échantillon d'échantillon à faible z et à faible métallicité pour construire le SED IR. Nous réalisons le montage SED, avec le but de se concentrer sur le SED IR. Le SED IR est très difficile à construire, car nous n'avons que des détections ALMA Band 7. Ainsi, nous utilisons une estimation préliminaire du SED de chaque galaxie pour trouver son flux de 200 µm au repos, utilisé pour normaliser les

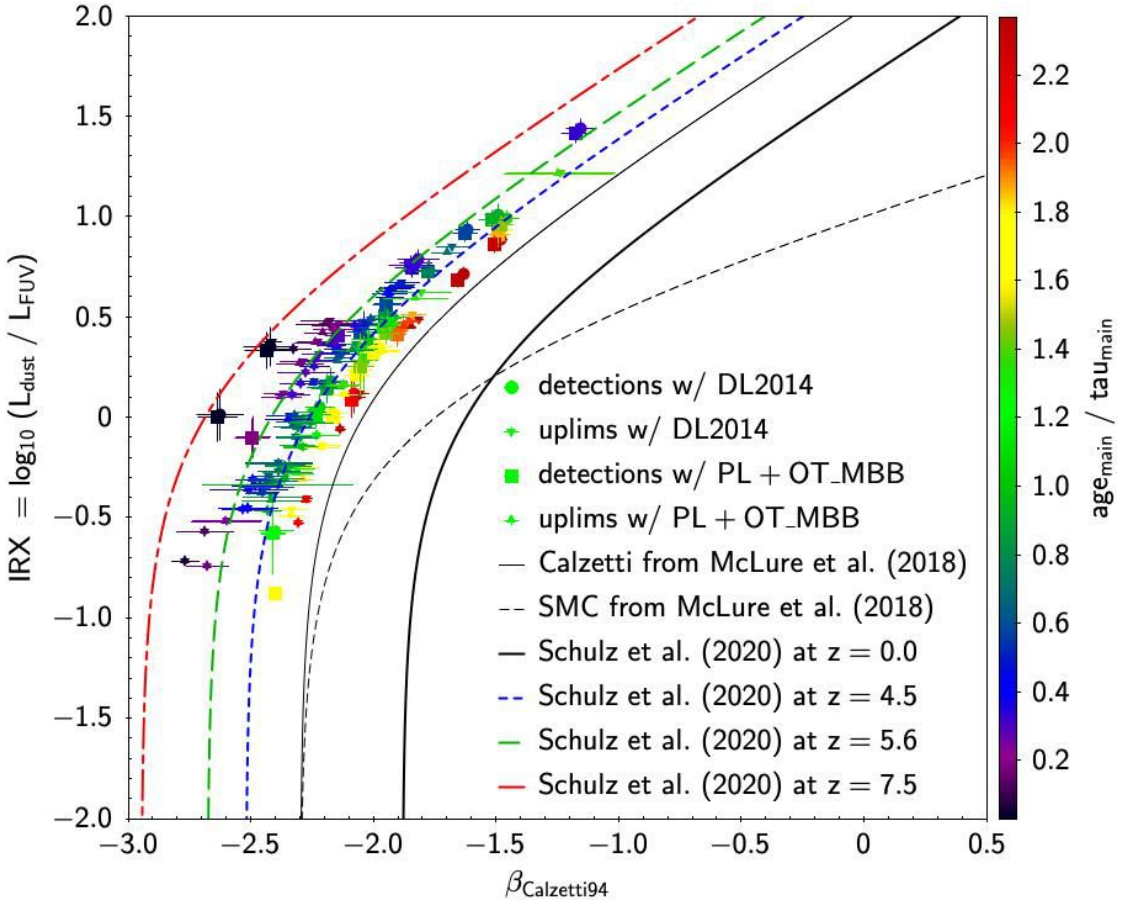

IRX - $\beta_{Cazetti-1994}$ diagramme. La ligne continue correspond à la loi de Calzetti originale et la ligne pointillée à la loi SMC, toutes deux issues de McLure et al. (2018). La couleur correspond aux valeurs de $\mathrm{age}_{\mathrm{main}}/\tau_{\mathrm{main}}$. Les cercles et les carrés représentent les modèles d'émission de poussière DL2014 et PL+OT_MBB. Graphique de Burgarella et al. (2021, in prep.).

observations ALMA de chaque galaxie. Ceci est fait dans le but de construire un seul SED à partir de l'échantillon entier dans le cadre de repos, en utilisant la dispersion naturelle du redshift pour couvrir une gamme de décalages vers le rouge.

Après avoir construit le modèle pour le SED IR en utilisant les observations ALMA combinées de l'échantillon ALPINE, nous effectuons un deuxième ajustement plus détaillé des galaxies individuelles en utilisant les paramètres du modèle d'émission de poussière que nous avons dérivés du premier ajustement. À l'aide de ces résultats, nous étudions certaines des propriétés globales de l'échantillon, telles que le diagramme sSFR-sMdust, la relation IRX-β, etc.

Enfin, nous mentionnons quelques autres voies possibles que nos futurs travaux pourraient emprunter, tout d'abord la possibilité d'étendre les travaux de notre premier article pour créer des catalogues mock réalistes de galaxies pouvant être utilisés pour tester des pipelines de traitement de données pour les futurs télescopes (JWST, MOONS) mais aussi dans le but de comparer avec les catalogues observés. Ensuite, nous prévoyons de continuer à travailler avec des modèles d'évolution chimique, de la même manière que Nanni et al. (2020). Nous prévoyons également de continuer à travailler sur les galaxies de l'Univers ancien, dont d'avantage d'observations avec ALMA et NOEMA sont attendues pour poursuivre nos projets actuels sur de nouveaux ensembles de données originales.

Le Chap. 5 concerne l'avenir de nos conclusions du Chap. 4, une œuvre qui n'en est qu'à ses débuts. Brièvement, ce que nous prévoyons de faire est très similaire aux travaux de Nanni et al. (2020), nous souhaitons étudier les modèles d'évolution chimique et les utiliser pour en savoir plus sur l'échantillon ALPINE. Nous prévoyons d'explorer davantage la possibilité d'une accumulation très rapide de poussière dans l'Univers primitif et de faire de nouveaux progrès pour expliquer ce phénomène.

Mots clés: Galaxies: evolution, Modélisation, Poussière cosmique

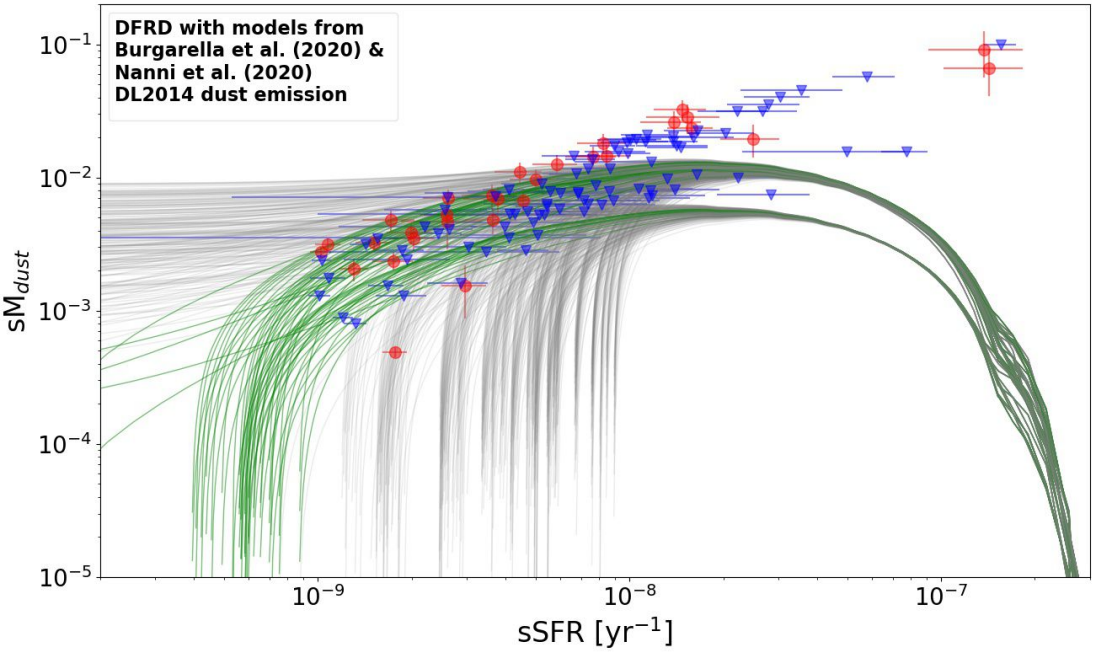

Relation entre la masse spécifique de poussière et le taux de formation d'étoiles spécifique, par rapport aux modèles définis dans Burgarella et al. (2020) et Nanni et al. (2020). Notez que le facteur 2,32 nécessaire pour faire correspondre les émissions PL+OT_MBB à DL2014 est appliqué dans ce graphique. Graphique de Burgarella et al. (2021, in prep.).

Abstract

My thesis is in the field of extragalactic astronomy, concerned with multi-wavelength data for distant (high-redshift) galaxies, combining the main galaxy parameters estimated by SED fitting with the study of cosmic dust. A review of the main concepts in this work is first shown: a brief history of the Universe that explains the place and environment of the galaxies of interest, an explanation of the models used when performing the SED fitting, particularly those included in the code CIGALE, an overview of the global parameters of galaxy populations in the high-redshift Universe, and a summary of the physical properties of dust, as a basis for future models of early Universe dust grains.

The theoretical introduction is followed by the findings reported in the paper I published during my PhD as the first author. This work relates the dust attenuation to the stellar mass of star-forming galaxies, and its evolution with redshift. A sample of galaxies with an estimate of the dust attenuation computed from the IRX which is the ratio of the dust luminosity to the far ultraviolet luminosity (L_{dust}/L_{FUV}) was used. The dust attenuation vs. stellar mass data, separated in redshift bins, was modelled by a single parameter linear function, assuming a nonzero constant apparent dust attenuation for low mass galaxies. The origin of this effect is still to be determined and several possibilities are explored (actual high dust content, variation of the dust-to-metal ratio, variation of the stars-dust geometry). The best-fitting parameter of this model is used to study the redshift evolution of the cosmic dust attenuation and is found to be in agreement with results from the literature. This work also gives evidence to a redshift evolution of the dust attenuation-stellar mass relationship, as is suggested by recent works in the highest redshift range.

Following is the chapter summarising the work that will shortly be published with me as a second author. We continue the work of Burgarella et al. (2020) using similar methods on the ALPINE galaxy sample, which provides a measurement of the [CII]158μm line of $4.5 < z < 6.5$ galaxies. This sample has been observed by various surveys, thus an extensive ancillary multi-wavelength data catalogue is available. We perform SED fitting on the ALPINE galaxies with CIGALE, aiming to determine the galaxy parameters, namely the stellar mass, SFR, stellar ages, dust mass, UV slope, etc. Using the results of the SED fitting, we extend the results of Burgarella et al. on several key diagnostic diagrams, which will be used to study the evolution of galaxies and the buildup of dust through cosmic times.

Finally, we mention some other possible paths our future work might take, firstly the possibility of extending the work of our first paper to create realistic mock catalogues of galaxies that can be used to test data treatment pipelines for future telescopes

(JWST, MOONS). Next, we plan to continue working with chemical evolution models, similarly to Nanni et al. (2020). We also plan to continue working with early-Universe galaxies, so more observations with ALMA are expected and further continuation of our current projects on new datasets is anticipated.

Keywords: Galaxies: evolution, Modelling, Cosmic Dust

Remerciements

I would like to take this opportunity to thank everyone that has helped me during my time as a PhD student. It would probably take books to express all of the gratitude I feel, so I will briefly mention the most important people in my life, and if I left someone out, please understand that I am writing this text under the pressure of finishing the thesis.

First of all, I wish to thank my supervisor Denis, who has been there for me every single time that I needed any help, no matter how basic or ridiculous, while at the same time allowing me to have my independence and treating me like a real scientist since the first day we started working together. He has taught me a lot about astrophysics, but also about the world of science, about how to manage my time better, and too many other things to name here. I would also like to thank Veronique, because her guidance, especially during my Masters years was invaluable.

Next, I want to thank my family, whose support I have always had unconditionally. Specifically, I would like to thank my mother Biljana for teaching me the most important things in life, and before all how to be myself; my father Goran, for teaching me to be persistent and methodical with my approach; my brother Matej for showing me what true dedication and focus looks like, as well as my grandparents that helped me see the beauty in knowledge for as long as I can remember. I would never be where I am without the inspiration and support from my family, and I hope that I have made them proud.

I would also like to thank my friends, some of whom I have known practically my entire life, and others that I met on my journey in France. They all have left a mark on my life by being there for me whenever I needed them, and for accepting me when I am being 100% myself. So, in no particular order, I would like to thank my friends Jorge, Junais, Gayathri, Elena (from Treviso), Arturo, Alessia, Ana, Natasha, Elena (from Bitola), Mateja and Maja.

Furthermore, I would like to thank everyone that supported my academic journey thus far: my primary high school teachers, University professors, MOOCs creators, administrative staff, etc. Maybe it is a bit unusual, but I would like to thank France, for accepting me and giving me a high-quality education worthy of a proper scientist. Finally, I would like to take this opportunity to thank the members of my jury: Dr Karina Caputi, Dr Hervé Dole, Dr Rychard Bouwens and Dr Daniel Schaerer, first for agreeing to be a part of my jury, but mostly for taking the time to read my manuscript and attend my thesis defence. It will be an honour to have you as part of my doctoral degree.

Contents

Résumé 7

Abstract 10

Remerciements 11

Contents 12

List of Figures 14

List of Tables 21

1 Introduction 22

Introduction 25

2 Theoretical considerations 26
2.1 History of the Universe . . . 27
2.1.1 Before the first galaxies . . . 27
2.1.2 The first galaxies: Cosmic reionisation . . . 29
2.2 SED fitting . . . 31
2.2.1 Star Formation History . . . 32
2.2.2 Single Stellar Population . . . 34
2.2.3 Dust attenuation . . . 36
2.2.4 Dust emission models . . . 39
2.2.5 Nebular emission, AGNs and redshifting . . . 41
2.2.6 Bayesian approach to estimate uncertainties . . . 42
2.2.7 Determining the physical parameters . . . 42
2.2.8 Determining the redshifts . . . 45
2.3 Cosmic properties of galaxies . . . 46
2.3.1 Luminosity and mass functions . . . 47
2.3.2 Luminosity and mass densities . . . 51
2.3.3 Star formation rate density and cosmic dust attenuation . . . 52
2.3.4 Main sequence of galaxies . . . 55
2.3.5 IRX - beta relation . . . 56
2.4 Physical properties of dust . . . 58
2.4.1 Roles of dust . . . 59

2.4.2 Life cycle of dust . . . 60

3 Evolution of the dust attenuation with stellar mass and redshift 63
3.1 The data used . . . 64
3.2 Evolution of the dust attenuation . . . 67
3.2.1 Dust attenuation as a function of stellar mass . . . 68
3.2.2 Redshift evolution of the dust attenuation . . . 69
3.3 Comparison with the cosmic dust attenuation . . . 71
3.4 Tested functions . . . 73
3.4.1 Fitting the dust attenuation - stellar mass relationship . . . 74
3.4.2 Fitting the dependence of the dust attenuation with redshift . . . 76
3.4.3 Integration limits for calculating the average dust attenuation . . . 77
3.4.4 Iterations to improve the fitting . . . 78
3.4.5 In 3D: dust attenuation as a function of both stellar mass and redshift . . . 80
3.5 Implications of this work . . . 81
3.5.1 The apparent dust attenuation of low-mass galaxies . . . 82
3.5.2 The evolution of the $A_{FUV} - M*$ relation with redshift . . . 88
3.5.3 Potential future uses . . . 89
3.5.4 Limits of this work . . . 92
3.6 Main points of the BB2020 paper . . . 93

4 Early evolution of the first dust grains 94
4.1 Background: summary of the work of Burgarella et al. (2020) . . . 95
4.1.1 Deriving the physical parameters . . . 95
4.1.2 Main results and conclusions . . . 97
4.2 The ALPINE-ALMA [CII] Survey . . . 99
4.3 Methodology . . . 102
4.4 Preliminary results . . . 105

5 Future work: The gas, metal, and dust evolution in low-metallicity local and high-redshift galaxies 110
5.1 Chemical evolution models . . . 110
5.2 Summary of Nanni et al. (2020) . . . 114
5.3 The future of our project . . . 116

6 Conclusion 119
6.1 Summary . . . 119
6.2 Perspectives . . . 121

Bibliography 124

APPENDIX 141

List of Figures

0.1 La dépendance de l'atténuation de la poussière UV sur la masse stellaire avec les paramètres dérivés par ajustement comme décrit dans la Sect. 3.2.1, montrant le modèle à différents redshifts. Les différentes lignes colorées montrent l'Eq. (3.1), pour la valeur de a calculée par Eq. (3.2) au redshift approprié. 4

0.2 IRX - $\beta_{Cazetti-1994}$ diagramme. La ligne continue correspond à la loi de Calzetti originale et la ligne pointillée à la loi SMC, toutes deux issues de McLure et al. (2018). La couleur correspond aux valeurs de $\mathrm{age}_{\mathrm{main}}/\tau_{\mathrm{main}}$. Les cercles et les carrés représentent les modèles d'émission de poussière DL2014 et PL+OT_MBB. Graphique de Burgarella et al. (2021, in prep.). 6

0.3 Relation entre la masse spécifique de poussière et le taux de formation d'étoiles spécifique, par rapport aux modèles définis dans Burgarella et al. (2020) et Nanni et al. (2020). Notez que le facteur 2,32 nécessaire pour faire correspondre les émissions PL+OT_MBB à DL2014 est appliqué dans ce graphique. Graphique de Burgarella et al. (2021, in prep.). . . . 8

1.1 A diagram representing some of the main fields of astronomy and extragalactic astronomy. The discipline that contains my thesis (evolution of galaxies) is in boldface. The classification is based on the navigation section *Major subfields of astronomy* from the *Astronomy* Wikipedia page. 23

2.1 Propagation of the initial fluctuation of the Universe with time. Figure from Percival (2009). 27

2.2 Representation of the history of the Universe in comoving coordinates, starting from today ($z = 0$) at the centre until the Big Bang ($z = \inf$), with a notation of the main epochs and their corresponding redshifts. Figure from Loeb (2010). 28

2.3 Another representation of the history of the Universe, this one depicting more clearly the creation of ionisation bubbles (yellow) around the first stars and galaxies, surrounded by the neutral hydrogen (grey), illustrating the continuous process of reionisation of the Universe as a function of cosmic time. Figure from Barkana (2006). 30

2.4 Summary of the stellar population synthesis technique. The final result is the composite stellar population emission (CSP, Eq. 2.1), the main ingredients of which are the star formation history (SFH), chemical composition, dust attenuation and extinction, as well as the emission of a single stellar population (SSP), which, in turn, is built from an initial mass function (IMF) combined with the isochrones from stellar evolution models, which leads to the appropriate number and type of spectra to be assigned. Figure from Conroy (2013). 33
2.5 The SFH options of CIGALE: `sfh2exp` (blue: two decreasing exponentials, orange: a single decreasing exponential, green: one increasing exponential), `sfhdelayed` (red and purple: delayed SFH with different timescales), and `sfhperiodic` (pink: periodic exponential, brown: periodic rectangular) modules, as well as the velocity-dependent SFH proposed by Buat et al. (2008) marked by the grey line. Figure from Boquien et al. (2019). 35
2.6 Comparison between the Salpeter (1955) and Larson (1998) IMFs. The different values quoted as m_c are for the different characteristic masses. Figure from Calura et al. (2013). 37
2.7 Examples of attenuation curves computed with CIGALE, using the `dustatt_modified_starburst` module. The blue, green, and red lines correspond to a value for δ of 0.00, -0.25, and -0.50. The solid, dotted, and dashed lines show the addition of the 220 nm bump with amplitude 0, 1.5, and 3, respectively. Figure from Boquien et al. (2019). 38
2.8 The different emission spectra produced by varying the parameters of the `dl2007` module. Two different values of q_{PAH} are given: $q_{PAH} = 4.6\%$ (panels *a* and *b*) and $q_{PAH} = 1.77\%$ (panels *c* and *d*), two values of U_{min}: $U_{min} = 1$ (panels *a* and *c*) and $U_{min} = 10$ (panels *b* and *d*), and five different values of γ, represented by the different coloured curves in each panel, the values being $\gamma = 0, 0.005, 0.01$ and 0.02. Figure from Draine & Li (2007). 40
2.9 An image of a field in three different filters where an example of a U-band drop-out galaxy is seen. The galaxy in the circle is seen in the red and green filters, but it is not detected in the UV filter. Figure from Schneider (2006, Chapter 9). 46
2.10 The LF for estimated for different redshifts, based on the VVDS rest-frame FUV luminosity, fitted with a Schechter (1976) function. The dashed lines represent an extrapolation of the LF beyond the magnitude limits of each redshift bin. Figure from Cucciati et al. (2012). 48

2.11 Left: The galaxy MFs in the redshift range $0.2 < z < 4$ of Ilbert et al. (2013). The redshift bins, each marked by a different colour, have a variable step size. As a reference, the local MFs from Moustakas et al. (2013) (triangles) and Baldry et al. (2012) squares are shown. Figure from Ilbert et al. (2013). Right: The galaxy MFs in the redshift range $4 < z < 8$ of Song et al. (2016). The local MF of Baldry et al. (2012) (grey line) is also given. Figure from Song et al. (2016). 50
2.12 The fitting of the Schechter parameters. The functions used are $\mathscr{M}^* = (k_1 + k_2 z)/(1 + (z/k_3)^{k_4})$, where $k_1 = 10.52$, $k_2 = 2.38$, $k_3 = 4.80$ and $k_4 = 1.15$; $\log\phi_* = (l_1 - 0.56z)$, with $l_1 = -2.47$; $\alpha = m_1 + m_2 z$, with parameters $m_1 = -1.25$ and $m_2 = -0.13$. 50
2.13 Top: Evolution of the Schechter mass function with cosmic time. The colour coding represents the passage of time, from red to blue. Bottom: Same colour coding, but this time the galaxy mass density is shown as a function of stellar mass. Figure from Wright et al. (2018) 51
2.14 Compilation of measurements of the evolution of the MD with redshift calculated by integrating the stellar MF in the work of multiple authors. The red stars marked as *this work*, come from integrating the Schechter functions found by Davidzon et al. (2017), while the brown stars are from fitting with a fixed $\mathscr{M}^*$. The references alongside their notation in the label are the following: Madau & Dickinson (2014): MD14 (grey solid line), Behroozi et al. (2013): B+13 (black dashed line), Caputi et al. (2011): C+11, Caputi et al. (2015): C+15, Duncan et al. (2014): D+14, Gonzalez et al. (2011): G+11, Grazian et al. (2015):G15, Ilbert et al. (2013): I+13, Mortlock et al. (2011): M+11, Mortlock et al. (2015): M+15, Muzzin et al. (2013), M+13, Reddy et al. (2012): R+12, Santini et al. (2012): S+12, Song et al. (2016): S+16, and Tomczak et al. (2014): T+14. The MD14 and B+13 lines are estimated by integrating their SFRD. Figure from Davidzon et al. (2017), their Fig. 17. 52
2.15 The history of cosmic star formation from FUV+IR rest-frame measurements. A conversion factor of 1.15×10^{-28} is used, (one that is around 20% lower than the classical Kennicutt (1998) value. The best-fit SFRD-z evolution is plotted with a full line and has the shape of $\psi(z) = 0.015 \frac{(1+z)^{2.7}}{1+[(1+z)/2.9]^{5.6}} \mathrm{M}_\odot \mathrm{year}^{-1} \mathrm{Mpc}^{-3}$. The notations of the data points are the following: Wyder et al. (2005): blue-grey hexagons, Schiminovich et al. (2005): blue triangles, Robotham & Driver (2011): dark green pentagons, Cucciati et al. (2012): green squares, Dahlen et al. (2007): turquoise pentagons, Reddy & Steidel (2009): dark green triangles, Bouwens et al. (2012): magenta pentagons, Schenker et al. (2013): black crosses, Sanders (2003): brown circles, Takeuchi et al. (2003): dark orange squares, Magnelli et al. (2011): red open hexagons, Magnelli et al. (2013): red filled hexagons, and Gruppioni et al. (2013): dark red filled hexagons. Fig. 9 of Madau & Dickinson (2014). 54

2.16 The MS of Speagle et al. (2014), represented by Eq. 2.33 computed in a range of redshifts, excluding the first and last 2 Gyr of their sample. Figure from Speagle et al. (2014). 56
2.17 A representation of different IRX-β relationships obtained by varying the slope of the dust attenuation law $S = A_{FUV}/A_V$ (notations along the curves). The bottom scale shows the β-slope calculated in the bands defined by Calzetti et al. (2000) and the top scale is β calculated from the continuum. The dashed lines show the dust attenuation in the V band, A_V. Figure from Salim & Narayanan (2020). 57
2.18 Grain surface interactions mechanism 60
2.19 A schematic representation of the life cycle of dust in the interstellar medium. Figure from Zhukovska & Henning (2014). 61

3.1 The dependence of the UV dust attenuation on stellar mass, showing the data from several references, along with the best-fitting model for the same redshift. Each panel represents the data from a different paper, with multiple different lines within one panel are models for different redshift bins. The dashed lines represent the model proposed in Eq. (3.3), while the full lines show the model of Eq. (3.1). 66
3.2 The dependence of the UV dust attenuation on stellar mass with the parameters derived by fitting as described in Sect. 3.2.1, showing the model at different redshifts. The different coloured lines show Eq. (3.1), for the value of a computed by Eq. (3.2) at the appropriate redshift. . . 69
3.3 Fitting the parameter a from the $A_{FUV} - M_*$ relationship in each redshift. Each point has been obtained by fitting the available data in that redshift. The black line represents the fit of these points, as fitted with the function of Eq. (3.2). 70
3.4 The evolution of the dust attenuation in the FUV with redshift. The full black line represents the integrated average dust attenuation, calculated with the model of Eqs. (3.2) and (3.1). In this case, $\overline{A_{FUV}}$ has been computed using the limits of $6 < \log M_* < 14$, analogous to the limits of integration used in the work of Burgarella et al. (2013). The shaded area around the full black line corresponds to the total estimated 1-σ uncertainty of the parameters of Eq. (3.1), alongside the errors of the fitting for the coefficients of Eq. (3.2). We note, however, that the uncertainties might be under-evaluated at low redshift. The origin of this under-evaluation is not clear but may come from the fitting of Eq. (3.2) for $z = 0$. The points represent the mean values estimated in this work for $z > 4$. The dotted green line and the shaded green area surrounding it comes from Burgarella et al. (2013). The line is the best-fitting model, and the shaded area is the error bars. The dashed dark blue line shows the results of Cucciati et al. (2012). 72

3.5 The evolution of the dust attenuation in the FUV with redshift. The full black line represents the integrated average dust attenuation, calculated with the model of Eqs. (3.3) and (3.2). The only galaxies included are those with $\log M_* > 9$. Consequently, the limits of integration for $\overline{A_{FUV}}$ have shifted to the range $9 < \log M_* < 14$. The shaded area around the full black line corresponds to the total estimated 1-σ uncertainty of the parameters of Eq. (3.3), namely the uncertainty of the intercept of the function estimated with the χ^2 method, alongside the errors of the fitting for the coefficients of Eq. (3.2). The points represent the mean value of the data we included in our work (Fig. 3.1) for $z > 4$, with the error bars representing the 1-σ dispersion around the mean value. The dotted green line and the shaded green area surrounding it come from Burgarella et al., 2013. The line is the best-fitting model and the shaded area is the error bars. The dashed dark blue line shows the results of Cucciati et al., 2012. 75
3.6 Left: A linear fit of the Salim et al. 2018 data, given as an example. The function is integrated to obtain the plot in the right panel, alongside similar data plots in different redshifts, not shown here for simplicity. Right: The average dust attenuation $A_{FUV} - z$ is computed by multiplying with the mass function and integrating within some limits. Each line of a different colour represents different integration limits. 78
3.7 An iterative process used to improve the functions used in this project. 79
3.8 The dependence of the dust attenuation in the UV on stellar mass and redshift. The surface represents the model shown in Eq. (3.4). If we take, for example, any value $\log M_* = \text{const.}$, we retrieve the dependence given by Eq. (3.2), shown in Fig. 3.3. Similarly, for any value of the redshift, we retrieve the models of Eq. (3.1), shown in Fig. 3.1. 80
3.9 The different phases of the ISM included in the G.A.S. models. The arrows between them show the relations between the phases and the processes that are considered in the models. Figure from Cousin et al. (2019a), G.A.S. Paper I. 83
3.10 The IRX-M_* diagram of the results from the G.A.S. simulations. The blue dots represent the objects, with a dashed line marking their median value. Comparison to the literature is also presented. Figure from Cousin et al. (2019b), G.A.S. Paper II. 84
3.11 The IRX-M_* diagram of the results from the FIRE-2 simulations. The black and red dots represent the objects with a different value of the f_{dust}. Each object is shown twice, once in red and once in black. The dashed line marks the consensus relation from Bouwens et al. (2016). Comparison to the literature is also presented. Figure from Ma et al. (2019). 85

3.12 A diagram showing the effects of the geometry on the attenuation curve. In the top panel the stars and dust are mixed, so the blue-ish attenuation is lower. On the other hand, the bottom panel shows a "clumpy" geometry, with the dust acting as a screen, and in this case the reddening produced is a lot more significant. Figure from Calzetti et al. (2000). . . 86
3.13 A diagram showing the ratio of the IR to the UV SFR as a function of stellar mass, which is analogous to the IRX-M_* diagram. The darker shaded area is, the more objects it represents. The circles are the median stacks from Whitaker et al. (2014), blue: $0.5 < z < 1.0$, green: $1.0 < z < 1.5$, yellow: $1.5 < z < 2.0$, and red $2.0 < z < 2.5$. The thin lines represent the completeness, and the dashed line shows the average relation if Murphy et al. (2011) SFR calibrations are used. Figure from Whitaker et al. (2017). 87
3.14 The relation between the M_* and dust attenuation proxy L_{TIR}/L_{FUV}. Figure from Takeuchi et al. (2010). 88
3.15 The MF retrieved after the cuts explained in the text have been performed. 90
3.16 Using Eqs. (3.1) and (3.2) to cut the models that conform to our prior. The dashed lines represent a scatter arbitrarily chosen to be $\Delta A_{FUV} = 1$ mag. 91

4.1 A template IR SED built from combining the restframe fluxes, normalised at $\lambda_{restframe} = 200\mu$m, of the combined Hi-z sample used by Burgarella et al. (2020) in the redshift range $5 < z < 10$. The coloured curves represent a modified blackbody model for different dust temperatures in the range $30 \leq T_{dust} \leq 85$. Figure from Burgarella et al. (2020). 96
4.2 The DFRD of both the Hi-z galaxies (upper panel) and the Low-zZ sample (lower panel). The colour coding represents the age of the main stellar population, which shows that the DFRD gives a picture of the temporal evolution of galaxies as seen from right to left. Figure from Burgarella et al. (2020). 98
4.3 An SED of a typical galaxy at $z = 5$ (adapted from Harikane et al., 2018). The marked sections show the multi-wavelength data available for the ALPINE sample, including the spectral features highlighted in red and the [CII] covered by the ALPINE survey. The numbering of the sections refers to the sections of the paper of Faisst et al. (2020). Figure from Faisst et al. (2020). 101
4.4 A template IR SED built from combining the restframe fluxes, normalised at $\lambda_{restframe} = 200\mu$m, of the ALMA detected objects from Burgarella et al. (2020) and Bethermin et al. (2020). The coloured curves represent a modified blackbody model for different dust temperatures in the range $30 \leq T_{dust} \leq 85$. This figure does not include the contribution from the stacked z=5.5 objects. Figure from Burgarella et al. (2021, in prep.). . . 104

4.5 IRX - $\beta_{Cazetti-1994}$ diagram. The continuous line corresponds to the original Calzetti law and the dashed line to the SMC law, both from McLure et al. (2018). The colour coding corresponds to values of $\mathrm{age}_{\mathrm{main}}/\tau_{\mathrm{main}}$. The circles and squares represent the DL2014 and PL+OT_MBB dust emission models. Figure from Burgarella et al. (2021, in prep.). 107
4.6 Dust Formation Rate Diagrams colour-coded with τ_{age}. The upper panel comes from fitting with a Dale et al. (2014) model, and the bottom panel from fitting with a Casey (2012) model. We see that the age sequence is correlated with the building of the stellar mass, from right to left. Figure from Burgarella et al. (2021, in prep.). 108

5.1 Left: sMdust as a function of sSFR for the Hi-z sample (black triangles) and the Low-zZ galaxies (red dots). The chemical evolutionary models shown have been computed using a Chabrier IMF or a top-heavy IMF ($\alpha = 1.35$) and different condensation fractions (colours are indicated in the legend). The SFH is characterised by $\tau = 300$Myr and $M_{gas} = 100 \times M_{stars}$ is assumed. Right: same as in the left panel, but the condensation fractions are varied. Figure from Nanni et al. (2020). 116
5.2 DFRD compared to models defined in Burgarella et al. (2020) and Nanni et al. (2020). Note that the factor 2.32 needed to match PL+OT_MBB emission to DL2014 is applied in this plot. Figure from Burgarella et al. (2021, in prep.). 117

List of Tables

3.1 Summary The literature used to obtain the data, the galaxy count in each data set, values The redshift bins from each reference, the type of data, the field the data belongs to, the selection criterion as well the IMF and SFH. All authors use Bruzual & Charlot, 2003 stellar population synthesis models. For Salim et al., 2016; Salim et al., 2018 the redshift is taken to be $z = 0.1$, which is the mean value of the redshifts of all the galaxies in the sample. A range is given for the Bouwens et al., 2016 data because individual galaxies are used, and the separation of the bins is performed specifically for this work. 65

3.2 Some of the functions that we used during our preliminary fitting of the $A_{FUV} - M_*$ data. A short reason for choosing not to use any of these functions is given, but the final choice was to get the best fit with the most simple solution. 74

3.3 Some of the functions that we used during our preliminary fitting of the $A_{FUV} - z$ data. A short reason is given for choosing not to use any of these functions, but the final choice was made to get the best fit with the most simple solution, using the AIC and BIC methods. 76

5.1 The parameters used in chemical evolution models. The total mass of the system is defined as $M_t = M_g + M_s + M_w$. The **global parameters** of the models need to be specified by the investigator and are usually normalised so that the total mass is one. The goal is to derive the fraction of metals $Z(t)$, either of each metal separately or as a group. 112

1 Introduction

I was not one of those little kids with telescopes. I did not know astronomy and astrophysics were my passion until I was already in my adulthood. What has always been my passion is the pursuit of knowledge. Only after discovering more and more about the world did I realise that personally to me, the most worthwhile subject to study is astrophysics. I am a lover of all knowledge, so when I learned that the word "physics" comes from the Greek word phýsis, meaning nature, it called to me. I wanted to know about nature. As I was getting to learn more and more about the different branches of physics, I believed that studying the Universe as a whole will include everything in it, so it is as general as it gets (in theory, I suppose).

But why galaxies? And why dust? Well, I have to admit that the course of my education took me there. I did not have any classes specifically on galaxies during my undergraduate studies, so during my Masters, I felt like I lacked a proper understanding of this subject, and I was trying to make up for it. A whole new universe opened up for me. It fascinates me that the field of extragalactic astronomy is relatively recent (only a hundred years!), yet the scientific community has made remarkable discoveries and advancements. I feel that, in a way, it is one of the fields of astronomy that still has a lot more to discover, mainly because of the late start it had. I also am fascinated by the fact that a galaxy contains many other parts studied, such as stars and planets. So, as galactic and extragalactic astronomers, we must rely on these fields and incorporate them into our work.

And finally, why dust? I always get funny looks when I mention the topic of my studies. But I believe that the study of dust is interesting because of its different aspects. Firstly, many discoveries are waiting to be made in a laboratory here on Earth - astrochemistry is very much an experimental science, leading to some inspiring results. Secondly, it is impossible to understand the overall evolution of galaxies without understanding the effects of dust. Star formation, chemical evolution, planet formation, are all parts of the life-cycle of galaxies, and they all rely on dust as one of their main mechanisms. And finally, dust plays a significant role in shaping the Spectral Energy Distribution (SED) of a galaxy. We need to first fully understand everything that the galaxy underwent and is undergoing in the present (or the time when the stars emitted their light). Then we will be able to model and perfectly reproduce the full SED.

So, I present to you my thesis in the field of extragalactic astrophysics (Fig. 1.1), concerned with, as the title says, the study of dust and stars in the early Universe. More specifically, during my PhD programme, I was focused on and interested in galaxy evolution from the perspective of multi-wavelength observations and SED

modelling. It includes three different projects: one concluded, focused on the relationship between the dust attenuation and stellar mass throughout cosmic time, one in progress, concerned with the physical properties of early-type galaxies, and one in its conception, comprising chemical and dust evolution modelling of galaxies. But what are generally the questions that my thesis aims to answer, and how relevant is it to the modern scientific community?

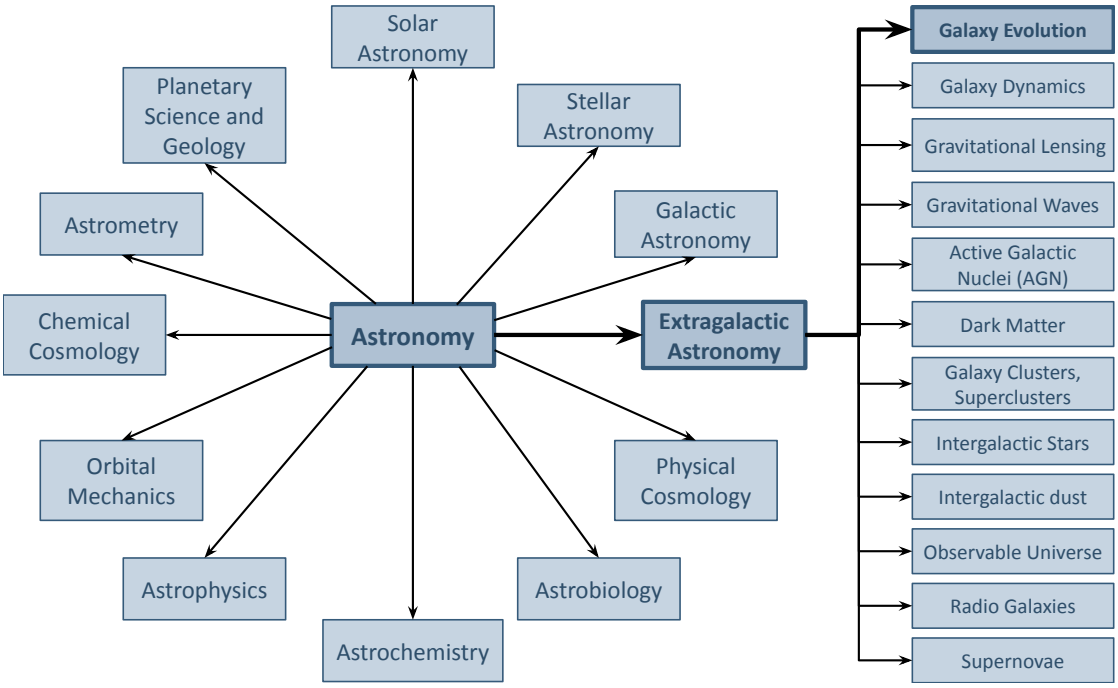

Figure 1.1: A diagram representing some of the main fields of astronomy and extragalactic astronomy. The discipline that contains my thesis (evolution of galaxies) is in boldface. The classification is based on the navigation section *Major subfields of astronomy* from the *Astronomy* Wikipedia page.

Let us look at the US National Research Council (NRC) document published by the National Academies after conducting a survey of astronomy and astrophysics for the 2010s (National Academies of Sciences, 2011). As the primary science goals, they state: *The exciting program of activities proposed here will help to advance understanding of* ***how the first galaxies formed and started to shine****. It will direct the discovery of the closest habitable planets beyond our solar system. It will use astronomical measurements to try to unravel the mysteries of gravity and will probe fundamental physics beyond the reach of Earth-based experiments. The committee found that the way to optimize the science return for the decade 2012-2021 within the anticipated resources was to focus on these three science objectives while also considering the discovery potential of a much broader research program. To achieve these objectives, a complementary effort of space-based, ground-based, and foundational, core research is required.*

NASA's decadal plan developed by the Astrophysics Subcommittee (APS) in 2013

(Kouveliotou et al., 2014): *In the next two decades existing and planned facilities will allow us to map the detailed mass assembly history of galaxies. We will be able to determine how fast the gas reservoirs in galaxies were consumed and measure how and why star formation varied, both from galaxy to galaxy and within galaxies. Since much of the star formation activity occurs deep inside dense clouds of molecular gas and dust, studying galaxies at far-infrared wavelengths, where the majority of their photons are emitted, will be extremely important. To peer into young star-forming regions on scales of a few thousand light-years will require high-spatial-resolution observations from a space-based far-infrared interferometer.*

We can see in these citations that the first galaxies are one of the most relevant questions for the astronomy and astrophysics scientific community. My research is concerned with studying the properties of galaxies, trying to go back in time as far as possible to understand the first galaxies better.

It is almost exactly one hundred years ago that our story begins. Only in the 1920s, with the work of Opik (1922), that we became convinced that there are objects outside our galaxy. In this work, he estimated the distance to the Andromeda galaxy, determining that it is an object outside the Milky Way. The observational work of Hubble (1929) followed, during which he found many objects outside the Milky Way, thus firmly establishing the foundations of extragalactic astronomy. Many worthwhile works have come since, definitely too many to mention here. I refer the reader to the review papers of Smith (2008) and Smith (2009) for a more detailed history of the field of extragalactic astronomy. The study of interstellar dust is also relatively new, starting in the 1930s with exploring the interstellar reddening, named *selective absorption* (Trumpler, 1930; Schalén, 1931). Jones et al. (2017) provide an excellent introduction to the development of this field.

We can see that this topic is still quite relevant in today's science. It is no mistake that I chose this topic, as the field seems to be promising and exciting. Some of the questions significant to the community today are the following:

- When and how did the first galaxies form?
- What mechanisms played a role in the formation and evolution of the first galaxies?
- When and how was the first dust created?

Of course, the main purpose of the PhD was to train me and introduce me to the world of galaxy evolution. I cannot claim that the discoveries that the reader will encounter in this thesis answer NRC's and NASA's questions. However, I believe that I have built a solid foundation that will be crucial for me to thrive in science and eventually play a role in answering these questions that have troubled humanity since we first looked up at the sky.

After this general introduction follows a more topic-specific theoretical introduction of the main concepts relevant to my work (Chap. 2), starting with a summary of the

known history of the Universe (Sect. 2.1) aiming to discuss the general conditions surrounding the galaxies that are of interest in this work. Then, SED fitting is being studied in some details, starting with the general ideas behind creating a galaxy SED and then focusing on the SED fitting code CIGALE (Sect. 2.2). Following are the global properties of galaxies that are useful for studying the general trends that galaxies show and attempting to find connections between them that can later help us understand the processes within the galaxies themselves (Sect. 2.3). Finally, Section 2.4 contains a summary of what we know about dust, learned from Milky Way studies. It includes the physical properties of dust, and the roles dust has in the overall processes of the galaxy.

Chapter 3 summarises my main work during the PhD. It is a more detailed explanation of the methods and results discussed in my first paper (Bogdanoska & Burgarella, 2020). The chapter starts by introducing the data that we used (Sect. 3.1). Our project uses data from the literature with information about the stellar mass and dust attenuation of galaxies at various redshifts. Section 3.2 explains our project's methodology and Sect. 3.3 presents the results we obtained. It includes both the fitting of the relationship between the stellar mass and dust attenuation and the evolution of the dust attenuation with redshift. The following section, Sect. 3.4 is the one that is most different from the published paper. Here, the different possible solutions that we tested during the project and the reasons we eventually decided against them are outlined. The last section (Sect. 3.5) discusses the implications of our results and other works that are relevant to our findings are cited. I also discuss some limitations of our results.

The chapter that follows (Chap. 4) summarises our ongoing project, during which we are using the ALPINE survey to study the physical characteristics of early-Universe galaxies, focusing on their IR emission and the dust properties we can learn from it. As it serves as a basis for our work, the recent paper of Burgarella et al. (2020) is first summarised (Sect. 4.1). Following is the description of the data we use in our project, namely the ALPINE galaxies (Sect. 4.2). Then, I present a more detailed and adapted version of the methods we are using in Sect. 4.3, and some preliminary results in Sect. 4.4. A summary and a discussion of the future work round off the chapter. However, Chap. 5 gives more details about the direction of our future work. We are interested in the more physical aspect of dust, so in Sect. 5.1 I summarise the basic chemical and dust evolution models. As the work of Burgarella et al. (2020) continues in the paper of Nanni et al. (2020), we summarise this paper and its findings in Sect. 5.2. We plan to continue in a similar matter, and although this project is still in its very early stages. I summarise the project plans in Sect. 5.3.

In Chap. 6, I rounded off the thesis with a summary of the chapters (Sect. 6.1), and the future of our work (Sect. 6.2). One appendix is also present, a reprint of the published paper (Bogdanoska & Burgarella, 2020, Chap. 3 of this thesis).

2 Theoretical considerations

Usually, when writing scientific papers, we tend to avoid including much information about the theoretical considerations and the ways of thinking that have led to the current work we are presenting. Therefore, even though scientists with a far more profound understanding of the field will read this thesis, I decided to include a detailed description of the theory behind concepts most relevant to my PhD. This way, I will have a record of what I have learned so far in my studies so that one day when I am an experienced scientist, I can look back and understand where my scientific journey started from and how far I will have reached.

The topics of the scientific chapters are all slightly different, especially if we compare Chap. 3 to Chaps. 4 and 5. However, this chapter covers the underlying principles relevant to the thesis's overall, needed to have a complete picture of the field. The following three chapters present the main projects that were part of my studies during these three years. The methodology sections of these chapters include some of the core theoretical considerations required to understand the work specific to that chapter.

My thesis belongs to the topic of extragalactic astronomy, so a short history of the Universe will open this chapter, as we are concerned with the earliest epochs of the Universe. It is essential to understand *where* (or is it *when*?) in the Universe the galaxies we are studying can be found and the environmental conditions that influenced their evolution. This part also includes a short mention of the cosmology that we used in our work.

Following this, there is an introduction of the core ideas and principles behind Spectral Energy Distribution (SED) fitting. As we use the SED fitting Code Investigating GALaxy Emission (CIGALE Boquien et al., 2019; Noll et al., 2009; Burgarella et al., 2005) in our work, the methods and models included are the ones that can be found in CIGALE, as they are the ones relevant to our work. I also outline some general ideas behind determining physical parameters and redshifts from the SED, which are not exclusive to CIGALE.

For the work in Chapter 3 and generally when studying distant galaxies, some statistical approaches are necessary. So, here we discuss the main ideas behind galaxy mass and luminosity functions, densities, some cosmic parameters and relations for the population of galaxies within the Universe.

Finally, as this thesis heavily focuses on cosmic dust, I believe it is essential to include a section on the current knowledge of dust properties. However, for the distant galaxies that we use in our work, the picture of dust might look dramatically different. Regardless, the information we have about local dust is the limit of what is currently known, and it serves as our best first approximation.

2.1 History of the Universe

Galaxies are the main building blocks of the Universe; this is why if we study the history of the galaxies, we cannot and should not avoid thinking about the history of the Universe as a whole. The processes of formation and evolution of galaxies are not independent of the overall evolution of the Universe, and it is of utmost importance to understand this connection. For this reason, I will present some of the main findings from cosmology that enable us to put the galaxies we study in the context of the Universe. It is easy to forget that galaxies are never separate from the Universe, even though the human mind needs to make the separation to study them more effectively.

The current cosmology is the standard spatially-flat 6-parameter Lambda Cold Dark Matter (ΛCDM) cosmology, implying that the Universe is made up of baryonic matter, dark matter, and the yet unknown dark energy denoted by the cosmological constant Λ. We use the values $(H_0, \Omega_m, \Omega_\Lambda) = (70, 0.3, 0.7)$, where H_0 is in the units of km s^{-1} Mpc^{-1}. The Planck 2018 results (Planck Collaboration, 2020, Table 1) give the most recent and precise values of the cosmological parameters.

2.1.1 Before the first galaxies

It all started with a Big Bang. In the beginning, our Universe was a hot and compact singularity from which it has been expanding ever since. During the first 10^{-36} to 10^{-32} seconds of the Universe, a phase transition called inflation happened. Next, quantum fluctuations caused initial overdensities in the primordial Universe, which we can today observe as temperature fluctuations in the Cosmic Microwave Background (CMB), thus planting the "seeds" of today's galaxies. The following evolution of the Universe was caused by gravity, leading denser regions to attract dark matter (DM), causing DM halos to form, as can be beautifully seen in Fig. 2.1.

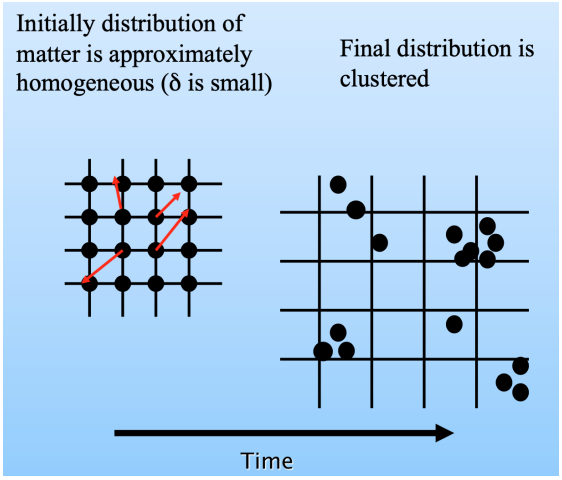

Figure 2.1: Propagation of the initial fluctuation of the Universe with time. Figure from Percival (2009).

These DM halos undergo hierarchical clustering, meaning the more massive ones swallow the less massive ones. changing the DM mass function to have a larger number of high-mass DM halos in later times, while the number of low-mass halos decreases. The Press-Schechter approach (Press & Schechter, 1974) gives the theoretical evolution of the number of DM halos, the particulars of which are beyond the scope of this thesis.

Following the Universe's history, the next significant stage is the birth of the first hydrogen atoms, named (re)combination. Only after the Universe cooled to a temperature below 3000 K did the density become low enough to allow recombination. Thus, the photons decoupled and could escape the hydrogen atoms at this exact moment, creating the Cosmic Microwave Background (CMB) radiation. This burst of light was followed by 400,000 years of darkness, called the dark ages, where no optical light was emitted until the creation of the first stars and galaxies. Fig. 2.2 (Fig. 2.2 of Loeb (2010)) summarises these early Universe stages.

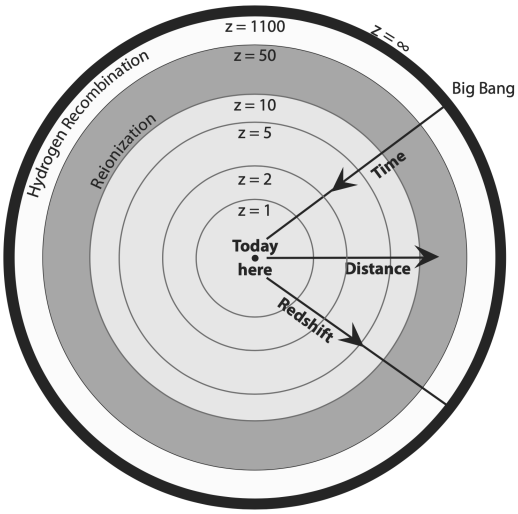

Figure 2.2: Representation of the history of the Universe in comoving coordinates, starting from today ($z = 0$) at the centre until the Big Bang ($z = \inf$), with a notation of the main epochs and their corresponding redshifts. Figure from Loeb (2010).

Another important event around this time is the first stars' creation, called Population III (PopIII) stars. These stars are made up of primordial gas, so they are metal-free and have been considered to be very massive and solitary, meaning only one star per DM halo, even though there is recent evidence suggesting otherwise. The study of these very first objects that shined a light in the Universe is indeed fascinating and a field of research on its own, so for more details, I refer the reader to the recent review of Klessen (2019) and references therein. However, these first stars are worth mentioning in this thesis, as the metals created within the cores of these stars shaped the galaxies we wish to study, thus setting the stage for their formation and evolution.

2.1.2 The first galaxies: Cosmic reionisation

The formation of the first galaxies is an exciting topic of study, and it is widely accepted that it marks the end of the Universe's dark ages and the beginning of the Epoch of Reionisation (EoR). The study of EoR touches many fields of astrophysics, which is why it is also appropriate for the theoretical introduction chapter of this thesis. Furthermore, determining the beginnings of the EoR is synonymous with defining the epoch in which the first objects were formed in the Universe, a goal I wish to contribute with the work that I will present later in this thesis and my future work. Finally, a very useful, albeit slightly beginner, resource on this topic is the book *The First Galaxies* (Wiklind et al., 2013), which helped me to find references on some of the topics I was less familiar with.

Until the end of the dark ages, the intergalactic medium (IGM) is neutral, with the first structures forming far and few between. As the Universe evolved, so did these structures that we currently call the first stars and galaxies became more and more common due to gravitational collapse. The first sources that emitted ionising light were the first stars and black holes. The surrounding gas efficiently absorbed their radiation, thus began the early reionisation. The first galaxies formed around redshift $z = 45$, marking the full-blown beginning of the EoR (e.g. review by Bromm & Yoshida, 2011).

During the EoR, the IGM becomes progressively more ionised, and during this transitional epoch, two very distinct phases of the IGM co-exist, the neutral regions and regions of ionised hydrogen. It is only in the immediate surroundings of the first stars and galaxies that the hydrogen is ionised, and these early-type radiation-emitting objects form *bubbles* consisting of HII created by the emitted UV radiation around them. As time progresses and the Universe enters deeper into the EoR, the number of sources producing these bubbles increases, and these bubbles expand beyond their initial dimensions, until they begin overlapping and eventually ionise the entire Universe (e.g. Barkana & Loeb, 2001), as can be seen in Fig. 2.3 (Fig. 1 of Barkana (2006)). The rate and efficiency at which the ionisation process was undergoing is still not completely understood but has been the topic of interest of many researchers and includes incorporating many different assumptions and processes (e.g. Ciardi & Ferrara, 2005). However, this process did not happen simultaneously throughout the Universe; as more sources increase the ionisation, regions with higher densities were quicker to ionise their surroundings, a feature that should be present in the power spectrum of low mass galaxies. Other details concerning this process still need to be determined, but this is beyond the scope of this thesis.

The exact sources of ionisation are still a mystery. It takes 13.6 eV to ionise hydrogen, and the origin of these UV photons in the Universe is an active field of research. Some of the most studied candidates are the first, Population III (PopIII), stars, as well as second-generation, Population II (PopII) stars (Bromm & Larson, 2004), alongside so-called mini-quasars powered by intermediate-mass black holes (Thomas & Zaroubi, 2008). Other possibilities are considered but not as well studied, such as dark matter

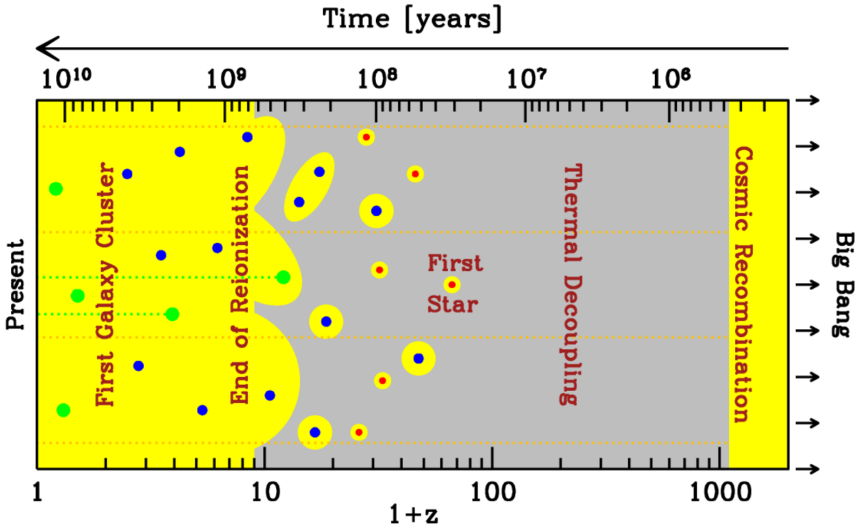

Figure 2.3: Another representation of the history of the Universe, this one depicting more clearly the creation of ionisation bubbles (yellow) around the first stars and galaxies, surrounded by the neutral hydrogen (grey), illustrating the continuous process of reionisation of the Universe as a function of cosmic time. Figure from Barkana (2006).

or cosmic strings.

From what is currently known, the limits of EoR in terms of redshift are $6 < z < 15$, which is within the domain of this thesis. A significant shift during this period is that dark matter dominated the building of the Universe's structure in the ages before, whilst from the EoR until now, the cosmic gas is the driver of the formation and evolution of structures on small scales. For further reading on the topics touched upon in this section, I refer the reader to the books *How Did the First Stars and Galaxies Form?* (Loeb, 2010) and *The First Galaxies in the Universe* (Loeb & Furlanetto, 2013).

Observationally studying the EoR requires using multiple probes, as it is a challenging region to observe. The various methods give information about different aspects of this era. For example, the total Thomson scattering of the CMB photons is an indicator of the optical depth of the Universe, which provides information that the Universe was predominantly neutral to start (after the emission of the CMB) and until 400 million years later when it became ionised. These measurements come from the CMB temperature and polarisation data most recently from the Planck satellite (Planck Collaboration, 2020) and is a topic with many reviews, e.g. Aghanim et al. (2008). Yet, this probe can determine neither the duration of the EoR nor the sources of its occurrence.

We know from observations of the Lyman α Forest (a spectral feature in distant quasars) that the present-day Universe is ionised to a large extent and that looking back in time, this ionised state changes to neutral around redshift $z = 6.5$, which marks the end of the EoR (e.g. review by Rauch, 1998). Some other probes include

studying the IGM at redshift $z < 6$, looking at the information from the cosmic infrared background and the soft X-ray background give us (Dijkstra et al., 2004), quasars in the high redshift Universe (Mortlock et al., 2011), Gamma-Ray Bursts (GRBs) (Bromm & Loeb, 2006), high-z metal abundances (Rudie et al., 2012), and the 21 cm HI fine transition redshifted line (review in the Chapter of Zaroubi (2013) in the *First Galaxies* (Wiklind et al., 2013) textbook).

2.2 SED fitting

The galactic properties data in this thesis mainly come from fitting the SED with state-of-the-art methods and models. It is the primary technique used throughout my work, even at times when done implicitly. That is why it is necessary to understand some of its basic principles: to deepen the understanding of the results, especially regarding how much we can trust them and improve them. To include all of the possible techniques, models, or even codes used to fit and model the SED of galaxies is well beyond the scope of this thesis, and relevant reviews on this topic are those by Walcher et al. (2011) and Conroy (2013). The focus of this section will be on the SED fitting included in the code CIGALE[1] (Burgarella et al., 2005; Noll et al., 2009; Boquien et al., 2019) created, constantly developed and improved at Laboratoire d'Astrophysique de Marseille (LAM). Being part of the LAM team, I have used CIGALE for the work shown in Chapters 3, 4 and 5.

An SED of a galaxy, meaning the distribution of its radiated energy over wavelength or frequency, comprises multi-wavelength photometric and spectroscopic data. When extracting relevant parameters from the SED, we usually compare it to many models generated from a range of assumed values for their parameters to find the one that fits the data best, and thus the parameters that best describe the physical properties of the studied galaxy.

Determining the most important quantities of galaxies is based on a good sampling of the SED, including multi-wavelength photometry in various filters, such as the rest-frame UV and optical from which the age of the galaxy can be estimated alongside the star formation rate, and the infrared (IR) where the dust and gas properties can be explored. Ideally, photometric data would be accompanied with spectroscopy, which hides information about the stellar populations, metallicity, and other relevant galaxy parameters.

The light emerging from a galaxy is the radiation of all of the stars within the galaxy, gas and dust emission, which is then partially diminished by dust extinction. Young stars have strong UV radiation, but the size of the dust grains is such that they are very efficient in absorbing this UV light, making it hard to study the star formation of the galaxy. But, the absorbed and scattered far-UV (FUV) radiation does not disappear into the vacuum of the Universe, it is re-emitted as an IR light, and it is this energy-balance principle that makes it possible to combine the UV and IR SEDs and to look

[1] https://cigale.lam.fr/

at the SED as a whole. CIGALE relies on the energy balance principle, making it very suitable for detailed studies of the influence of dust on the light emerging from the galaxy.

Modelling the SED is based on determining the emission of a Composite Stellar Population (CSP) that includes stars with a range of ages and metallicities and dust contribution. We define it with the following equation:

$$f_{CSP}(t) = \int_{t'=0}^{t'=t} \int_{Z=0}^{Z_{max}} \Big(\mathrm{SFR}(t-t') P(Z, t-t') f_{SSP}(t', Z) e^{-\tau_d(t')} + A f_{dust}(t', Z) \Big) \mathrm{d}t' \mathrm{d}Z \tag{2.1}$$

The integration in Eq. (2.1) is by t', the stellar population age and Z, the metallicity. A diagram explaining this procedure is shown in Fig. 2.4 (Fig. 1 of Conroy (2013)). $P(Z, t)$ is a time-dependent metallicity distribution, which is usually modelled with a δ-function, meaning we assume that the whole stellar population has the same metallicity. The term $\mathrm{SFR}(t-t')$ gives the star formation rate as a function of time, i.e. the star formation history. The function $f_{SSP}(t, Z)$ gives the emission of the single stellar population (SSP) explained below. The attenuation by dust is represented by the exponential decay factor, expressed through the time-varying optical depth parameter $\tau_d(t)$. The dust emission is denoted by f_{dust}, with the value of A coming from the energy balance principle.

Today's SED modelling techniques sprouted their roots in the 1970s' with the papers of Searle et al. (1973) and Larson & Tinsley (1978). They estimated the optical SED (U, B and V colours) of modelled galaxies: they assumed an initial mass function (Eq. 2.7) expressed with a parameter α and an exponential decay of the SFR characterised by a parameter β. They also adopted a value for the galaxy's age (of around 10^{10} Myr) and included theoretical evolutionary tracks of individual stars. They use the term "star cluster" to mean a group of stars of the same age with some mass distribution (analogous to the SSP, Sect. 2.2.2) for which they compute multiple evolutionary tracks. Then, by using the (L, T_{eff}) information from the isochrones, they divide the evolutionary tracks into luminosity classes, for which conversion tables containing the values of $B-V$ and $U-B$ for each class were available. Finally, they used a relation similar to Eq. (2.6) is used to estimate to estimate each colour's total intensity.

2.2.1 Star Formation History

The star formation history (SFH) is one of the main components of the SED, and it represents the change of the galaxy's SFR with time. The shape of the SFH can be arbitrary, so in CIGALE, it is possible to use any form of the SFH as a file giving values for t and SFH. However, in practice, a few "standard", relatively simple functions describe the SFH, some of which are presented in Fig. 2.5. Usually, the SFH is normalised so that the final mass of the stars is equal to $1 M_{\odot}$, by defining a normalisation constant C_{SFH} as:

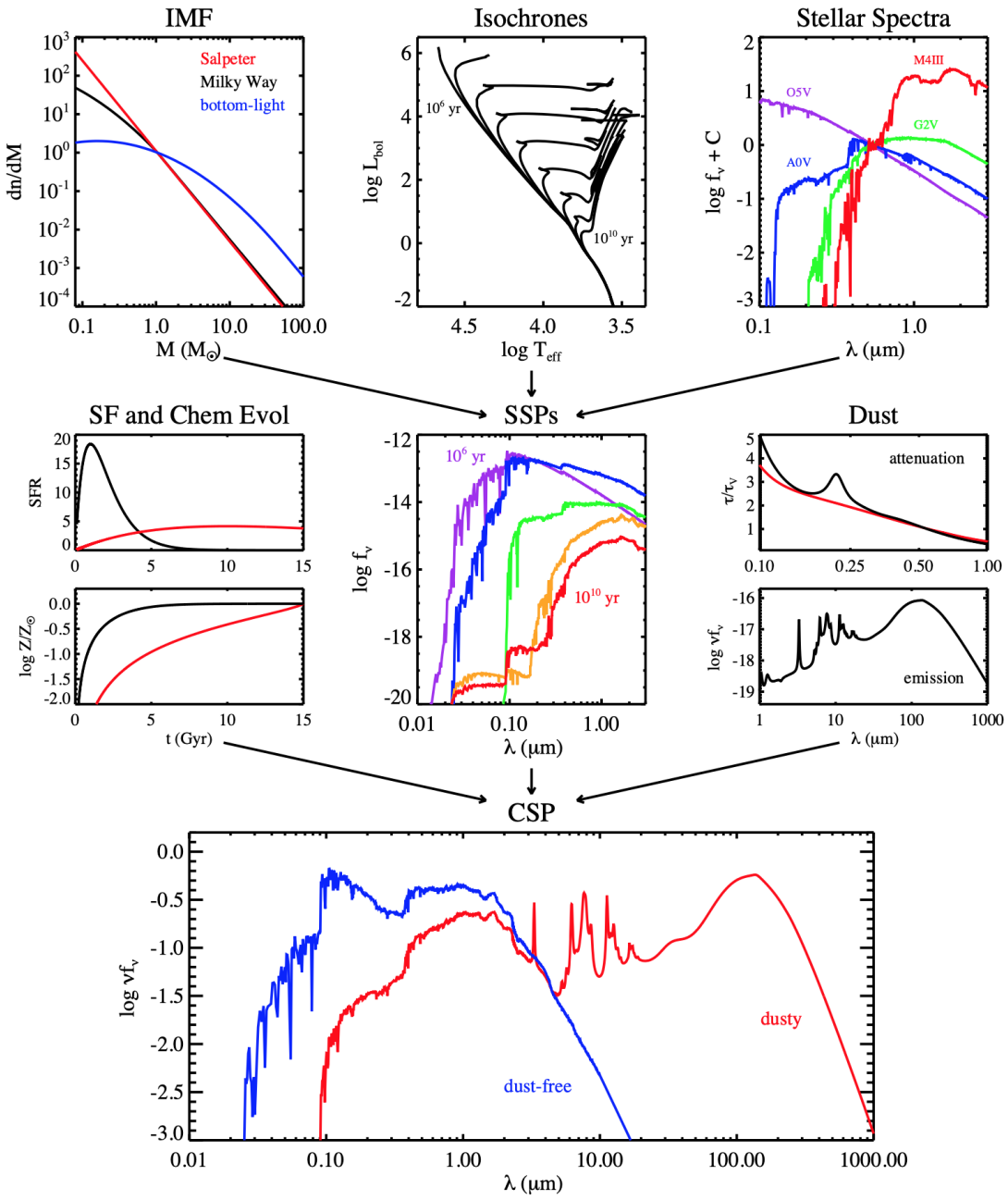

Figure 2.4: Summary of the stellar population synthesis technique. The final result is the composite stellar population emission (CSP, Eq. 2.1), the main ingredients of which are the star formation history (SFH), chemical composition, dust attenuation and extinction, as well as the emission of a single stellar population (SSP), which, in turn, is built from an initial mass function (IMF) combined with the isochrones from stellar evolution models, which leads to the appropriate number and type of spectra to be assigned. Figure from Conroy (2013).

$$C_{\mathrm{SFH}} = \frac{1 M_{\odot}}{\int_0^{t_{end}} \mathrm{SFR}(t')\mathrm{d}t'} \tag{2.2}$$

The SFH has one of the following equations:

- `sfh2exp`: one or two exponentials; t_0 is the time the galaxy started creating stars, t_1 is the time that marks the beginning of the second burst relative to t_0 (e.g. $t_0 = 13$ Gyrs ago is the time the galaxy started forming stars, and the burst appeared more recently, so at, e.g. $t_1 = 100$ Myr). τ_0 and τ_1 are the e-folding times of the two exponents, and k is the relative amplitude of the second exponential:

$$\mathrm{SFR}(t) = C_{\mathrm{SFH}} \begin{cases} \exp(t - \tau_0), & \text{if} \quad t < t_0 - t_1 \\ \exp(t - \tau_0) + k \times \exp(-t/\tau_1), & \text{if} \quad t \geq t_0 - t_1 \end{cases} \tag{2.3}$$

- `sfhdelayed`: starts with a nearly linear increase of the SFR, peaks at $t = \tau$, and then smoothly decreases. This module also allows for a burst, which is not included in the following equation:

$$\mathrm{SFR}(t) = C_{\mathrm{SFH}} \frac{t}{\tau^2} \times \exp(-t/\tau) \text{for} \quad 0 \leq t \leq t_0 - t_1 \tag{2.4}$$

- `sfh_buat08`: a, b and c depend on the rotational velocity of the galaxy, and in CIGALE uses the values of Buat et al. (2008):

$$\mathrm{SFR}(t) = C_{\mathrm{SFH}} 10^{a + b\log(t) + c t^{1/2}} \tag{2.5}$$

2.2.2 Single Stellar Population

Including the Single Stellar Population (SSP) emission is a crucial component of building the SED. It models the emission of stars of the same age, metallicity and metal abundances, analogously to stars created in the same instant from the same cloud, e.g. in stellar clusters. In Eq. 2.1, the SSP emission is marked with $f_{SSP}(t, Z)$, and the equation for determining it is the following:

$$f_{SSP}(t, Z) = \int_{m_{min}}^{m_{max}} f_{star}[T_{eff}(M), \log g(M) | t, Z] \phi(M) \mathrm{d}M \tag{2.6}$$

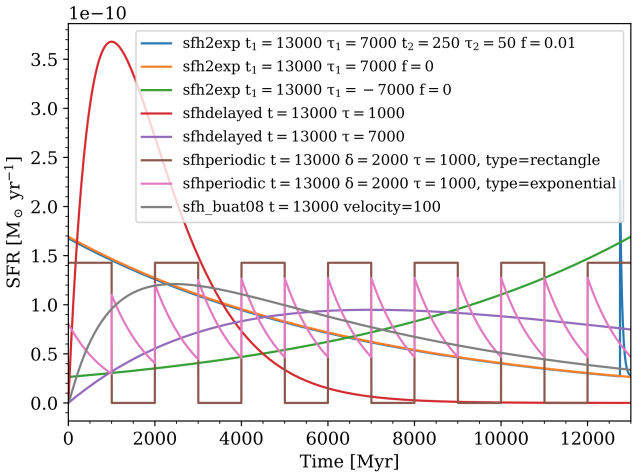

Figure 2.5: The SFH options of CIGALE: `sfh2exp` (blue: two decreasing exponentials, orange: a single decreasing exponential, green: one increasing exponential), `sfhdelayed` (red and purple: delayed SFH with different timescales), and `sfhperiodic` (pink: periodic exponential, brown: periodic rectangular) modules, as well as the velocity-dependent SFH proposed by Buat et al. (2008) marked by the grey line. Figure from Boquien et al. (2019).

In this equation, all of the components represented in Fig. 2.4 (top row) are included: the initial mass function (IMF) is denoted as $\phi(M)$, the isochrones dictate the relation between $T_{eff}(M)$ and $\log g(M)$ (effective temperature and surface gravity, the quantities on an H-R diagram) at a time t, for a metallicity Z, which together, in turn, determine the stellar spectrum f_{star} from predefined libraries. The integration is carried out within mass limits that include masses as low as $m_{min} = 0.1 M_{\odot}$, as the lower limit stellar mass for which hydrogen burning is possible, and masses as high as $m_{max} = 100 M_{\odot}$, approximately the highest mass determined by stellar evolution models. Some commonly used SSP models are the ones proposed by Leitherer (1999), Bruzual & Charlot (2003), Maraston (2005), and Vazdekis et al. (2010). In CIGALE, the available SSP modules are `bc03` (Bruzual & Charlot, 2003) and `m2005` (Maraston, 2005).

Stellar astronomers provide the stellar spectra and isochrones, and we usually include them in SED fitting codes in a way that does not require specific knowledge of stellar astrophysics. However, the IMF is a crucial galactic parameter that deserves some discussion. The IMF determines the number of stars per mass interval (more on mass function in Sect. 2.3.1), but only in the initial moment, i.e. when the SSP was born. It tells us the number of stars of each mass and thus their contribution to the spectrum. To include the evolution of the SSP, time evolution of the MF is necessary, and this is where the SFH (Sect. 2.2.1) comes into play: it accounts for the change of the number of stars with time, so that at any given moment we know the number of stars per mass, allowing us to combine the correct number and type of spectra. Moreover, it determines the overall normalisation of the mass-to-light ratio.

Choosing the correct IMF is not a simple task, as it has a huge influence on the physical parameters determined from the SED. That is why many proposed models for the IMF exist, some of which I will present here, mainly the ones that are relevant to our work:

- Salpeter (1955) IMF: power-law distribution, with the parameter $\alpha = 2.35$. In the same way, a Larson (1998) IMF, also called a "top-heavy" IMF, is defined with the parameter α having values of 1, 1.35 or 1.5, and the functional form being:

$$\phi(M) = C_{\mathrm{IMF}} m^{-\alpha} \tag{2.7}$$

- Chabrier (2003) IMF: opposing candidate of the previous IMF, with $k_1 = 0.158$ and $k_2 = 0.0443$, defined as:

$$\phi(m) = C_{\mathrm{IMF}} \begin{cases} k_1 m^{-1} e^{-\frac{1}{2}\left(\frac{\log m - \log 0.079}{0.69}\right)^2}, & m < 1M_\odot \\ k_2 m^{-2.3}, & m > 1M_\odot \end{cases} \tag{2.8}$$

The constant C_{IMF} in both cases being the normalisation factor, such that the IMF is normalised to $1M_\odot$:

$$C_{\mathrm{IMF}} = \frac{1M_\odot}{\int_{m_{min}}^{m_{max}} \phi(m')\mathrm{d}m'} \tag{2.9}$$

In Fig. 2.6 a comparison between the Salpeter (1955) ($\alpha = 2.35$) and Larson (1998) ($\alpha = 1.35$) is presented (Fig. 1 of Calura et al. (2013). However, in CIGALE, only the Salpeter (1955) and Chabrier (2003) IMFs are available for the `bc03` SSP, while for the `m2005`, the Salpeter (1955) and Kroupa (2001) IMFs are the proposed options. Shortly, an addition of a top-heavy IMF will be available, as it seems to be more suitable for the early Universe (Nanni et al., 2020). A "top-heavy" IMF implies that there is a relatively high proportion of high-mass stars when the stellar population is born, which has an impact in the resulting evolution of the M/L ratio in the galaxy.

2.2.3 Dust attenuation

After the stellar emission of a galaxy, we next need to determine the amount of light that has been diminished by dust. After the stellar emission of a galaxy, we next need to determine the amount of light that has been diminished by dust. Of the bottom panel of Fig. 2.4, I have only discussed the ingredients to create the blue line. This section and the following will outline models used to estimate the dust extinction from the UV part of the SED and the re-emission by dust in the IR.

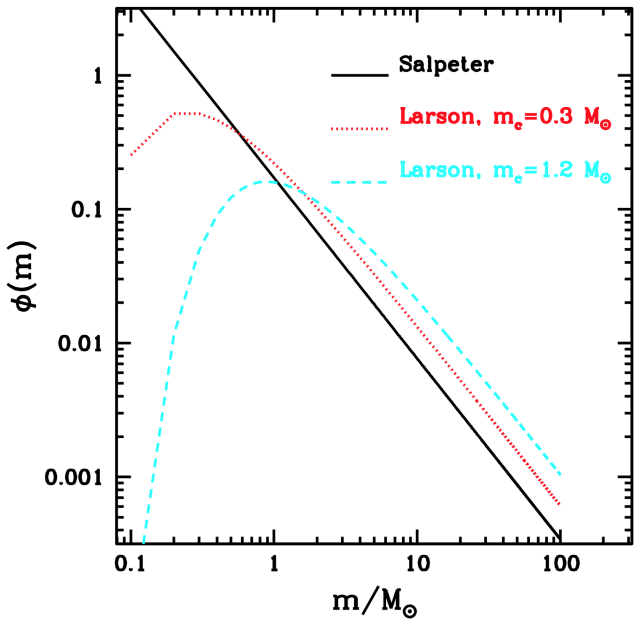

Figure 2.6: Comparison between the Salpeter (1955) and Larson (1998) IMFs. The different values quoted as m_c are for the different characteristic masses. Figure from Calura et al. (2013).

Dust extinction represents the amount of light that has been scattered or absorbed from the line of sight. We usually talk about extinction when observing a single object (e.g. a star), the light of which passes through a region of dust, which causes extinction. It is studied at different wavelengths and is usually represented as a function of the inverse of the wavelength, a plot called the attenuation or "reddening" law, implying that the red/IR wavelengths will be less affected than the blue/UV wavelengths, with an approximately linear behaviour, thus making the object redder than it would be otherwise. This curve strongly depends on the composition and the size distribution of the dust grains.

When modelling the SED of a galaxy, we are usually not able to separate a single source + screen configuration; the light that we receive from a galaxy has been scattered, absorbed, and sometimes re-emitted into our line of sight, possibly multiple times before it reaches us, so we use the term *dust attenuation*. It differs from dust extinction because it depends on the geometry of a galaxy, and is usually taken to be a cumulative property of the entire galaxy, similarly to its stellar mass or SFR.

In practice, templates are used for the attenuation law, a large variety of which can be found in the literature (Charlot & Fall, 2000; Calzetti et al., 2000; Wild et al., 2011; Reddy et al., 2015; Lo Faro et al., 2017; Salim et al., 2018; Decleir et al., 2019; Buat et al., 2020, and many others). CIGALE has two dust attenuation modules, the `dustatt_modified_CF00` module, based on the models of Charlot & Fall (2000) and the `dustatt_modified_starburst` module, inspired from the models of Calzetti et

al. (2000).

The `dustatt_modified_CF00` module assumes two different power laws for the dust attenuation of birth clouds (BC) and the ISM. The shape is given as $A_\lambda \propto \lambda^\delta$ with the value of the slope being different for BCs (default value $\delta_{\mathrm{BC}} = -1.3$) and the ISM (default value $\delta_{\mathrm{ISM}} = -0.7$). These two power laws are linked through a parameter μ, which gives a relation between the V-band attenuation of the BC ($A_{\mathrm{V}}^{\mathrm{BC}}$) and the ISM ($A_{\mathrm{V}}^{\mathrm{ISM}}$), defined as:

$$\mu = \frac{A_{\mathrm{V}}^{\mathrm{ISM}}}{A_{\mathrm{V}}{}^{\mathrm{BC}} + A_{\mathrm{V}}^{\mathrm{ISM}}} \tag{2.10}$$

The free parameters of the module are the power slopes δ_{BC} and δ_{ISM}, μ and the ISM attenuation in the V-band $A_{\mathrm{V}}^{\mathrm{ISM}}$.

The `dustatt_modified_starburst` module contains the starburst Calzetti et al. (2000) law, combined with the Leitherer et al. (2002) law. This module also allows a modification of the slope δ, with the addition that a bump can be added around 220 nm, which has a Drude profile (D_λ) and an input of an E(B-V) value, which renormalises the curve. The effects these parameters have on the curve can be seen in Fig. 2.7 (Fig. 4 of Boquien et al. (2019)).

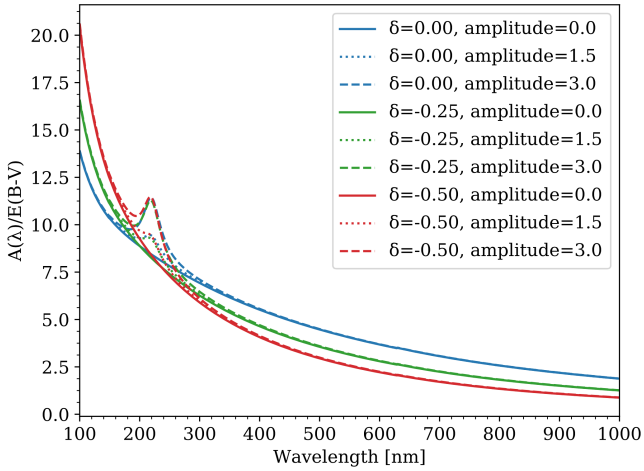

Figure 2.7: Examples of attenuation curves computed with CIGALE, using the `dustatt_modified_starburst` module. The blue, green, and red lines correspond to a value for δ of 0.00, -0.25, and -0.50. The solid, dotted, and dashed lines show the addition of the 220 nm bump with amplitude 0, 1.5, and 3, respectively. Figure from Boquien et al. (2019).

2.2.4 Dust emission models

The final block for building the SED is the dust emission. After estimating the amount of attenuated light, we can apply the energy balance principle to constrain the total IR emission.

Usually, the three main components of the dust are the polycyclic aromatic hydrocarbons (PAH), which are a transition between enormous molecules and tiny dust grains, the small and hot dust grains, and the big and relatively cold dust grains. These three components can have different compositions and metallicities. Therefore, they influence the IR SED alongside the incident radiation field. n this section, I will describe the dust emission models used in CIGALE, but this is an active field of research, so there will be many dust emission models left unmentioned.

One of the dust emission modules used in CIGALE, named `dale2014`, uses the templates provided by Dale et al. (2014) based on the work of Dale & Helou (2002). They build upon the study of dust emission within Milky Way regions by Desert et al. (1990) and Dale et al. (2001), whose models divide the contribution of the dust emission into three parts: the PAHs, tiny dust grains and large dust grains. The first two are assumed to be only stochastically heated, while the large dust grains are in thermal equilibrium. Dale et al. (2001) developed semi-empirical IR SEDs for an extensive range of interstellar radiation fields U ($0.3 \leq U \leq 10^5$, normalised such that $U = 1$ is the local interstellar radiation field) and assumed a power-law distribution, represented by (their Eq. 2):

$$dM_d(U) \propto U^{\alpha} dU \tag{2.11}$$

In this equation, $M_d(U)$ is the mass of the dust heated by the radiation field with intensity U, and the parameter α represents the relative contribution of their local empirical SEDs. Dale & Helou (2002) expand the dust emission model to include a variable emissivity of the dust grains, such that $\epsilon \propto \nu^{-\beta}$. The power-law slope β usually has values between 1 and 2 and can be computed as:

$$\beta = 2.5 - 0.4 \log U, \qquad \text{for } \lambda > 100 \mu\text{m} \tag{2.12}$$

Finally, the latest modification by Dale et al. (2014) are improvements in the PAH emission and addition to AGN emission since the previous authors only include star-forming systems. To summarise, this module is convenient because of its simplicity (it only depends on the parameter α). Nevertheless, this parameter does not model the PAH emission very accurately.

The second dust emission module included in CIGALE is the `dl2007` module, based on the models of Draine & Li (2007). These models include amorphous silicate and graphitic grains as well as different amounts of PAHs, and can be described with three free parameters: q_{PAH} gives the mass fraction of PAHs, and with that, the type of dust

considered is defined, U_{min} is the lower cutoff for the stellar radiation distribution, and γ - the fraction of dust that is heated by stellar radiation with intensity $U > U_{min}$. How these parameters impact the emission is shown in Fig. 2.8 (Fig. 18 of Draine & Li, 2007), and the functional form is the following (Eq. (23) of Draine & Li, 2007):

$$\frac{dM_{dust}}{dU} = (1-\gamma) M_{dust} \delta(U - U_{min}) \tag{2.13}$$

$$+ \gamma M_{dust} \frac{\alpha - 1}{U_{min}^{1-\alpha} - U_{max}^{1-\alpha}} , U^{-\alpha}; \quad \alpha \neq 1 \tag{2.14}$$

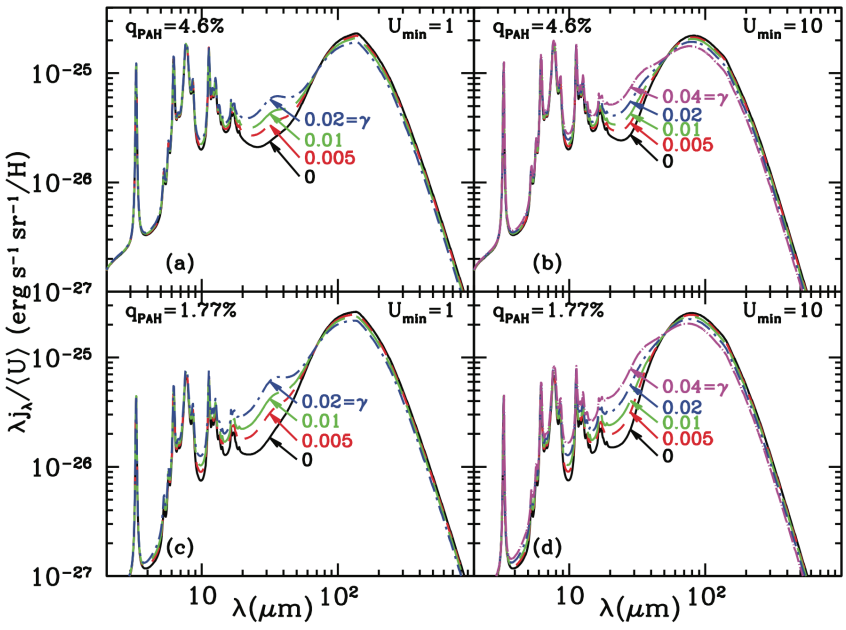

Figure 2.8: The different emission spectra produced by varying the parameters of the `dl2007` module. Two different values of q_{PAH} are given: $q_{PAH} = 4.6\%$ (panels *a* and *b*) and $q_{PAH} = 1.77\%$ (panels *c* and *d*), two values of U_{min}: $U_{min} = 1$ (panels *a* and *c*) and $U_{min} = 10$ (panels *b* and *d*), and five different values of γ, represented by the different coloured curves in each panel, the values being $\gamma = 0, 0.005, 0.01$ and 0.02. Figure from Draine & Li (2007).

Here, dM_{dust} is the amount of dust heated by radiation dU, and M_{dust} is the total dust mass. The parameter q_{PAH} is not included in this equation because it only determines the type of dust that is considered, and it does not influence the curve further. We can separate the dust emission into two parts: the $(1-\gamma)$ regions of diffuse emission, where the delta function dictates that a single intensity U_{min} heats the dust, and the γ star-forming regions heated by a power-law dependence of the intensity. Their models have a set power of $\alpha = -2$, and the maximum radiation to $U_{max} = 10^5$,

so the three parameters described above determine the shape of the emission curve and estimate the dust mass from observed fluxes (Draine & Li, 2007).

Later, these models were improved by Draine et al. (2014), and this exists as a separate module in CIGALE, called `dl2014`. In this work, they have expanded the range of intensities and PAH fractions that are available. In addition, they added an option to vary the power-law index α, they changed the value of U_{max} to 10^7 and the treatment of graphite and renormalised the dust masses. Another module is available in CIGALE that uses the same parametrisation, and that is the `themis` dust model presented by Jones et al. (2017), while Nersesian et al. (2019) present a more detailed implementation in CIGALE. This module has a lot more freedom in choosing the radiation fields and PAH emission, which also comes at a higher computational cost.

The last dust emission module in CIGALE is the `casey2012` module, presented in the work of Casey (2012), consisting of three parameters, the dust temperature, the emissivity of the dust and a power-law index determining the mid-IR emission. The emission of the reprocessed starlight is modelled as a single temperature grey body, on which a mid-IR emission is joined, which represents the emission of hot dust heated by AGNs or hot and clumpy starburst regions. However, in this module, the contribution of the PAHs is not included.

2.2.5 Nebular emission, AGNs and redshifting

In this section, the modules of CIGALE are mentioned, with a less detailed description, as they are not as relevant to the thesis as the ones discussed in the previous sections.

Emission lines are also included in CIGALE through the module `nebular`. This module contains nebular templates that have been generated using CLOUDY (Ferland et al., 1998; Ferland et al., 2013) as an improved version of the templates of Inoue (2011). The free parameter in the module is the ionisation parameter U, which determines the template used alongside the metallicity Z. The line width, the fraction of Lyman continuum photons escaping the galaxy, and the fraction absorbed by dust can also be set. The module predicts the relative intensities of 124 lines commonly found in HII regions in the wavelength range of 30.38nm $< \lambda <$ 205.4μm.

The presence of AGN can also be modelled by CIGALE, using either the module `casey2012` when only fitting the IR SED, or the `dale2014` module if the AGN is a quasar. In the former module, the slope of the power-law α models the AGN, while in the latter, the AGN fraction is the ratio $L_{\mathrm{AGN}}/(L_{\mathrm{AGN}} + L_{dust})$.

Lastly, the `redshifting` module is applied as a mandatory module in CIGALE. It uses the redshift of the galaxy to bring the modelled SED to the observed wavelength (from the initially modelled restframe) by multiplying the wavelengths by $(1+z)$ and dividing the SED flux also by $(1+z)$. This module also accounts for the IGM absorption dependent on the redshift, according to the recipe of Meiksin (2006).

2.2.6 Bayesian approach to estimate uncertainties

As input, CIGALE takes the measured fluxes in each filter alongside their uncertainties. The output is the main galaxy parameters, both the value that gives the best-fitting model (denoted with subscript *best* in the results output file), as well as the value estimated by an approach based on Bayesian inference methods (noted with subscript *bayesian*) (more details in, e.g. Han & Han, 2014), which I would like to discuss in this section. The *best* values come directly from the fitting; once all of the models from the selected grid are calculated, the best-fitting model is one with the lowest χ^2, found by calculating the value for the parameter a_i that minimises the following expression for each model i, (according to Eq. (1) of Salim et al., 2007):

$$\chi_i^2 = \sum_X \left(\frac{F_{obs,X} - a_i F_{mod,X}}{\sigma(F_{obs,X})} \right)^2 \tag{2.15}$$

The summation in this expression is over all of the filters included in the fitting (i.e. all of the available data points), and $F_{obs,X}$ and $F_{mod,X}$ are the observed flux values and the fluxes estimated by the model, respectively. In Eq. 2.15, the uncertainties of the fluxes are denoted by $\sigma(F_{obs,X})$. For including more complicated cases where, e.g. only upper limits are given, refer to the work of Boquien et al. (2019)

After calculating the χ^2 values for all the models, the next step is finding a weight associated to each model. It is usually assumed for the weight to have the value $w_n = \exp(-\chi^2/2)$. Then, these weights are used to build the probability distribution function (PDF) of each parameter: the parameter values are given on the x-axis, while the sum of weights w_n of all the models that include each given value is on the y-axis. So, the better the fit of the model, the lower χ^2 it will have and with that a higher weight; the more well-fitted models a particular value of the parameter produces, the higher the total sum of the weights will be, and this translates to a higher probability of the value of the parameter.

The CIGALE user usually gives a grid of parameter values, and CIGALE returns a PDF showing the parameter's *bayesian* value. The PDF can be interpolated when a peak is visible, so the *bayesian* value that CIGALE gives as output is not necessarily equal to any of the values the user has given, or the *best* value. Finally, due to the spread in the PDF, the error bars of each parameter can be estimated.

2.2.7 Determining the physical parameters

The fitting and modelling of the SED of a galaxy are one of the tools used to extract the essential parameters of the galaxy, and in this section, I will mention some of the methods used to obtain the stellar mass, Star Formation Rate (SFR) and dust attenuation, as the most relevant quantities to my work to date.

The value for the stellar mass is usually estimated using the mass-to-light ratio, multiplied by a measured NIR luminosity:

$$\frac{M_*}{L_{\rm NIR}} = 0.6\frac{M_\odot}{L_\odot}, \tag{2.16}$$

where the $L_{\rm NIR}$ is commonly at 1.65μm (Ciesla et al., 2014, H band), 2.15μm (Bell et al., 2003, K band), or 3.6μm (Cook et al., 2014). Sometimes, however, the stellar mass is estimated from the UV absolute magnitude M_{1600} (Schaerer et al., 2015):

$$\log\left(\frac{M_*}{\rm M_\odot}\right) = -0.45 \times (M_{1600} + 20) + 9.11 \tag{2.17}$$

In practice, the stellar mass is an output parameter in CIGALE (as well as other SED fitting codes). It is only necessary to choose the SSP templates and IMF and fit the data, so sometimes a correction needs to be applied. Different authors use different IMFs, so there are differences between the stellar masses' values. Throughout this thesis, only the conversion from Chabrier (2003) to Salpeter (1955) IMF is relevant and can be represented by a multiplicative factor in terms of the mass (or an additive constant when the mass is in logarithmic units). The correction we apply is the one given in Eq. 12 by Longhetti & Saracco (2009):

$$\log M_{*[Salpeter]} = \log M_{*[Chabrier]} + 0.26\,dex \tag{2.18}$$

Determining the SFR is usually done by using the classical calibration of Kennicutt (1998). When regions of the UV continuum where young stars dominate are observed (between 1250 and 2500 Å), this luminosity can be converted to SFR with a simple relation, derived using stellar population synthesis:

$$\mathrm{SFR}(M_\odot \mathrm{yr}^{-1}) = 1.4 \times 10^{-28} L_\nu (\mathrm{ergs}^{-2}\mathrm{Hz}^{-1}) \tag{2.19}$$

Other relations for conversion to SFR from spectral lines and IR luminosity (for starbursts) are also given in Kennicutt (1998).

For estimating the dust attenuation of a galaxy, the procedure is slightly more complicated, and there are multiple paths available to reach the same goal giving us an incredible opportunity to compare results derived from different data sets. In our work, when we say *dust attenuation*, we are referring to the FUV dust attenuation A_{FUV} at 1600 Å, so we need to look at the entire SED of the galaxy, both the UV light coming from the stars and the dust emission in the IR, so we require observations of both. A quantity called Infrared Excess (IRX) is used to estimate the dust attenuation, defined as:

$$\mathrm{IRX} = \log \frac{L(\mathrm{TIR})}{L(\mathrm{FUV})} \tag{2.20}$$

$$L(\mathrm{FUV}) = \nu L_\nu (1600\,\text{Å}) \tag{2.21}$$

The symbol L(TIR) stands for total infrared luminosity, and L(FUV) is the luminosity in the FUV, at 1600 Å. We also assume that the IRX estimated from SED fitting is close to Eq. (2.20) (Małek et al., 2018, for instance). From this quantity, we can estimate the dust attenuation in the FUV by using, for example, the following equation (Hao et al., 2011):

$$A_{\mathrm{FUV}} = 2.5 \log\left(1 + (0.46 \pm 0.12) \times 10^{\mathrm{IRX}}\right) \tag{2.22}$$

Buat et al. (2005) give another relation, with F_{dust} the total dust emission and F_{FUV} the flux of the GALEX (Galaxy Evolution Explorer) band in the FUV (in the range from 1350 Å to 1750 Å, with λ_{mean} = 1538,62 Å), stated as:

$$\begin{aligned} y &= \log \frac{F_{\mathrm{dust}}}{F_{\mathrm{FUV}}} \\ A_{\mathrm{FUV}} &= -0.0333\,y^3 + 0.3522\,y^2 + 0.4967 \end{aligned} \tag{2.23}$$

Comparing the calibrations given by Eqs. (2.22) and (2.23) does not give results that are very different from each other (Cook et al., 2014).

I would like to mention that it is also possible to find the colour excess $E(B-V)$ (such as the one in Finkelstein et al. (2015)), and then use a dust attenuation law, e.g. the Calzetti et al. (2000) law $A_{\mathrm{FUV}} = 4.39E(B-V)$, to determine the dust attenuation at wavelength 1600 Å, the same that we are using to calculate the IRX.

A second method to estimate the dust attenuation is to use the power-law slope of the UV continuum β, defined by Meurer et al. (1999) as a function of the flux density per wavelength interval f_λ as:

$$f_\lambda \propto \lambda^\beta \tag{2.24}$$

The β-slope value depends on the age of the stars that heat the dust, the geometry and relative positions of the dust and stars, dust properties.

The last method to estimate the dust attenuation that I will mention in this thesis is to use the attenuation of the H_α line through the use of the Balmer decrement (the ratio of the fluxes in the H_α and H_β lines). First, however, we require a conversion from the attenuation of H_α (A_{H_α}) to attenuation in the far-UV (FUV) (A_{FUV}), which means assuming a dust attenuation law (Sect. 2.2.3).

Finally, the quantities mentioned in this section are closely connected. More pre-

cisely, the IRX can be estimated from the β-slope (Meurer et al., 1999; Bouwens et al., 2012), which is extremely useful when no IR data is available above $z \approx 4$. More details on this in Sect. 2.3.5.

Additionally, the relation between IRX (or A_{FUV}) and stellar mass (M_*) is yet another tool that allows estimating the dust attenuation in galaxies from the stellar mass of galaxies. Because M_* mirrors the previous star formation activity of galaxies responsible for producing dust particles, the stellar mass may be a good, and easy to estimate, tracer of the dust content in galaxies. This is one of our main motivations for the work presented in Chap. 3.

2.2.8 Determining the redshifts

As this thesis includes galaxies with an extensive range of redshifts, namely $0 < z \lesssim 10$, it is important to be familiar with obtaining the redshift values. The easiest way to calculate the redshift, in theory, is to use spectroscopy. If we have the spectrum of an object, we can find known spectral lines and compare their measured wavelength to their theoretical one. In reality, for galaxies with a large redshift, it is hard enough to obtain photometric data, let alone to measure a spectrum. Getting useful spectroscopic data requires a higher signal-to-noise ratio, which is hard to bring in our case since most of the objects are far away and relatively faint. So, we turn to other techniques to calculate the redshift until we have more powerful telescopes to measure the spectra of many distant galaxies (e.g. the JWST).

Determining the redshift of a galaxy without its spectrum is possible with the use of multi-wavelength photometric data. If such measurements are available, we can model the SED of the object and thus estimate the redshift. We can do that because some spectroscopic features of galaxies span larger wavelength intervals, so they are detected even with broadband measurements. Such features include the Lyman and Balmer break, and strong emission of a spectroscopic line (as is the case for Lyman Alpha Emitters-LAEs).

An excellent example of the use of photometry to determine the redshift of galaxies is the work of Steidel et al. (1996), which uses the Lyman break to detect star-forming galaxies at redshift $z \sim 3$, known as *Lyman-Break Galaxies (LBG)*, or drop-out galaxies. The Steidel et al. (1996) method assumes that the spectrum is flat in the far-UV but that a break occurs at the Lyman limit at 912 Å, which corresponds to the ionisation energy of hydrogen. Thus, any photons with higher energy are absorbed, and a break is created.

The galaxies are observed with three broadband filters, with wavelengths $\lambda_1 < \lambda_2 < \lambda_3$. Due to the Lyman break, the galaxy will be detected by the filters λ_2 and λ_3 while being very faint or not detectable in the filter λ_1, as shown in Fig. 2.9. The redshift z of the galaxy has caused the Lyman break to change its wavelength to fall between λ_1 and λ_2. This condition can be written as (Schneider, 2006, Chapter 9):

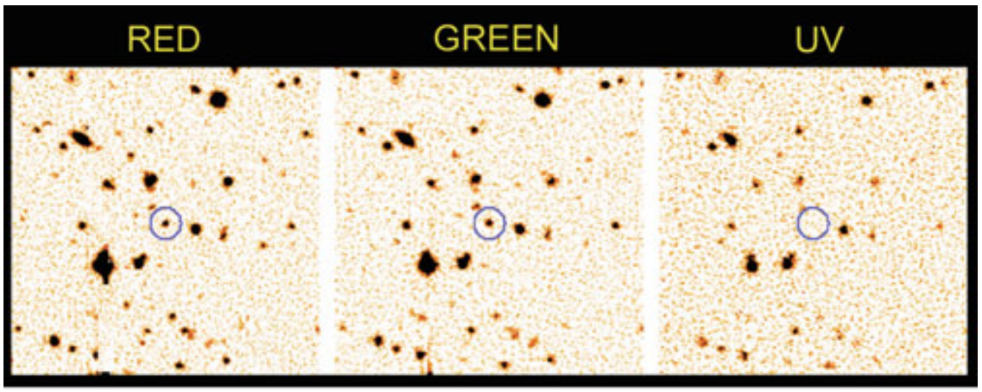

Figure 2.9: An image of a field in three different filters where an example of a U-band drop-out galaxy is seen. The galaxy in the circle is seen in the red and green filters, but it is not detected in the UV filter. Figure from Schneider (2006, Chapter 9).

$$\lambda_1 \lesssim (1+z)\,912\text{Å} \lesssim \lambda_2 \tag{2.25}$$

One of the benefits of this method is that we can estimate the redshift of many galaxies at the same time. Even though the redshift precision obtained in this way is not very high (we only know it is somewhere between z_1 and z_2), this type of observations eases the redshift estimation via follow-up spectroscopy. Furthermore, this technique is useful when studying statistical properties, as in this case, the exact redshift of each galaxy does not need to be known with great precision.

In practice, photometric redshift codes are used. One such example is the code EAZY [2] or LEPHARE [3]. In such algorithms, a grid of redshifts is used, such that for each redshift, a synthetic spectrum is created. Then, using a minimizing technique, such as the χ-square technique, the spectrum which is the best fit with the observed photometric data is found (Brammer et al., 2008). Once the best fit spectrum is determined, either the redshift for which it was calculated is taken to be the galaxy's redshift or further statistical analysis is performed. An example of this is the Bayesian statistics described in Sect. 2.2.6.

2.3 Cosmic properties of galaxies

When studying the history of the Universe with a focus on the evolution of galaxies, we must observe objects that are very old, meaning they are distant from us. Although, it is it currently impossible to study individual objects in too many details since taking

[2] Available at http://www.github.com/gbrammer/eazy-photoz.
[3] Available at http://www.cfht.hawaii.edu/~arnouts/LEPHARE/lephare.html.

the whole spectra of high-redshift galaxies is still a task beyond the capabilities of the current observatories. Therefore, we must turn to a different approach: observing galaxy populations as a whole, not just individual galaxies. This way, we can combine the measurements we can obtain, and get the most information out of them.

2.3.1 Luminosity and mass functions

One important method of characterising the cosmic properties of galaxies is by studying the Luminosity Function (LF), defined as the number of galaxies per unit luminosity and unit volume. A luminosity function $\phi(L)$ is a statistical distribution defined as:

$$\mathrm{d}n(L) = \phi(L)\mathrm{d}L \tag{2.26}$$

where $\mathrm{d}n(L)$ is the number density of galaxies, i.e. the number of galaxies contained in a unit of co-moving volume with luminosity in the interval defined by $\mathrm{d}L$, such that $L \in [L + \mathrm{d}L, L - \mathrm{d}L]$. The luminosity function of galaxies is usually approximated by a Schechter (1976) function:

$$\phi(L)\mathrm{d}L = \phi^* \left(\frac{L}{L^*}\right)^{\alpha} \exp\left(-\frac{L}{L^*}\right)\frac{\mathrm{d}L}{L^*} \tag{2.27}$$

In Equation (2.27), ϕ^*, L^* and α are known as the Schechter parameters, with ϕ^* the normalisation of the luminosity function, L^* the characteristic luminosity, and α the faint-end slope. These parameters can and do vary with redshift because the galaxies themselves evolve with cosmic times. An example of the luminosity function for different redshifts is shown in Fig. 2.10 (Fig. 2 of Cucciati et al. (2012)).

Analogously to the luminosity function, with M_* the stellar mass, and $\mathrm{d}n(M_*)$ the number density of galaxies with stellar mass in the interval $[M_* + \mathrm{d}M_*, M_* - \mathrm{d}M_*]$, a mass function $\phi(M_*)$ is defined as:

$$\mathrm{d}n(M_*) = \phi(M_*)\mathrm{d}M_* \tag{2.28}$$

The galaxy stellar mass function (MF) is also represented by the Schechter function in Equation (2.27). In this case, the Schechter parameters will be the same, except L^*, which $\mathscr{M}^*$, the characteristic mass, replaces. Another function that fits well the MF is the double Schechter function (Pozzetti et al., 2010), which has been used, for example, by Ilbert et al. (2009) (plotted in Fig. 2.11, left, Fig. 3 of Ilbert et al. (2013)), defined as:

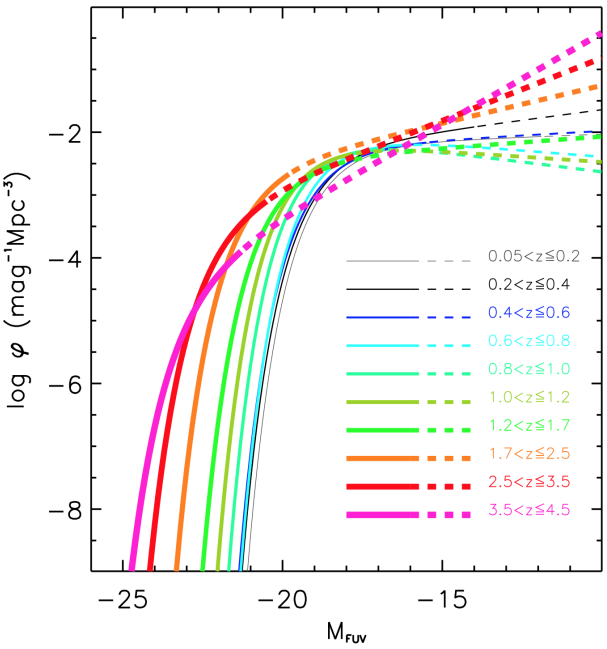

Figure 2.10: The LF for estimated for different redshifts, based on the VVDS rest-frame FUV luminosity, fitted with a Schechter (1976) function. The dashed lines represent an extrapolation of the LF beyond the magnitude limits of each redshift bin. Figure from Cucciati et al. (2012).

$$\phi(M_*)\mathrm{d}M_* = \exp\left(-\frac{M_*}{\mathscr{M}^*}\right)\left[\phi_1^*\left(\frac{M}{\mathscr{M}^*}\right)^{\alpha_1} + \phi_2^*\left(\frac{M}{\mathscr{M}^*}\right)^{\alpha_2}\right]\frac{\mathrm{d}M}{\mathscr{M}^*} \tag{2.29}$$

Both the luminosity function (Fig. 2.10) and MF (Fig. 2.11) evolve with redshift. Knowing this evolution would give us information about the assembly of mass throughout the evolution of the Universe. It can also reveal the major paths taken by different galaxy populations across cosmic time (Ilbert et al., 2013), bringing us knowledge about the evolution of these populations of galaxies.

From their results, Ilbert et al. (2013) conclude that the faint end slope remains steep and does not evolve much with redshift. There is however an evolution in the number of galaxies, as the curves for redshift $z \geq 2$ are significantly below their lower redshift counterparts. For the high-mass end, there is almost no evolution detected. This is because massive star-forming galaxies are more efficiently quenched over time compared to the galaxies with lower masses, a fact confirmed by the difference of slopes for the low-mass and high-mass ends.

The models of Song et al. (2016), which are also presented in Fig. 2.11 (right, their Fig. 13) for redshift $4 \leq z \leq 8$, have been obtained by using the data from Finkelstein et al. (2015). In this case, a mass function in the form of a Schechter function (Equation (2.27)) is used to compute the curves shown in the figure. From these results, Song et al. (2016) conclude that the low-mass-end slope (α) decreases with increasing redshift, meaning the curve becomes steeper in the low mass range. It is also shown that the value of ϕ_* decreases with redshift, while M_* remains constant within the uncertainty limits.

In addition to the aforementioned MFs, in our work, we include the MFs given by Mortlock et al. (2015), Tomczak et al. (2014), Grazian et al. (2015), Song et al. (2016), and Wright et al. (2018). In fact, what we do is collect the Schechter parameter values from each of the papers, and fit them to be able to retrieve their value at any given redshift (Fig. 2.12); the values for the $\mathscr{M}^*$ parameter are fitted with the function $\mathscr{M}^* = (k_1 + k_2 z)/(1 + (z/k_3)^{k_4})$, and the best-fitting is for $k_1 = 10.52$, $k_2 = 2.38$, $k_3 = 4.80$ and $k_4 = 1.15$, for ϕ_* we have $\log\phi_* = (l_1 - 0.56z)$, with $l_1 = -2.47$ giving the best-fitting, and for α the function is a line $\alpha = m_1 + m_2 z$, with parameters $m_1 = -1.25$ and $m_2 = -0.13$. The shape of the MF is very relevant to our work since we are working with an MF weighted average of the dust attenuation (Chap. 3, Sect. 3.3).

Let us take as an example the MF proposed by Wright et al. (2018) in Fig. 2.13 (their Fig. 1). We can see that for low mass galaxies, such as $\log M_* = 7$ for the first three redshift bins (for $z < 0.2$), the number is as high as 10^{-1} galaxies per unit volume, whilst in the higher stellar mass range, e.g. for $\log M = 11$ the number is two orders of magnitude lower, so it is roughly 10^{-3} galaxies per unit volume. Modelling the MF with a Schechter function means that when including galaxies with down to $\log M \sim 6$, as we do in our work, our computed average value will be heavily influenced by this large number of low mass objects, which ultimately led us to propose a slightly unusual treatment of these objects in our models (e.g. Fig. 3.2).

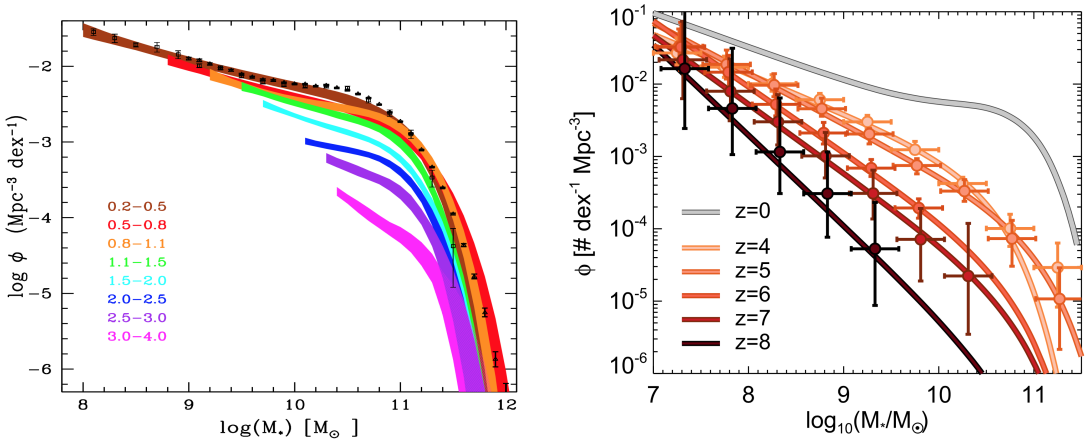

Figure 2.11: Left: The galaxy MFs in the redshift range $0.2 < z < 4$ of Ilbert et al. (2013). The redshift bins, each marked by a different colour, have a variable step size. As a reference, the local MFs from Moustakas et al. (2013) (triangles) and Baldry et al. (2012) squares are shown. Figure from Ilbert et al. (2013). Right: The galaxy MFs in the redshift range $4 < z < 8$ of Song et al. (2016). The local MF of Baldry et al. (2012) (grey line) is also given. Figure from Song et al. (2016).

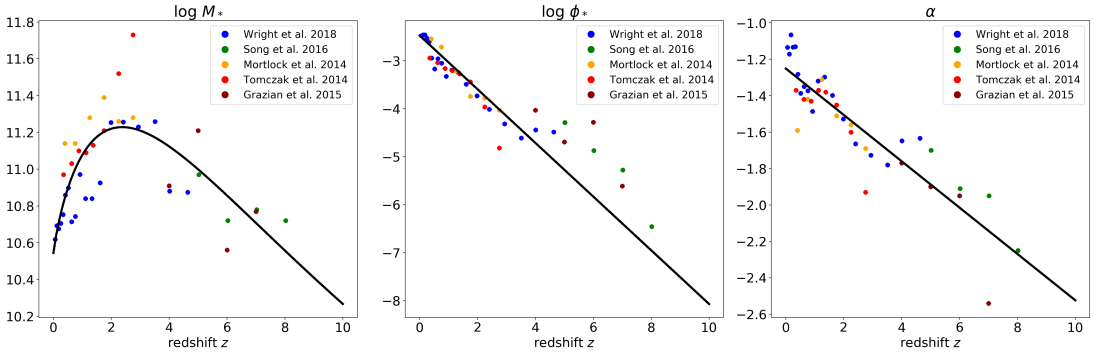

Figure 2.12: The fitting of the Schechter parameters. The functions used are $\mathscr{M}^* = (k_1 + k_2 z)/(1 + (z/k_3)^{k_4})$, where $k_1 = 10.52$, $k_2 = 2.38$, $k_3 = 4.80$ and $k_4 = 1.15$; $\log\phi_* = (l_1 - 0.56z)$, with $l_1 = -2.47$; $\alpha = m_1 + m_2 z$, with parameters $m_1 = -1.25$ and $m_2 = -0.13$.

2.3.2 Luminosity and mass densities

Moreover, we can compute the luminosity density (LD) per volume, and analogously the mass density (MD) per volume of galaxies, by integrating the LF and MF. The MF is usually integrated between 10^8 and $10^{13} M_\odot$. The MD is a useful parameter to study as it gives information about the mass assembly of the Universe and the LD is interesting because it can be used as a proxy to find the Star Formation Rate Density (SFRD), discussed in Sect. 2.3.3. More specifically, using the notation from the previous section, the LD and MD are defined as:

$$LD = \int_{L_{\min}}^{L_{\max}} \phi(L) \mathrm{d}L \tag{2.30}$$

$$MD = \int_{M*_{\min}}^{M*_{\max}} \phi(M_*) \mathrm{d}M_* \tag{2.31}$$

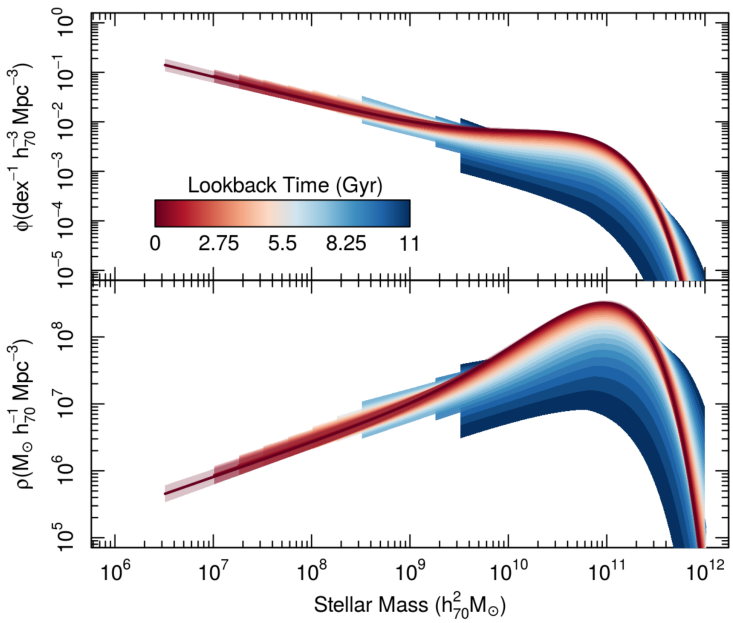

Figure 2.13: Top: Evolution of the Schechter mass function with cosmic time. The colour coding represents the passage of time, from red to blue. Bottom: Same colour coding, but this time the galaxy mass density is shown as a function of stellar mass. Figure from Wright et al. (2018)

The shape of the MD as a function of mass is represented in Fig. 2.13. The MD (as well as the LD) also varies with redshift. An illustration of the increase of the mass density of the universe with cosmic time can be seen in Fig. 2.14 (Fig. 17 of Davidzon et al. (2017)), as well as in the work of Caputi et al. (2011), Ilbert et al. (2013), Madau & Dickinson (2014), and Davidzon et al. (2017) etc (see more references in the caption of

Fig. 2.14.

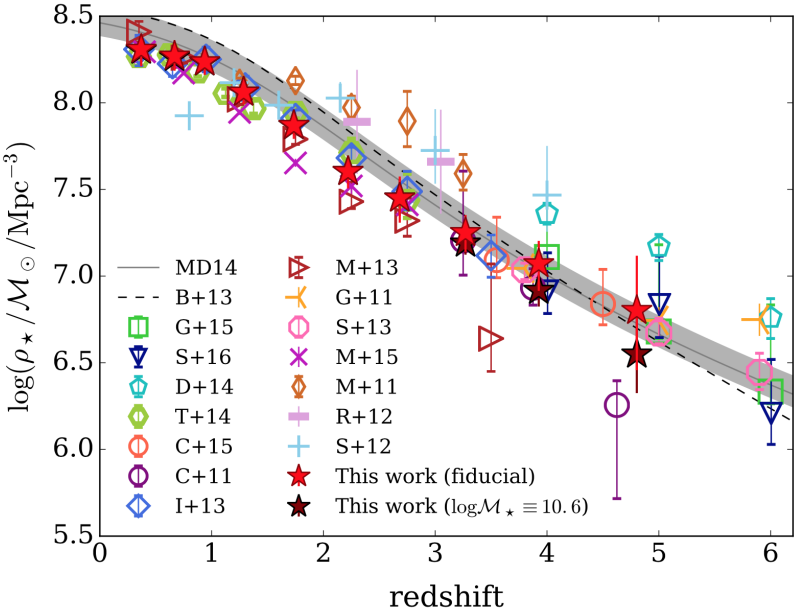

Figure 2.14: Compilation of measurements of the evolution of the MD with redshift calculated by integrating the stellar MF in the work of multiple authors. The red stars marked as *this work*, come from integrating the Schechter functions found by Davidzon et al. (2017), while the brown stars are from fitting with a fixed $\mathscr{M}^*$. The references alongside their notation in the label are the following: Madau & Dickinson (2014): MD14 (grey solid line), Behroozi et al. (2013): B+13 (black dashed line), Caputi et al. (2011): C+11, Caputi et al. (2015): C+15, Duncan et al. (2014): D+14, Gonzalez et al. (2011): G+11, Grazian et al. (2015):G15, Ilbert et al. (2013): I+13, Mortlock et al. (2011): M+11, Mortlock et al. (2015): M+15, Muzzin et al. (2013), M+13, Reddy et al. (2012): R+12, Santini et al. (2012): S+12, Song et al. (2016): S+16, and Tomczak et al. (2014): T+14. The MD14 and B+13 lines are estimated by integrating their SFRD. Figure from Davidzon et al. (2017), their Fig. 17.

2.3.3 Star formation rate density and cosmic dust attenuation

For a galaxy population, we can compute the LD (Eq. (2.30)), or more specifically the UV LD (where first we compute the UV LF, by using the UV luminosity in Eqs. (2.26) and (2.27)). Then, since the UV emission is dominated by young and short-lived massive stars thus being an indicator of star formation, we can use the UV LD to estimate the cosmic density of star formation, known as the Star Formation Rate Density (SFRD).

From this, we can deduce how the galaxies were building their stellar mass during cosmic times in a complementary way to the cosmic MD, by representing the famous SFRD-z plot, which was first published in 1996 (Madau et al., 1996; Madau et al., 1998), with the most famous compilation of findings given in the review by Madau & Dickinson (2014), shown in Fig. 2.15 (Fig. 9 of Madau & Dickinson (2014)), and this being an active field of research to this day, aiming to improve the measurements by better calibrating the UV luminosity to SFR relation, by accurately correcting for dust extinction, by probing this phenomenon in higher redshifts, and by forming a clearer picture for the mechanisms that instigate this behaviour.

This shape of the SFRD redshift evolution a very interesting find, we can see a rise from the beginning of the Universe (more precisely, as early in the Universe as we have data) until $z \sim 2$. This means that the galaxies and stars did not form in one instantaneous burst, but it is a continuous and ongoing process. One possible explanation for this is that stars form heavier metals that later turn into dust, which in turn enables the process of star formation. At $z \sim 2$ the SFRD reaches a plateau and keeps declining until the local Universe. Conversely, the exact mechanisms that caused the process of star formation to drop after $z > 2$ are still not fully understood. One possible explanation would be the depletion of the gas reservoir available in the galaxies, or the presence of some mechanism that is so powerful that it can slow down the formation of new stars, e.g. the presence of an Active Galactic Nucleus (AGN) is thought to be capable of reducing the number of stars being formed per year.

Another global property that we are interested in, particularly in the work described in Chap. 3 is the cosmic dust attenuation. There are multiple different ways to obtain this quantity, some of which I will mention here. Finkelstein et al. (2012) use the median UV-slope β of binned galaxies from the CANDELS (The Cosmic Assembly Near-IR Deep Extragalactic Legacy Survey, Grogin et al. (2011) and Koekemoer et al. (2011)) data at several redshifts between $4 < z < 8$ translated to A_{FUV} using the Meurer et al. (1999) calibration. Burgarella et al. (2013) use the evolving UV and IR LFs to compute the UV and IR LDs, and analogously to the IRX, they estimate the dust attenuation from the IR LD to UV LD ratio (more details in Chap. 3, Sect. 3.3). Finally, Cucciati et al. (2012) use the E(B-V) of individual objects to find the mean E(B-V) and then convert to A_{FUV} (using an extinction curve), the redshift evolution of which they also present.

In our work, we attempt to estimate the cosmic dust attenuation by computing the average dust attenuation for all of the stellar masses, meaning even those for which we do not have any data. We use the general definition of an average, assuming that the dust attenuation of a galaxy is a function of its stellar mass $A_{FUV}(M_*)$, then the mean of this function would be:

$$\overline{A_{FUV}} = \frac{\int_{M_{*\min}}^{M_{*\max}} A_{FUV}(M_*)\phi(M_*)\mathrm{d}M_*}{\int_{M_{*\min}}^{M_{*\max}} \phi(M_*)\mathrm{d}M_*} \tag{2.32}$$

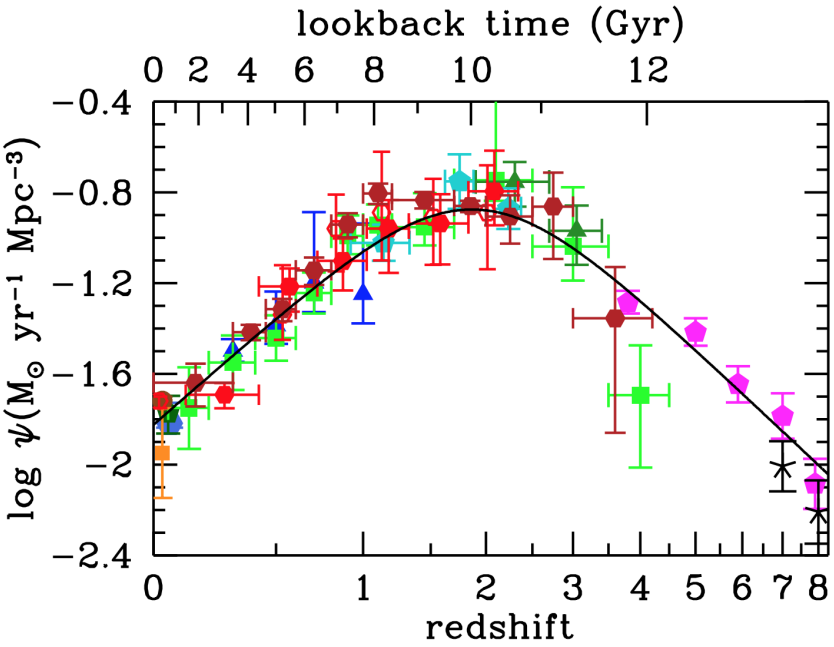

Figure 2.15: The history of cosmic star formation from FUV+IR rest-frame measurements. A conversion factor of 1.15×10^{-28} is used, (one that is around 20% lower than the classical Kennicutt (1998) value. The best-fit SFRD-z evolution is plotted with a full line and has the shape of $\psi(z) = 0.015\frac{(1+z)^{2.7}}{1+[(1+z)/2.9]^{5.6}}\mathrm{M}_{\odot}\mathrm{year}^{-1}\mathrm{Mpc}^{-3}$. The notations of the data points are the following: Wyder et al. (2005): blue-grey hexagons, Schiminovich et al. (2005): blue triangles, Robotham & Driver (2011): dark green pentagons, Cucciati et al. (2012): green squares, Dahlen et al. (2007): turquoise pentagons, Reddy & Steidel (2009): dark green triangles, Bouwens et al. (2012): magenta pentagons, Schenker et al. (2013): black crosses, Sanders (2003): brown circles, Takeuchi et al. (2003): dark orange squares, Magnelli et al. (2011): red open hexagons, Magnelli et al. (2013): red filled hexagons, and Gruppioni et al. (2013): dark red filled hexagons. Fig. 9 of Madau & Dickinson (2014).

Here, $\phi(M_*)$ is the mass function (MF), which in this case acts as a normalisation. We use the functional form of Schechter (1976), described in Sect. 2.3.1.

In practice, we set up a grid of redshifts, and for each value z_i we calculate first the coefficient a_{z_i}, and then $A_{FUV}(M_*, z_i)$, using the model we found in our paper (Bogdanoska & Burgarella (2020), Chap. 3). For the same z_i we estimate the Schechter (1976) parameters and compute the corresponding MF. We then use the MF as the weight for calculating the average dust attenuation $\overline{A_{FUV}}$, according to Eq. (2.32). The results of this computation are represented in Chap. 3 Sect. 3.3.

2.3.4 Main sequence of galaxies

A linear relationship between the SFR and M_* (in logarithmic space) has been observed for large populations of galaxies, with very little scatter. This has been named the Main Sequence (MS) of galaxies, a relation that defines a distinction between Star-Forming Galaxies (SFG) - those that lie on the MS, while those that are below the MS are typically called quiescent galaxies, and those above are classified as starbursts. Even though the characteristics of these different galaxy types are distinguished (e.g. Silverman et al., 2018), the precise limits of this classification are not very well defined, and different authors propose different methods of separation (Rodighiero et al., 2011; Speagle et al., 2014; Elbaz et al., 2018; Donevski et al., 2020).

The rapid quenching between $z = 0$ and 2 indicates that in the earlier Universe the stars were formed at higher rates, which has also been confirmed by multiple studies of the galaxy MS (Daddi et al., 2007; Elbaz et al., 2007; Whitaker et al., 2012; Sobral et al., 2014). An evolution of the MS in redshift has been a field of interest to many authors (Tasca et al., 2015; Tomczak et al., 2016; Pearson et al., 2018; Khusanova et al., 2020).

An important model of the time-evolving MS of galaxies was presented by Speagle et al. (2014). They collect the available measurement of the MS relationship from different sources in the literature within the redshift range $0 < z < 6$, and after making sure the corresponding calibrations have been carried out to account for the different methods used to estimate the SFR and M_*, they present their best fit relation, which we have used in our work as the definition of an SFG, and is also represented in Fig. 2.16 (their Fig. 8):

$$\log \mathrm{SFR}(M_*, t) = (0.84 \pm 0.02 - 0.026 \pm 0.003 \times t) \log M_* \tag{2.33}$$
$$- (6.51 \pm 0.24 - 0.11 \pm 0.03 \times t) \tag{2.34}$$

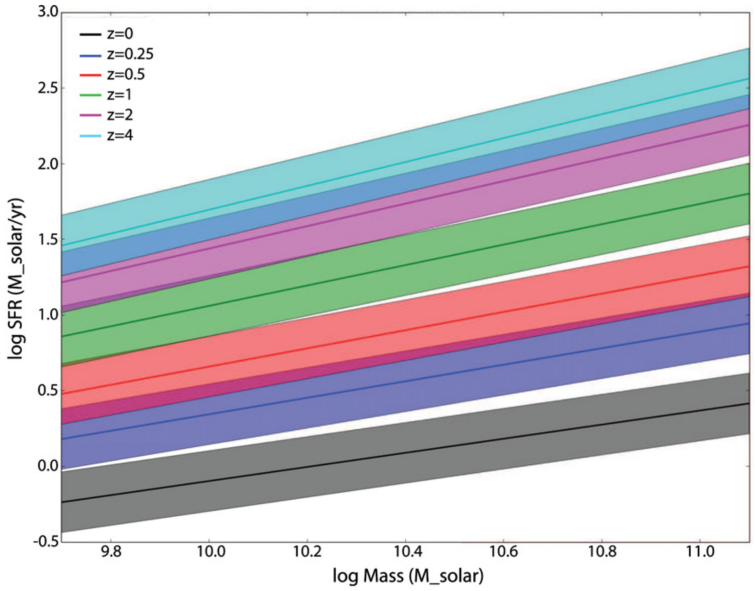

Figure 2.16: The MS of Speagle et al. (2014), represented by Eq. 2.33 computed in a range of redshifts, excluding the first and last 2 Gyr of their sample. Figure from Speagle et al. (2014).

2.3.5 IRX - beta relation

One important method of studying the dust attenuation of galaxies is the relationship between the UV-slope β (Eq. (2.24)) and the IRX, first studied by Meurer et al. (1995) and Meurer et al. (1999) for local starbursts, which was re-evaluated by Takeuchi et al. (2012). Meurer et al. (1999) present a linear relationship between the FUV dust attenuation A_{FUV} and β and assuming a calibration from IRX to A_FUV given by the following equations:

$$A_{FUV} = 4.43 + 1.99\beta \tag{2.35}$$

$$IRX = \log\left(10^{0.4A_{FUV}} - 1\right) + 0.076 \tag{2.36}$$

It is understandable to have a correlation between the β-slope and IRX, firstly because it has been shown that the intrinsic dust-free slope varies very little (Leitherer, 1999; Calzetti, 2001) meaning dust is the cause of the reddening, and secondly because it is the UV light that is absorbed and re-emitted to the IR due to the presence of dust. Most authors are in agreement that the root cause of this relationship is the attenuation law (e.g. Boquien et al., 2019; Boquien et al., 2012; Mao et al., 2014; Salim & Boquien, 2019; Alvarez-Marquez et al., 2019), as can be seen in Fig. 2.17, however, the reason behind the attenuation law itself is a lot more difficult to determine, especially since there is a degeneracy between the dust properties, such as the grain size distribution, chemical composition and optical properties of the grains, and the

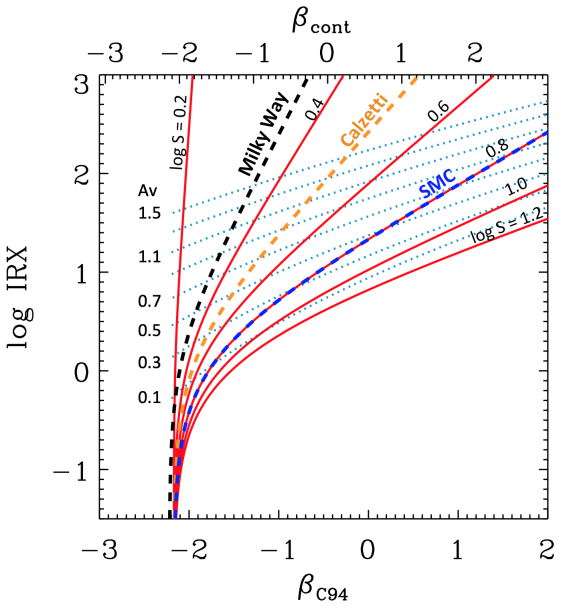

Figure 2.17: A representation of different IRX-β relationships obtained by varying the slope of the dust attenuation law $S = A_{FUV}/A_V$ (notations along the curves). The bottom scale shows the β-slope calculated in the bands defined by Calzetti et al. (2000) and the top scale is β calculated from the continuum. The dashed lines show the dust attenuation in the V band, A_V. Figure from Salim & Narayanan (2020).

geometry of the galaxy, practically the level of decoupling between stars and dust, with larger separation producing redder galaxies.

This relationship is especially useful for high-redshift galaxies which have scarce IR observations (Bouwens et al., 2009); it allows to estimate the dust attenuation solely from UV observations. However, this relationship could be potentially biased because the Meurer et al. (1999) sample consists only of starbursts, and it could potentially evolve with cosmic time. Reddy et al. (2012) confirmed the Meurer et al. (1999) relation for $z \sim 2$, Heinis et al. (2013) for $z \sim 1.5$ then later To et al. (2014) for $z \sim 4$ LBGs. In contrast, e.g. Bauer et al. (2011) find that their sample lies above the Meurer et al. (1999) relation, not a surprising find considering their sample is comprised of ULIRGs. Another important work on this topic is that of Casey et al. (2014), where they explore this relation for a heterogeneous sample galaxies with redshifts $0 < z < 5$ in the COSMOS field, finding that indeed the IRX-β relationship is above that of Meurer et al. (1999), and consistent with corrected versions of it, such as the one of Takeuchi et al. (2012).

2.4 Physical properties of dust

The study of dust has many peculiarities that need to be addressed, which makes it a complex subject. However, the contribution of dust in the overall system that is a galaxy is too great to be ignored, thus making the study of dust essential. There is a lot about interstellar dust that is known, but incomparably more that is unknown, meaning the road to understanding dust is only just beginning and can bring interesting results in the future.

In this section, I would like to mention some of the properties of dust that have been discovered mainly through the study of Milky Way dust, by observing nearby molecular clouds or even by examining meteorites that were found and thought to be samples of interstellar dust. Even though this kind of study in the early Universe is currently impossible, some of the properties of dust might remain the same during the majority of cosmic times, allowing us to make predictions based on comparison with the local Universe. In any case, I believe that cosmic dust is a very interesting phenomenon, so I decided to devote a section to it, hoping that in the future I will have an opportunity to work directly on studying the details about cosmic dust that are just beyond the scope of current telescopes.

The interstellar dust is only 1% of the vast interstellar medium (ISM). The interstellar medium is everything that is not the stars themselves, i.e. gas and dust, which coexist in a gas-to-dust ratio of around 100, and it is mostly comprised of hydrogen, with about 90% and helium with 9%. The last per cent accounts for all of the heavier elements or *metals*, like carbon, oxygen, silicon, iron, etc. which are especially important for the interstellar dust. The ISM is a region with extreme conditions, with temperatures ranging from 10 to 10^6 K and densities ranging from 10^4 to 10^9 atoms m^3 with an average of 10^6 atoms m^3 . The distribution of this density is nowhere near uniform

with most matter found in so-called *interstellar clouds*.

Even though there have been many advances towards answering this question of the composition of dust, it is still not known with high certainty. We have some knowledge that the dust contains silicates, graphite and iron, as well as "dirty ice", meaning frozen water which contains ammonia, methane or similar compounds. But this is nowhere near the full story.

One very important source of information is the extinction curve, which gives vital clues as to which materials can be found in the interstellar dust as well as the sizes of the dust grains. Many models exist one of the most famous models being the "MNR" model (Mathis-Rumpl-Nordsieck model) (Mathis et al., 1977). This gives a simple power-law with an exponent of -3.5. The sizes vary from size $a_{min} = 5$ nm to $a_{max} = 250$ nm. This distribution can be written, with a the size and n_H the density of H atoms, as:

$$n_i(a)da = A_i n_H a^{-3,5} da \tag{2.37}$$

The constant A_i is used to include the chemical composition in the equation, thus it has different values for different chemical compositions, e.g., for silicates this constant is $A_{sil} = 7.8 \cdot 10^{-26} \text{cm}^{2.5}/\text{H}_{\text{atom}}$, and for graphite $A_{gra} = 6.9 \cdot 10^{-26} \text{cm}^{2.5}/\text{H}_{\text{atom}}$. Some more complicated models exist, such as getting a value for the size distribution assuming it is created by steady accretion, or the Weingartner & Draine (2001) model, which employs a relatively simple empirical function, that does not have a strong theoretical basis.

The range of sizes of the dust grains usually falls in the sub-micrometre domain, and the typical size is taken as $\sim 0.1\mu$m. There are observations and models, however, that show that sizes span from the sub-nanometre to the micrometre size (Li et al., 2014). Grains with sizes from a few angstroms until $a \sim 50$ Å can be found, and are referred to as very large molecules. On the upper size limit, there are very large grains with radii of $\sim 2\mu$m. Some even larger interstellar dust grains have been discovered, with a radius over 20 μm, as meteorites that entered the Earth's atmosphere (Taylor et al., 1996). Concerning the shape of dust grains, they are often approximated as spherical, or as elongated and rodlike in more precise models, a shape that was deduced based on polarimetric studies (e.g. Hildebrand & Dragovan (1995)).

2.4.1 Roles of dust

For astrochemistry to be possible at all, dust in the interstellar medium must be present. For the creation of H_2 to be possible, when two hydrogen atoms meet, they must give off energy to a third body, otherwise, a chemical reaction will not occur. This is true for the creation of most of the molecules found in the ISM. Furthermore, dust is crucial for the process of creating molecules is the fact that atoms accumulate on the surface of dust grains, and thus have a higher probability of meeting another

atom than in the surrounding low-density medium. As was said by Tielens (2010): *Grain surfaces are the "watering holes" of astrochemistry where species come to meet and mate.*

The process of forming molecules from atoms (or other molecules) is shown in Fig. 2.18. First, species of atoms or molecules are accreted (i.e. *adsorbed*). Then, the particles must move along the surface of the grain to come in contact with another particle (known as *migration*). It is only after that that a chemical reaction occurs, followed by a release of energy, which causes the newly formed molecule to detach from the grain (*desorption*) and any extra energy is absorbed by the grain. If the energy is not enough for the molecule to detach, then the molecule is stuck on the grain until some external source contributes and the molecule is released back into the ISM, or when the molecule acquires enough energy from thermal fluctuations and it evaporates from the surface.

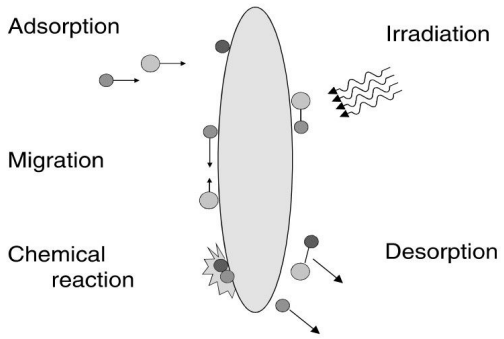

Figure 2.18: Grain surface interactions mechanism

The most important reaction that occurs on the surface of grains is the formation of H_2. For a reaction to occur, one of the H atoms needs to be strongly bound to the surface of the grain (or *chemisorbed*), while the other one migrates freely until it reaches the first one. During this reaction, energy is released, parts of which is absorbed by the molecule and turned into its rotational or translational motion, or as excitation. This is the end of the grain surface interaction, as the molecule leaves the grain and becomes a part of the wilderness that is the interstellar medium.

Dust also has a few very important roles in the process of star formation. Primarily, dust removes some of the energy that collapsing molecular clouds give of in the form of IR emission. Secondly, dust grains shield the molecular clouds from the light emitting from the stars, which reduces the ionisation that would normally oppose the creation of a star (Ciolek, 1995). This means that dust is very closely connected to star formation, and thus can help the study of these star-forming regions in better detail.

2.4.2 Life cycle of dust

A schematic showing the evolution is given in Fig. 2.19. The cycle starts with the stage of an intercloud medium, which then continues to form a cold cloud that does

not exist indefinitely, but further tansforms, either by cloud destruction or by being included in other processes, such as star formation. Both of these mechanisms lead to the return of the cloud to the stage of the interstellar medium.

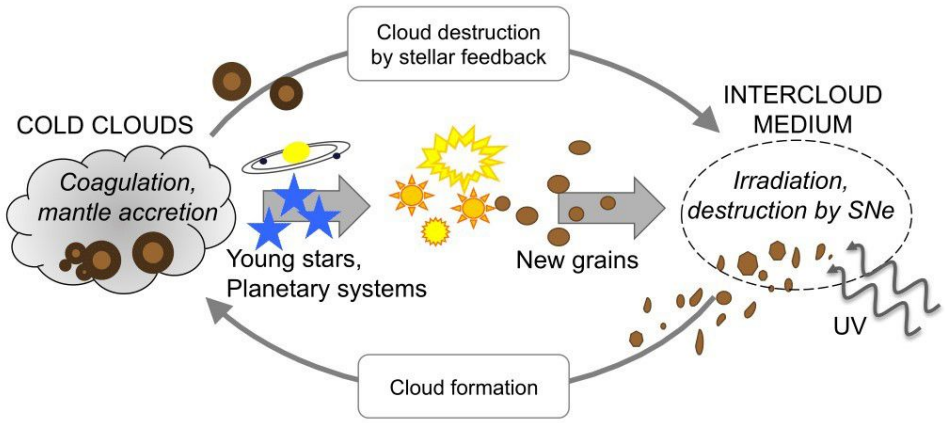

Figure 2.19: A schematic representation of the life cycle of dust in the interstellar medium. Figure from Zhukovska & Henning (2014).

How the dust initially appears in the interstellar medium is a very interesting question. Knowing that some of the main ingredients of dust are carbonaceous materials, silicates and other heavier components, it is natural to deduce that dust must be created somewhere in the insides of stars. A very peculiar source would be the supernova explosions, which create heavy elements in a very short time. The other source is the stellar ejecta, such as stellar winds, which enrich the interstellar medium with the elements created in stars.

There are mainly two ways the grains are created and grown in the ISM, the first is the direct collision between two grains, called coagulation, which depends on the velocities of the grains as well as their composition and structure, while the second is the accumulation of atoms and molecules on the surface, known as *mantle growth*. The main difference between these two mechanisms is that the latter influences the gas-to-dust ratio in the ISM, by creating new dust grains from the gas materials. The first mechanism only redistributes the gas mass between grains. For both mechanisms, the rate of growth increases with the rate of the collisions between the dust (or dust with atoms and molecules), and consequently with the density of the cloud itself.

A supernova (SN), with all the material it ejects during its explosion, is the prime candidate for the source of interstellar dust. It is known that the needed components of dust are created during this event, so it likely contributes to the overall dust abundance. However, there is the possibility that a large fraction of the dust created will be immediately destroyed by the shocks of the SN itself. So, even though the SN does contribute to dust creation, it is unlikely to be its only creation centre (Zhukovska & Henning, 2014).

Another source of dust are the low-mass to intermediate-mass stars in the asymptotic giant branch (AGB) of the H-R diagram. These stars eject matter into the surrounding medium, some of which is in the form of dust. It is difficult to quantify this ejection because it is strongly dependent on metallicity. Some models predict some values for the dust ejected from stars (Zhukovska & Henning, 2014), but there is a large variation between them.

After the dust has been initially created it might stay in the interstellar clouds, or it could participate in the process of stellar formation and the creation of planetary systems around it. During this process, the dust is "used up", which means it is no longer dust, but a part of a star or a planet, so it is destroyed. This stage of the life cycle does not last forever, so eventually, the dust is returned to the interstellar medium.

If dust remains in the interstellar medium after star and planet formation has taken place, it will be eventually destroyed by a supernova blast. The shock velocities that are produced during an SN are powerful enough to disintegrate the dust and turn it back into gas. With that, the life cycle of the dust is concluded and the elements of which it was comprised are free in the ISM to either move on to other astrophysical formations or restart the cycle and go through all of the stages once more.

Conclusion

This chapter includes some of the theoretical considerations that are typical for more pedagogical documents, such as reports or theses, so it perhaps includes some basic level information that usually is assumed to be known. However, as this thesis will be read by astronomers with potentially varied backgrounds it is necessary to make sure we are all on the same page. Furthermore, I hope one day I will have students of my own who will be able to use this thesis as a resource to start diving into the fields that I can help them improve in.

It is impossible to cover the entirety of background information relevant to the topics I have been working on during my studies, so I have surely missed some topics that also might be seen as important. Thus, this chapter contains some of the main concepts that are brought up later on, in the more scientific chapters. I believed it was better to give them a separate chapter to avoid cluttering the text later on, where I can focus more specifically on the work that was done. Seen as the topics are slightly different from each other, the chapters themselves will also include some background information that is only relevant to the specific work.

I like to think of this "theory" chapter as containing the list of ingredients of the recipe that is a thesis, and now the following chapters will focus more on the cooking instructions, i.e. the methods and techniques used to obtain the results.

3 Evolution of the dust attenuation with stellar mass and redshift

I will present the main work of my PhD studies in this chapter. It has been published in *MNRAS*, and the final version can be found as an Appendix to this manuscript. The results in this chapter are the same ones as in the Bogdanoska & Burgarella (2020) paper, whilst the methods that we used are described in more detail in this thesis. More precisely, an in-depth explanation will be presented, as I believe it is relevant in understanding how we arrived at the final results of the work.

You will notice that this chapter, unlike the following two, focuses more on the results and findings that we published in our paper and their justification. The reason for this is that the process of publishing this paper lasted for a long time. We tested multiple variations of our approach during this time, although some were met with suspicion either by my supervisor and me or eventually by the referee. It is the paper that includes most of my original work. For some of the data (photometric data of the sample of Bouwens et al. (2016)), I even performed the SED fitting myself, which helped me immensely to continue with the work we are currently undertaking (described in Chap. 4).

We started working on this project as a masters thesis in the distant 2018. I found this topic to be interesting and challenging enough to inspire me to do a PhD on it, especially the methods of SED fitting and all of the possibilities they offer. As time moved forward, I wished to expand my horizons slightly and learn more about dust specifically, so you will notice that I have a section on chemical evolution models in Chapter 5. I believe that including more topics in my field of expertise, especially topics that are so closely related, has given me a more stable stepping stone towards my future career in science.

Wishing to improve the current knowledge of the global properties of galaxies, we propose a new function that describes the dust attenuation in relation to the stellar mass of galaxies that includes an evolution in redshift. To do this, we start by suggesting a function for the dust attenuation - stellar mass ($A_{\rm FUV} - M_*$) dependence. Then, by assuming this dependence evolves with redshift, we find a function that interpolates between the $A_{\rm FUV} - M_*$ models of different redshifts to estimate the $A_{\rm FUV} - M_*$ relationship at any redshift. We have used this to include the redshift evolution of the dust attenuation $A_{\rm FUV}(z)$. We also compute the cosmic dust attenuation throughout cosmic time and so that we can compare it to other data of this type.

The first billion years of the universe is still uncharted territory. If we are interested in the Universe as a whole, we need to turn to cosmology for answers. However, the

processes within one of its main building blocks, galaxies, remain vastly unknown. Understanding and describing the creation and evolution of galaxies is one of the most critical achievements modern science aims to reach. This dream is becoming a reality with the help of cutting-edge telescopes and satellites, alongside the most advanced scientific methods to date.

This chapter begins with a short description of the data we used in our project (Sect. 3.1). Then, the most noteworthy results published in our paper are given in Sects. 3.2 and 3.3, without any particular explanation or justification, unlike the paper itself. The reason for this is that the following sections describe how exactly we reached this result (Sect. 3.4), and why we believe there is scientific evidence for them (Sect. 3.5). I also discuss some of the shortcomings of our work in Sect. 3.5.4, including an exciting recent paper that cites our work. Finally, I add the conclusions of the paper (Sect. 3.6) summarising our results and answering some of the questions included in my thesis.

We use a Salpeter (1955) Initial Mass Function (IMF) for the stellar masses used throughout our work, as well as a ΛCDM cosmology with $(H_0, \Omega_m, \Omega_\Lambda) = (70, 0.3, 0.7)$, where H_0 has the units of $\mathrm{km\,s^{-1}\,Mpc^{-1}}$.

3.1 The data used

We select data from the literature to build our sample. The selection criteria are that the IRX (Sect. 2.2.7, Eq. (2.20)) values have been estimated either from a direct IR-to-UV ratio or by SED fitting that includes multi-wavelength data over a wavelength range that at least covers the rest-frame UV to the optical - near IR. We do not keep samples where IRX is estimated from the UV slope β. Although we think β could be a useful dust tracer, it has problems for dusty galaxies that are known not to follow the Meurer et al. (1999) relation (Burgarella et al., 2005; Casey et al., 2014). The reason for this departure is not studied here. We do not use the Balmer decrement because galaxies selected from emission lines are generally younger, impacting our statistics. Since IRX is the ratio of L_{IR} to L_{UV}, only the galaxies with measured L_{IR} and L_{UV} are usable for our study. We also assume that the IRX estimated from SED fitting is close to L_{IR} / L_{UV} (Małek et al., 2018, for instance). More precisely, we define the IR luminosity L_{IR} as the total integrated luminosity in the IR and the UV luminosity L_{FUV} as the flux measured with a filter (e.g. *GALEX*).

We summarise the data included in our project in the published paper. Here, however, I summarised the most critical points in a table, Table 3.1. There, you can find the number of galaxies in each sample, their redshifts and the type of data included in the sample (individual sources or stacked). We also give information about the field the data belongs to, the selection criterion, and some information about the SED fitting, namely the IMF and SFH. The stellar population synthesis model is not mentioned, as all authors use the models of (Bruzual & Charlot, 2003). They are also shown in Fig. 3.1, alongside the fits described in the following sections.

Table 3.1: Summary The literature used to obtain the data, the galaxy count in each data set, values The redshift bins from each reference, the type of data, the field the data belongs to, the selection criterion as well the IMF and SFH. All authors use Bruzual & Charlot, 2003 stellar population synthesis models. For Salim et al., 2016; Salim et al., 2018 the redshift is taken to be $z = 0.1$, which is the mean value of the redshifts of all the galaxies in the sample. A range is given for the Bouwens et al., 2016 data because individual galaxies are used, and the separation of the bins is performed specifically for this work.

Reference	Galaxy Count	z	type of data	Field/survey	Selection criterion	IMF	SFH
Salim et al., 2016; Salim et al., 2018	≈ 400,000	< 0.3	individual	GALEX-SDSS-WISE Legacy Catalog (GSWLC)	Magnitude limited	Chabrier, 2003	two-component exponential
Pannella et al., 2015	≈ 50,000	0.7, 1, 1.3, 1.7, 2.3, 3.3	stacked	GOODS-N field	UV-selected	Salpeter, 1955	exponentially declining
Heinis et al., 2014	≈ 40,000	1.5, 3, 4	stacked	COSMOS + Herschel MultiTiered Extragalactic Survey (HerMES)	UV-selected	Chabrier, 2003	exponentially declining
Alvarez-Marquez et al., 2016	≈ 22,000	3	stacked	COSMOS field	U-dropout LBGs	Chabrier, 2003	exponentially declining
Fudamoto et al., 2017	39	3.2	individual	COSMOS field	UV-selected	Chabrier, 2003	exponentially declining
Schaerer et al., 2015	5	6.5 – 7.5	individual	GOODS-N field		Salpeter, 1955	exponentially declining
Fudamoto et al., 2020b	23	4 – 5	individual	ALPINE		Chabrier, 2003	constant
Bouwens et al., 2016	78	4 – 10	individual	Hubble Ultra Deep Field (HUDF)	UV-selected LBGs	Salpeter, 1955	exponentially declining
Burgarella et al., 2020	18	5 – 10	individual		FUV-selected	Chabrier, 2003	exponentially declining

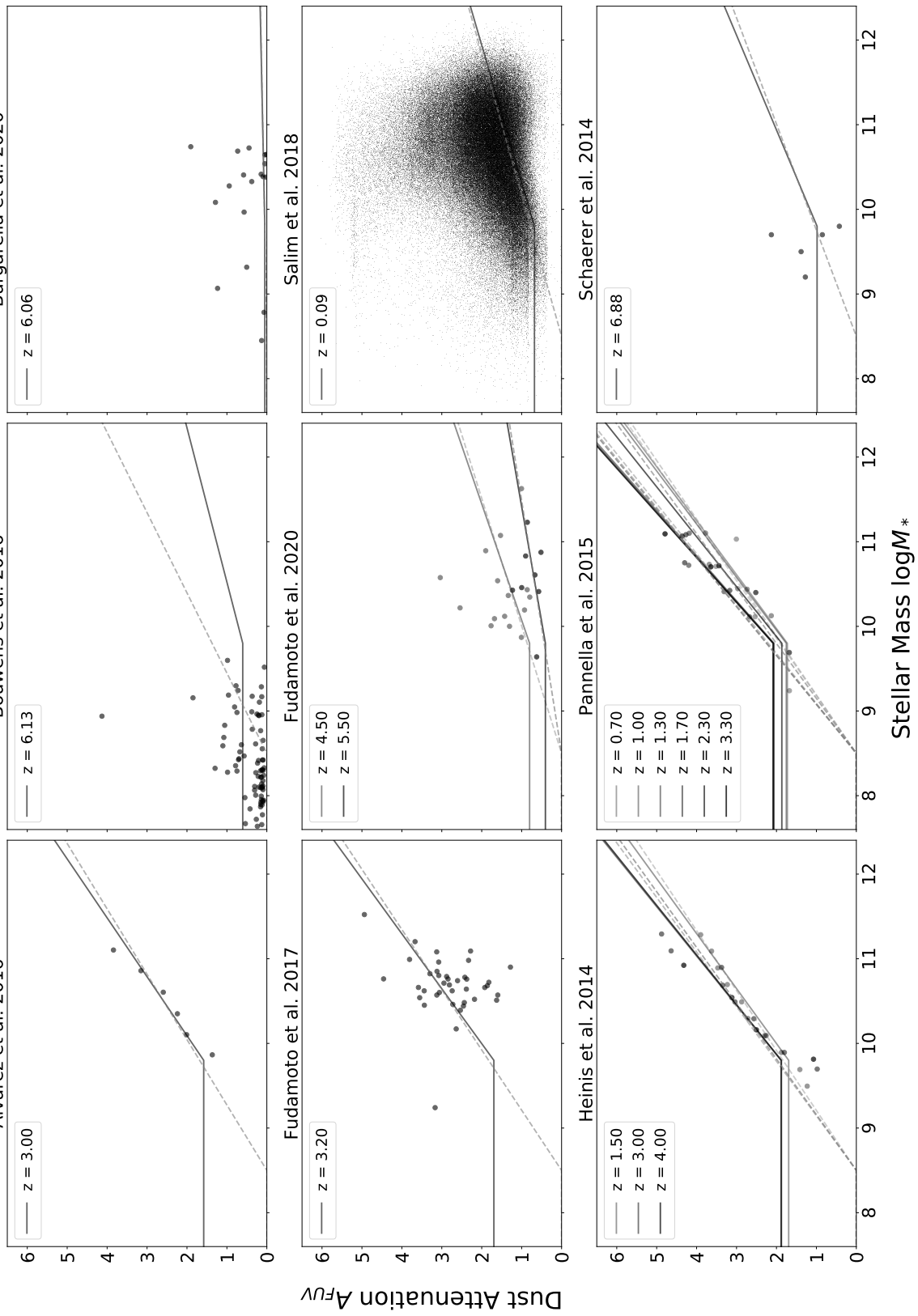

Figure 3.1: The dependence of the UV dust attenuation on stellar mass, showing the data from several references, along with the best-fitting model for the same redshift. Each panel represents the data from a different paper, with multiple different lines within one panel are models for different redshift bins. The dashed lines represent the model proposed in Eq. (3.3), while the full lines show the model of Eq. (3.1).

3.2 Evolution of the dust attenuation

This section, similarly to the eponymous section of our paper, is dedicated to studying the relationship between the stellar mass of star-forming galaxies and their average dust attenuation in the FUV, as estimated by the IRX from the galaxies' SEDs. Exploring this relationship is not a simple matter, especially since neither the stellar mass nor the dust attenuation is directly observable. However, they are two very intuitive parameters of the galaxies, so understanding this relationship will lead to a better understanding of the overall evolution of galaxies.

This relationship between the dust attenuation and the stellar mass has been the subject of many studies during the last two decades (e.g. Burgarella et al., 2005; Martin et al., 2007; Xu et al., 2007; Pannella et al., 2009; Buat et al., 2012; Heinis et al., 2014; Whitaker et al., 2014; Pannella et al., 2015; Alvarez-Marquez et al., 2016; Bouwens et al., 2016; McLure et al., 2018; Reddy et al., 2018; Koprowski et al., 2018; Theios et al., 2019; Alvarez-Marquez et al., 2019; Fudamoto et al., 2020a; Fudamoto et al., 2020b). Although it is usually assumed that the IRX-M_* relationship is the same at all redshifts, it is still an active research topic. However, the work of Bouwens et al. (2016) suggests either an evolution of the dust temperature or a change in the relationship at large redshift. The latter might be confirmed in the most recent works. For instance, Fudamoto et al. (2017) and Fudamoto et al. (2020b) observe an evolution of the IRX – M_{star} relationship between $z \sim 3$ and $z \sim 6$ by about 0.24 dex. We based our work on the assumption that the $A_{\mathrm{FUV}} - M_*$ relationship does indeed depend on redshift. We attempt to find a relationship between the dust attenuation and the stellar mass for each redshift. Later on, we try to reconcile this relationship with the evolution of the average dust attenuation with cosmic time (Section 3.2.2).

In this project, there are three parameters involved: the stellar mass, the redshift and, of course, the dust attenuation. We wish to avoid dealing with all three of them at once, even though it was one of the suggested pathways for this project (see Sect. 3.4). The most efficient way to do that is to bin the data according to one of the parameters and then study each bin separately. Thus, the very first step of this project is to divide the data into redshift bins. Already this gives us an advantage: as the bins naturally divide the data, we can safely include different types of data in our project, as long as they are not in the same bin. By "different types of data", we refer to stacked observations instead of observations of individual galaxies. The stacked data are already binned by redshift, and we keep these bins in our work, even though in some cases, it means we have more than one bin at the same redshift as we want to avoid mixing the data provided by different authors. The individual object data published by Bouwens et al. (2016) and Burgarella et al. (2020) were divided in two bins each, and kept as a single bin for Salim et al. (2018) and Schaerer et al. (2015).

The aim was to fit the dust attenuation with a two-parameter function which we can write as $A_{FUV}(M_*, z)$. Following the idea of separating the dependence of the dust attenuation on the stellar mass from that on the redshift, we express it as a product of two independent functions, $f(M_*)$ and $a(z)$. Each of these functions has only one

variable. Thus we can write the dust attenuation as $A_{FUV} = f(M_*) \times a(z)$, allowing us to treat separately each of these dependencies.

When the data are binned, we assume that the bin has only one redshift, disregarding the redshift scatter within each bin, allowing us to fit the function simply as $A_{FUV} = f(M_*)$, as has been done many times before (Sect. 3.2.1). Once we ascertain this relation, in Sect. 3.2.2 we focus on the $a(z)$ part of the function by comparing the results between redshift bins.

3.2.1 Dust attenuation as a function of stellar mass

The usual approach is to fit with a linear function either in IRX or directly in A_{FUV}. Because we adopt a more global approach, we modify this dependence and assume a broken line: a linear function until a particular value for the stellar mass and constant below. More details about why and how we found that this solution is the most appropriate to our problem, given what is currently known, can be found in Sect. 3.4. Assuming that the function has the same *shape* for any redshift, the only differing variable is a scaling factor that we call a. The function we propose is the following:

$$A_{FUV}(\log M_*) = a \begin{cases} 1.1, & \log M_* < 9.8 \\ \log M_* - 8.7, & \log M_* \geq 9.8 \end{cases} \tag{3.1}$$

The value of the parameter a is different for each of the redshift bins. The displacement of the $A_{\rm FUV}(M_*)$ function in the vertical direction, as well as the steepness of the upward slope, is governed solely by the value of a, thus making it sufficient only to perform fitting for the value of this parameter in each redshift bin. The best fits of the data are shown in Fig. 3.1.

However, Eq. (3.1) includes two parameters that we have defined not to change between redshifts. The first parameter, the intercept of the function with the x-axis, i.e. the stellar mass for which A_{FUV} would be zero if we only used an unbroken line, has the value $p_1 = 8.7 \pm 0.1$ in our function. The second parameter determines where the function break happens, meaning the stellar mass for which A_{FUV} changes from linear to constant behaviour and has a value of $p_2 = 9.8 \pm 0.1$. The value of the constant part is set to ensure continuity of the function, more precisely $A_{\rm FUV}(9.8) = 1.1$.

These values are also determined by fitting the data. The procedure consisted of fitting all of the data multiple times, testing for different combinations of the two parameters. In each iteration, a pair of values (p_1, p_2) was chosen. Then for this pair, the data in all of the redshift bins was fitted, giving a set of values for a. For each bin, the χ^2 of the fit is computed as well. Finally, we compared the values for the χ^2 with the different pairs (p_1, p_2) that we tested to find the minimum, and this is how we found the values presented in Eq. (3.1). The main idea behind this is to keep the redshift dependence as simple as possible and contain it only in the value of a.

We include data with redshifts $z \geq 6$, for which detections of low-mass galaxies are

non-existent or, at best, scarce. So, the relation we propose for the low mass galaxies in this redshift range comes from drawing an analogy to low-redshift galaxies. We discuss the evidence for this later on in this chapter (Sect. 3.5.1), but we do not claim to precisely determine the relation for the low mass galaxies. What we do is set the simplest possible form as a first approximation: a constant. Our tests let us determine that having a non-zero value for the low-mass galaxies is necessary. Still, the exact shape and behaviour cannot yet be determined from available data. Thus, in the conclusion of our paper, we state that we have found evidence that low-mass galaxies have an *apparent* dust attenuation greater than zero. Due to a large scatter and lack of data, the simplest way to include this in our models is to keep it constant. We show the modelled plots for arbitrary redshifts in Fig. 3.2.

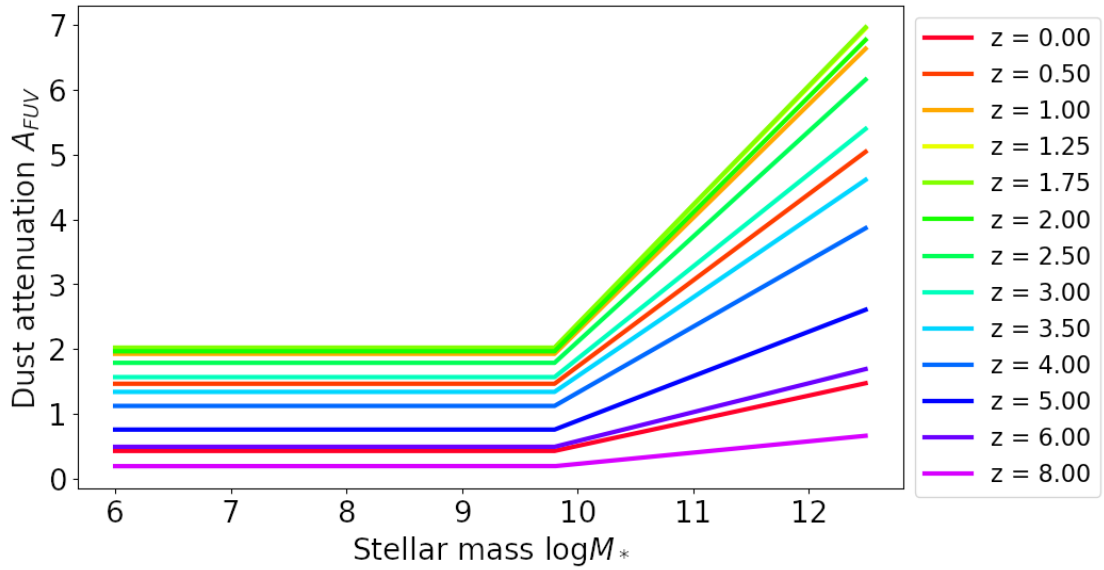

Figure 3.2: The dependence of the UV dust attenuation on stellar mass with the parameters derived by fitting as described in Sect. 3.2.1, showing the model at different redshifts. The different coloured lines show Eq. (3.1), for the value of a computed by Eq. (3.2) at the appropriate redshift.

3.2.2 Redshift evolution of the dust attenuation

Starting from the work shown in Sect. 3.2.1, we continued investigating the evolution of the dust attenuation of star-forming galaxies with redshift. We have taken from Eq. (3.1) the only parameter that varies between redshifts - the fitting parameter of the $A_{FUV} - M_*$ relation, with the difference that this time we view it not as a simple constant a, but as a function of redshift, i.e. $a(z)$. Compiling the best-fitting value of a from each redshift bin and then using these values as our new "data points", we use the following function best to describe the evolution of $a(z)$:

$$a(z) = \left(z+\gamma\right)\cdot\alpha^{\left(\beta-(z+\gamma)\right)}, \tag{3.2}$$

the coefficients have the following values: $\alpha = 1.84 \pm 0.11$, $\beta = 1.84 \pm 0.12$, and $\gamma = 0.14 \pm 0.04$. We propose this function as it has a similar shape to the one used by Madau & Dickinson, 2014 and Burgarella et al., 2013, but giving a better fit.

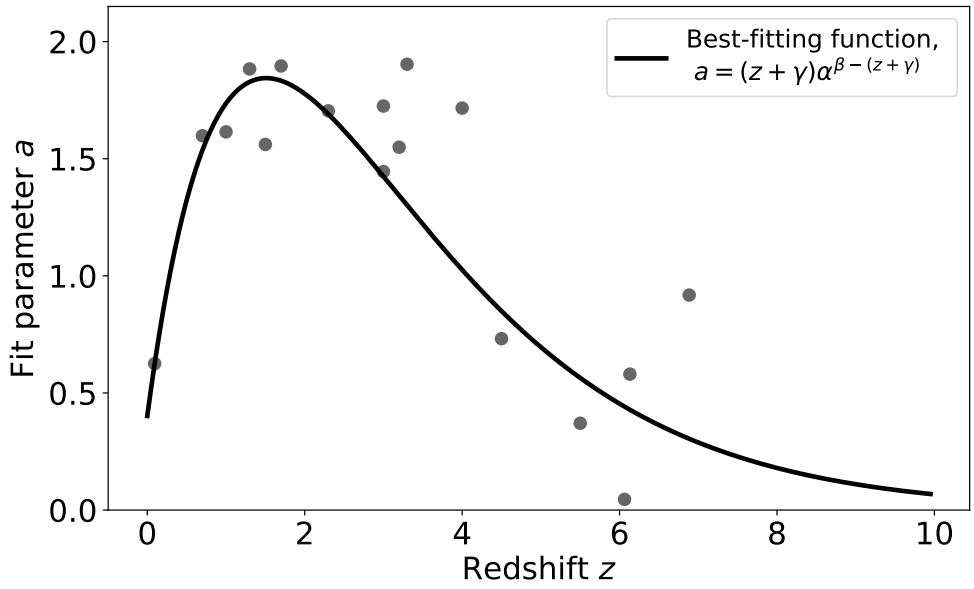

Figure 3.3: Fitting the parameter a from the $A_{FUV} - M_*$ relationship in each redshift. Each point has been obtained by fitting the available data in that redshift. The black line represents the fit of these points, as fitted with the function of Eq. (3.2).

We show in Fig. 3.3 this evolution with redshift of the parameter a, alongside the best-fitting function of Eq. (3.2) represented by the black line. The data points are the values of the fit from Fig. 3.1. Note here that the difference between the line and the points in Fig. 3.3 translates to a difference between the lines we used to fit the data in Fig. 3.1 and the models we reproduce at each redshift in Fig. 3.2.

Except as a parameter of Eq. (3.1), a does not have a physical interpretation. We get something meaningful only when we plug it back in Eq. (3.1): a relationship between the dust attenuation and stellar mass at the redshift for which the parameter a has been calculated. It represents a surface in the three-dimensional space of $A_{FUV}(M_*, z)$ (more on this in Sect. 3.4). Another way to connect the values of a with the dust attenuation is to explore this relationship at a single stellar mass. Like we did within each redshift bin, we can look at the $A_{FUV}(z)$ function in different stellar mass bins.

However, to our knowledge, this type of plot has not been published in the literature. Thus we included cosmic dust attenuation in our work. I have explained in Chapter 2 (Sect. 2.3) the method we use to compute this average or *cosmic* dust attenuation, and the following section is devoted to our findings on this topic.

3.3 Comparison with the cosmic dust attenuation

We wish to compare our findings from Sect. 3.2 to the available results in the literature, and we do this by computing the evolution with redshift of the average dust attenuation in galaxies that we will call the cosmic dust attenuation (Sect. 2.3). We need to calculate the function's average representing the $A_{FUV}(M_*)$ relation, including *all* star-forming galaxies. We estimate the weighted average of the dust attenuation, the weights being the Mass Function (MF) for star-forming galaxies (Sect. 2.3.1). It accounts for our assumption that the $A_{FUV} - M*$ relation can represent the dust attenuation of all star-forming galaxies, given their stellar mass. The results are shown in Fig. 3.4.

It is interesting to see that the shape of the curve is very similar to the curve obtained by other authors, such as Burgarella et al. (2013) and Cucciati et al. (2012), even though the methods used in both cases are different (different from each other and different from our work). E.g. Burgarella et al., 2013 use the UV and IR luminosity functions (LF) (Sect. 2.3.1) redshift evolution to estimate the IRX, and consequently, the $A_{\rm FUV}$. They use the FUV LFs from Wyder et al. (2005) and the FIR LFs from Takeuchi et al. (2005) at redshift $z \sim 0$, and the Cucciati et al. (2012) FUV LFs combined with the FIR LFs of Gruppioni et al. (2013) for redshifts $0 < z < 4$, from which they compute the IR and UV luminosity densities (LD) (Sect. 2.3.2) by integrating in the luminosity range $\log(L/L_\odot) = [7,14]$ for the FUV and $\log(L/L_\odot) = [8,14]$ in the FIR. They determine the IRX from the ratio between the FIR LD to the FUV LD and then use the relation of Burgarella et al. (2005) to convert to A_{FUV}. Cucciati et al. (2012) use the Calzetti et al. (2000) recipe to determine the dust attenuation at 1500 Åfrom the E(B-V) value estimated by the SED fitting of individual objects. They find the mean E(B-V) of galaxies above the magnitude limit of their observation and claim that it does not depend on the range of luminosities within the redshift bins.

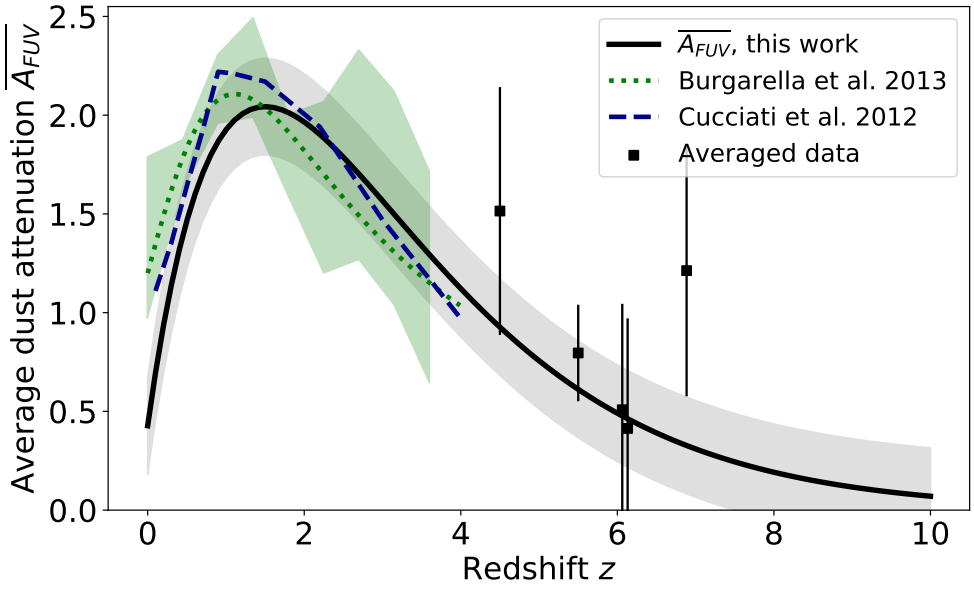

Figure 3.4: The evolution of the dust attenuation in the FUV with redshift. The full black line represents the integrated average dust attenuation, calculated with the model of Eqs. (3.2) and (3.1). In this case, $\overline{A_{FUV}}$ has been computed using the limits of $6 < \log M_* < 14$, analogous to the limits of integration used in the work of Burgarella et al. (2013). The shaded area around the full black line corresponds to the total estimated 1-σ uncertainty of the parameters of Eq. (3.1), alongside the errors of the fitting for the coefficients of Eq. (3.2). We note, however, that the uncertainties might be under-evaluated at low redshift. The origin of this under-evaluation is not clear but may come from the fitting of Eq. (3.2) for $z = 0$. The points represent the mean values estimated in this work for $z > 4$. The dotted green line and the shaded green area surrounding it comes from Burgarella et al. (2013). The line is the best-fitting model, and the shaded area is the error bars. The dashed dark blue line shows the results of Cucciati et al. (2012).

Another work that estimates the average dust attenuation is presented in Bouwens et al. (2009). We did not include this work in our analysis in Fig. 3.4 because their sample includes only LBGs, and there is some additional contribution to the UV-based SFRD from other types of galaxies and the IR-based SFRD. Nonetheless, their results are qualitatively in agreement with the works listed in Fig. 3.4. They estimate the dust attenuation at 1600 Å from the UV-slope β using the Meurer et al. (1999) relation and estimate the *effective* dust attenuation by integration of the LFs from Reddy & Steidel (2009) at $z \sim 3$ and those of Bouwens et al. (2007) at $4 < z < 6$, within limiting luminosity up to $0.3L^*_{z=3}$.

Furthermore, this curve is closely related to the classical Madau & Dickinson, 2014 SFRD curve. As Burgarella et al. (2013) noted, the peak of the cosmic dust attenuation is delayed compared to the peak of the SFRD, suggesting that a *dusty era* started at $z \approx 3$, around the same time that a universal star-formation event happened. They propose an explanation for this in the dust creation mechanisms but conclude that the timescales of this delay would be too short. A more reasonable suggestion they give is that there is a global movement of galaxies in the $[\log(L_{FIR}/L_{FUV})$vs$\log(L_{FIR}+L_{FUV})$ diagram (Buat et al., 2009), with high redshift galaxies moving towards lower IRX for a given luminosity.

Even though the shape is quite close, as was noticed above, the curve representing the cosmic dust attenuation (Fig. 3.4) is not to be confused with the fitting parameter values a (Fig. 3.3). The cosmic dust attenuation is a physical parameter that has consistently been studied, The parameter a is an internal "stepping stone" to get us from a simple view of unchanging $A_{FUV} - M_*$ relationship to one that evolves throughout cosmic times.

3.4 Tested functions

In the previous sections (Sects. 3.2 and 3.3), I presented the results of our paper directly, without explicitly saying how we reached those results or how we decided they were the ones we want to publish. The following part will give more details on the journey that led us to the results presented above. In Sect. 3.5 I will also give evidence from other scientific publications that support our hypothesis, but in this thesis, I want to discuss some of our "failed" attempts, more precisely some of the functions or methods we tested but did not publish.

The $A_{FUV} - M_*$ relationship seems to be simple enough to fit; it has been done numerous times and should not pose a problem. Nonetheless, due to how we have set our problem, determining this relationship is not independent of the redshift evolution of the cosmic dust attenuation, so it was required to repeat the entire process multiple times. I will not report and give all the small details, but I will provide the functions themselves because some may eventually find their place among the better models with new data. I hope this could save someone else's time by not having to test these functions again.

The results presented in our final paper come from a series of tests we have performed with the data given. We did not wish to overload the text by detailing every step that led us to those conclusions. However, we understand that it might not be evident why we have chosen this particular set of results as the best one. Hence, we show the evolution of our idea from its conception to the published results.

3.4.1 Fitting the dust attenuation - stellar mass relationship

The initial work included the data from Ciesla et al., 2014 and Cook et al., 2014, which we ultimately replaced by the GALEX-SDSS-WISE Legacy Catalog (GSWLC) of Salim et al., 2018, which in theory already contains all of the sources in the previous two papers.

When we started this project, we did not wish to assume any shape of the function and instead tested the most popular choices found in the literature. We started with a simple line for $A_{FUV} - \log M_*$, as often practised in the literature (although usually as IRX$-\log M_*$) We started with a simple line (in terms of A_{FUV} and $\log M_*$). Polynomial functions were also tested, as this is one of the forms the IRX - A_{FUV} relation usually assumes (e.g. Buat et al., 2005). We also wished to include some flattening for the high-mass end of the function, as seen in Whitaker et al., 2017, but eventually, we moved on from this view as it did not contribute much to our results. We ultimately calculate the cosmic dust attenuation, which contains within itself the MF. According to the MF, high-mass galaxy contribution is negligible due to their deficient number, so our results did not show a difference. A summary of the functions we tested and a short reason against each of them is given in Table 3.2. Admittedly, in the end, we discarded these functions to make up for the issue of the low-mass galaxies.

Conversely, when we tested the parabolic shape of the $A_{FUV} - M_*$ relation, we also arrived at some reasonable results. The minimum of the function as estimated by similar methods as described in Sect. 3.2 was around $\log M_* \approx 7$. But, this kind of function predicts an increase of the dust attenuation for galaxies with $\log M_* < 7$. Considering that these low-mass galaxies are numerous, they significantly raise the average dust attenuation value. This rise is enough to be in the range of the values already found in the literature. However, we decided against this function because we cannot predict the behaviour of this function at such low masses, so the safest assumption we could make was the flattening that we introduced in the paper.

Table 3.2: Some of the functions that we used during our preliminary fitting of the $A_{FUV} - M_*$ data. A short reason for choosing not to use any of these functions is given, but the final choice was to get the best fit with the most simple solution.

Function	Reason against it
$A_{FUV} = a(\log M - b)$	Negative for $\log M < b$
$A_{FUV} = a(\log M - b)^2$	Increases for $\log M < b$
$A_{FUV} = a(\log M - b)^n$	Very computationally demanding
$A_{FUV} = \frac{a}{\exp(b \log M)}$	Too low for low-mass galaxies
$A_{FUV} = a\big(k(n - d\log M) \times (c^{(n-p\log M)}) + b\big)$	Too many parameters

The closest function that we found that avoided the piece-wise shape was the usual linear relation, with the constraint that we only include galaxies with $\log M_* > 9$ in our investigation. We justify this choice by pointing out that data for galaxies with

$\log M_* < 9$ are scarce at all redshifts. This function is plotted in Fig. 3.1 with a dashed line. It serves as a further illustration of the need for a flattening at the low-mass end.

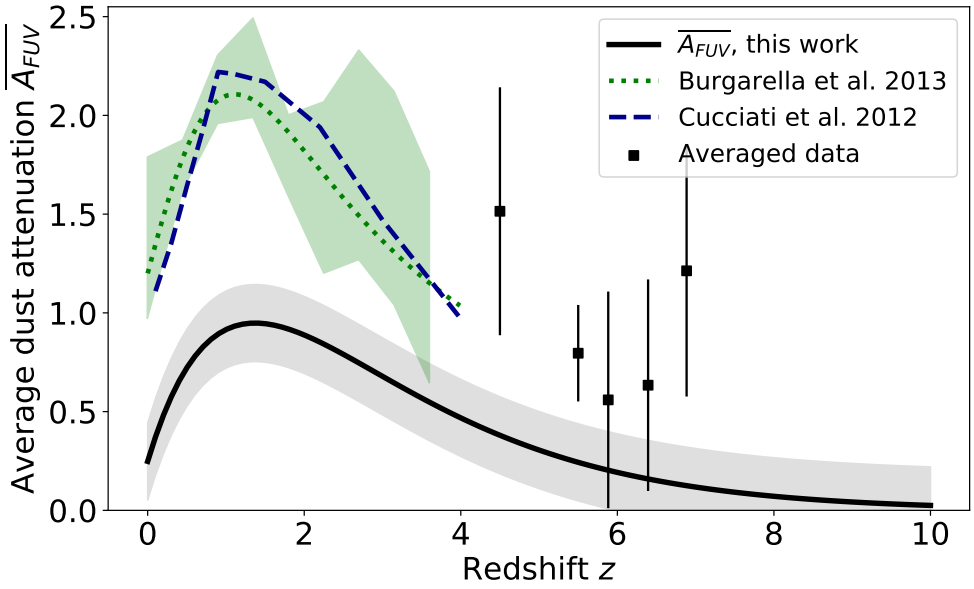

Figure 3.5: The evolution of the dust attenuation in the FUV with redshift. The full black line represents the integrated average dust attenuation, calculated with the model of Eqs. (3.3) and (3.2). The only galaxies included are those with $\log M_* > 9$. Consequently, the limits of integration for $\overline{A_{FUV}}$ have shifted to the range $9 < \log M_* < 14$. The shaded area around the full black line corresponds to the total estimated 1-σ uncertainty of the parameters of Eq. (3.3), namely the uncertainty of the intercept of the function estimated with the χ^2 method, alongside the errors of the fitting for the coefficients of Eq. (3.2). The points represent the mean value of the data we included in our work (Fig. 3.1) for $z > 4$, with the error bars representing the 1-σ dispersion around the mean value. The dotted green line and the shaded green area surrounding it come from Burgarella et al., 2013. The line is the best-fitting model and the shaded area is the error bars. The dashed dark blue line shows the results of Cucciati et al., 2012.

The fitting gives a slightly different value of the zero of the function, and this value is not included in the integration limits, so the function we use is the following:

$$A_{FUV}(\log M_*) = a(\log M_* - 8.5) \tag{3.3}$$

This function is used to calculate the cosmic dust attenuation, and the results are shown in Fig. 3.5. We seem to be seriously underestimating the average dust

attenuation throughout cosmic times. The cause of this is seemingly the ratio of low-mass to high-mass galaxies, i.e. the shape of the mass function; the number of low-mass galaxies is much higher, so they contribute a lot more to the cosmic average. The best way to reconcile this discrepancy was to modify the $A_{FUV} - M_*$ relationship and to finally decide on the function shown in Eq. (3.1).

3.4.2 Fitting the dependence of the dust attenuation with redshift

Fitting the $A_{\mathrm{FUV}} - z$ relationship seemed to cause us somewhat fewer troubles - we only need to fit a function to the values of the parameter a, and this is a lot simpler than trying to include data from many different sources. I would like to point out that the overall shape of the $a(z)$ curve showed up consistently no matter which functions from Table 3.2 we used in the previous step. This consistency encouraged us to pursue our work in this direction and keep the assumption about a redshift-dependent $A_{\mathrm{FUV}} - M_*$ relation.

As in the previous section, we tested multiple functions, some of which are listed in Table 3.3. We got our inspiration for the shape from the work of Burgarella et al., 2013 and Madau & Dickinson, 2014, and even though their exact function was not the best fitting for our data points, we eventually chose a very similar function. Another strong contestant for the final function was the sum of two Gaussians. The approach might not seem very intuitive, but it made it possible to include what appears to be a plateau in the range $1 < z < 4$. We believe this plateau is a physical phenomenon. It does account for why other authors did not find a redshift evolution in the $A_{\mathrm{FUV}} - M_*$ relation - they mainly studied data within this range. In the end, we decided against including this plateau, and we hope that future observations will give us more information about this epoch.

Table 3.3: Some of the functions that we used during our preliminary fitting of the $A_{FUV} - z$ data. A short reason is given for choosing not to use any of these functions, but the final choice was made to get the best fit with the most simple solution, using the AIC and BIC methods.

Function	Reason against it
$A_{FUV} = \frac{a+bz}{1+(z/c)^d}$	High-z data changes the overall shape
$A_{FUV} = A_1 \exp\left(\frac{-(z-\mu)^2}{2\sigma^2}\right) + b$	Declines too fast for high-z
$A_{FUV} = A_1 \exp\left(\frac{-(z-\mu_1)^2}{2\sigma_1^2}\right) + A_2 \exp\left(\frac{-(z-\mu_2)^2}{2\sigma_2^2}\right)$	Too many parameters
$A_{FUV} = A_1 \exp\left(\frac{-(z-\mu_1)^2}{2\sigma_1^2}\right) + A_2 \exp\left(\frac{-(z-\mu_2)^2}{2\sigma_2^2}\right) + \mathrm{b}$	Too many parameters

We tested multiple functions by comparing the χ^2 differenve of the fit to the data, the Akaike Information Criterion (AIC) and Bayesian Information Criterion (BIC), to arrive at Eq. (3.2). These criteria determine the goodness of fit of a model relative to other models, similarly to the χ^2 method. However, they provide further information on whether adding parameters to the model is justified and preventing overfitting. Models with lower AIC and BIC are preferred. The AIC is computed as $\mathrm{AIC} = 2k - 2\ln(\mathrm{RSS})$, with k the number of parameters in the models, and RSS the residual sum of squares, while $\mathrm{BIC} = k\ln(n) - n\ln(\mathrm{RSS}/n)$, with n representing the number of data points. The values of these criteria do not have a particular meaning. They are only compared between models, so if two models have a difference $\Delta\mathrm{BIC} > 10$, there is strong evidence against the model with the higher BIC.

3.4.3 Integration limits for calculating the average dust attenuation

Due to the method we use to estimate cosmic dust attenuation (Chap. 2, Sect. 2.3), one crucial question is which galaxies do we use in our models. More specifically, the upper and lower limits for the stellar masses that we want to include in the integration of Eq. (3.1). We touched upon the problem of the integration limits in Sect. 3.4.1, namely, what happens when we exclude galaxies with $\log M < 9$. This section aims to demonstrate how big of an impact the integration limits have on our results and why it is imperative to remove this impact, even if it slightly complicates our function from a simple line to a piecewise function.

An obvious place to start is to integrate with the limits where we have actual data. We quickly rejected this option because these limits are different within each redshift bin, so that would mean that the quantity we are computing is not the same in each redshift. The next logical step is to take integration limits to be the minimum and maximum stellar mass of our complete sample of galaxies, regardless of redshift. Let us then take, for example, the limits $8.5 < \log(M_*/M_\odot) < 11.5$. Using the linear function of Eq. (3.3), we compute the curve shown in the right panel of Fig. 3.6. We can see that with this particular chosen function, the curve closely matches previous work. Unfortunately, this seems just a happy (?) coincidence and not a robust scientific methodology.

The problem can be easily seen when we try to play around with the integration limits. If we take the lower limit different by even 0.5 dex, so we would have $9.0 < \log(M_*/M_\odot) < 11.5$, the difference is enormous. Thus, this way of deciding on the limits is biased: we can pick and choose them to obtain the results we want.

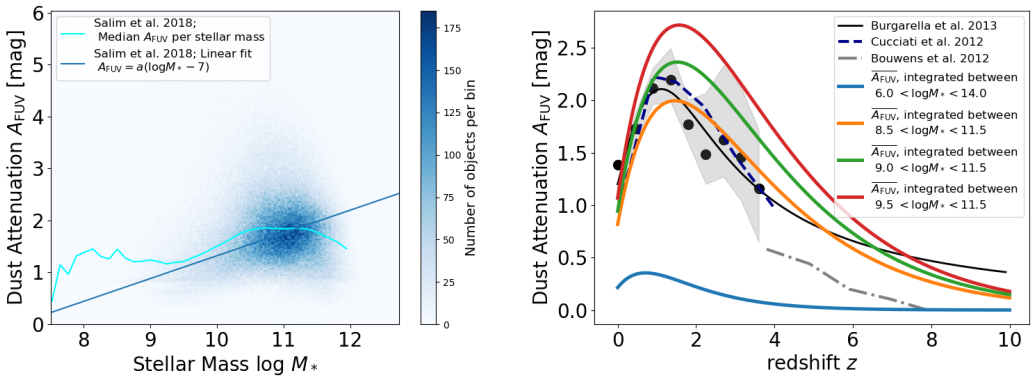

Figure 3.6: Left: A linear fit of the Salim et al. 2018 data, given as an example. The function is integrated to obtain the plot in the right panel, alongside similar data plots in different redshifts, not shown here for simplicity. Right: The average dust attenuation $A_{FUV} - z$ is computed by multiplying with the mass function and integrating within some limits. Each line of a different colour represents different integration limits.

In the end, we turned to an external factor: the literature. We have decided to have the same limits as Burgarella et al., 2013. They work with luminosities, so if we use the relation between stellar mass and absolute magnitude given in Song et al. (2016) (Table 1, value for $z = 4$), the limits we obtain are $4.6 < \log(M_*/M_\odot) < 14.0$. As objects with stellar masses lower than $\log(M_*/M_\odot) < 6.0$ cannot be classified as galaxies, and objects with $\log(M_*/M_\odot) > 12.0$ are either non-existent or extremely rare, we slightly modify the initial results, and we conclude that by taking the limits as $6.0 < \log(M_*/M_\odot) < 12.0$, we have included all of the galaxies in the Universe.

3.4.4 Iterations to improve the fitting

At the beginning of the project, we considered a wide range of functions (Tables 3.2 and 3.3). However, we needed to make sure that the results that we were getting made sense, so in reality, we had to re-iterate the entire process described in Sect. 3.2 multiple times before deciding on the final functions.

Mainly, our definition of "the results making sense" was a rough comparison with the results of Burgarella et al. (2013). Thus, if any function did not give us results that were at least somewhat close, we threw it out immediately (mainly, we were getting $A_{FUV} \approx 0$ everywhere, so there was no need to define better what we mean *close* to the results of Burgarella et al. (2013)). Before deciding to fix the integration limits we used this method, although it proved not very useful. However, we carried out our work in a few iterations, as shown in Fig. 3.7.

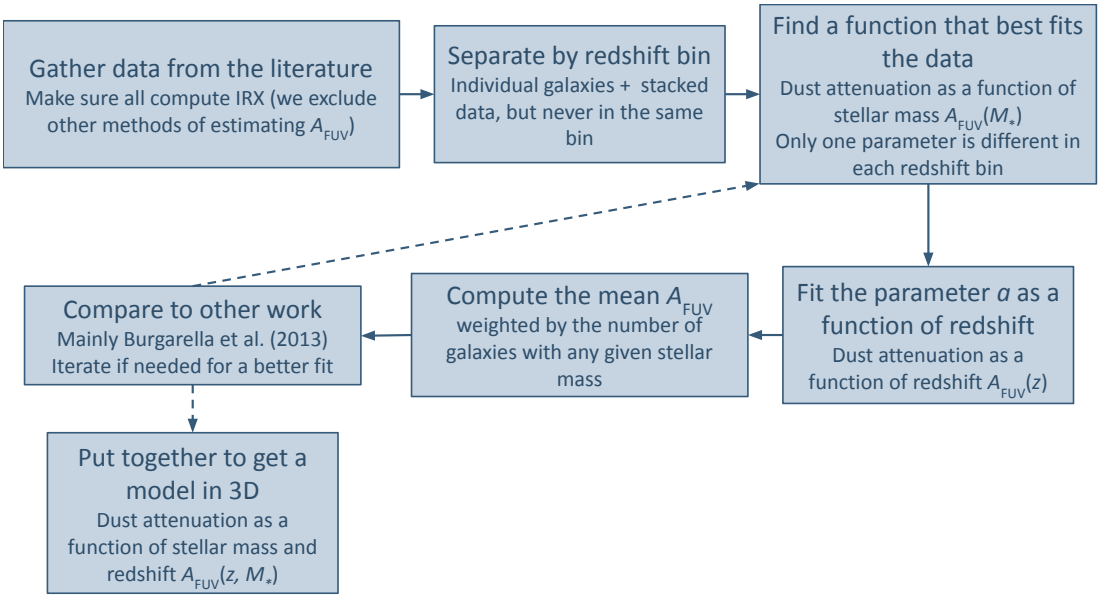

Figure 3.7: An iterative process used to improve the functions used in this project.

1. Choose a function for the $A_{\mathrm{FUV}} - M_*$ relation, with only one free parameter, a (usually a scaling factor or an offset)
2. Fit the available data in each redshift by using the chosen $A_{\mathrm{FUV}} - M_*$ function, i.e. find the best fit value of a for each redshift
3. Fit the dependence of the free parameter on redshift, $a(z)$
4. Integrate the function (times the mass function) for stellar masses in the range $6.0 < \log(M_*/M_\odot) < 12.0$ in any redshift range, using the fit for $a(z)$; this gives $\overline{A_{\mathrm{FUV}}} - z$
5. Compare $\overline{A_{\mathrm{FUV}}} - z$ to the model of Burgarella et al. (2013)
6. Check if the fit is close to the Burgarella et al. (2013) function:
   a) If so, we have found both our $A_{\mathrm{FUV}} - M_*$ and $\overline{A_{\mathrm{FUV}}} - z$ relations, and we can proceed to put them together to make a 3D function
   b) If not, repeat everything from step (i), but choose a different function for the $A_{\mathrm{FUV}} - M_*$ relation in step (i), again with only one free parameter. The new function can have a completely different form or simply a different value for one of the parameters in the function, which we keep constant between different redshifts.

3.4.5 In 3D: dust attenuation as a function of both stellar mass and redshift

As we are interested in dust attenuation as a function of both stellar mass and redshift, our task would be incomplete if we did not show this result. We have this as an appendix in our paper as it does not show any additional results, but it is merely a different way of representing the same thing given by Eqs. (3.1) and (3.2).

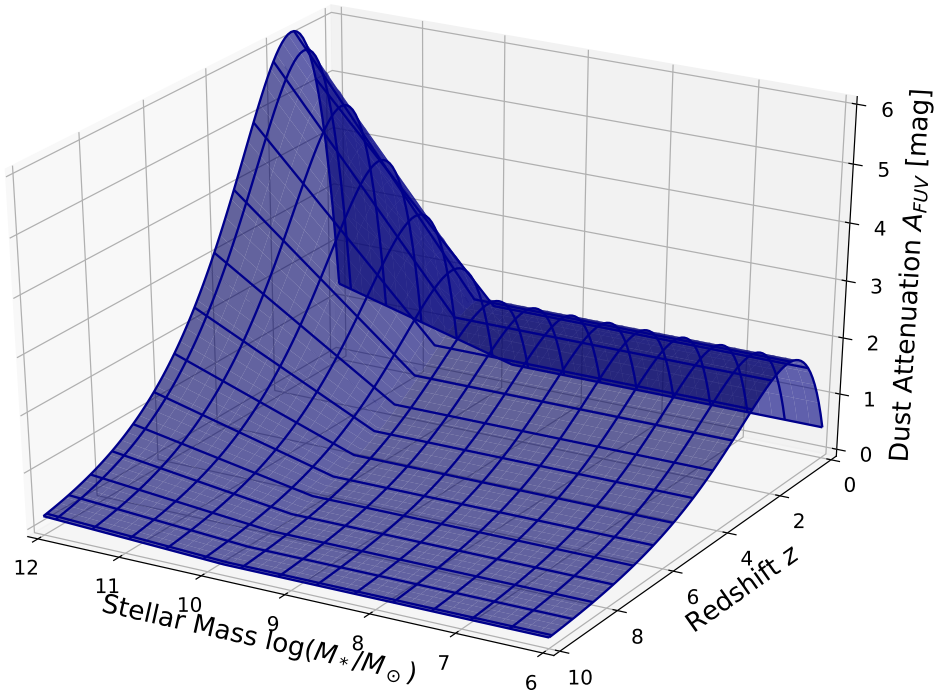

Figure 3.8: The dependence of the dust attenuation in the UV on stellar mass and redshift. The surface represents the model shown in Eq. (3.4). If we take, for example, any value $\log M_* = \text{const.}$, we retrieve the dependence given by Eq. (3.2), shown in Fig. 3.3. Similarly, for any value of the redshift, we retrieve the models of Eq. (3.1), shown in Fig. 3.1.

We already have a functional form of both the dependencies we require, $A_{FUV}(M_*)$ and $A_{FUV}(z)$, by fitting the parameter $a(z)$, and we can directly replace it in Eq. (3.1). Thus, we get the relation for $A_{FUV}(z, M_*)$:

$$A_{FUV} = \big(z+\gamma\big)\cdot\alpha^{(\beta-(z+\gamma))} \times \begin{cases} 1.1, & \log M_* \leq 9.8 \\ \log M_* - 8.7, & \log M_* > 9.8 \end{cases} \tag{3.4}$$

The parameters of this function are the same ones that are determined with the models discussed in Sect. 3.2, and thus, their values remain the same. The 3D plot of this relationship is shown in Fig. 3.8.

We also attempted to fit all of our data directly as 3D points. However, this became impossible when we included the data of Salim et al. (2018). Regardless, it is vital to implement the phases described in Sect. 3.2 because some of the initial data have already been binned and stacked. Apart from unwisely mixing two different types of data, this also means that we only have a few data points in the redshifts where the data is stacked. In contrast, in the other redshift bins, this number is more significant. This difference of data points does not exist in reality, as the number of galaxies belonging to the stacks is quite large.

3.5 Implications of this work

Understanding in its entirety the formation and evolution of galaxies require knowledge on the subject of cosmic dust. This work uses the fact that the scientific community is apt and confident about estimating the stellar mass M_* of a galaxy. We are striving towards developing a model that would calculate the FUV dust attenuation of a galaxy from its stellar mass and redshift. Such a model would enable us to estimate better the SFR of a galaxy and give us insight into the overall evolution of distant galaxies.

Some of the recently published works argue against this approach, as the $A_{FUV} - M_*$ relation evolution has been doubted (Heinis et al., 2014; Bouwens et al., 2016; Whitaker et al., 2017). This work aims to review this question with a larger set of data covering an extensive redshift range from $z = 0$ to the highest redshift galaxies. On the other hand, Bernhard et al. (2014) suggest that there is some evolution, only limited to $z < 1$. They use the relation from Heinis et al. (2014) as the basis, and for $z < 1$, they vary the normalisation as $IRX_0' = IRX_0 - 0.5 \times (1 - z)$.

To assess the validity of our work, we compare to the relevant literature Cucciati et al., 2012; Burgarella et al., 2013; Madau & Dickinson, 2014 until redshift $z < 4$. We can see in Fig. 3.4 that the values obtained by our models (Eq. (3.1), combined with Eq. (3.2)) do indeed follow a similar trend as those found in the literature, even with results obtained by using a completely different method to estimate the dust attenuation.

Notable work on this topic is the paper by Garn & Best (2010), whose work attempted to determine whether the effects of the stellar mass, star formation rate (SFR) and metallicity of a galaxy can be disentangled from each other in their relations to the dust extinction. They show that the dust extinction increases with increasing either the stellar mass, SFR, or the dust attenuation and that the relation dust attenuation-stellar mass is the dominant factor. I should note that they estimate the dust extinction using the Balmer decrement method, which means that they have selected a different type of galaxies (younger and more active in star formation).

Garn & Best (2010) fit the dust extinction-stellar mass dependence with a polynomial

(however, they find even better results when they add an SFR-dependent term). They explain this relationship by indicating that the dust content is increased over time, following the buildup of stellar mass. Thus it is not at all unexpected to have high mass galaxies with significant dust attenuation. They also explain that another contributing factor is that gravitational force is weaker for the low mass galaxies, making them more prone to losing metals through galactic winds.

3.5.1 The apparent dust attenuation of low-mass galaxies

When using our method described in Sect. 3.2, we implicitly assume that the shape of the function of the $A_{FUV} - M_*$ relation is the same throughout all redshifts. We can see, for example, in the data from Salim et al. (2016) and Salim et al. (2018) (Fig. 3.1) an apparent flattening towards the lower mass end. This sample includes galaxies with stellar masses as low as $\log M_* \approx 7$, with a large dispersion in the A_{FUV} and the values of the dust attenuation being as low as $A_{FUV} = 0.25$, and with some objects having a value as high as $A_{FUV} = 5$. We can conclude from this data that the low-mass galaxies have a large scatter in their FUV dust attenuation and a mean significantly different from zero. We believe this justifies approximating this part of the $A_{FUV} - M_*$ dependence with a nonzero constant average value.

To further justify our hypothesis, we have tried to gather different pieces of evidence in the literature. On the theoretical side, the work of Cousin et al. (2019b) presents a semi-analytical model called Galaxy Assembler from dark-matter Simulation (G.A.S.), which predicts the dust attenuation of galaxies by computing the IRX. The G.A.S. model shown in Cousin et al. (2019a) (G.A.S. Paper I) is based on a pure N-body simulation of dark matter mergers, where the dark matter halos grow from steady accretion. They introduce a semi-analytical model that includes the most realistic representation of the gas cycle to date (Fig. 3.9; Fig. 6 of Cousin et al. (2019a), G.A.S. Paper I.), where the ISM is divided into *a warm diffuse phase, cold, fragmented non-star-forming phase, a very dense star-forming gas phase*, while the gas cycles between them. They also account for SNe and AGNs and track the chemical evolution of the main ISM elements (H, He, C, N, O, and Fe). They associate a SED with every step of the evolution of each stellar population. The treatment of dust is presented in the G.A.S. Paper-II (Cousin et al., 2019b). They include three types of dust, PAHs, very small grains (VSG) and big grains (BG), whose mass fractions are determined at each step of the evolution. Then, to estimate the dust attenuation, they assume an attenuation curve using the `DustEM` model (Compiègne et al., 2011) and include the geometry of the galaxy, different for the different phases of the ISM.

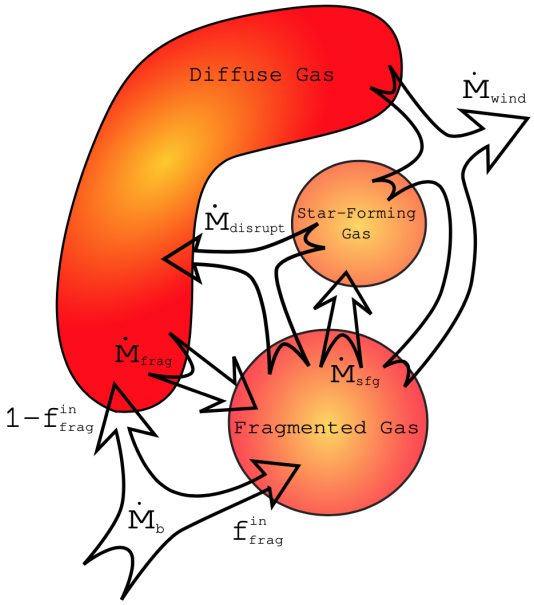

Figure 3.9: The different phases of the ISM included in the G.A.S. models. The arrows between them show the relations between the phases and the processes that are considered in the models. Figure from Cousin et al. (2019a), G.A.S. Paper I.

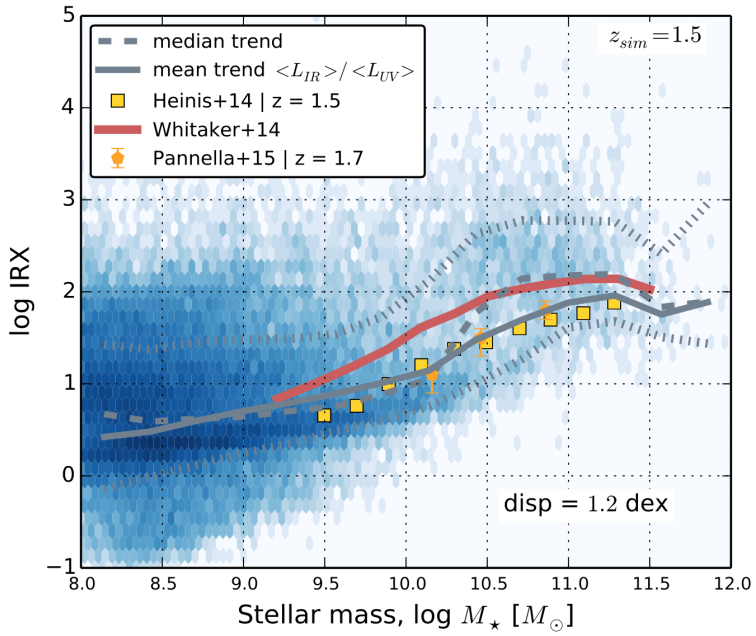

Figure 3.10: The IRX-M_* diagram of the results from the G.A.S. simulations. The blue dots represent the objects, with a dashed line marking their median value. Comparison to the literature is also presented. Figure from Cousin et al. (2019b), G.A.S. Paper II.

After running their models, they compare the IRX with other galaxy properties to ensure that the known relations are reproduced, including the IRX-M$_*$ relation of interest. We can see in Fig. 3.10 (Fig. 9 of Cousin et al. (2019b)) a flattening for lower stellar masses similar to the one we find using our parametrisation, accompanied with a large scatter. We believe such results obtained from theoretical assumptions give evidence that our prediction about the dust attenuation of low-mass galaxies is logical and worthy of further studies. For reference, log IRX = 0.25 corresponds to A_{FUV} = 0.97, according to the relation of Hao et al., 2011. Additionally, they show in their Fig. 11 an evolution of the IRX-Mass relation.

Similarly, a flattening and an increased scatter of the $A_{FUV} - M_*$ relation for galaxies with low stellar masses ($\log M_* < 8$) can equally be seen in simulations, such as the high-resolution cosmological zoom-in simulations FIRE-2 Ma et al. (2019). They compute galaxy SEDs and mock images using a radiative transfer code adopting a Small Magellanic Cloud (SMC)-type distribution of dust grain sizes, which is preferred for galaxies at higher redshift. In Ma et al. (2019), one important parameter is the dust-to-metal ratio ($M_{dust} = f_{dust} M_{metal}$). In their simulations, f_{dust} includes all the processes in the dust cycle (dust production, growth and destruction) and is taken to be constant for a given model. Multiple values are tested (see Fig. 3.11, Fig. 14 of Ma et al., 2019), and it is suggested that f_{dust} could be observationally constrained. They find a larger scatter and possible flattening for low-mass galaxies, regardless of the

value of f_{dust} and independently of the redshift.

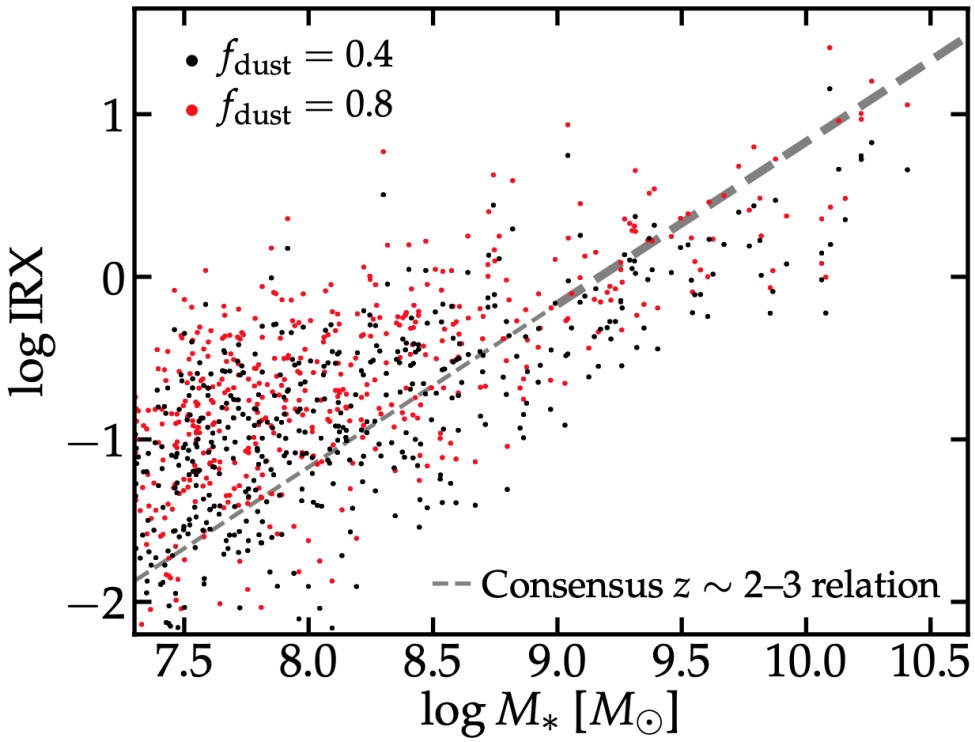

Figure 3.11: The IRX-M_* diagram of the results from the FIRE-2 simulations. The black and red dots represent the objects with a different value of the f_{dust}. Each object is shown twice, once in red and once in black. The dashed line marks the consensus relation from Bouwens et al. (2016). Comparison to the literature is also presented. Figure from Ma et al. (2019).

However, the absorption coefficient α is proportional to two main parameters: the opacity κ_{dust} and f_{dust}, $\alpha \propto \kappa_{dust}\ f_{dust}$. The absorption coefficient is used in the radiative transfer equation and impacts both the dust temperature and emissivity, thus creating a degeneracy between them.

The unexplained behaviour at low stellar mass could be linked to an intrinsic dust attenuation with a surprisingly large amount of dust in these low-mass galaxies. Dust could be building very fast in low-mass objects (e.g. Burgarella et al., 2020) and could quickly reach a minimum (statistical) threshold close to the value found here, qualitatively speaking, because dust builds from metals, in a way similar to the pop.III - pop.II critical metallicity, (e.g., Bromm et al., 2001; Schneider et al., 2002; Jaacks et al., 2018).If so, we could observe a flattening of the relation between dust attenuation and metallicity. It is challenging to confirm this, but such a flattening of the dust attenuation as a function of the metallicity is not excluded by Garn & Best (2010), Xiao et al. (2012), Koyama et al. (2015), and Qin et al. (2019). These results imply that the

present relation does not remain infinitely flat but should present a sharp rise at some low stellar mass.

However, other origins are possible, such as a more clumpy geometry where young stars would be included in dense, dusty shells. We can see from Fig. 3.12 that the relative positions of the dust and stars play a prominent role in building the attenuation curve, which is a significant ingredient in the IRX/dust attenuation recipes. Another source could be the more "bursty" nature of the star formation of these low-mass galaxies (e.g. Gerola et al., 1980; Stinson et al., 2007; McQuinn et al., 2010; Weisz et al., 2011; Gonzalez et al., 2011; El-Badry et al., 2016; Albers et al., 2019; Zick, 2020; Emami et al., 2020).

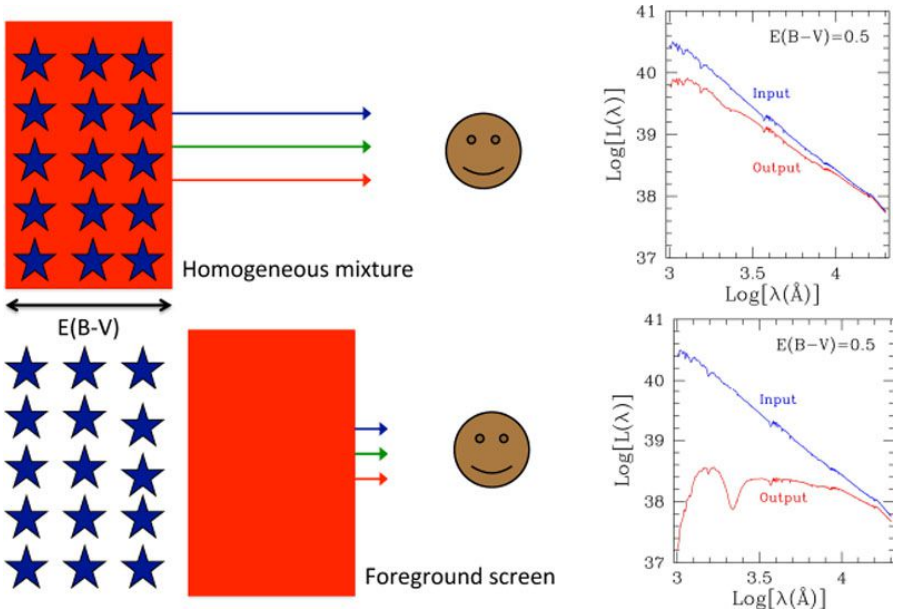

Figure 3.12: A diagram showing the effects of the geometry on the attenuation curve. In the top panel the stars and dust are mixed, so the blue-ish attenuation is lower. On the other hand, the bottom panel shows a "clumpy" geometry, with the dust acting as a screen, and in this case the reddening produced is a lot more significant. Figure from Calzetti et al. (2000).

Finally, a modification of f_{dust} with metallicity could also explain this behaviour at low masses. As suggested by Rémy-Ruyer et al. (2014), this ratio could potentially decrease at low metallicities. More studies are necessary for this assumption, however, as it has been made for galaxies in the local Universe, and we cannot take for granted that the high-z ISM will have the same characteristics as those of the local galaxies.

Apart from theoretical evidence, thanks to telescopes' increasing power, we now see more and more observational proof that the simple low-mass low-A_{FUV} assumption might not be entirely valid.

A scatter suggested in Fig. 2 of Whitaker et al. (2017) and shown in Fig. 3.13 of this thesis, shows that for stellar masses around $\log M_* = 9$, the dust attenuation

can be in the range $0.5 < A_{FUV} < 2.5$. The observed range is in agreement with our results (outliers in the top left corner of the same figure; the value of $f_{\rm obscured} = 0.55$ corresponds to $A_{FUV} = 0.5$ and the value of $f_{\rm obscured} = 0.95$ corresponds to $A_{FUV} = 2.5$, after first converting $f_{\rm obscured}$ to IRX, and then using the Hao et al., 2011 relation to get A_{FUV}).

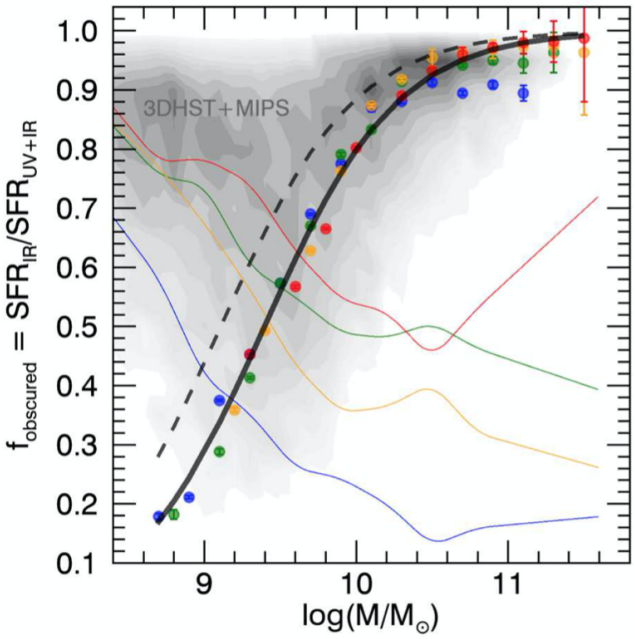

Figure 3.13: A diagram showing the ratio of the IR to the UV SFR as a function of stellar mass, which is analogous to the IRX-M_* diagram. The darker shaded area is, the more objects it represents. The circles are the median stacks from Whitaker et al. (2014), blue: $0.5 < z < 1.0$, green: $1.0 < z < 1.5$, yellow: $1.5 < z < 2.0$, and red $2.0 < z < 2.5$. The thin lines represent the completeness, and the dashed line shows the average relation if Murphy et al. (2011) SFR calibrations are used. Figure from Whitaker et al. (2017).

We can also notice the objects reported in the work of Takeuchi et al. (2010) (Fig. 3.14 here, their Fig. 16), where we see galaxies with stellar masses as low as $7 < \log M_* < 8$ which have A_{FUV} values in the range $0.3 < A_{FUV} < 4.1$. Indeed, to be sure that low mass galaxies have a higher average dust attenuation than is predicted by previous work, we would need more statistics for fainter galaxies. The following steps of this work would include considering the scatter around the average value proposed by our model. Instead of offering one average value for all low-mass galaxies, we could give a range of possible values. This is, however, beyond the scope of this paper and thesis.

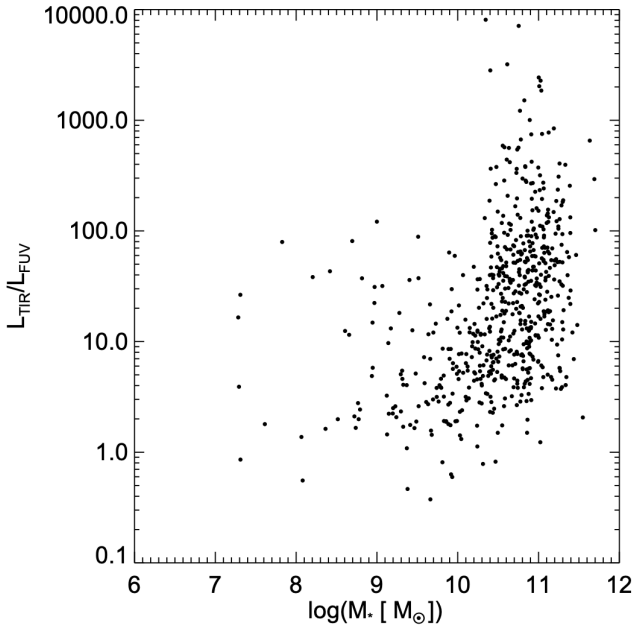

Figure 3.14: The relation between the M_* and dust attenuation proxy L_{TIR}/L_{FUV}. Figure from Takeuchi et al. (2010).

The behaviour of this $A_{FUV} - \log M_*$ law at low mass is puzzling. However, it is necessary to match the low redshift data with that of high-redshift sources such as IZw18 or SBS 0335-052 (Rémy-Ruyer et al., 2015; Hunt et al., 2003; Lebouteiller, 2019; Reines et al., 2008; Cormier et al., 2017; Wu et al., 2007; Cannon et al., 2002). The dust attenuation-stellar mass relationship also needs to match the AFUV (z) shape consistently obtained using a large variety of methods (e.g. Madau & Dickinson, 2014).

3.5.2 The evolution of the $A_{FUV} - M*$ relation with redshift

At high redshift, we also have more and more evidence from objects extracted from deep ALMA maps that the 'consensus' law is not valid anymore. Some authors (e.g. Fudamoto et al., 2017; Fudamoto et al., 2020b) suggest a significant redshift evolution of the IRX – M_{star} relation between $z \sim 3$ and $z \sim 6$ by about 0.24 dex. This hypothesis is supported by the rest of the data at $z > 4-5$ presented in this paper.

In short, the low stellar mass galaxies at low redshift exhibit a large scatter in A_{FUV}, which can be fitted by a constant function. Based on this, we assume that the $A_{FUV} - M_*$ relation is constant in this mass range for all redshifts. We leave the option of the constant value to vary between redshifts by fitting the parameter a in Eq. (3.3). Considering that we do not have low-mass galaxy data for higher redshifts, we attempt to counterbalance this by assuming that the evolution of the average A_{FUV} follows the function proposed by Burgarella et al. (2013). We then try to find such a parametrisation for $A_{FUV} - M_*$ that would give similar values for the $A_{FUV} - z$

relationship of Burgarella et al. (2013), when weighted by the MF and integrated to compute the mean A_{FUV}. So, fitting the literature data assures we have a function that reproduces the data well in the higher mass range. Then, by comparing to Burgarella et al. (2013) we try to atone for the lack of data in the low mass range and predict expected values for the A_{FUV} of such objects.

We are interested in gaining as much knowledge about the early Universe as possible, and understanding the dust attenuation far back in cosmic time is no exception. As shown in Table 3.1, we have included some galaxies with high redshift, a small number of objects until redshift $z < 8$. So, until more observations are carried out, and more advanced telescopes are used, we can only make predictions about how the dust attenuation behaves farther into the history of the Universe, at redshift $z \sim 10$. We give Eq. (3.4) as a recipe for predicting the dust attenuation of galaxies given their redshift and stellar mass. Furthermore, we can use this equation to estimate the dust attenuation where no data is available, and to make predictions and simulations further to push the limits of the knowledge of this field.

3.5.3 Potential future uses

When we first envisioned this project, we had a plan to use our findings to produce simulated catalogues of galaxies extending to higher redshifts than those of our data sample by extrapolating the relation in Eqs. (3.1) and (3.2). This type of catalogues could predict what will be observed with upcoming facilities, such as, e.g. JWST or MOONS, which would make it possible to develop the data analysis pipelines to be ready when the first data arrive. We already did some preliminary work on this topic, which I will briefly describe in this section. However, I decided to take a different path and focus my last year of the PhD on learning about dust evolution models (Chap. 5).

The vision we had for the project was the following. The first step is to get the correct number of galaxies, so we needed to interpolate and extrapolate existing data on MF, similar to what we did for the paper itself except for the extrapolated part. Thus, we collected data from multiple authors (Mortlock et al., 2015; Tomczak et al., 2014; Grazian et al., 2015; Song et al., 2016; Wright et al., 2018), and we fitted the Schechter parameters with the functions shown in Chap. 2 (Sect. 2.3.1). Next, we include the observatory characteristic, such as the field of view and limiting magnitude. We then have an elementary number of galaxies to use in our investigations (Fig. 3.15).

Then, the idea is to use CIGALE to create a grid of models that will later be used to simulate the final SEDs. In this part, we included different ranges of parameters, hoping to cover as best as possible the parameter space that we are working with, mainly to get as many different values for the Mstar, SFR, IRX, etc.

For the final sample, we need to select the models that give us the type and number of galaxies we require for our work. For this purpose, we use the MS of galaxies, as defined by Speagle et al. (2014), for each redshift that we compute the MF. Our models only refer to star-forming galaxies, so this was the first thing we needed to include in our mock sample. The following condition our galaxies need to fulfil is the

$A_{FUV} - M_*$ relation that we propose (Eqs. (3.1) and (3.2)), shown in Fig. 3.16. The full line represents the exact model, while the dashed lines give an arbitrary scatter. We did not get farther into the project to provide a better precision of this scatter.

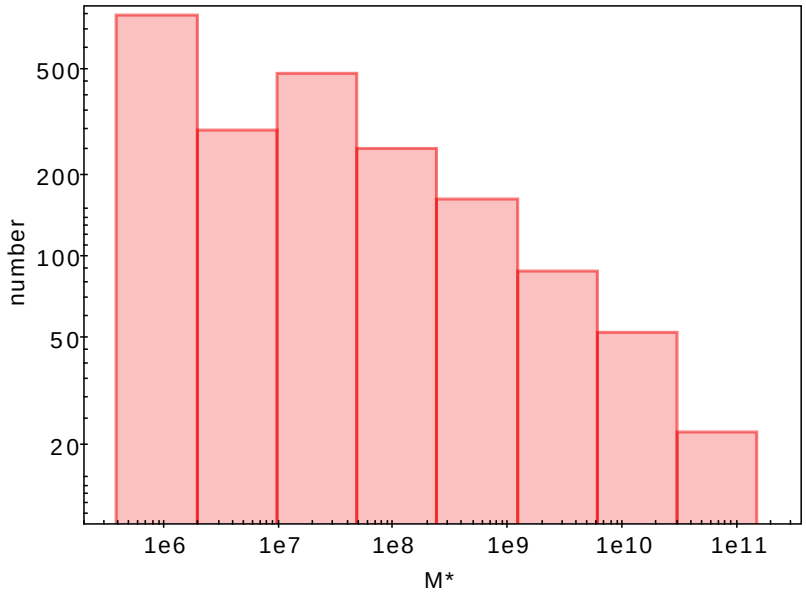

Figure 3.15: The MF retrieved after the cuts explained in the text have been performed.

Finally, we combine the models of CIGALE with the MF. With a random draw, we take the number of models in our pre-selected sample that the MF dictates. When the models are selected, we use the CIGALE `results.txt` file, which also contains the input parameters used to calculate the model chosen. The next step is to once more run CIGALE on the models that we selected, this time including a filter (or filters) of our choosing. The choice is based on the project requirements, e.g. a filter planned for the telescope that we are simulating. We never reached this step in our project, so we do not have any results to show. However, if we did produce such a catalogue, the next step would be to check if it is consistent with the global properties. We would treat it as a data sample, use CIGALE to fit the SED that we have, and then study the results actual data.

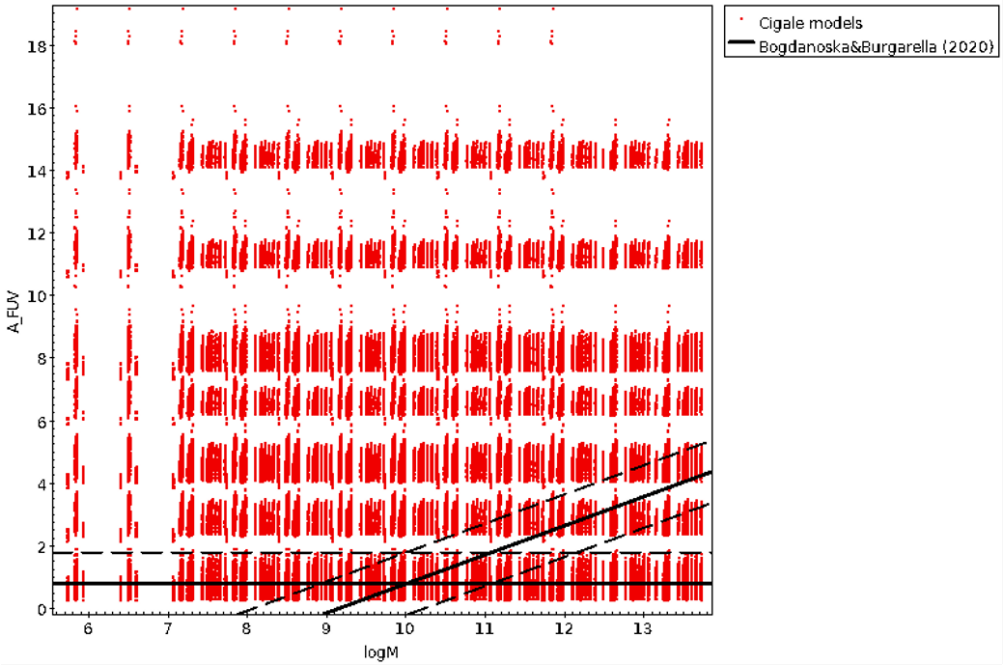

Figure 3.16: Using Eqs. (3.1) and (3.2) to cut the models that conform to our prior. The dashed lines represent a scatter arbitrarily chosen to be $\Delta A_{FUV} = 1$ mag.

We need to perform the main tests to check if we retrieve the constraints we put in the models, i.e. the MF, MS, and $A_{FUV} - M_*$ dependence. If all of this checks out, we can estimate the mass density, luminosity function, cosmic star formation density etc.

Once such a catalogue is created, we can take it one step forward and create simulated images. Here again, the instrument's characteristics come into play, such as the Point Spread Function (PSF), detection limit, etc. Also, we need to account for the morphologies of the galaxies, more precisely their sizes, shapes, inclinations and light profiles. Finally, we should consider the gravitational effects in the high redshift Universe, where clustering and Large Scale Structure (LSS) are relevant. Once all of these things are included, we can add noise appropriate for the given instrument.

As this project was never completed, there is a possibility we will once again take it up in the future. However, I would like to point out that such catalogues exist; an excellent example is the work of Williams et al. (2018). They created the JAGUAR: JWST Extragalactic mock catalogue[1], which includes similar methods as I have described in this section. The main difference between what they have done is that we wish to use CIGALE for our models instead of BEAGLE[2] (Chevallard & Charlot, 2016), giving us the advantage to include more flexibility of the SFH and the dust emission/attenuation treatment. A very significant advantage of CIGALE is that it extends from the X-rays to the radio.

[1] https://fenrir.as.arizona.edu/jaguar/
[2] http://www.jacopochevallard.org/beagle/

3.5.4 Limits of this work

One main limitation of our work is that the data we collected is not fully complete. We include IR and UV/optical data, so there is immediately a difference in their qualities, as UV-dominated galaxies have better detection limits.

We attempted to include as high of a redshift range as possible. However, when going to higher redshifts ($z > 3$), the low-mass galaxies are getting harder to detect and fall below our observational limit. Dusty objects will still appear as they would be brighter in the IR, so our results might be biased towards them. On the other hand, for the local Universe, it is harder to detect rarer objects (i.e. the more massive galaxies), so this introduces an additional bias. This difference is not only limited between different redshifts - massive galaxies, in general, are harder to study because of their scarceness, and low-mass galaxies also pose a difficulty as they are far fainter, even though they are greater in number. Their large numbers are the primary source of our uncertainty, as we are interested in the global properties concerning all galaxies.

In conclusion, we understand that this work is probably not the final word about the redshift evolution of the IRX-M_* relation. But we need to move beyond the simple linear and constant view about this relationship that was consensual. The results at low and high redshifts suggest that this is not a complete view of the phenomena acting in galaxies. The simple fact that this IRX-M_* needs to produce results consistent with the redshift evolution of the average galaxy attenuation presented in the literature (Cucciati et al., 2012; Burgarella et al., 2013; Madau & Dickinson, 2014, etc.) means that we have to understand it better. One place to start is to use an approach checking that the assumptions agree with the dust evolution at cosmological scales.

A recent work of Riccio et al. (2021, in prep) has shown some of the limitations of our work. They are interested in MS galaxies that will be observed during the *Legacy Survey of Space and Time* (LSST) and are in the process of improving the procedures for treating the data. For that purpose, they use the *Herschel Extragalactic Legacy Project* (HELP) sample (Małek et al., 2018; Shirley et al., 2019; Shirley et al., 2021), and use CIGALE for the SED fitting, as well as to create simulated fluxes.

They start by estimating the parameters from the HELP sample using CIGALE to select only the type of galaxies that will be observed in LSST. They also use galaxies only to redshift $z < 2.5$ to keep only the highest quality data in their selected fields. They also remove any non-MS galaxies and objects that are classified as stars by GAIA. Then, from the CIGALE fitted SED, they obtain fluxes in the LSST bands (*ugrizy*) to compare the results of SED fitting done with only LSST data and the full UV-to-FIR SED.

What they find is that the stellar mass is very well estimated by LSST data alone. However, the SFR is highly overestimated, from which they conclude that CIGALE overestimates the dust attenuation. So, they attempt to introduce a prior in CIGALE - the relation for A_{FUV} that we propose (Bogdanoska & Burgarella, 2020). Unfortunately, our relation resulted in underestimating the SFR. The sample selection can explain this difference; they work with IR-bright galaxies to better fit the SED. They do, however,

end up using a similar approach to ours and find a relationship that fits their sample specifically that could indeed be used as a prior in CIGALE. I believe this finding is very relevant to our work, as it shows that this relation is not universal and that the $A_{FUV} - M_*$ question is a lot more complicated than it first seemed.

3.6 Main points of the BB2020 paper

This chapter is slightly extended and contains some information that we could not include in the paper. The number of pages for a scientific paper is limited and must ideally provide all the relevant information to the readers but not more. In our paper (Bogdanoska & Burgarella, 2020), we estimate the evolution with redshift of the dust attenuation in the FUV by first exploring the evolution of the relationship between the dust attenuation and the stellar mass throughout cosmic times. We strongly suggest assuming that the $A_{FUV} - M_*$ relationship shows an evolution with redshift.

We can summarise the main points of the paper with the following conclusions:

1. The $A_{FUV} - M_*$ relationship needs to be described with a more complicated function as opposed to the consensus linear (in terms of $\log M_*$) relationship, such as the one proposed in Eq. (3.1). Such a function needs to be able to incorporate the influence of the low mass galaxies on the global average of the dust attenuation.

2. Assuming the $A_{FUV} - M_*$ relationship does not evolve with redshift is not consistent with other studies concerning the cosmic evolution of the dust attenuation. On the other hand, starting from the assumption that this relation is not the same at all cosmic times gives results similar to those found by groups studying the same phenomenon using different methods.

3. The $A_{FUV} - M_*$ relationship for lower stellar masses has a large scatter, with an average value that is likely to be larger than zero throughout most cosmic times. The physical origin of this offset cannot be derived from the present data. However, some works mentioned in Sect. 3.5 suggest that this flattening can have different sources that we need to explore: simply a significant dust content in these low-mass galaxies, which is the most straightforward conclusion but poses the question on how a large dust mass can build up in these low stellar mass objects, the stars-dust geometry, the dust-to-metal ratio, etc.

4 Early evolution of the first dust grains

The beginnings of this project were born during the summer of 2020. It all started with a meeting between me, my supervisor, and our very close coworker Dr Ambra Nanni. We were on the verge of completing our first-authored papers (all relevant to my thesis and described in Chapters 3, 4 and 5)We planned our future work in a direction similar to theirs, as I wanted to expand my knowledge to a new, but related, topic. Life, unfortunately, is not very predictable, so during the last year of my PhD, I managed to accomplish very few of the goals I had set for myself during that meeting. Unpredictable, however, can sometimes also be a good thing, so I now know I will have the opportunity to continue my collaboration with Dr Burgarella and Dr Nanni due to my position at the Ss. Cyril and Methodius University in Skopje, Macedonia.

Following the internal meeting with Dr Burgarella and Dr Nanni was a video conference with our colleagues Dr Seiji Fujimoto, Dr Kotaro Kohno and Dr Masami Ouchi on 5 June 2020. We discussed the possibility of future collaborations. More specifically, they offered us suggestions about data sets we might be able to use, and we presented our projects and how we plan to use that data. As the project is not advancing as quickly as we had initially planned, we have not yet begun working with any of these data sets, but discussions and plans are still being carried on. I would like to take this opportunity to comment that this was a very fruitful meeting, especially since it led me to consider continuing this project into a postdoc with Dr Ouchi (some indications of the planned project are presented in Chapter 6).

During the last year of my PhD, after we decided to use the ALPINE data, I was in charge of preparing the data so that it is compatible with CIGALE, and carrying out some preliminary tests on CIGALE to get a feel for the data and the possible results. As my time as a PhD student was coming to an end, I needed to devote time to the write-up of the thesis manuscript, and at the same time, start teaching at my home university in Skopje. So we decided, in the interest of time (meaning so that we would not need to postpone the advancement of this project until after my thesis defence), to promote Dr Burgarella to the principal investigator of this paper. The results that I will show later on in Sect. 4.4 are still preliminary results, while the final results will be published as Burgarella et al. (2021, A& A, in prep.).

Thus, the natural outline of this chapter is the following. Firstly, since the paper of Burgarella et al. (2020) is a crucial predecessor of this project, a detailed summary follows (Sect. 4.1). Secondly, I discuss the data we are using, namely the ALPINE survey in Sect. 4.2. Many of the methods we use in this project are very similar to those

described in Burgarella et al. (2020). However, a more detailed summary is presented in Sect. 4.3. The preliminary results, the current state of the project and plans for the future are discussed in Sect. 4.4.

4.1 Background: summary of the work of Burgarella et al. (2020)

Studying the evolution of galaxies, especially during their early stages shortly after their formation, is a prevalent topic in the scientific community. Part of this broad topic is the study of the early dust that has a crucial role in the overall cycle of the galaxy (Sect. 2.4.2). Burgarella et al. (2020) work on a sample of LBGs with spectroscopic redshifts in the range $5 < z < 10$. For these objects, mm observations have been attempted, principally with the ALMA Bands 6 and 7. As the physical parameters need to be determined from the SED, only data with a minimum of 5 UV/optical rest-frame observations have been included. The main physical parameters they are interested in include the stellar mass M_*, dust mass M_{dust}, SFR, FUV and dust luminosities L_{FUV} and L_{dust}, age of the main stellar population age_{main} and the UV-slope β.

The data has been collected from several references (Bouwens et al., 2016; Capak et al., 2015; Faisst et al., 2017; Scoville et al., 2016; Willott et al., 2015; Aravena et al., 2016; Hashimoto et al., 2018). They also include a local low metallicity sample to calibrate the dust models (referred to as the Low-zZ sample in the paper), the data can be found in the work of Rémy-Ruyer et al. (2015), and more detailed work with this sample is carried out in the paper of Nanni et al. (2020). This sample comes from the Hershel Dwarf Galaxy Survey (DGS), and it includes data of 48 local dwarf galaxies in the IR range between 55-500 μm, which Burgarella et al. (2020) have expanded using available NASA Extragalactic Database (NED) data in the FUV, NUV, B and R bands.

The central assumption is that these local low-metallicity dwarf galaxies, with $12 + \log(O/H) \leq 8.4$, might have a similar shape of the IR SED to the high redshift galaxies included in this study, and by using them to calibrate the dust models, they make it possible to make up for the lack of IR data for the LBGs. The hypothesis is tested in the paper.

4.1.1 Deriving the physical parameters

The work published in this paper begins with an SED analysis of all of the available objects using the code CIGALE (Boquien et al., 2019; Noll et al., 2009; Burgarella et al., 2005). The authors use a Bruzual & Charlot (2003) SSP model and test different SFH, such as the delayed, delayed+burst and constant SHF. The delayed SFH is kept in the end, but they state that also the delayed+burst and constant SFHs give close results. They choose a Chabrier (2003) IMF, even though a top-heavy IMF is preferred for this type of galaxies (Nanni et al., 2020), but it is not yet included as an option in CIGALE. For the dust attenuation law, they use a `dustatt_modified_starburst` law

(Sect. 2.2.3, Fig. 2.7), and the `dale2014` and the `dl2006` `CIGALE` modules for the dust emission (Sect. 2.2.4). They model the nebular emission with the `nebular` module of CIGALE and assume no AGN emission presence (Sect. 2.2.5).

The SED fitting is carried out in several stages, a method we also use in our current project that will be discussed in more detail later on in Sect. 4.3. In short, an initial phase during which Burgarella et al. (2020) test the general limits of the fitting and obtain some broad intervals for the values of the physical parameters, such as the SFH and dust attenuation. After this initial phase, they perform again SED fitting with CIGALE, this time with many priors, and they get some of the results that they eventually include in their paper. The main parameter that they look for in this phase is the 200μm flux, as it is believed that the dust is optically thin at this wavelength (e.g. Casey, 2012), and they use this flux to normalise the ALMA flux of each of the detected LBGs. They combine these normalised fluxes, and they build an IR SED of the LBG sample (Fig 4.1, Fig. 1 of Burgarella et al., 2020) by taking advantage of the redshift range of their data set

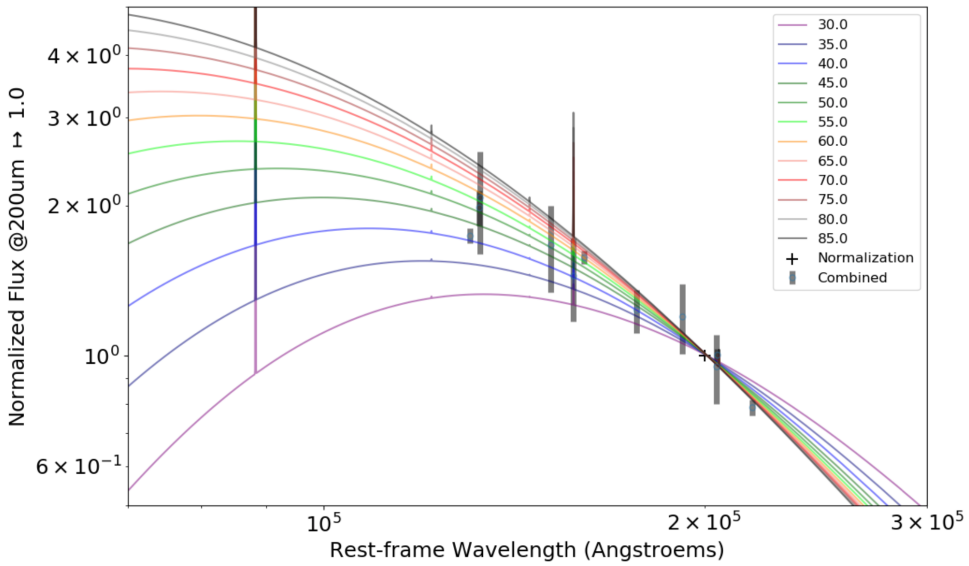

Figure 4.1: A template IR SED built from combining the restframe fluxes, normalised at $\lambda_{restframe} = 200\mu$m, of the combined Hi-z sample used by Burgarella et al. (2020) in the redshift range $5 < z < 10$. The coloured curves represent a modified blackbody model for different dust temperatures in the range $30 \leq T_{dust} \leq 85$. Figure from Burgarella et al. (2020).

The next step is based on the assumption that the Hi-z LBGs and the Low-zZ galaxies share similar physical conditions that produce a similar IR SED. A similar SED fitting is performed on the Low-zZ sample, using the same priors as the first fitting of the LBGs, aiming to confirm that the physical parameters concerning the dust are in agreement. From this step, the q_{PAH} and γ parameters are determined, with q_{PAH}

being the fraction of PAHs present in the dust mass, for which they use the minimum value due to its correlation to metallicity (Ciesla et al., 2014), and γ being the fraction of the dust heated by starlight, the value of which Burgarella et al. (2020) cannot constrain from the LBGs. Still, they assume that the best value for the Low-zZ sample is also applicable in the case of the LBGs. Thus, once these parameters have been set, another fitting primarily of the IR SED is carried out, where the LGBs are grouped to give only one IR SED (called IR template) from which the parameters of the whole sample are estimated. The last step is to take all that was learned in the previous phases and fit the UV-to-IR SED of all galaxies individually, mainly the Hi-z LBGs and the Low-zZ, as a secondary check of the IR SED template.

4.1.2 Main results and conclusions

One of the most important results of the Burgarella et al. (2020) paper is what they define a dust formation rate diagram (DFRD), where they represent the specific dust mass (sMdust = Mdust/Mstar) as a function of the specific SFR (sSFR = SFR/Mstar). They also add a colour-coded dependence of the age and the IRX, and from this, it can be seen (Fig. 4.6) that younger objects have higher sSFR, demonstrating an evolutionary sequence from right to left. The right part of the DFRD represents the formation of the first dust grains, and as we move towards the left, we can see the results of their destruction. The decline is seen in both the Hi-z and the Low-zZ samples,but it is more prominent in the Hi-z LBGs (Fig. 4.2, Fig. 5 of Burgarella et al., 2020).

In the Low-zZ sample, a flattening of sMdust with age is observed, giving some evidence that they might not be perfect analogues of the Hi-z counterparts due to the possible presence of Low-zZ that might not have as low metallicity as expected. The authors compare the metallicities of the Low-zZ sample with an estimate of the metallicities from the IRX of the Hi-z sample and find an offset of about $12 + log10(O/H) = 0.5$ between the samples, with the Low-zZ having the slightly greater average metallicity. Due to the dependence of dust formation on metallicity, this could be an indication that higher metallicity could give rise to more dust growth in the ISM (Asano et al., 2013), which in turn contributes to the overall dust formation, it is logical that this increase of sMdust is seen in the Low-zZ sample, and not for the LBGs.

The last part of Burgarella et al. (2020) is very similar to the work of Nanni et al. (2020), which will be discussed in greater detail in Chapter 5 of this thesis. In short, they add the chemical evolution models of the work of Nanni et al. (2020) to their DFRD diagram, comparing the data available to the best model. They show models obtained with a delayed SFH (and the CIGALE results obtained with the same SFH) and do not include any grain growth in the ISM. They find that models with a more significant condensation fraction give a better fit and a sharp drop of the dust mass at higher ages. The latter requires very rapid destruction and outflow of dust grains but helps explain the differences in detectability of galaxies of this type. However, they have is to reach the high dust mass points at the early stages of the evolution,

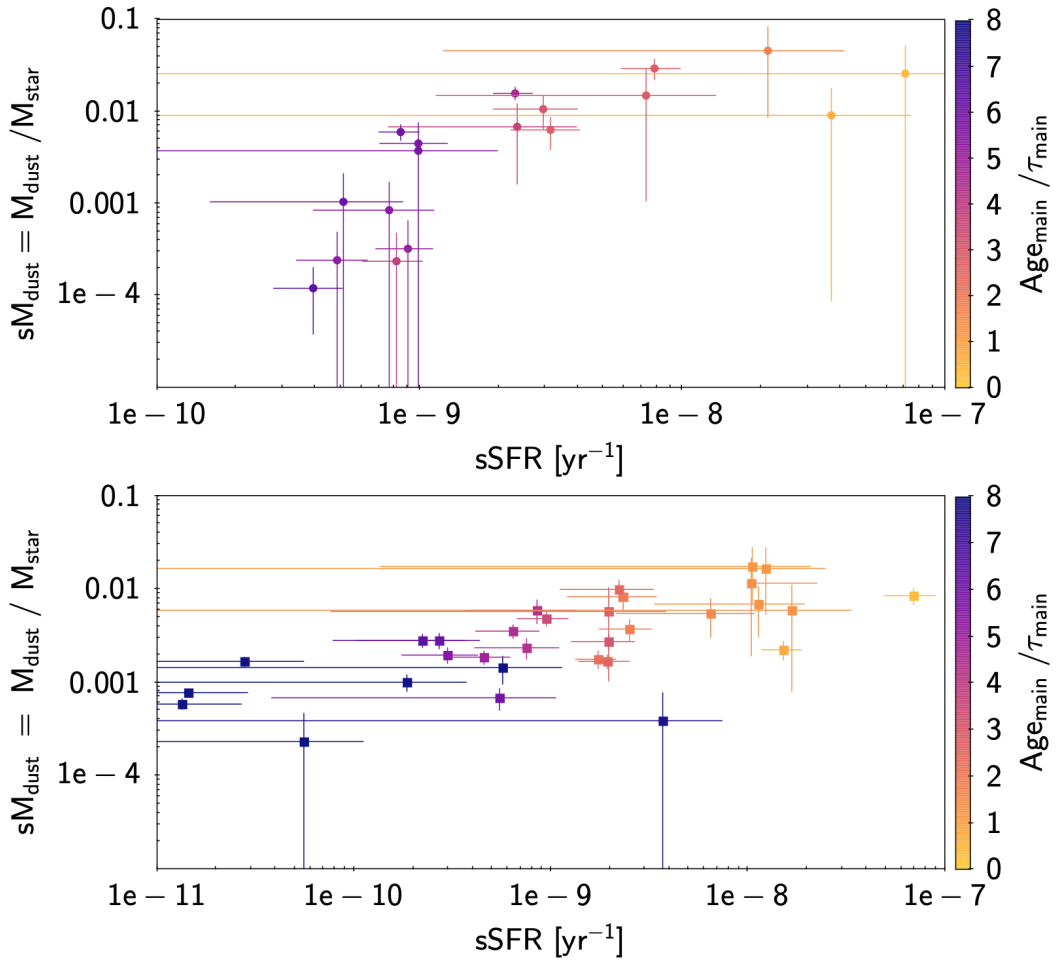

Figure 4.2: The DFRD of both the Hi-z galaxies (upper panel) and the Low-zZ sample (lower panel). The colour coding represents the age of the main stellar population, which shows that the DFRD gives a picture of the temporal evolution of galaxies as seen from right to left. Figure from Burgarella et al. (2020).

which indicates that the current picture we have about dust creation mechanisms is incomplete.

4.2 The ALPINE-ALMA [CII] Survey

We are interested in studying the formation and evolution of dust grains, starting from the first dust grains up to more recent cosmic times. It is an important part of our study to determine the data we believe will bring us closer to our goals. We use SED fitting as the primary tool for determining the dust quantities, so we are interested in samples where multi-wavelength data are available. Ideally, we wish to expand our study to that of the chemical evolution models (which will be discussed in Chap. 5). So, the data that we use need to include information about the metallicity of the galaxies in the sample. Determining the metallicity is challenging when considering high-redshift sources, as it requires at least some spectroscopy to determine the metallicity. Consequently, the method of Burgarella et al. (2020) is quite handy (but still provides a proxy to be further tested) - combining our sample with that of Burgarella et al. (2020) to build a template of the IR, which we can use to fit the SED of our sample, extending to a more extensive redshift range. For that purpose, we have been using the ALPINE sample.

The objective of the ALMA-ALPINE [CII] survey, which I will refer to as ALPINE throughout this thesis, is to push the limits of the current knowledge about the properties of normal star-forming galaxies. It is a sample of 118 galaxies with redshifts in the range of $4 < z < 6$ that have all been observed in the [CII]-158μm line, and in their FIR continuum emission. This redshift range is of interest because it is at the end of the reionisation epoch and hides many pieces of the puzzle that is galaxy evolution. The science goals of this survey include: estimating the SFR from [CII] emission, calculating the star formation rate density (SFRD) at this cosmic time, including the contribution of dust-obscured star formation, improve the characterisations of the ISM that are currently known, measure the dynamical masses alongside the stellar masses and estimates of dark matter halo masses, measure the dust content and gas fraction and their evolution, quantifying outflows and feedback, and, of course, to leave a legacy catalogue that will be used for many other studies in the future that are not yet included in their initial scientific goals.

The PI of the project is Dr Olivier Le Fèvre, whom I had the honour to meet as a professor on one of my master courses. The references to the ALPINE survey are the work of Le Fèvre et al. (2020) for the survey design, Bethermin et al. (2020), where the ALMA data is described, and the work of Faisst et al. (2020) that presents the ancillary catalogue, where the information in this section comes from, including the ALMA ALPINE [CII] Survey website[1], where the DR1 catalogues can be found.

The ALPINE team started their observations in May 2018 and finished them in February 2019 with a total of 69 observational hours, with each target having been

[1] https://cesam.lam.fr/a2c2s/

observed for 30 minutes up to 1 hour. Using the Band 7 of the Atacama Large Millimetre/submillimetre Array (ALMA) observatory, they successfully observed a sample of galaxies that comes from two well-studied fields. ALPINE includes 105 galaxies are situated in the Cosmic Evolution Survey field (COSMOS) (Scoville et al., 2007), and the remaining 13 belong to the Extended Chandra Deep Field South (ECDFS) (Giacconi et al., 2002). Of these galaxies, 64% have been detected in [CII] with 3.5σ above the noise, and 21% were detected in the continuum.

The included galaxies have been selected to have an absolute UV magnitude brighter than $M_{1500} = -20.2$ and to have had their redshift spectroscopically confirmed from lines in Lyα emission or UV absorption. The sample can also be separated in two redshift ranges of $4.40 < z < 4.65$ (median value $\langle z \rangle = 4.5$, containing 67 galaxies) and $5.05 < z < 5.90$ (median value $\langle z \rangle = 5.5$, containing 51 galaxies), naturally separated by a gap in the transmission of the atmosphere. The ALPINE sample consists of SFG, defined as belonging to the main sequence of the SFR-M_* diagram of their redshift (e.g. Speagle et al., 2014).

As the galaxies included in the ALPINE sample belong to well-studied fields, they come with a rich ancillary data set compiled and presented by Faisst et al. (2020). Due to the nature of the selection of these galaxies, they all have spectroscopic observations in rest-frame UV, performed with the Keck telescope and the European Very Large Telescope (VLT). A plethora of photometric observations is also available, from ground-based observatories in the UV to optical, from HST in the UV, and Spitzer above the Balmer break (all rest-frame features).

The spectroscopic data in the rest-frame UV of the COSMOS galaxies comes from the DEIMOS survey (Capak et al., 2004; Mallery et al., 2012; Hasinger et al., 2018) performed with the Keck telescope in Hawaii. The galaxies have been selected based on the drop-out technique, narrow-band surveys or purely photometric redshifts, but a few also from the 4.5μm excess and X-ray emission. The rest of the spectroscopic data have been observed with the VLT in Chile as part of the VIMOS Ultra Deep Survey (Le Fèvre et al., 2015; Tasca et al., 2017, VUDS), and the primary selection criterion was the photometric redshift, accompanied by the Lyman-break drop-out technique (details on these techniques in Chap. 2, Sect. 2.2.8). Similarly, most of the galaxies in the ECDFS field have been observed with the VLT, using VIMOS and FORS2 spectrographs (Vanzella et al., 2007; Vanzella et al., 2008; Balestra et al., 2010), and only 2 have been observed with the HST, as part of the survey GRAPES (Malhotra et al., 2005; Rhoads et al., 2009), and the galaxies have been colour-selected for the most part. For a summary of the ancillary spectroscopic data, refer to Table 1 in the paper of Faisst et al. (2020).

The photometric data used in the ALPINE ancillary data catalogue is based on the catalogues COSMOS2015 (Laigle et al., 2016) and the 3D-HST (Brammer et al., 2012; Skelton et al., 2014, for the ECDFS field). The COSMOS2015 catalogue provides observations in the u_3-band (MegaCam on CFHT), the B, V, r+, i+, z++, 12 intermediate-band and two narrow-band filters (Suprime-Cam on Subaru), the YHSC-band (Hyper Suprime-Cam on Subaru), the near-IR bands Hw and Ksw (WIRCam on CFHT) and Y,

J, H, and Ks (VIRCAM on the VISTA telescope). These observations of the COSMOS field have been supplemented by Spitzer observations from the SPLASH survey (Capak et al., 2012; Steinhardt et al., 2014; Laigle et al., 2016), containing flux from the four channels at 3.6 μm, 4.5 μm, 5.8 μm, and 8.0 μm. Observations of the ECDFS field include the U38, b, v, Rc, and I broad-band filters (Wide Field Imager on the MPG/ESO telescope), the U and R bands (VIMOS on the VLT), the Jv, Hv, and Ksv filters (ISAAC on the VLT), Jw and Ksw bands (WIRCam on the CFHT), and 14 intermediate-band filters from the Suprime-Cam on the Subaru telescope. Spitzer observations in the four channels are also available for the ECDFS field, and HST photometry in the F435W, F606W, F775W, F 814W , and F850LP bands (ACS) and the F125W and F160W bands (WFC3) from the 3D-HST catalogue. The photometry has been beautifully summarised in Tables 2 and 3 in the paper of Faisst et al. (2020). A summary of the available data for the ALPINE sample galaxies is shown in Fig. 4.3 (Fig. 1 of Faisst et al., 2017).

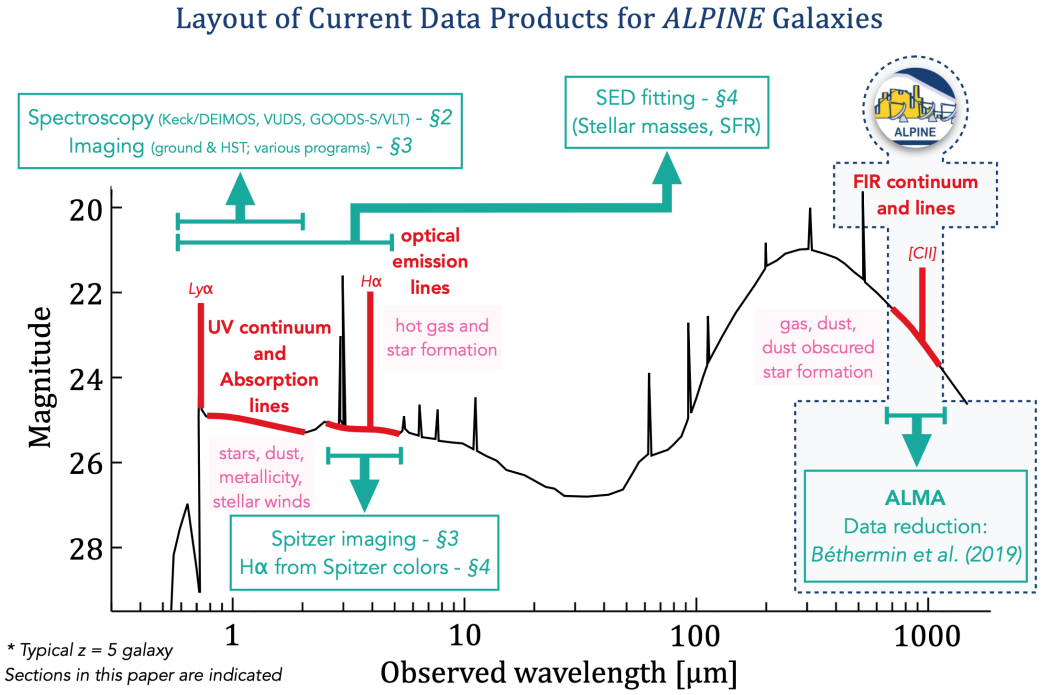

Figure 4.3: An SED of a typical galaxy at $z = 5$ (adapted from Harikane et al., 2018). The marked sections show the multi-wavelength data available for the ALPINE sample, including the spectral features highlighted in red and the [CII] covered by the ALPINE survey. The numbering of the sections refers to the sections of the paper of Faisst et al. (2020). Figure from Faisst et al. (2020).

The ALPINE catalogue was made public just in time for our project (DR1, 5 June 2020), so we decided to take advantage of this. The ALPINE team has already determined the main galaxy properties by performing SED fitting, but since our project

is a continuation from the work of Burgarella et al. (2020), we need to be consistent in the use of SED models, so we started directly from the flux data contained in the ancillary catalogue, and described in the work of Faisst et al. (2020). By using CIGALE, we estimate the physical parameters of the sample in a manner that is as close to Burgarella et al. (2020) as the data allow it.

We needed to do a few modifications to the data - first, we had to combine the ancillary catalogue with the ALMA data and change to the units used in CIGALE. We also only include the measurements in bands other than ALMA having signal-to-noise ratio SNR > 2.5 and more than 5 photometric data points. The main change that we did was to convert the [CII]158μm line flux measured by the ALPINE team to SFR, which can be used as a constraining property in CIGALE. The conversion relation we used is the one of Schaerer et al. (2020):

$$\log(L([\mathrm{CII}])/L_{\odot}) = 7.09 \pm 0.21 + 0.84 \pm 0.13 \times \log\left(\mathrm{SFR}/M_{\odot}yr^{-1}\right) \tag{4.1}$$

4.3 Methodology

I devoted an entire section Burgarella et al. (2020) because it is the basis of the work that will be published as our following paper. It is understandable then that the contents of this section will be similar to some of the things described in Sect. 4.1. As was explained in the previous section (Sect. 4.2), we are working with the ALPINE-ALMA [CII] survey, and we do not use directly a Low-zZ sample to which we can compare our IR SED, except by using some of the priors proposed by Burgarella et al. (2020).

Phase 0: Preliminary "full-SED" fitting Similarly to Burgarella et al. (2020), our project starts with performing SED fitting on our data using CIGALE, also in a few phases, starting with fitting the SED of each galaxy, using the entire ancillary catalogue of ALPINE (Faisst et al., 2020). This way, we can begin to constrain the physical parameters derived from the UV SED, such as the SFH, so that when we later focus on the IR SED alone. We also minimise the number of input parameters in CIGALE used in the preliminary testing stage, and with that, the number of models we run (to save on computational time). Our first starting point is very similar to Table 2 of Burgarella et al. (2020). We use the Bruzual & Charlot (2003) SSP, with Chabrier (2003) IMF, the closest one to the top-heavy IMF suggested by Nanni et al. (2020) that is currently available in CIGALE, and we select a metallicity of $Z = 0.004$. We use a delayed SFH, without a contribution from a burst, the `nebular` module with its default CIGALE values of ionisation parameter $\log U = -1.5$ and line width of 100 km/s. For the dust attenuation law, we use the `dustatt_modified_starburst` module, while we use the `dl2014` module for the dust emission. These are only the modules from the preliminary testing stage; the entirety of the modules proposed and compared can

be seen in Sect. 4.4.

During the preliminary fitting of the entire SED, as we are focused more on the UV part, we keep the number of dust emission parameters in our models to a minimum, so we use the values of Burgarella et al. (2020) as a first approximation. Specifically, we take $q_{PAH} = 0.47$, $U_{min} = 4.0$, $\alpha = 2.2$ and $\gamma = 0.75$ (For the explanation of these parameters refer to Chap. 2, Sect. 2.2.4, or Draine et al. (2014) and references therein).

Phase 1: Building the IR SED template Once we have a general idea of some of the UV SED parameters, we move on to the most relevant and most challenging phase to fit (due to lack of data) part of the SED - the IR range. This time we limit the parameters that govern the UV part of the SED (to save on CIGALE running time), and we try to determine the parameters of the dust emission module independently of the other modules. During this stage, we check whether the values of Burgarella et al. (2020) are suitable for our sample. This stage is where we find some constraints on the IR SED to improving the dust emission template for EoR galaxies.

After obtaining the best fitting models for the SEDs of the galaxies in our sample (both the sample of Burgarella et al. (2020) and ALPINE), we can combine all galaxies to sample the IR SED template better. Thus, instead of having N galaxies with one flux in the ALMA band 7, we will have N fluxes of "one galaxy" in each of the band 7 ALMA fluxes' rest-frame equivalents, the dispersion depending on our redshift range. We call this method *using the Universe as a spectrograph*.

The sample used in Burgarella et al. (2020) has an advantage over ours regarding the redshift range; they include galaxies in the range $6 < z < 10$. However, we make up for it with the higher number of objects, and with the fact that our sample lies between $4.5 < z < 5.5$, which is an extension of the Burgarella et al. (2020) sample. So, we can both expand and verify their results, and we have added their objects to our sample.

To obtain the IR template, we must first have a model SED to work with, as part of the process requires normalising the ALMA fluxes to be comparable to each other. As for the normalisation, we will use the 200μm flux, same as Burgarella et al. (2020), because dust is thought to be transparent at this wavelength. Thus, when we model the SED, we need to include a filter that will give us the SED value at the rest-frame $\lambda = 200\mu$m. We then use this value to normalise the entire model SED, and the observed ALMA fluxes of interest. Before building the IR SED template, the final step is to bring the observed fluxes to their proper rest-frame wavelength.

Then, finally, we have a better sampling of the IR wavelength range. We include all of the detections and non-detections of the ALPINE sample. We use the available flux-restframe wavelength data to fit the IR SED using CIGALE. The template IR SED is given in Fig. 4.4.

We have tested multiple dust emission models to fit the IR template, namely the Draine et al. (2014) models with power-law slope values $\alpha = 1.0, 2.0$, and 3.0 (Sect. 2.2.4, Eq. (2.13)), as well as the modified black body plus power-law model, included in the `casey2012` CIGALE module (Sect. 2.2.4). Two versions of this module were defined, one with the general opacity formula and one with the optically thin formula.

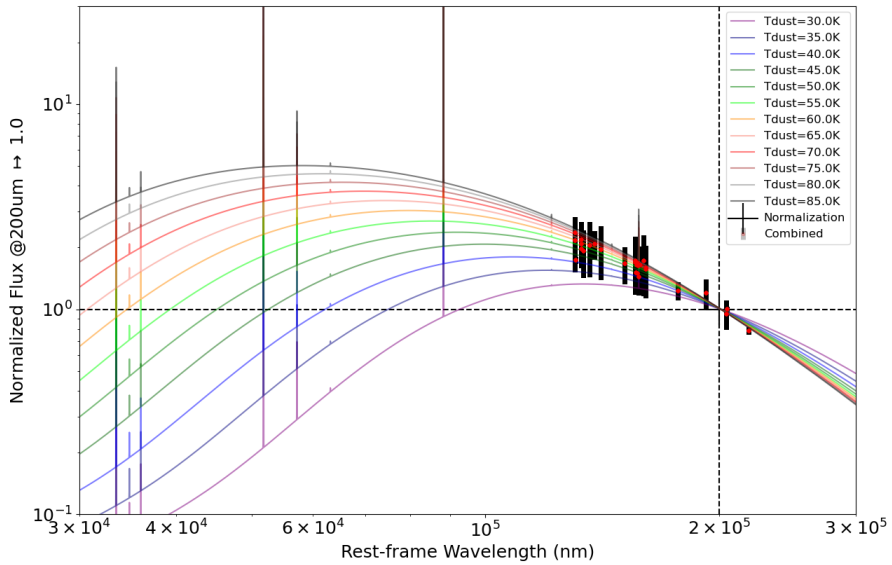

Figure 4.4: A template IR SED built from combining the restframe fluxes, normalised at $\lambda_{restframe}$ = 200μm, of the ALMA detected objects from Burgarella et al. (2020) and Bethermin et al. (2020). The coloured curves represent a modified blackbody model for different dust temperatures in the range $30 \leq T_{dust} \leq 85$. This figure does not include the contribution from the stacked z=5.5 objects. Figure from Burgarella et al. (2021, in prep.).

A MIR power law is added to both. We concluded that the optically thin assumption is better, based on Eq. (2) of Jones et al. (2020).

The simplifications that we can make when fitting the IR SED is to assume a fraction of PAHs in the dust of $q_{PAH} = 0.47$ as we expect our galaxies to have low metallicity (Castellano et al., 2014; Yuan et al., 2019), and the fraction $\gamma = 0.5$, as suggested by Burgarella et al. (2020) and Nanni et al. (2020) for the `dl2014` module. Similarly, for the `casey2012` module, we assume the default value of the slope $\alpha = 2$, and we tested fixed values of the dust emissivity, i.e. $\beta_{RL} = 1.0, 1.5$ and 2.0. These simplifications are necessary due to the lack of data.

Phase 2: Galaxy parameters from full-SED After constraining the IR SED template to the best of the abilities of our data, we turn to fit the SEDs of individual galaxies once more. This time, we are not worried about computational time, and we compute a large number of models, in different runs, to precise the galaxy parameters. To make up for the lack of IR data, we use the template we created using the complete sample (including the stacks and non-detections). In practise, this means that we used the following values of the `dl2014` module parameters: $q_{PAH} = 0.47$, $U_{min} = 10.0$, $\alpha = -2.4$ and $\gamma = 0.53$, and the `casey2012` module parameters: $T_{dust} = 42.8$, $\beta_{RL} = 1.3$ and $\alpha_{PL} = 2.0$[2].

4.4 Preliminary results

This section is devoted to some of the preliminary results we have obtained at the time of writing this thesis (June 2021), and that will be published as Burgarella et al. (2021, in prep.). As can be expected from the methods described in Sect. 4.3, the results produced as part of this project are the galaxy properties estimated by fitting the SEDs of the ALPINE sample galaxies with CIGALE and the conclusions we can draw from them about the overall process of galaxy evolution in the redshift range of interest. In this thesis, I will present the relevant diagnostic diagrams that we use to test how well we fitted the SEDs and some global conclusions we can make based on the results we have thus far. Our focus is to get a better idea of the properties of early dust in the early Universe, so by better constraining the IR SEDs of the sample, we hope to acquire a clearer picture of what dust was like in the earlier epochs of the Universe.

Due to the UV-selected nature of the ALPINE sample, the galaxies we study are "normal" star-forming galaxies, and as such, should be found lying on the main sequence of galaxies (Sect. 2.3). We compare the specific SFR (sSFR = SFR/M_*) as a function of the stellar masses (M_*). The criteria we use for the MS of galaxies are those proposed by Speagle et al. (2014) and Pearson et al. (2018). As a general trend, we find that the ALPINE galaxies have values of M_* and sSFR such that they can indeed be defined as MS galaxies. Moreover, we test the mass-metallicity relation of ALPINE. To find the metallicities of the sample, we use the calibration relation found by Burgarella

[2]Values might still be subject to change. Check Burgarella et al. (2021, in prep.) for possible correction

et al. (2020): $12 + \log(\mathrm{O/H}) = 0.2829 \times \log(\mathrm{IRX}) + 7.8155$. We compare our findings to the evolving mass-metallicity relation proposed by Ma et al. (2019) for the redshift range $0 < z < 6$, and we find a relatively good agreement, especially for the lower-z bin of $z \approx 4.5$ of ALPINE.

The following diagnostic is more specifically related to the dust: we test the A_{FUV} (or IRX) - M_* relationship, using our previous results (Bogdanoska & Burgarella, 2020, Chap. 3). We use the limits of the relationship as given by the error bars of the parameters, even though we expect the scatter to be higher. We find that the ALPINE galaxies are somewhat in general agreement with the $A_{FUV} - M_*$ relationship for $z = 5$, with a higher scatter than that of the estimation of our parameters.

One of the most important relations that we study in our work is the IRX-β relationship (Sect. 2.3.5). The first observation that we can make about our sample, compared to some classical IRX-β relations (Meurer et al., 1999; Bouwens et al., 2009), is that our sample is systematically above them; our objects are bluer than those used in previous literature. This result is not too surprising, as an evolution in the β slope has already been proposed and examined. We use the relationship of Schulz et al. (2020), who use the simulations from the IllustrisTNG Project (Nelson et al., 2018; Marinacci et al., 2018; Springel et al., 2018; Naiman et al., 2018; Pillepich et al., 2018), to determine the redshift evolution in β_z up to $z < 4$. Our galaxies are beyond this range, so we use an extrapolation of the Schulz et al. (2020) relation, given as:

$$\log \mathrm{IRX}_z = \log 1.68 + \log 10^{0.4(3.85+1.96\beta+\beta_z)} \tag{4.2}$$

$$\beta_z(z) = 0.142z - 0.081 \tag{4.3}$$

Eq. (4.2) follows from the work of Overzier et al. (2011), with the addition of the term β_z. The value of β_z varies with redshift and is determined by Schulz et al. (2020) to have the values given by Eq. (4.3). By using Eqs. (4.2) and (4.3) to extrapolate to higher redshifts, we compare our results to the models of Schulz et al. (2020). We find that this way, the IRX-β relation is a lot bluer than our sample (opposite problem of what we had before we included the redshift evolution). Thus, we estimate the relationship of β_z for $z > 4$ from our sample, by calculating $\beta_z = \beta - \beta_{Overzieretal.2010}$, where β are the values of our sample estimated by CIGALE (following Calzetti et al. (1994)).

The redshift evolution of the IRX-β relationship is helpful because of its simplicity: usually, the redshift for the studied galaxies is known. However, a more physical explanation of the change of β with cosmic time is that as we look at earlier epochs, the stellar populations are younger. Because of that, quantities such as the ratio age_{main}/τ_{main} (Burgarella et al., 2020) or the mass-weighted mean stellar population ages $\langle t_{age} \rangle$ (Schulz et al., 2020), the latter of which we also adopt in our work. Schulz et al. (2020) presume that the intrinsic UV-slope β_0 (the slope before it undergoes dust attenuation) changes depending on the stellar population ages. They plot the dependence of IRX on $\beta - \beta_0$ and state that this is a more direct measurement of the dust attenuation. Salim & Boquien (2019) come to a similar conclusion: the scatter in

the UV-slope comes from the variation in the dust attenuation law.

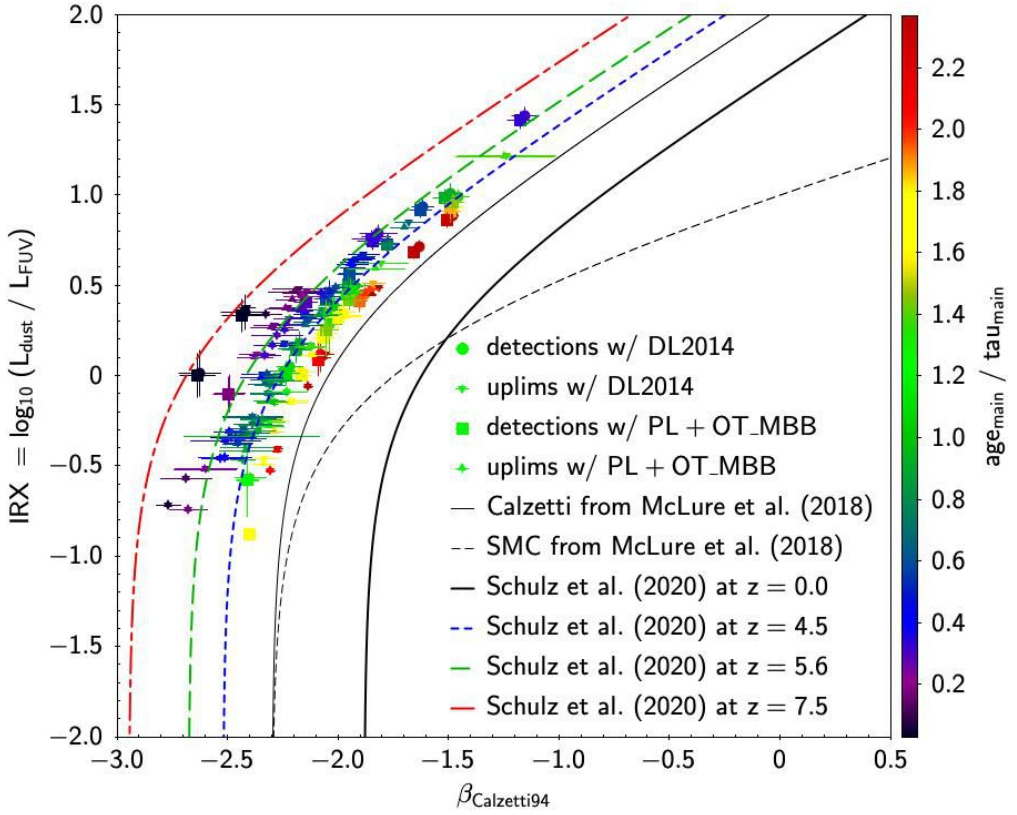

Figure 4.5: IRX - $\beta_{Cazetti-1994}$ diagram. The continuous line corresponds to the original Calzetti law and the dashed line to the SMC law, both from McLure et al. (2018). The colour coding corresponds to values of $\text{age}_{\text{main}}/\tau_{\text{main}}$. The circles and squares represent the DL2014 and PL+OT_MBB dust emission models. Figure from Burgarella et al. (2021, in prep.).

In our results, we present the estimated β values of the ALPINE sample on the IRX-β diagram, where they are colour-coded according to their $\langle t_{age} \rangle$ (Fig. 4.5). We then model β_z as a linear function of $\langle t_{age} \rangle$, and use this relation to place our objects on a diagram that compares to the models of Schulz et al. (2020).

Finally, we determine the DFRD of our sample (Sect. 4.1.2 and Chap. 5), as shown in Fig. 4.6, which is the basis of our future work. In this paper, we only present the values of our SED fitting on the DFRD diagram and compare them to the models suggested by Nanni et al. (2020). The modelling of the chemical evolution to fit this data specifically has not yet been carried out.

What we find about the DFRD is consistent with the results of Burgarella et al. (2020). There is a clear evolutionary component in this diagram: from the colour-coding of the stellar ages, we see that the young stellar populations have a high sSFR, i.e. we can find them to the right of the DFRD. As we move to the left, the ages increase and the older populations can be found. Similarly to the results of Burgarella et al. (2020), a

quick buildup of dust in the early stages of galaxy evolution are expected, as well as a steady decline as the galaxy, along with the stars within it, ages.

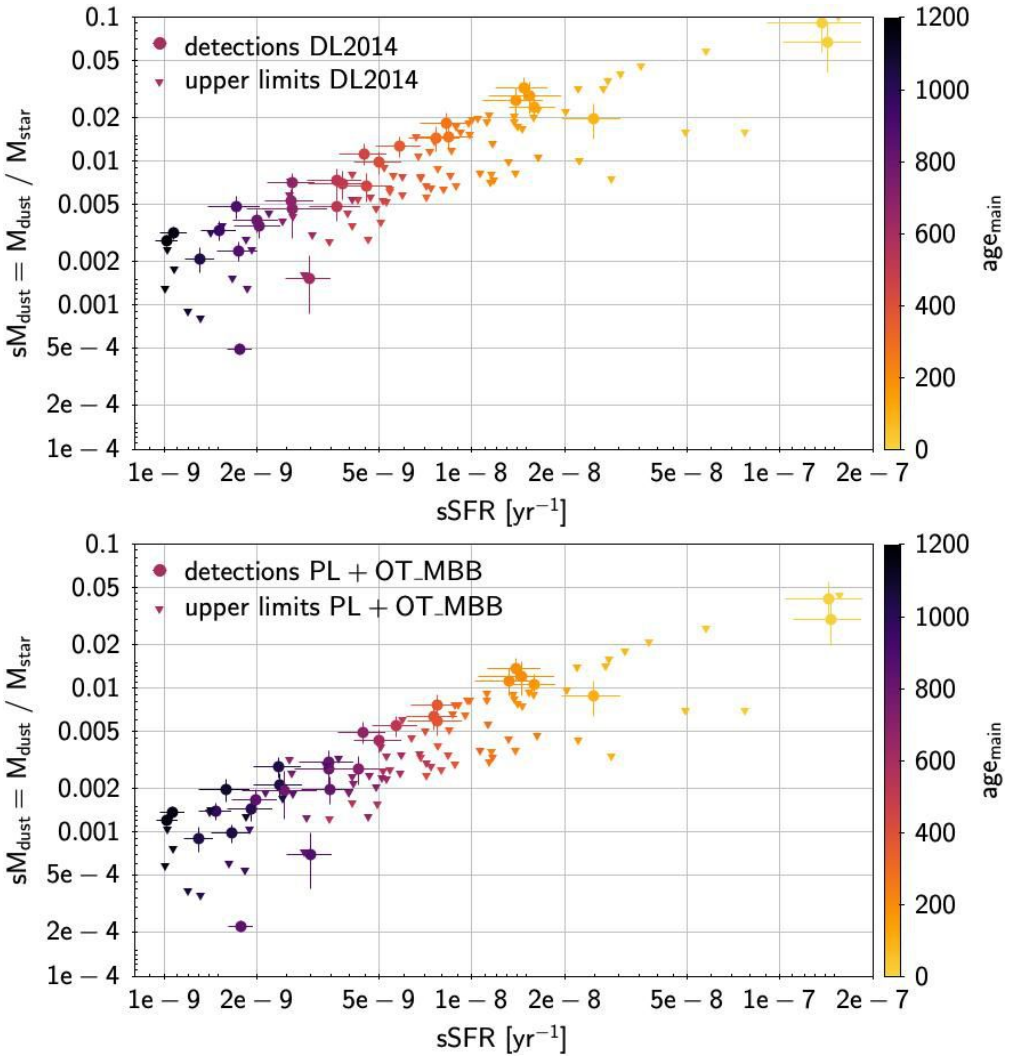

Figure 4.6: Dust Formation Rate Diagrams colour-coded with τ_{age}. The upper panel comes from fitting with a Dale et al. (2014) model, and the bottom panel from fitting with a Casey (2012) model. We see that the age sequence is correlated with the building of the stellar mass, from right to left. Figure from Burgarella et al. (2021, in prep.).

Conclusion

This project is very near the publication of a paper. To date, we have used methods described in the work of Burgarella et al. (2020) as a basis that we then implemented on the ALPINE sample to estimate galaxy parameters, with a particular focus on the

dust properties, as defined by dust emission models. This chapter has summarised the work of Burgarella et al. (2020), mainly their methods and results. A description of the ALPINE survey is also provided, as this represents the most significant number of objects included in our sample.

Moreover, the adapted methods that we use in our work are described in detail. Mainly, our work consists of building a template IR SED by combining ALMA band 7 flux data for galaxies at different redshifts - which gives us fluxes at different restframe wavelengths. The Burgarella et al. (2020) data is also included, the ALPINE sample with both detections and upper limits, and the stacking analysis results of Bethermin et al. (2020). We use CIGALE's dust emission modules to build the IR template.

Once the template is constrained, we fit the SEDs to estimate the physical properties of all of the ALPINE galaxies (again, using CIGALE). Using these results, we represent the relevant diagnostic diagrams, focusing on those that will help determine dust's overall properties in the early Universe: the sSFR-M_*, $A_{FUV} - M_*$, metallicity - M_*, IRX - β and finally, the DFRD.

Even though this work is still incomplete, we have made significant progress so that some preliminary conclusions can be drawn from our results:

- The results of the SED fitting of the ALPINE sample are consistent with those of Burgarella et al. (2020)
- For lower redshifts (redshift bin around $z = 4.5$), the consistency compared to Burgarella et al. (2020) is weaker, implying the existence of a possible difference in the dust mechanisms present during this epoch
- We can provide a template IR SED that could simplify the SED fitting of high-redshift galaxies for which very few restframe IR observations are currently available

The future of this project will be explored in more detail in the following chapter (Chap. 5). In short, we will use the DFRD we have found for the ALPINE sample and combine it with models of the chemical and dust evolution of galaxies to better constrain properties of the galaxy populations during the EoR and earlier. The basis of this future project is the work of Nanni et al. (2020). As a preliminary check, we have only compared our results with their published models, and it seems that our data are generally in good agreement. Shortly, we will compute chemical evolution models for our sample specifically, the results of which might lead to a better understanding of the dust processes governing the evolution of galaxies during the first gigayear of the Universe.

5 Future work: The gas, metal, and dust evolution in low-metallicity local and high-redshift galaxies

During the PhD, I wished to slightly change direction and start working with the more physical aspects of dust in galaxies. For this reason, I had the opportunity to follow the work of Dr Ambra Nanni, who was a postdoc at LAM, and is now in the National Centre for Nuclear Research, in Warsaw, Poland. Unfortunately, I did not have enough time during the PhD to pursue this particular project, so what I have learned about this topic is now part of the plans of my scientific career. The following chapter includes an introduction to chemical evolution models better to understand the models we plan to use to study the properties of dust and metals in the early Universe.

The chemical evolution of galaxies includes examining the chemical enrichment of the ISM through the study of the stellar processes (star creation, ejection and death), dust processes (grain creation, growth and destruction) and the exchange of material between the galaxy and its environment (inflows and outflows). A lot of these processes are tough to characterise for high-redshift galaxies, so we use low-z samples that we believe are in some ways similar to the early-type galaxies: low-metallicity galaxies. For this purpose, the focus of most studies in a similar topic includes the SFR of galaxies, their metallicity, dust-to-gas ratio, gas fraction, ages, and similar parameters. The following section describes how these variables determine the chemical evolution and conclusions we can make from the current knowledge.

5.1 Chemical evolution models

The basis of Nanni et al. (2020) are models for the chemical evolution of galaxies. Thus, I have devoted this section to a brief review of some of the commonly used models, which will help the reader to understand the place and relevance of Nanni et al. (2020). Firstly, a short presentation of the main ingredients that go into the models will be presented, as well as some assumptions different authors decide to make to simplify the calculations, and secondly the basic equations for the galaxy evolution will be explained, most of which are consistently being used throughout the literature. An excellent resource on this topic was a *Journal of Physics: Conference Series* article by Matteucci (2016), a shorter version of a complete textbook written by the same author (Matteucci, 2012), which was a practical guide for writing this section.

A classical paper on this subject is the work of Tinsley (1980). In this paper, she gives the main variables of the chemical evolution and the parameters. In recent years, many models are extensions from the work of either Dwek (1998) or Lisenfeld & Ferrara (1998). The computed quantities are the rate of change of the galactic gas mass, mass fractions of heavy elements, and dust mass.

Chemical evolution is part of the galaxy evolution field of study concerned with the rate of change of the abundances of chemical elements produced in stars during the lifetime of the galaxy. Heavy elements are created by stellar nucleosynthesis and later ejected in the ISM during the stars' lifetime or at the end of their lives. Violent deaths in the form of supernovae (SNe) are responsible for the creation of all elements heavier than ^{56}Fe.

All the chemical elements we study are created in stars. Thus, the main ingredients in the chemical evolution models are the parameters related to the stars and their formation: SFH, IMF, stellar evolution and heavy element production (metal yields). Of course, the conditions under which the stars (and with that the entire galaxy) are born also play a crucial role, such as the initial quantity of gas available and the number of metals at the initial moment of the model. Called the *backward approach*, this approach aims to constrain the SFH, IMF, and other parameters in the models by reproducing the observed (current time) quantities. The initial time is set to be at the moment of the galaxy's creation, so this approach can be used at any redshift, given that we make assumptions about the conditions at the appropriate cosmic time.

Firstly, when modelling the chemical evolution of a galaxy, what needs to be assumed are the initial conditions, particularly the total initial mass of the galaxy. The total mass is also the total initial gas mass, as we take that the stars form from this gas during the lifetime of the galaxy. This value influences the rate of change of metal concentration, with a smaller initial gas mass, producing higher concentrations more quickly (if the SFH is fixed). Another initial condition is the composition of this gas. We can choose pristine gas if we are talking about high redshift galaxies, which stars have not previously enriched. For younger galaxies, this is a consideration that needs to be taken into account. Finally, a decision must be made to determine whether an open or closed box model will be considered, thus deciding whether an infall or outflow of baryonic matter is present.

Once the initial conditions have been set, the chemical evolution models are concerned with the abundance of elements formed by the stars. To correctly calculate the metal quantities, we need to model the evolution of the number of stars, similarly to SED modelling. Conversely, when we access stellar libraries, we are not interested in their spectra but the abundance of metals they produce. Thus, the SFH and IMF play a very similar role in the chemical evolution models as they do in building the SED, details of which can be found in Chap. 2, Sects. 2.2.1, and 2.2.2 and I do not wish to repeat here.

Detailed nucleosynthesis analysis is required to determine the stellar yields from stars of different masses. The yield includes the newly created material ejected by the star. It also consists of the ejected material that was not reprocessed but was present

in the star since its creation. Even though it requires a lot of knowledge of the nuclear reactions undergoing in stars and the initial abundances of elements, practically, we use available libraries. Such an example is FRUITY (Cristallo et al., 2011; Cristallo et al., 2015), accessed on their web interface (http://fruity.oa-teramo.inaf.it/modelli.pl) and requiring for input only the stellar mass and the metallicity. The output is a quantity commonly used in the literature, the stellar yield.

Table 5.1: The parameters used in chemical evolution models. The total mass of the system is defined as $M_t = M_g + M_s + M_w$. The **global parameters** of the models need to be specified by the investigator and are usually normalised so that the total mass is one. The goal is to derive the fraction of metals $Z(t)$, either of each metal separately or as a group.

Global variables

Symbol	Description
$M_g(t)$	Total mass of interstellar gas
$M_s(t)$	Total mass of stars
$M_w(t)$	Total mass of stellar remnants (white dwarfs)
$M_t(t)$	Total mass of the system
$E(t)$	Rate of mass ejection from stars
$E_Z(t)$	Rate of metal ejection from stars
$W(t)$	Creation rate of stellar remnants

Global parameters

Symbol	Description
$\Psi(t)$	Rate of star formation
$f(t)$	Rate of infall or outflow of material from the system
$Z_f(t)$	Metal abundance of the infall (or outflow) material
$\phi(m)$	Initial Mass Function
w	Mass of a stellar remnant
τ_m	Main-sequence lifetime of a star
m_{tn}	Turnoff mass of a population with t = τ
p_z	Stellar recyclable mass fraction that is converted to metal z and then ejected into space.

Then, finally, the chemical evolution of a galaxy comes down to the following fundamental equations, defined by Tinsley (1980), and still widely used today:

$$\frac{dM_t}{dt} = f \tag{5.1}$$
$$\frac{dM_s}{dt} = \Psi - E - W \tag{5.2}$$
$$\frac{dM_g}{dt} = -\Psi + E + f \tag{5.3}$$
$$\frac{dM_w}{dt} = W \tag{5.4}$$
$$\frac{d(ZM_g)}{dt} = -Z\Psi + E_Z + Z_f f \tag{5.5}$$

The symbols of these equations are explained in Table 5.1. Equation (5.1) is simply the mass conservation equation. Eq. (5.2) describes the stellar mass evolution, where the SFR increases the number of stars while the ejection and remnant creation rates decrease it. Eq. (5.4) gives directly the rate of creation of stellar remnants. It should be noted here that $M_t = M_s + M_g + M_w$, so that leaves Eq. (5.3) to be simply Eq. (5.1) - Eq. (5.2) - Eq. (5.3). Finally, in Eq. (5.5), $-Z\Psi$denotes the number of metals lost from the ISM to form stars, E_Z is the rate of metal ejection into the ISM from the stars, and $Z_f f$ tells the abundance of metals ejected from or injected into the galaxy.

When talking about the specific metals, usually, an equation for each element i is written in terms of the mass fraction $X_i = M_i/M_g$, where M_i is the mass of the element. Then, from Eq. (5.3), and with using $E_i = X_i E$ to signify the ejection rate of the element i, we can write the following equation, corresponding to Eq. (7) of Lisenfeld & Ferrara (1998) (with some of the symbols changed to match those of Table 5.1):

$$\frac{dM_i}{dt} = \frac{d}{dt}(X_i M_g) = -X_i\Psi + E_i - X_i f \tag{5.6}$$

Finally, when discussing dust, several other terms need to be included to account for the creation and destruction of dust. We can denote the mass ratio of the dust mass and the element i, $f_d = M_d/M_i = M_d/X_i M_g$. We can also set $D = M_d/M_g$ as the dust-to-gas mass ratio and write $f_d = D/X_i$. Then, the equation will be the following (e.g. Lisenfeld & Ferrara, 1998, Eq. (8)):

$$\frac{dM_d}{dt} = \frac{d}{dt}(DM_g) = -\alpha D\Psi + f_{in}E_i - \frac{DM_g}{\tau_{SN}} - \delta D f \tag{5.7}$$

The newly introduced parameters here refer to the dust properties. Specifically, αf_d is the fraction of dust destroyed during star formation, f_{in} gives the fraction of dust in the injected material, and δ is the fraction of dust in the outflow. Their characteristic timescale τ_{SN} shows the destruction of dust by SNe.

The chemical evolution processes are complex, and many are yet to be understood and included in the models. Consequently, the study of chemical evolution is complicated, and the equations contain a large number of parameters that need to be included. However, this makes the task more challenging and exciting - we need to find a way to bring our models as close to reality as possible, and we can only do this by finding different ways to take advantage of observational data.

5.2 Summary of Nanni et al. (2020)

The main objective of the work of Nanni et al. (2020) is to use chemical evolution models (Sect. 5.1) and to compare the findings to the SED fitting results of Burgarella et al. (2020). They used the code OMEGA (One-zone Model for the Evolution of GAlaxies; Côté et al., 2017; Ritter et al., 2018), as well as external routines. This code gives the mass of the gas, metals and dust at each time step, which is later used to build the DFRD.

The data samples used in this work are the same ones as in the paper of Burgarella et al. (2020), i.e. a Low-zZ sample of DGS galaxies ($12 + log(O/H) < 8.5$) and a Hi-z LBG sample, discussed in Chapter 4, Sect. 4.1, along with SED fitting, used to estimate the physical parameters. The most relevant parameters to this work are τ, the characteristic timescale of the SFH (Chap. 2, Sect. 2.2.1, Eq. (2.7)), the SFR, and the total stellar (M_*) and dust masses (M_{dust}). Other data are also available for the Low-zZ sample: metallicity, gas fraction, dust-to-gas ratio, and circumgalactic dust fraction (Rémy-Ruyer et al., 2013; Rémy-Ruyer et al., 2014). As in Burgarella et al. (2020), a DFRD is plotted by setting the x-axis to be the sSFR (=SFR/M_*) and the y-axis to be the sMdust (=Mdust/Mstar), and on this type of plot, different chemical evolution models are compared.

They use the equations for the chemical evolution (Sect. 5.1, Eqs. 5.1-5.5) and assume different values for their parameters. They choose an IMF, condensation fraction, stellar masses of the SN progenitors, galactic outflow efficiency, destruction by SNe, initial gas content, and physical properties (mainly sSFR and sMdust). Then these values are estimated at each time step and compared to the data obtained from the SED fitting. The resulting plots in the paper of Nanni et al. (2020) are the different chemical evolution tracks, where usually a single parameter is varied to show the effects it has on the evolutionary track.

The grid of evolutionary tracks is also used to constrain the physical parameters: they compute a probability density distribution for each parameter from the residuals between the values found in each step of the chemical evolution models and the values from the SED fitting with CIGALE. The properties are then estimated by finding the average and standard deviation of the probability density distribution, and these estimates can be compared to those of CIGALE. As a result, Nanni et al. (2020) improve upon the stellar mass estimates of Rémy-Ruyer et al. (2015). In the latter paper only IR

data is used, while NED photometry [1] complements the IR data in the former. They also find an average value for the characteristic timescale ($\tau = 83$ Myr for the LBGs and 5 of the Low-zZ galaxies, and $\tau = 300$ Myr for the remaining DGS galaxies). The values they find for the sSFR is $10^{-11} - 10^{-7}\mathrm{yr}^{-1}$ for the LBGs and $10^{-9} - 10^{-7}\mathrm{yr}^{-1}$ for the Low-zZ sample. The Mdust is $10^{-4} - 6 \times 10^{-2}$ for the LBGs and $10^{-4} - 10^{-2}$ for the Low-zZ sample. Specifically for the DGS galaxies, they also find metallicity values between $7.1 < 12 + log(O/H) < 8.4$, gas fraction of $0.4 < f_{gas} < 1$, and dust-to-gas ratio between $10^{-5} < \mathrm{D/G} < 10^{-3}$.

Nanni et al. (2020) find general constraints concerning these populations of galaxies, apart from the physical properties. They find that a top-heavy IMF is necessary to reproduce the quick rise of the sMdust at the early stages of galaxy evolution, which is impossible to do with a Chabrier (2003) IMF, regardless of whether dust grain growth in the ISM is included in the model or not. A top-heavy IMF leads to a more significant number of SNe in the early times, which is required to explain the early rise of Mdust, Fig. 5.1, left panel (Fig. 4 of Nanni et al. (2020), top panel). Similar reasoning indicates that the condensation fraction f_{cond} should be at least around $25 - 50\%$ to reproduce the high sSFR end of the observed values. However, even with these conditions met, it is still not possible to completely match the observations. The authors give some suggestions why this might be the case, such as that the assumed chemical composition of the dust might be determined from the IR emission with a more conciderable uncertainty than expected, as seen in the right panel of Fig. 5.1 (also Fig. 4 of Nanni et al. (2020), bottom panel).

One of the most prominent features of the DFRD is the decline of the sMdust with increasing age (decreasing sSFR, moving towards the left of the DFRD). It is most likely a combination of multiple physical processes, namely star formation (which increases the total stellar mass), the transformation of dust into stars, dust destruction (as an effect of SN shocks), and dust loss due to galactic outflows. In their paper, Nanni et al. (2020) show that including outflows is necessary to reproduce this decline, as only dust destruction and astration are not enough to lower the sMdust to the observed values. They also test the effects of dust growth in the ISM, and they find that it is not necessary to include it to reproduce the data, unlike the outflows. Galactic inflows are also considered, but their effects are ultimately not included in the models.

Furthermore, Nanni et al. (2020) constrain the star formation efficiency and the initial baryon mass by using the available metallicity data for the Low-zZ sample. They find that an initial baryon mass of 10 to 100 times greater than the final stellar mass is required. The star formation efficiency can take on a range of values, making it possible to account for the different metallicites. Finally, the conclusion that metal yields that favour a fast enrichment, such as those of Kobayashi et al. (2006), reproduce the rise of the sMdust so early in the evolutionary sequence has been made. To arrive at this conclusion, Nanni et al. (2020) consider the theoretical yields for Type II Supernovae (SNe II), thermally pulsing asymptotic giant branch (TP-AGB) stars, and population

[1] https://ned.ipac.caltech.edu/

III (PopIII) stars. They find that SNe Ia, TP-AGB stars and PopIII stars give a negligible contribution to the yield because of the top-heavy IMF. So, they arbitrarily choose the theoretical yields by Iwamoto et al. (1999) for Type Ia SNe, Cristallo et al. (2015) for TP-AGB stars, and Heger & Woosley (2010) for Pop III.

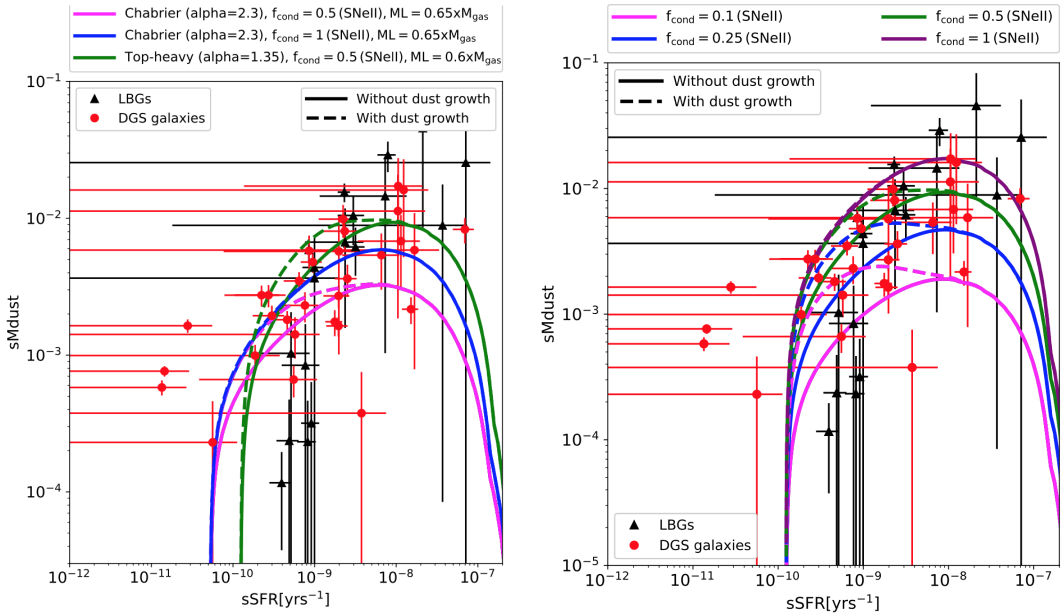

Figure 5.1: Left: sMdust as a function of sSFR for the Hi-z sample (black triangles) and the Low-zZ galaxies (red dots). The chemical evolutionary models shown have been computed using a Chabrier IMF or a top-heavy IMF ($\alpha = 1.35$) and different condensation fractions (colours are indicated in the legend). The SFH is characterised by $\tau = 300$Myr and $M_{gas} = 100 \times M_{stars}$ is assumed. Right: same as in the left panel, but the condensation fractions are varied. Figure from Nanni et al. (2020).

5.3 The future of our project

The models described in the previous section (Sects. 5.1 and 5.2) include many physical quantities that we are studying in our currently ongoing project (Chap. 4). Starting from the equations for the chemical evolution (Eq. (5.1)) and assuming realistic initial conditions, we should, in theory, reproduce the results of Burgarella et al. (2020) and Burgarella et al. (2021, in prep.). It would mean that the physical processes behind the metals and dust formation of early galaxies are entirely understood. Currently, we are far from understanding the complete picture. Still, with every new improvement of the models and with every new observation of early-Universe galaxies, we can get one step closer to discovering the dusty secrets of these galaxies.

The natural progression of our project is to follow that of Burgarella et al. (2020) into the work of Nanni et al. (2020). We have determined the same parameters as Burgarella et al. (2020), only for more galaxies and at a different redshift. The redshift range will help us use similar studies about lower redshift galaxies to bridge the gap towards the high redshift galaxies and find similarities and differences between low and high redshift dust mechanisms.

The first step is relatively simple. We have already started some preliminary examinations about this: compare the DFRD parameters of our sample to the models published by Nanni et al. (2020). It is the first check to confirm that our findings are consistent. We can see in Fig. 5.2) that we find a similar time evolution of the dust buildup: a swift buildup of dust in the early age of the galaxy and then a steady decrease after a peak. It is challenging to explain and model this early burst of dust creation: it is almost impossible to create such a chemical model that follows exactly our results. As in all scientific studies, there are two explanations: either we have a problem with the observation, or our models are incomplete (or both).

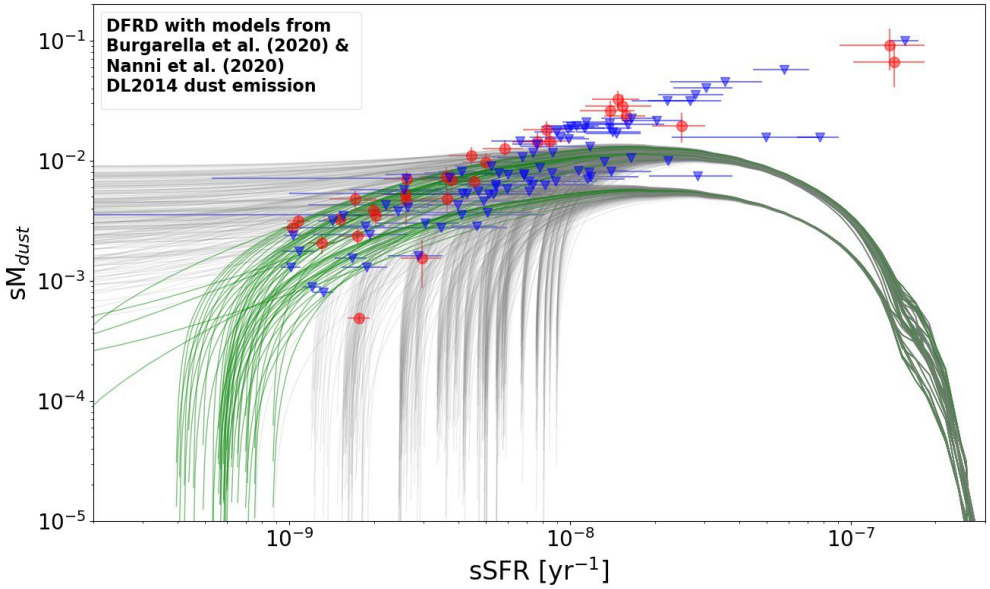

Figure 5.2: DFRD compared to models defined in Burgarella et al. (2020) and Nanni et al. (2020). Note that the factor 2.32 needed to match PL+OT_MBB emission to DL2014 is applied in this plot. Figure from Burgarella et al. (2021, in prep.).

In terms of the observations, we know that it is challenging to observe galaxies this early in the Universe, especially their restframe IR dust emission. We can only hope that once JWST launches we will finally understand better the dust processes in the early Universe. When speaking of the models, it is hard to say where the problem is. One possibility is that the currently accepted mechanisms of dust creation are not enough to explain the creation of dust fully. There is plenty of evidence for this

possibility, e.g. the work of Michałowski (2015). They estimate the amount of dust produced by the different mechanisms (AGB stars, SNe, ISM buildup) and compare it to measurements of high redshift galaxies. They find that unless we assume that the SNe do not destroy any of the dust they create with their shocks (which does not seem like a very physical solution), we cannot explain the high amount of dust in the observed objects.

Nanni et al. (2020) model the chemical and dust evolution of a galaxy, and this includes choosing the mechanisms that will be included in the equations. The work of Asano et al. (2013) is an example of this: they include the ISM buildup of dust in their models. However, N20 show that this term in the equations does not have a specifically high contribution. So it would seem that the ISM buildup is not the missing component to our models. Although we still do not have enough data to provide significant conclusions, it is still an open and fascinating question.

The next step is to follow the procedure of N20 and compute models that correspond to our new sample. We will also get more precise results for the ALPINE galaxies' physical properties and get a better constrain of the chemical and dust evolution models. Finally, we hope to draw conclusions about the overall behaviour of these galaxies and uncover the history of the Universe during this epoch between redshifts $4 < z < 6$.

6 Conclusion

It is scary how one document can contain all the work done in three years of my life. PhD theses are a unique kind of document - sometimes the work in them is not too well connected, which I find to be a positive thing. It means that the PhD candidate took some time to dip their toe in a few different subjects and have gathered experience from diverse topics.

In this last conclusions chapter, I summarise and comment on the take-home messages extracted from this thesis. I would like to remind the reader of some of the main questions this thesis attempted to answer:

- Can we expect the relationship between the stellar mass and dust attenuation to remain identical throughout all cosmic times? How can we explain the change, if any?
- What can we predict about the dust attenuation of low-mass galaxies going back in the history of the universe?
- How can we combine the results from SED fitting with those of cosmic properties of galaxies?
- What information can we extract about the dust content (i.e. the dust mass) through studying the SED of a galaxy?
- How can we implement chemical evolution models on distant galaxies (for which we lack metallicity data)?

Of course, in this thesis, I tackle questions that are not as general as those mentioned in the introduction. But, I hope I have contributed to the overall scientific picture, even if only in a small way. So, a summary of the previous chapters is hopefully a start towards answering some of these questions.

6.1 Summary

This thesis started with a background of the theoretical considerations (Chapter 2). I wrote this chapter with a few different goals in mind:

- Making sure that everyone who reads this thesis is familiar with the background information necessary to follow the rest of the text,

- Serving as a summary of the main principles that I have learned throughout my years as a PhD student,
- Allowing me to review some literature that I did not have a chance to explore before,
- Leaving behind a relatively pedagogical text that might serve any future students that I, or my close collaborators, might have in the future that we would like to bring up to speed with the concepts relevant to our field.

Even though they serve the same goals as those above, the following chapters are more devoted explicitly to our scientific findings. Indeed, these discoveries have already been published (or soon will be). Their inclusion within this thesis aims to explain my side of the work and how I have understood it.

Chapter 3 contains the work that was published in my first work as a first author. I started this work during my master's thesis, and it took a long time to reach its final state. The whole story behind this project, even the unpublished parts, are included in the thesis. The outline is slightly different from that of the paper, as I took an entire section to discuss some of the things that did not work, but I did not wish for them to be lost as some notes I once took.

So, in Chap. 3, we start by describing the data that we used: a collection from the literature that contains UV selected samples of galaxies at different redshift, for which both UV and IR data is available. We made sure that the samples included were as similar as possible, that data about the galaxies' stellar masses and dust attenuation estimated through the IRX were available. The values of IRX are then converted to dust attenuation in the FUV (A_{FUV}). Next, the data is separated into redshift bins, and for each bin, a relationship for the stellar mass - dust attenuation is fitted. The main findings of our work are concerned with this relationship. We show that it is reasonable to assume an evolution with redshift of the $A_{FUV} - M_*$ dependence. We also offer evidence that assuming a non-zero apparent A_{FUV} for low-mass galaxies agrees with cosmic dust attenuation results in the literature.

The redshift-evolving $A_{FUV} - M_*$ relationship is then used to calculate the cosmic average dust attenuation. This is done by estimating the average dust attenuation weighted by the stellar MF. Using the redshift evolution of the $A_{FUV} - M_*$ relationship, we reproduce the shape of the cosmic $A_{FUV} - z$ curve of other authors (Burgarella et al., 2013; Cucciati et al., 2012), a shape that matches the classical SFRD plot (Madau & Dickinson, 2014). This result is expected, as the dust and the formation of stars usually are found together in the Universe.

The following chapter (Chap. 4) describes the work that we are currently working on. The topic is slightly different from that of Chap. 3, although the theme of SED fitting is still prevalent. In this work, we study high redshift galaxies, focusing on the ALPINE survey. The methods used are based on Burgarella et al. (2020), who work with galaxies with redshift $z > 6$ that they compare to a sample of low-z and low metallicity galaxies to build the IR SED. We perform the SED fitting, with a particular focus on the

IR SED. The IR SED is tough to fit, as we only have ALMA Band 7 detections. Thus, we use a preliminary estimate of the SED of each galaxy to find its rest-frame 200 μm flux, used to normalise the ALMA observations of each galaxy. We do this with the purpose of building a single SED from the entire sample in the rest-frame, using the natural redshift dispersion to cover a range of redshifts.

After we have built the template for the IR SED using the combined ALMA observations of the ALPINE sample, we perform a second, more detailed fitting of the individual galaxies using the parameters for the dust emission model we derived from the first fitting. Using these findings, we study some of the global properties of the sample, such as the sSFR-sMdust diagram, or the IRX-β relationship.

Finally, Chap. 5 is concerned with the future of our findings from Chap. 4, a work that is still in its early stages. Briefly, what we plan to do is very similar to the work of Nanni et al. (2020). We wish to study the chemical evolution models and use them to find out more about the ALPINE sample. We plan to explore further the possibility of a rapid buildup of dust in the early Universe and further explain this phenomenon.

6.2 Perspectives

Future of the current projects

A PhD thesis is a time-limited project, defined to end with a defence. However, the research undertaken during this time is not something that will ever be finished, as is the case with all science - there are always more questions that can be asked and always more to be learned. Although my time as a PhD student has come to an end, the projects continue.

Chapter 3 was initially planned to develop into creating a simulated field of galaxies useful for testing data pipelines of future telescopes (Sect. 3.5.3). We have not yet brought this project to life, as my work changed its focus to a slightly different topic. However, CIGALE is a potent tool that is very competent in creating simulated observations, so it would still be a relevant project to undertake. The first step would be to create a grid of models with CIGALE to cover as best as possible the parameters space of the galaxy properties (stellar mass, SFR, IRX, stellar ages, metallicities). From these models, using different selection criteria, CIGALE would create a realistic sample of galaxies. The sample would conform to the galaxy stellar mass function, LF, IRX-beta relationship, and our model for the stellar mass-dust attenuation relationship. At the same time, it would be a sample that reproduces the main global properties, such as the SFRD and SMD diagrams, the cosmic dust attenuation curve, and many more.

As the primary goal of this type of mock observations is to predict what kind of fields would be observed with specific telescopes (e.g. James Webb Space Telescope - JWST), realistic observation limits need to be incorporated. It would allow us to estimate up to which certainty we will be able to test our proposed relation for the stellar mass-dust attenuation and similar predictions made for the high-redshift Universe once actual data from these facilities will be available.

New observational data

Nearby galaxies are being studied in detail, especially by exploiting recent surveys such as the Sloan Digital Sky Survey (SDSS) and other wide-field surveys. To study the formation and evolution of galaxies, it is imperative that we also study the galaxies of early cosmic times. To date, the ALPINE survey has the most significant number of such objects (118) with some of the best ALMA data and an excellent multi-wavelength coverage because the objects are located in the COSMOS and Chandra Deep Field South well-observed fields. I have already presented this sample and how we use it in our project in Chap. 4. In this sample, the high-redshift galaxy data comes from studying individual objects. These objects are not enough to build reliable statistics on the early-type galaxies. Thus, more data is needed.

I wish to continue studying the formation and evolution of galaxies, going back in cosmic time deep into the reionisation epoch when the first galaxies formed. I would like to continue estimating the physical parameters of these galaxies that are available to us today, such as their stellar masses, star formation rates, gas and dust masses, information on their histories, dust attenuation, and many more. Thanks to the most recent and most advanced observational facilities, both ground and space-based, we can collect this data and develop the different models that come into play when fitting the SED. There is already a large amount of multi-wavelength data available on numerous galaxies, mainly in UV, optical and IR. However, these early epoch galaxies that we are interested in are very distant from us, and their redshift is higher than z=6. Observationally, this means that to study the full SEDs of the galaxies, we need observations in the millimetre and sub-millimetre ranges. Therefore, ALMA is ideal for our future projects.I, alongside my collaborators from LAM, Poland and Japan, aim to get observational time for as many new objects in this range and use the available data to draw conclusions and predictions about these early cosmic times.

I am very interested in exploring the dust evolution models using multi-wavelength data, i.e. continuing the projects presented in Chaps. 3, 4 and 5 and the current work done by some of my collaborators in LAM. This part of the research aims to use the photometric data to gain information on the physical parameters of the galaxies, which will serve us to explore the chemical evolution and the building/destruction of the dust mass with the cosmic times.

Shortly, we plan to submit proposals to ALMA and the JWST to obtain more high-quality information on a large enough sample of objects (several tens in the next 2-3 years) and to study the general properties of galaxies in such early cosmic times. In the meantime, we will collect data with ALMA and JWST (with already accepted programmes – and also submitted ones) and already available in the literature to build a catalogue of galaxies with which we will be able to continue our studies. Our future projects will focus on performing the SED fitting on these galaxies, first on existing data and later on new. We will be using CIGALE and its diverse applications for our scientific goals.

It is a beautiful time to explore the deep universe, with the upcoming new knowledge

promised by the JWST and future ground-based observatories, such as the Extremely Large Telescopes. Our future research will help fill the gap between the information we have already gathered and the exciting new data about to come. We will be able to make the most of the current observational capabilities and to shine more light on the puzzle that is galaxy formation.

The new ALMA data will allow us to investigate further the metal and dust content of galaxies in the early universe, as it will enable us to explore the rest-frame IR part of their SED, where information about the dust properties of galaxies hides. This new insight will be fascinating, as we cannot expect the dust at early cosmic times to be the same as what we observe in the nearby galaxies; even though the dust represents only one per cent of the interstellar medium of galaxies, its significance is vast, it contributes to the majority of the galaxy emission, it is a tracer for star and planet formation, and it is closely connected to the evolution of the metallicity of a galaxy. My group in Marseille is also involved in a JWST proposal (CEERS), and they are part of several JWST proposals that wish to further observe galaxies in the early universe. This research will help revolutionise the chemical and dust evolution models, improving the overall image of galaxy evolution we have today. This research will also provide a wealth of information on the dust cycle in the early universe.

Bibliography

AGHANIM, Nabila et al., 2008. *Reports on Progress in Physics*. Vol. 71, p. 066902. ISSN 0034-4885. Available from DOI: 10.1088/0034-4885/71/6/066902 (cit. on p. 30).

ALBERS, Saundra M. et al., 2019. *Monthly Notices of the Royal Astronomical Society*. Vol. 490, pp. 5538–5550. ISSN 0035-8711. Available from DOI: 10.1093/mnras/stz2903 (cit. on p. 86).

ALVAREZ-MARQUEZ, J. et al., 2016. *Astronomy and Astrophysics*. Vol. 587. ISSN 0004-6361. Available from DOI: 10.1051/0004-6361/201527190 (cit. on pp. 65, 67).

ALVAREZ-MARQUEZ, J. et al., 2019. *Astronomy and Astrophysics*. Vol. 630, A153. ISSN 0004-6361. Available from DOI: 10.1051/0004-6361/201935719 (cit. on pp. 56, 67).

ARAVENA, M. et al., 2016. *The Astrophysical Journal*. Vol. 833, p. 71. ISSN 0004-637X. Available from DOI: 10.3847/1538-4357/833/1/71 (cit. on p. 95).

ASANO, Ryosuke S. et al., 2013. *Earth, Planets and Space*. Vol. 65, pp. 213–222. ISSN 1880-5981. Available from DOI: 10.5047/eps.2012.04.014 (cit. on pp. 97, 118).

EL-BADRY, Kareem et al., 2016. *The Astrophysical Journal*. Vol. 820, p. 131. ISSN 0004-637X. Available from DOI: 10.3847/0004-637X/820/2/131 (cit. on p. 86).

BALDRY, I. K. et al., 2012. *Monthly Notices of the Royal Astronomical Society*. Vol. 421, pp. 621–634. ISSN 0035-8711. Available from DOI: 10.1111/j.1365-2966.2012.20340.x (cit. on p. 50).

BALESTRA, I. et al., 2010. *Astronomy and Astrophysics*. Vol. 512, A12. ISSN 0004-6361. Available from DOI: 10.1051/0004-6361/200913626 (cit. on p. 100).

BARKANA, R. & LOEB, A., 2001. *Physics Reports*. Vol. 349, pp. 125–238. ISSN 0370-1573. Available from DOI: 10.1016/S0370-1573(01)00019-9 (cit. on p. 29).

BARKANA, Rennan, 2006. *Science*. Vol. 313, pp. 931–934. ISSN 0036-8075. Available from DOI: 10.1126/science.1125644 (cit. on pp. 29, 30).

BAUER, A. E. et al., 2011. *Monthly Notices of the Royal Astronomical Society*. Vol. 417, pp. 289–303. ISSN 0035-8711. Available from DOI: 10.1111/j.1365-2966.2011.19240.x (cit. on p. 58).

BEHROOZI, Peter S. et al., 2013. *The Astrophysical Journal*. Vol. 770, p. 57. ISSN 0004-637X. Available from DOI: 10.1088/0004-637X/770/1/57 (cit. on p. 52).

BELL, Eric F. et al., 2003. *The Astrophysical Journal Supplement Series*. Vol. 149, pp. 289–312. ISSN 0067-0049. Available from DOI: 10.1086/378847 (cit. on p. 43).

BERNHARD, E. et al., 2014. *Monthly Notices of the Royal Astronomical Society*. Vol. 442, no. 1, p. 509. Available from DOI: 10.1093/mnras/stu896 (cit. on p. 81).

BETHERMIN, M. et al., 2020. *arXiv:2002.00962 [astro-ph]*. Available also from: http://arxiv.org/abs/2002.00962 (cit. on pp. 99, 104, 109).

BOGDANOSKA & BURGARELLA, 2020. *Monthly Notices of the Royal Astronomical Society*. Vol. 496, pp. 5341–5349. ISSN 0035-8711. Available from DOI: 10.1093/mnras/staa1928 (cit. on pp. 25, 55, 63, 92, 93, 106).

BOQUIEN, M. et al., 2012. *Astronomy and Astrophysics*. Vol. 539, A145. ISSN 0004-6361. Available from DOI: 10.1051/0004-6361/201118624 (cit. on p. 56).

BOQUIEN, M. et al., 2019. *Astronomy and Astrophysics*. Vol. 622, A103. Available from DOI: 10.1051/0004-6361/201834156 (cit. on pp. 26, 31, 35, 38, 42, 56, 95).

BOUWENS, R. J. et al., 2007. *The Astrophysical Journal*. Vol. 670, pp. 928–958. ISSN 0004-637X. Available from DOI: 10.1086/521811 (cit. on p. 72).

BOUWENS, R. J. et al., 2009. *The Astrophysical Journal*. Vol. 705, pp. 936–961. ISSN 0004-637X. Available from DOI: 10.1088/0004-637X/705/1/936 (cit. on pp. 58, 72, 106).

BOUWENS, R. J. et al., 2012. *The Astrophysical Journal*. Vol. 754, p. 83. ISSN 0004-637X. Available from DOI: 10.1088/0004-637X/754/2/83 (cit. on pp. 45, 54).

BOUWENS, Rychard J. et al., 2016. *The Astrophysical Journal*. Vol. 833, p. 72. ISSN 0004-637X. Available from DOI: 10.3847/1538-4357/833/1/72 (cit. on pp. 63, 65, 67, 81, 85, 95).

BRAMMER, Gabriel B. et al., 2008. *The Astrophysical Journal*. Vol. 686, pp. 1503–1513. ISSN 0004-637X. Available from DOI: 10.1086/591786 (cit. on p. 46).

BRAMMER, Gabriel B. et al., 2012. *The Astrophysical Journal Supplement Series*. Vol. 200, p. 13. ISSN 0067-0049. Available from DOI: 10.1088/0067-0049/200/2/13 (cit. on p. 100).

BROMM, V. et al., 2001. *Monthly Notices of the Royal Astronomical Society*. Vol. 328, pp. 969–976. ISSN 0035-8711. Available from DOI: 10.1046/j.1365-8711.2001.04915.x (cit. on p. 85).

BROMM, Volker & LARSON, Richard B., 2004. *Annual Review of Astronomy and Astrophysics*. Vol. 42, pp. 79–118. ISSN 0066-4146. Available from DOI: 10.1146/annurev.astro.42.053102.134034 (cit. on p. 29).

BROMM, Volker & LOEB, Abraham, 2006. *The Astrophysical Journal*. Vol. 642, pp. 382–388. ISSN 0004-637X. Available from DOI: 10.1086/500799 (cit. on p. 31).

BROMM, Volker & YOSHIDA, Naoki, 2011. *Annual Review of Astronomy and Astrophysics*. Vol. 49, pp. 373–407. ISSN 0066-4146. Available from DOI: 10.1146/annurev-astro-081710-102608 (cit. on p. 29).

BRUZUAL, G. & CHARLOT, S., 2003. *Monthly Notices of the Royal Astronomical Society*. Vol. 344, no. 4, pp. 1000–1028. ISSN 0035-8711, ISSN 1365-2966. Available from DOI: 10.1046/j.1365-8711.2003.06897.x (cit. on pp. 35, 64, 65, 95, 102).

BUAT, V. et al., 2005. *The Astrophysical Journal Letters*. Vol. 619, no. 1, p. L51. ISSN 1538-4357. Available from DOI: 10.1086/423241 (cit. on pp. 44, 74).

BUAT, V. et al., 2008. *Astronomy and Astrophysics*. Vol. 483, pp. 107–119. ISSN 0004-6361. Available from DOI: 10.1051/0004-6361:20078263 (cit. on pp. 34, 35).

BUAT, V. et al., 2009. *Astronomy and Astrophysics*. Vol. 507, no. 2, p. 693. Available from DOI: 10.1051/0004-6361/200912024 (cit. on p. 73).

BUAT, V. et al., 2012. *Astronomy and Astrophysics*. Vol. 545, A141. ISSN 0004-6361. Available from DOI: 10.1051/0004-6361/201219405 (cit. on p. 67).

BUAT, Véronique et al., 2020. Vol. 341, pp. 70–73. Available from DOI: 10.1017/S1743921319002692. Conference Name: Panchromatic Modelling with Next Generation Facilities (cit. on p. 37).

BURGARELLA, D. et al., 2005. *Monthly Notices of the Royal Astronomical Society*. Vol. 360, pp. 1413–1425. ISSN 0035-8711. Available from DOI: 10.1111/j.1365-2966.2005.09131.x (cit. on pp. 26, 31, 64, 67, 71, 95).

BURGARELLA, D. et al., 2013. *Astronomy and Astrophysics*. Vol. 554, A70. Available from DOI: 10.1051/0004-6361/201321651 (cit. on pp. 53, 70–73, 75, 76, 78, 79, 81, 88, 89, 92, 120).

BURGARELLA, D. et al., 2020. *Astronomy and Astrophysics*. Vol. 235, p. 459.02. Available also from: http://adsabs.harvard.edu/abs/2020AAS...23545902B (cit. on pp. 8, 25, 65, 67, 85, 94–99, 102–109, 114, 116, 117, 120).

CALURA, Francesco et al., 2013. *Monthly Notices of the Royal Astronomical Society*. Vol. 438. Available from DOI: 10.1093/mnras/stt2329 (cit. on pp. 36, 37).

CALZETTI, Daniela, 2001. *Publications of the Astronomical Society of the Pacific*. Vol. 113, pp. 1449–1485. ISSN 0004-6280. Available from DOI: 10.1086/324269 (cit. on p. 56).

CALZETTI, Daniela et al., 1994. *The Astrophysical Journal*. Vol. 429, p. 582. Available from DOI: 10.1086/174346 (cit. on p. 106).

CALZETTI, Daniela et al., 2000. *The Astrophysical Journal*. Vol. 533, pp. 682–695. ISSN 0004-637X. Available from DOI: 10.1086/308692 (cit. on pp. 37, 38, 44, 57, 71, 86).

CANNON, John M. et al., 2002. *The Astrophysical Journal*. Vol. 565, pp. 931–940. ISSN 0004-637X. Available from DOI: 10.1086/324691 (cit. on p. 88).

CAPAK, P. et al., 2004. *The Astronomical Journal, Volume 127, Issue 1, pp. 180-198*. Vol. 127, no. 1, p. 180. ISSN 0004-6256. Available from DOI: 10.1086/380611 (cit. on p. 100).

CAPAK, P. L. et al., 2015. *Nature*. Vol. 522, pp. 455–458. ISSN 0028-0836. Available from DOI: 10.1038/nature14500 (cit. on p. 95).

CAPAK, Peter et al., 2012. *Spitzer Proposal*. Available also from: http://adsabs.harvard.edu/abs/2012sptz.prop90042C (cit. on p. 101).

CAPUTI, K. I. et al., 2011. *Monthly Notices of the Royal Astronomical Society*. Vol. 413, pp. 162–176. ISSN 0035-8711. Available from DOI: 10.1111/j.1365-2966.2010.18118.x (cit. on pp. 51, 52).

CAPUTI, K. I. et al., 2015. *The Astrophysical Journal*. Vol. 810, p. 73. ISSN 0004-637X. Available from DOI: 10.1088/0004-637X/810/1/73 (cit. on p. 52).

CASEY, C. M. et al., 2014. *The Astrophysical Journal*. Vol. 796, p. 95. ISSN 0004-637X. Available from DOI: 10.1088/0004-637X/796/2/95 (cit. on pp. 58, 64).

CASEY, Caitlin M., 2012. *Monthly Notices of the Royal Astronomical Society*. Vol. 425, pp. 3094–3103. ISSN 0035-8711. Available from DOI: 10.1111/j.1365-2966.2012.21455.x (cit. on pp. 41, 96, 108).

CASTELLANO, M. et al., 2014. *Astronomy & Astrophysics, Volume 566, id.A19, <NUMPAGES>17</NUMPAGES> pp.* Vol. 566, A19. ISSN 0004-6361. Available from DOI: 10.1051/0004-6361/201322704 (cit. on p. 105).

CHABRIER, Gilles, 2003. *Publications of the Astronomical Society of the Pacific*. Vol. 115, no. 809, pp. 763–795. ISSN 0004-6280, ISSN 1538-3873. Available from DOI: 10.1086/376392 (cit. on pp. 36, 43, 65, 95, 102, 115).

CHARLOT, Stéphane & FALL, S. Michael, 2000. *The Astrophysical Journal*. Vol. 539, pp. 718–731. ISSN 0004-637X. Available from DOI: 10.1086/309250 (cit. on p. 37).

CHEVALLARD, Jacopo & CHARLOT, Stéphane, 2016. *Monthly Notices of the Royal Astronomical Society*. Vol. 462, no. 2, pp. 1415–1443. ISSN 0035-8711, ISSN 1365-2966. Available from DOI: 10.1093/mnras/stw1756. arXiv: 1603.03037 (cit. on p. 91).

CIARDI, Benedetta & FERRARA, Andrea, 2005. *Space Science Reviews*. Vol. 116, pp. 625–705. ISSN 0038-6308. Available from DOI: 10.1007/s11214-005-3592-0 (cit. on p. 29).

CIESLA, L. et al., 2014. *Astronomy and Astrophysics*. Vol. 565, A128. ISSN 0004-6361. Available from DOI: 10.1051/0004-6361/201323248 (cit. on pp. 43, 74, 97).

CIOLEK, G. E., 1995. In: vol. 80, p. 174. Available also from: http://adsabs.harvard.edu/abs/1995ASPC...80..174C (cit. on p. 60).

COMPIÈGNE, M. et al., 2011. *Astronomy and Astrophysics*. Vol. 525, A103. ISSN 0004-6361. Available from DOI: 10.1051/0004-6361/201015292 (cit. on p. 82).

CONROY, Charlie, 2013. *Annual Review of Astronomy and Astrophysics*. Vol. 51, pp. 393–455. ISSN 0066-4146. Available from DOI: 10.1146/annurev-astro-082812-141017 (cit. on pp. 31–33).

COOK, David O. et al., 2014. *Monthly Notices of the Royal Astronomical Society*. Vol. 445, pp. 899–912. ISSN 0035-8711. Available from DOI: 10.1093/mnras/stu1787 (cit. on pp. 43, 44, 74).

CORMIER, D. et al., 2017. *Monthly Notices of the Royal Astronomical Society*. Vol. 468, pp. L87–L91. ISSN 0035-8711. Available from DOI: 10.1093/mnrasl/slx034 (cit. on p. 88).

CÔTÉ, Benoit et al., 2017. *The Astrophysical Journal*. Vol. 835, p. 128. ISSN 0004-637X. Available from DOI: 10.3847/1538-4357/835/2/128 (cit. on p. 114).

COUSIN, M. et al., 2019a. *Astronomy and Astrophysics*. Vol. 627, A131. ISSN 0004-6361. Available from DOI: 10.1051/0004-6361/201834673 (cit. on pp. 82, 83).

COUSIN, M. et al., 2019b. *Astronomy and Astrophysics*. Vol. 627, A132. Available from DOI: 10.1051/0004-6361/201834674 (cit. on pp. 82, 84).

CRISTALLO, S. et al., 2011. *The Astrophysical Journal Supplement Series*. Vol. 197, p. 17. ISSN 0067-0049. Available from DOI: 10.1088/0067-0049/197/2/17 (cit. on p. 112).

CRISTALLO, S. et al., 2015. *The Astrophysical Journal Supplement Series*. Vol. 219, p. 40. ISSN 0067-0049. Available from DOI: 10.1088/0067-0049/219/2/40 (cit. on pp. 112, 116).

CUCCIATI, O. et al., 2012. *Astronomy and Astrophysics*. Vol. 539, A31. ISSN 0004-6361. Available from DOI: 10.1051/0004-6361/201118010 (cit. on pp. 47, 48, 53, 54, 71, 72, 75, 81, 92, 120).

DADDI, E. et al., 2007. *The Astrophysical Journal*. Vol. 670, pp. 156–172. ISSN 0004-637X. Available from DOI: 10.1086/521818 (cit. on p. 55).

DAHLEN, Tomas et al., 2007. *The Astrophysical Journal*. Vol. 654, pp. 172–185. ISSN 0004-637X. Available from DOI: 10.1086/508854 (cit. on p. 54).

DALE, Daniel A. & HELOU, George, 2002. *The Astrophysical Journal*. Vol. 576, pp. 159–168. ISSN 0004-637X. Available from DOI: 10.1086/341632 (cit. on p. 39).

DALE, Daniel A. et al., 2001. *The Astrophysical Journal*. Vol. 549, pp. 215–227. ISSN 0004-637X. Available from DOI: 10.1086/319077 (cit. on p. 39).

DALE, Daniel A. et al., 2014. *The Astrophysical Journal*. Vol. 784, p. 83. ISSN 0004-637X. Available from DOI: 10.1088/0004-637X/784/1/83 (cit. on pp. 39, 108).

DAVIDZON, I. et al., 2017. *Astronomy and Astrophysics*. Vol. 605, A70. ISSN 0004-6361. Available from DOI: 10.1051/0004-6361/201730419 (cit. on pp. 51, 52).

DECLEIR, Marjorie et al., 2019. *Monthly Notices of the Royal Astronomical Society*. Vol. 486, pp. 743–767. ISSN 0035-8711. Available from DOI: 10.1093/mnras/stz805 (cit. on p. 37).

DESERT, F.-X. et al., 1990. *Astronomy and Astrophysics*. Vol. 237, pp. 215–236. ISSN 0004-6361. Available also from: http://adsabs.harvard.edu/abs/1990A%5C%26A...237..215D (cit. on p. 39).

DIJKSTRA, Mark et al., 2004. *The Astrophysical Journal*. Vol. 613, pp. 646–654. ISSN 0004-637X. Available from DOI: 10.1086/422167 (cit. on p. 31).

DONEVSKI, D. et al., 2020. *Astronomy and Astrophysics*. Vol. 644, A144. ISSN 0004-6361. Available from DOI: 10.1051/0004-6361/202038405 (cit. on p. 55).

DRAINE, B. T. & LI, Aigen, 2007. *The Astrophysical Journal*. Vol. 657, pp. 810–837. ISSN 0004-637X. Available from DOI: 10.1086/511055 (cit. on pp. 39–41).

DRAINE, B. T. et al., 2014. *The Astrophysical Journal*. Vol. 780, p. 172. ISSN 0004-637X. Available from DOI: 10.1088/0004-637X/780/2/172 (cit. on pp. 41, 103).

DUNCAN, K. et al., 2014. *Monthly Notices of the Royal Astronomical Society*. Vol. 444, pp. 2960–2984. ISSN 0035-8711. Available from DOI: 10.1093/mnras/stu1622 (cit. on p. 52).

DWEK, Eli, 1998. *The Astrophysical Journal*. Vol. 501, p. 643. ISSN 0004-637X. Available from DOI: 10.1086/305829 (cit. on p. 111).

ELBAZ, D. et al., 2007. *Astronomy and Astrophysics*. Vol. 468, pp. 33–48. ISSN 0004-6361. Available from DOI: 10.1051/0004-6361:20077525 (cit. on p. 55).

ELBAZ, D. et al., 2018. *Astronomy and Astrophysics*. Vol. 616, A110. ISSN 0004-6361. Available from DOI: 10.1051/0004-6361/201732370 (cit. on p. 55).

EMAMI, N. et al., 2020. Vol. 235, p. 155.03. Available also from: http://adsabs.harvard.edu/abs/2020AAS...23515503E. Conference Name: American Astronomical Society Meeting Abstracts #235 (cit. on p. 86).

FAISST, A. L. et al., 2020. *The Astrophysical Journal Supplement Series*. Vol. 247, no. 2, p. 61. ISSN 1538-4365. Available from DOI: 10.3847/1538-4365/ab7ccd (cit. on pp. 99–102).

FAISST, Andreas L. et al., 2017. *The Astrophysical Journal*. Vol. 847, p. 21. ISSN 0004-637X. Available from DOI: 10.3847/1538-4357/aa886c (cit. on pp. 95, 101).

FERLAND, G. J. et al., 1998. *Publications of the Astronomical Society of the Pacific*. Vol. 110, pp. 761–778. ISSN 0004-6280. Available from DOI: 10.1086/316190 (cit. on p. 41).

FERLAND, G. J. et al., 2013. *Revista Mexicana de Astronomia y Astrofisica*. Vol. 49, pp. 137–163. ISSN 0185-1101. Available also from: http://adsabs.harvard.edu/abs/2013RMxAA..49..137F (cit. on p. 41).

FINKELSTEIN, Steven L. et al., 2012. *The Astrophysical Journal*. Vol. 756, p. 164. ISSN 0004-637X. Available from DOI: 10.1088/0004-637X/756/2/164 (cit. on p. 53).

FINKELSTEIN, Steven L. et al., 2015. *The Astrophysical Journal*. Vol. 814, no. 2, p. 95. ISSN 1538-4357. Available from DOI: 10.1088/0004-637X/814/2/95 (cit. on pp. 44, 49).

FUDAMOTO, Y. et al., 2017. *Monthly Notices of the Royal Astronomical Society*. Vol. 472, no. 1, pp. 483–490. ISSN 0035-8711. Available from DOI: 10.1093/mnras/stx1948 (cit. on pp. 65, 67, 88).

FUDAMOTO, Yoshinobu et al., 2020a. *Monthly Notices of the Royal Astronomical Society*. Vol. 491, pp. 4724–4734. ISSN 0035-8711. Available from DOI: 10.1093/mnras/stz3248 (cit. on p. 67).

FUDAMOTO, Yoshinobu et al., 2020b. *arXiv e-prints*. Vol. 2004, arXiv:2004.10760. Available also from: http://adsabs.harvard.edu/abs/2020arXiv200410760F (cit. on pp. 65, 67, 88).

GARN, Timothy & BEST, Philip N., 2010. *Monthly Notices of the Royal Astronomical Society*. Vol. 409, no. 1, p. 421. Available from DOI: 10.1111/j.1365-2966.2010.17321.x (cit. on pp. 81, 85).

GEROLA, H. et al., 1980. *The Astrophysical Journal*. Vol. 242, pp. 517–527. ISSN 0004-637X. Available from DOI: 10.1086/158485 (cit. on p. 86).

GIACCONI, R. et al., 2002. *VizieR Online Data Catalog*, J/ApJS/139/369 (cit. on p. 100).

GONZALEZ, Valentino et al., 2011. *The Astrophysical Journal Letters*. Vol. 735, p. L34. ISSN 0004-637X. Available from DOI: 10.1088/2041-8205/735/2/L34 (cit. on pp. 52, 86).

GRAZIAN, A. et al., 2015. *Astronomy and Astrophysics*. Vol. 575, A96. Available from DOI: 10.1051/0004-6361/201424750 (cit. on pp. 49, 52, 89).

GROGIN, Norman A. et al., 2011. *The Astrophysical Journal Supplement Series*. Vol. 197, no. 2, p. 35. ISSN 0067-0049, ISSN 1538-4365. Available from DOI: 10.1088/0067-0049/197/2/35. arXiv: 1105.3753 (cit. on p. 53).

GRUPPIONI, C. et al., 2013. *Monthly Notices of the Royal Astronomical Society*. Vol. 432, pp. 23–52. ISSN 0035-8711. Available from DOI: 10.1093/mnras/stt308 (cit. on pp. 54, 71).

HAN, Yunkun & HAN, Zhanwen, 2014. *The Astrophysical Journal Supplement Series*. Vol. 215, p. 2. ISSN 0067-0049. Available from DOI: 10.1088/0067-0049/215/1/2 (cit. on p. 42).

HAO, Cai-Na et al., 2011. *The Astrophysical Journal*. Vol. 741, no. 2, p. 124. ISSN 0004-637X. Available from DOI: 10.1088/0004-637X/741/2/124 (cit. on pp. 44, 84, 87).

HARIKANE, Yuichi et al., 2018. *APJ*. Vol. 859, no. 2, p. 84. Available from DOI: 10.3847/1538-4357/aabd80 (cit. on p. 101).

HASHIMOTO, Takuya et al., 2018. *Nature*. Vol. 557, pp. 392–395. ISSN 0028-0836. Available from DOI: 10.1038/s41586-018-0117-z (cit. on p. 95).

HASINGER, G. et al., 2018. *The Astrophysical Journal*. Vol. 858, p. 77. ISSN 0004-637X. Available from DOI: 10.3847/1538-4357/aabacf (cit. on p. 100).

HEGER, Alexander & WOOSLEY, S. E., 2010. *The Astrophysical Journal*. Vol. 724, pp. 341–373. ISSN 0004-637X. Available from DOI: 10.1088/0004-637X/724/1/341 (cit. on p. 116).

HEINIS, S. et al., 2013. *Monthly Notices of the Royal Astronomical Society*. Vol. 429, pp. 1113–1132. ISSN 0035-8711. Available from DOI: 10.1093/mnras/sts397 (cit. on p. 58).

HEINIS, S. et al., 2014. *Monthly Notices of the Royal Astronomical Society*. Vol. 437, no. 2, p. 1268. Available from DOI: 10.1093/mnras/stt1960 (cit. on pp. 65, 67, 81).

HILDEBRAND, Roger H. & DRAGOVAN, Mark, 1995. *The Astrophysical Journal*. Vol. 450, p. 663. ISSN 0004-637X. Available from DOI: 10.1086/176173 (cit. on p. 59).

HUBBLE, E. P., 1929. *The Astrophysical Journal*. Vol. 69. ISSN 0004-637X. Available from DOI: 10.1086/143167 (cit. on p. 24).

HUNT, Leslie K. et al., 2003. *The Astrophysical Journal*. Vol. 588, pp. 281–298. ISSN 0004-637X. Available from DOI: 10.1086/368352 (cit. on p. 88).

ILBERT, O. et al., 2009. *The Astrophysical Journal*. Vol. 690, no. 2, p. 1236. ISSN 0004-637X. Available from DOI: 10.1088/0004-637X/690/2/1236 (cit. on p. 47).

ILBERT, O. et al., 2013. *Astronomy & Astrophysics*. Vol. 556, A55. ISSN 0004-6361, ISSN 1432-0746. Available from DOI: 10.1051/0004-6361/201321100 (cit. on pp. 47, 49–52).

INOUE, Akio K., 2011. *Monthly Notices of the Royal Astronomical Society*. Vol. 415, pp. 2920–2931. ISSN 0035-8711. Available from DOI: 10.1111/j.1365-2966.2011.18906.x (cit. on p. 41).

IWAMOTO, Koichi et al., 1999. *The Astrophysical Journal Supplement Series*. Vol. 125, pp. 439–462. ISSN 0067-0049. Available from DOI: 10.1086/313278 (cit. on p. 116).

JAACKS, Jason et al., 2018. *Monthly Notices of the Royal Astronomical Society*. Vol. 475, no. 4, pp. 4396–4410. ISSN 0035-8711. Available from DOI: 10.1093/mnras/sty062 (cit. on p. 85).

JONES, A. P. et al., 2017. *Astronomy and Astrophysics*. Vol. 602, A46. ISSN 0004-6361. Available from DOI: 10.1051/0004-6361/201630225 (cit. on pp. 24, 41).

JONES, G. C. et al., 2020. *mnras*. Vol. 498, no. 3, pp. 4109–4118. Available from DOI: 10.1093/mnras/staa2689 (cit. on p. 105).

KENNICUTT Jr., Robert C., 1998. *Annual Review of Astronomy and Astrophysics*. Vol. 36, pp. 189–232. ISSN 0066-4146. Available from DOI: 10.1146/annurev.astro.36.1.189 (cit. on pp. 43, 54).

KHUSANOVA, Y. et al., 2020. *arXiv e-prints*. Vol. 2007, arXiv:2007.08384. Available also from: http://adsabs.harvard.edu/abs/2020arXiv200708384K (cit. on p. 55).

KLESSEN, Ralf S., 2019. *arXiv:1807.06248*, pp. 67–97. Available from DOI: 10.1142/9789813227958_0004. arXiv: 1807.06248 (cit. on p. 28).

KOBAYASHI, Chiaki et al., 2006. *The Astrophysical Journal*. Vol. 653, pp. 1145–1171. ISSN 0004-637X. Available from DOI: 10.1086/508914 (cit. on p. 115).

KOEKEMOER, Anton M. et al., 2011. *The Astrophysical Journal Supplement Series*. Vol. 197, no. 2, p. 36. ISSN 0067-0049, ISSN 1538-4365. Available from DOI: 10.1088/0067-0049/197/2/36. arXiv: 1105.3754 (cit. on p. 53).

KOPROWSKI, M. P. et al., 2018. *Monthly Notices of the Royal Astronomical Society*. Vol. 479, pp. 4355–4366. ISSN 0035-8711. Available from DOI: 10.1093/mnras/sty1527 (cit. on p. 67).

KOUVELIOTOU, Chryssa et al., 2014 (cit. on p. 24).

KOYAMA, Yusei et al., 2015. *Monthly Notices of the Royal Astronomical Society*. Vol. 453, no. 1, pp. 879–892. ISSN 0035-8711. Available from DOI: 10.1093/mnras/stv1599 (cit. on p. 85).

KROUPA, Pavel, 2001. *Monthly Notices of the Royal Astronomical Society*. Vol. 322, pp. 231–246. ISSN 0035-8711. Available from DOI: 10.1046/j.1365-8711.2001.04022.x (cit. on p. 36).

LAIGLE, C. et al., 2016. *The Astrophysical Journal Supplement Series*. Vol. 224, p. 24. ISSN 0067-0049. Available from DOI: 10.3847/0067-0049/224/2/24 (cit. on pp. 100, 101).

LARSON, R. B. & TINSLEY, B. M., 1978. *The Astrophysical Journal*. Vol. 219, pp. 46–59. ISSN 0004-637X. Available from DOI: 10.1086/155753 (cit. on p. 32).

LARSON, Richard B., 1998. *Monthly Notices of the Royal Astronomical Society*. Vol. 301, pp. 569–581. ISSN 0035-8711. Available from DOI: 10.1046/j.1365-8711.1998.02045.x (cit. on pp. 36, 37).

LE FÈVRE, O. et al., 2015. *Astronomy and Astrophysics*. Vol. 576, A79. ISSN 0004-6361. Available from DOI: 10.1051/0004-6361/201423829 (cit. on p. 100).

LE FÈVRE, O. et al., 2020. *AAP*. Vol. 643, A1. Available from DOI: 10.1051/0004-6361/201936965 (cit. on p. 99).

LEBOUTEILLER, Vianney, 2019. Vol. 344, pp. 259–262. Available from DOI: 10.1017/S1743921318005239 (cit. on p. 88).

LEITHERER, C., 1999. Vol. 186, p. 243. Available also from: http://adsabs.harvard.edu/abs/1999IAUS..186..243L. Conference Name: Galaxy Interactions at Low and High Redshift (cit. on pp. 35, 56).

LEITHERER, Claus et al., 2002. *The Astrophysical Journal Supplement Series*. Vol. 140, pp. 303–329. ISSN 0067-0049. Available from DOI: 10.1086/342486 (cit. on p. 38).

LI, Aigen et al., 2014. In: vol. 40. Available also from: http://adsabs.harvard.edu/abs/2014cosp...40E1806L (cit. on p. 59).

LISENFELD, U. & FERRARA, A., 1998. *The Astrophysical Journal*. Vol. 496, pp. 145–154. ISSN 0004-637X. Available from DOI: 10.1086/305354 (cit. on pp. 111, 113).

LO FARO, B. et al., 2017. *Monthly Notices of the Royal Astronomical Society*. Vol. 472, pp. 1372–1391. ISSN 0035-8711. Available from DOI: 10.1093/mnras/stx1901 (cit. on p. 37).

LOEB, Abraham, 2010. *How Did the First Stars and Galaxies Form? By Abraham Loeb. Princeton University Press, 2010. ISBN: 978-1-4008-3406-8*. Available also from: http://adsabs.harvard.edu/abs/2010hdfs.book.....L (cit. on pp. 28, 30).

LOEB, Abraham & FURLANETTO, Steven R., 2013. *The First Galaxies in the Universe, by Abraham Loeb and Steven R. Furlanetto. ISBN: 9780691144917. Princeton, NJ: Princeton University Press*. Available also from: http://adsabs.harvard.edu/abs/2013fgu..book.....L (cit. on p. 30).

LONGHETTI, M. & SARACCO, P., 2009. *Monthly Notices of the Royal Astronomical Society*. Vol. 394, no. 2, pp. 774–794. ISSN 0035-8711. Available from DOI: 10.1111/j.1365-2966.2008.14375.x (cit. on p. 43).

MA, Xiangcheng et al., 2019. *Monthly Notices of the Royal Astronomical Society*. Vol. 487, pp. 1844–1864. ISSN 0035-8711. Available from DOI: 10.1093/mnras/stz1324 (cit. on pp. 84, 85, 106).

MADAU, Piero & DICKINSON, Mark, 2014. *Annual Review of Astronomy and Astrophysics*. Vol. 52, p. 415. Available from DOI: 10.1146/annurev-astro-081811-125615 (cit. on pp. 51–54, 70, 73, 76, 81, 88, 92, 120).

MADAU, Piero et al., 1996. *Monthly Notices of the Royal Astronomical Society*. Vol. 283, pp. 1388–1404. ISSN 0035-8711. Available from DOI: 10.1093/mnras/283.4.1388 (cit. on p. 53).

MADAU, Piero et al., 1998. *The Astrophysical Journal*. Vol. 498, pp. 106–116. ISSN 0004-637X. Available from DOI: 10.1086/305523 (cit. on p. 53).

MAGNELLI, B. et al., 2011. *Astronomy and Astrophysics*. Vol. 528, A35. ISSN 0004-6361. Available from DOI: 10.1051/0004-6361/200913941 (cit. on p. 54).

MAGNELLI, B. et al., 2013. *Astronomy and Astrophysics*. Vol. 553, A132. ISSN 0004-6361. Available from DOI: 10.1051/0004-6361/201321371 (cit. on p. 54).

MAŁEK, K. et al., 2018. *Astronomy and Astrophysics*. Vol. 620, A50. Available from DOI: 10.1051/0004-6361/201833131 (cit. on pp. 44, 64, 92).

MALHOTRA, S. et al., 2005. *The Astrophysical Journal*. Vol. 626, pp. 666–679. ISSN 0004-637X. Available from DOI: 10.1086/430047 (cit. on p. 100).

MALLERY, Ryan P. et al., 2012. *The Astrophysical Journal*. Vol. 760, p. 128. ISSN 0004-637X. Available from DOI: 10.1088/0004-637X/760/2/128 (cit. on p. 100).

MAO, Ye-Wei et al., 2014. *The Astrophysical Journal*. Vol. 789, p. 76. ISSN 0004-637X. Available from DOI: 10.1088/0004-637X/789/1/76 (cit. on p. 56).

MARASTON, Claudia, 2005. *Monthly Notices of the Royal Astronomical Society*. Vol. 362, pp. 799–825. ISSN 0035-8711. Available from DOI: 10.1111/j.1365-2966.2005.09270.x (cit. on p. 35).

MARINACCI, Federico et al., 2018. *Monthly Notices of the Royal Astronomical Society*. Vol. 480, no. 4, pp. 5113–5139. ISSN 0035-8711. Available from DOI: 10.1093/mnras/sty2206 (cit. on p. 106).

MARTIN, D. Christopher et al., 2007. *The Astrophysical Journal Supplement Series*. Vol. 173, pp. 415–431. ISSN 0067-0049. Available from DOI: 10.1086/522088 (cit. on p. 67).

MATHIS, J. S. et al., 1977. *The Astrophysical Journal*. Vol. 217, pp. 425–433. ISSN 0004-637X. Available from DOI: 10.1086/155591 (cit. on p. 59).

MATTEUCCI, Francesca, 2012. 1st ed. Springer-Verlag Berlin Heidelberg. Astronomy and Astrophysics Library. ISBN 978-3-642-22490-4 (cit. on p. 110).

MATTEUCCI, Francesca, 2016. Vol. 703, p. 012004. Available from DOI: 10.1088/1742-6596/703/1/012004. Conference Name: Journal of Physics Conference Series Place: eprint: arXiv:1602.01004 (cit. on p. 110).

MCLURE, R. J. et al., 2018. *Monthly Notices of the Royal Astronomical Society*. Vol. 476, no. 3, p. 3991. Available from DOI: 10.1093/mnras/sty522 (cit. on pp. 6, 67, 107).

MCQUINN, Kristen B. W. et al., 2010. *The Astrophysical Journal*. Vol. 724, pp. 49–58. ISSN 0004-637X. Available from DOI: 10.1088/0004-637X/724/1/49 (cit. on p. 86).

MEIKSIN, Avery, 2006. *Monthly Notices of the Royal Astronomical Society*. Vol. 365, pp. 807–812. ISSN 0035-8711. Available from DOI: 10.1111/j.1365-2966.2005.09756.x (cit. on p. 41).

MEURER, G. R. et al., 1995. *The Astronomical Journal*. Vol. 110, p. 2665. ISSN 0004-6256. Available from DOI: 10.1086/117721 (cit. on p. 56).

MEURER, Gerhardt R. et al., 1999. *The Astrophysical Journal*. Vol. 521, no. 1, p. 64. Available from DOI: 10.1086/307523 (cit. on pp. 44, 45, 53, 56, 58, 64, 72, 106).

MICHAŁOWSKI, Michał J., 2015. *Astronomy and Astrophysics*. Vol. 577, A80. Available from DOI: 10.1051/0004-6361/201525644 (cit. on p. 118).

MORTLOCK, Alice et al., 2015. *Monthly Notices of the Royal Astronomical Society*. Vol. 447, no. 1, p. 2. Available from DOI: 10.1093/mnras/stu2403 (cit. on pp. 49, 52, 89).

MORTLOCK, Daniel J. et al., 2011. *Nature*. Vol. 474, pp. 616–619. ISSN 0028-0836. Available from DOI: 10.1038/nature10159 (cit. on pp. 31, 52).

MOUSTAKAS, John et al., 2013. *The Astrophysical Journal*. Vol. 767, p. 50. ISSN 0004-637X. Available from DOI: 10.1088/0004-637X/767/1/50 (cit. on p. 50).

MURPHY, E. J. et al., 2011. *APJ*. Vol. 737, no. 2, p. 67. Available from DOI: 10.1088/0004-637X/737/2/67 (cit. on p. 87).

MUZZIN, Adam et al., 2013. *The Astrophysical Journal*. Vol. 777, p. 18. ISSN 0004-637X. Available from DOI: 10.1088/0004-637X/777/1/18 (cit. on p. 52).

NAIMAN, Jill P. et al., 2018. *Monthly Notices of the Royal Astronomical Society, Volume 477, Issue 1, p.1206-1224*. Vol. 477, no. 1, p. 1206. ISSN 0035-8711. Available from DOI: 10.1093/mnras/sty618 (cit. on p. 106).

NANNI, A. et al., 2020. *Astronomy and Astrophysics*. Vol. 641, A168. ISSN 0004-6361. Available from DOI: 10.1051/0004-6361/202037833 (cit. on pp. 8, 25, 36, 95, 97, 102, 105, 107, 109, 110, 114–118, 121).

NATIONAL ACADEMIES OF SCIENCES Engineering, and Medicine, 2011. The National Academies Press. Available from DOI: 10.17226/12951 (cit. on p. 23).

NELSON, Dylan et al., 2018. *Monthly Notices of the Royal Astronomical Society*. Vol. 475, no. 1, pp. 624–647. ISSN 0035-8711. Available from DOI: 10.1093/mnras/stx3040 (cit. on p. 106).

NERSESIAN, A. et al., 2019. *Astronomy and Astrophysics*. Vol. 624, A80. ISSN 0004-6361. Available from DOI: 10.1051/0004-6361/201935118 (cit. on p. 41).

NOLL, S. et al., 2009. *Astronomy and Astrophysics*. Vol. 507, pp. 1793–1813. ISSN 0004-6361. Available from DOI: 10.1051/0004-6361/200912497 (cit. on pp. 26, 31, 95).

OPIK, E., 1922. *The Astrophysical Journal*. Vol. 55. ISSN 0004-637X. Available from DOI: 10.1086/142680 (cit. on p. 24).

OVERZIER, Roderik A. et al., 2011. *The Astrophysical Journal Letters*. Vol. 726, p. L7. ISSN 0004-637X. Available from DOI: 10.1088/2041-8205/726/1/L7 (cit. on p. 106).

PANNELLA, M. et al., 2009. *The Astrophysical Journal Letters*. Vol. 698, pp. L116–L120. ISSN 0004-637X. Available from DOI: 10.1088/0004-637X/698/2/L116 (cit. on p. 67).

PANNELLA, M. et al., 2015. *The Astrophysical Journal*. Vol. 807, no. 2, p. 141. Available from DOI: 10.1088/0004-637X/807/2/141 (cit. on pp. 65, 67).

PEARSON, W. J. et al., 2018. *Astronomy and Astrophysics*. Vol. 615, A146. ISSN 0004-6361. Available from DOI: 10.1051/0004-6361/201832821 (cit. on pp. 55, 105).

PERCIVAL, Will, 2009. In: *Introduction to statistics*. Ginowan City, Okinawa Prefecture, p. 142. Available also from: http://www.resceu.s.u-tokyo.ac.jp/workshops/resceu09s/files/Percival.pdf (cit. on p. 27).

PILLEPICH, Annalisa et al., 2018. *Monthly Notices of the Royal Astronomical Society*. Vol. 475, no. 1, pp. 648–675. ISSN 0035-8711. Available from DOI: 10.1093/mnras/stx3112 (cit. on p. 106).

PLANCK COLLABORATION, 2020. *Astronomy & Astrophysics*. Vol. 641, A6. ISSN 0004-6361, ISSN 1432-0746. Available from DOI: 10.1051/0004-6361/201833910. Publisher: EDP Sciences (cit. on pp. 27, 30).

POZZETTI, L. et al., 2010. *Astronomy and Astrophysics*. Vol. 523, A13. ISSN 0004-6361. Available from DOI: 10.1051/0004-6361/200913020 (cit. on p. 47).

PRESS, William H. & SCHECHTER, Paul, 1974. *The Astrophysical Journal*. Vol. 187, pp. 425–438. ISSN 0004-637X. Available from DOI: 10.1086/152650 (cit. on p. 28).

QIN, Jianbo et al., 2019. *Monthly Notices of the Royal Astronomical Society*. Vol. 485, no. 4, p. 5733. Available from DOI: 10.1093/mnras/stz763 (cit. on p. 85).

RAUCH, Michael, 1998. *Annual Review of Astronomy and Astrophysics*. Vol. 36, pp. 267–316. ISSN 0066-4146. Available from DOI: 10.1146/annurev.astro.36.1.267 (cit. on p. 30).

REDDY, Naveen A. & STEIDEL, Charles C., 2009. *The Astrophysical Journal*. Vol. 692, pp. 778–803. ISSN 0004-637X. Available from DOI: 10.1088/0004-637X/692/1/778 (cit. on pp. 54, 72).

REDDY, Naveen A. et al., 2012. *The Astrophysical Journal*. Vol. 754, p. 25. ISSN 0004-637X. Available from DOI: 10.1088/0004-637X/754/1/25 (cit. on pp. 52, 58).

REDDY, Naveen A. et al., 2015. *The Astrophysical Journal*. Vol. 806, p. 259. ISSN 0004-637X. Available from DOI: 10.1088/0004-637X/806/2/259 (cit. on p. 37).

REDDY, Naveen A. et al., 2018. *The Astrophysical Journal*. Vol. 853, p. 56. ISSN 0004-637X. Available from DOI: 10.3847/1538-4357/aaa3e7 (cit. on p. 67).

REINES, Amy E. et al., 2008. *The Astronomical Journal*. Vol. 136, pp. 1415–1426. ISSN 0004-6256. Available from DOI: 10.1088/0004-6256/136/4/1415 (cit. on p. 88).

RÉMY-RUYER, A. et al., 2013. *Astronomy and Astrophysics*. Vol. 557, A95. ISSN 0004-6361. Available from DOI: 10.1051/0004-6361/201321602 (cit. on p. 114).

RÉMY-RUYER, A. et al., 2014. *Astronomy and Astrophysics*. Vol. 563, A31. ISSN 0004-6361. Available from DOI: 10.1051/0004-6361/201322803 (cit. on pp. 86, 114).

RÉMY-RUYER, A. et al., 2015. *Astronomy and Astrophysics*. Vol. 582, A121. ISSN 0004-6361. Available from DOI: 10.1051/0004-6361/201526067 (cit. on pp. 88, 95, 114).

RHOADS, James E. et al., 2009. *The Astrophysical Journal*. Vol. 697, pp. 942–949. ISSN 0004-637X. Available from DOI: 10.1088/0004-637X/697/1/942 (cit. on p. 100).

RITTER, C. et al., 2018. *Monthly Notices of the Royal Astronomical Society*. Vol. 480, pp. 538–571. ISSN 0035-8711. Available from DOI: 10.1093/mnras/sty1729 (cit. on p. 114).

ROBOTHAM, A. S. G. & DRIVER, S. P., 2011. *Monthly Notices of the Royal Astronomical Society*. Vol. 413, pp. 2570–2582. ISSN 0035-8711. Available from DOI: 10.1111/j.1365-2966.2011.18327.x (cit. on p. 54).

RODIGHIERO, G. et al., 2011. *The Astrophysical Journal Letters*. Vol. 739, p. L40. ISSN 0004-637X. Available from DOI: 10.1088/2041-8205/739/2/L40 (cit. on p. 55).

RUDIE, Gwen C. et al., 2012. *The Astrophysical Journal*. Vol. 750, p. 67. ISSN 0004-637X. Available from DOI: 10.1088/0004-637X/750/1/67 (cit. on p. 31).

SALIM, Samir & BOQUIEN, Médéric, 2019. *The Astrophysical Journal*. Vol. 872, p. 23. ISSN 0004-637X. Available from DOI: 10.3847/1538-4357/aaf88a (cit. on pp. 56, 106).

SALIM, Samir & NARAYANAN, Desika, 2020. *Annual Review of Astronomy and Astrophysics*. Vol. 58, pp. 529–575. ISSN 0066-4146. Available from DOI: 10.1146/annurev-astro-032620-021933 (cit. on p. 57).

SALIM, Samir et al., 2007. *The Astrophysical Journal Supplement Series*. Vol. 173, pp. 267–292. ISSN 0067-0049. Available from DOI: 10.1086/519218 (cit. on p. 42).

SALIM, Samir et al., 2016. *The Astrophysical Journal Supplement Series*. Vol. 227, p. 2. ISSN 0067-0049. Available from DOI: 10.3847/0067-0049/227/1/2 (cit. on pp. 65, 82).

SALIM, Samir et al., 2018. *The Astrophysical Journal*. Vol. 859, p. 11. ISSN 0004-637X. Available from DOI: 10.3847/1538-4357/aabf3c (cit. on pp. 37, 65, 67, 74, 81, 82).

SALPETER, Edwin E., 1955. *The Astrophysical Journal*. Vol. 121, p. 161. ISSN 0004-637X. Available from DOI: 10.1086/145971 (cit. on pp. 36, 37, 43, 64, 65).

SANDERS, D. B., 2003. *Journal of Korean Astronomical Society*. Vol. 36, pp. 149–158. ISSN 1225-4614. Available from DOI: 10.5303/JKAS.2003.36.3.149 (cit. on p. 54).

SANTINI, P. et al., 2012. *Astronomy and Astrophysics*. Vol. 538, A33. ISSN 0004-6361. Available from DOI: 10.1051/0004-6361/201117513 (cit. on p. 52).

SCHAERER, D. et al., 2015. *Astronomy & Astrophysics*. Vol. 574, A19. ISSN 0004-6361, ISSN 1432-0746. Available from DOI: 10.1051/0004-6361/201424649 (cit. on pp. 43, 65, 67).

SCHAERER, D. et al., 2020. *Astronomy & Astrophysics*. Vol. 643 id.A3, p. 10. ISSN 0004-6361. Available from DOI: 10.1051/0004-6361/202037617 (cit. on p. 102).

SCHALÉN, C., 1931 [online]. Vol. 6, p. 376 [visited on 2021-06-18]. Available from: https://ui.adsabs.harvard.edu/abs/1931PAAS....6Q.376S. Conference Name: Publications of the American Astronomical Society (cit. on p. 24).

SCHECHTER, P., 1976. *The Astrophysical Journal*. Vol. 203, p. 297. Available from DOI: 10.1086/154079 (cit. on pp. 47, 48, 55).

SCHENKER, Matthew A. et al., 2013. *The Astrophysical Journal*. Vol. 768, p. 196. ISSN 0004-637X. Available from DOI: 10.1088/0004-637X/768/2/196 (cit. on p. 54).

SCHIMINOVICH, D. et al., 2005. *The Astrophysical Journal Letters*. Vol. 619, pp. L47–L50. ISSN 0004-637X. Available from DOI: 10.1086/427077 (cit. on p. 54).

SCHNEIDER, Peter, 2006. Available also from: https://link.springer.com/book/10.1007/978-3-642-54083-7 (cit. on pp. 45, 46).

SCHNEIDER, R. et al., 2002. *The Astrophysical Journal*. Vol. 571, pp. 30–39. ISSN 0004-637X. Available from DOI: 10.1086/339917 (cit. on p. 85).

SCHULZ, Sebastian et al., 2020. *Monthly Notices of the Royal Astronomical Society*. Vol. 497, pp. 4773–4794. ISSN 0035-8711. Available from DOI: 10.1093/mnras/staa1900 (cit. on pp. 106, 107).

SCOVILLE, N. et al., 2007. *APJs*. Vol. 172, no. 1, pp. 1–8. Available from DOI: 10.1086/516585 (cit. on p. 100).

SCOVILLE, N. et al., 2016. *The Astrophysical Journal*. Vol. 820, p. 83. ISSN 0004-637X. Available from DOI: 10.3847/0004-637X/820/2/83 (cit. on p. 95).

SEARLE, Leonard et al., 1973. *The Astrophysical Journal*. Vol. 179, pp. 427–438. ISSN 0004-637X. Available from DOI: 10.1086/151882 (cit. on p. 32).

SHIRLEY, R. et al., 2021. *arXiv e-prints*. Vol. 2105, arXiv:2105.05659. Available also from: http://adsabs.harvard.edu/abs/2021arXiv210505659S (cit. on p. 92).

SHIRLEY, Raphael et al., 2019. *Monthly Notices of the Royal Astronomical Society*. Vol. 490, pp. 634–656. ISSN 0035-8711. Available from DOI: 10.1093/mnras/stz2509 (cit. on p. 92).

SILVERMAN, J. D. et al., 2018. *The Astrophysical Journal*. Vol. 867, p. 92. ISSN 0004-637X. Available from DOI: 10.3847/1538-4357/aae25e (cit. on p. 55).

SKELTON, Rosalind E. et al., 2014. *APJs*. Vol. 214, p. 24. ISSN 0067-0049. Available from DOI: 10.1088/0067-0049/214/2/24 (cit. on p. 100).

SMITH, Robert W., 2008. *Journal for the History of Astronomy*. Vol. 39, no. 134, pp. 91–119. Available from DOI: 10.1177/002182860803900106 (cit. on p. 24).

SMITH, Robert W., 2009. *Journal for the History of Astronomy*. Vol. 40, pp. 71–107. ISSN 0021-8286. Available from DOI: 10.1177/002182860904000106 (cit. on p. 24).

SOBRAL, David et al., 2014. *Monthly Notices of the Royal Astronomical Society*. Vol. 437, pp. 3516–3528. ISSN 0035-8711. Available from DOI: 10.1093/mnras/stt2159 (cit. on p. 55).

SONG, Mimi et al., 2016. *The Astrophysical Journal*. Vol. 825, no. 1, p. 5. ISSN 0004-637X. Available from DOI: 10.3847/0004-637X/825/1/5 (cit. on pp. 49, 50, 52, 78, 89).

SPEAGLE, J. S. et al., 2014. *APJS*. Vol. 214, no. 2, p. 15. Available from DOI: 10.1088/0067-0049/214/2/15 (cit. on pp. 55, 56, 89, 100, 105).

SPRINGEL, Volker et al., 2018. *Monthly Notices of the Royal Astronomical Society*. Vol. 475, no. 1, pp. 676–698. ISSN 0035-8711. Available from DOI: 10.1093/mnras/stx3304 (cit. on p. 106).

STEIDEL, Charles C. et al., 1996. *The Astrophysical Journal Letters*. Vol. 462, p. L17. ISSN 0004-637X. Available from DOI: 10.1086/310029 (cit. on p. 45).

STEINHARDT, Charles L. et al., 2014. *The Astrophysical Journal Letters*. Vol. 791, p. L25. ISSN 0004-637X. Available from DOI: 10.1088/2041-8205/791/2/L25 (cit. on p. 101).

STINSON, G. S. et al., 2007. *The Astrophysical Journal*. Vol. 667, pp. 170–175. ISSN 0004-637X. Available from DOI: 10.1086/520504 (cit. on p. 86).

TAKEUCHI, T. T. et al., 2010. *Astronomy and Astrophysics*. Vol. 514, A4. Available from DOI: 10.1051/0004-6361/200913476 (cit. on pp. 87, 88).

TAKEUCHI, Tsutomu T. et al., 2003. *The Astrophysical Journal Letters*. Vol. 587, pp. L89–L92. ISSN 0004-637X. Available from DOI: 10.1086/375181 (cit. on p. 54).

TAKEUCHI, Tsutomu T. et al., 2005. *Monthly Notices of the Royal Astronomical Society*. Vol. 362, no. 2, p. 592. Available from DOI: 10.1111/j.1365-2966.2005.09337.x (cit. on p. 71).

TAKEUCHI, Tsutomu T. et al., 2012. *The Astrophysical Journal*. Vol. 755, p. 144. ISSN 0004-637X. Available from DOI: 10.1088/0004-637X/755/2/144 (cit. on pp. 56, 58).

TASCA, L. A. M. et al., 2015. *Astronomy and Astrophysics*. Vol. 581, A54. ISSN 0004-6361. Available from DOI: 10.1051/0004-6361/201425379 (cit. on p. 55).

TASCA, L. A. M. et al., 2017. *Astronomy and Astrophysics*. Vol. 600, A110. ISSN 0004-6361. Available from DOI: 10.1051/0004-6361/201527963 (cit. on p. 100).

TAYLOR, A. D. et al., 1996. *Nature*. Vol. 380, pp. 323–325. ISSN 0028-0836. Available from DOI: 10.1038/380323a0 (cit. on p. 59).

THEIOS, Rachel L. et al., 2019. *The Astrophysical Journal*. Vol. 871, p. 128. ISSN 0004-637X. Available from DOI: 10.3847/1538-4357/aaf386 (cit. on p. 67).

THOMAS, Rajat M. & ZAROUBI, Saleem, 2008. *Monthly Notices of the Royal Astronomical Society*. Vol. 384, pp. 1080–1096. ISSN 0035-8711. Available from DOI: 10.1111/j.1365-2966.2007.12767.x (cit. on p. 29).

TIELENS, A. G. G. M., 2010. 1 edition. Cambridge, UK; New York: Cambridge University Press. ISBN 978-0-521-53372-0 (cit. on p. 60).

TINSLEY, B. M., 1980. *Fundamentals of Cosmic Physics*. Vol. 5, pp. 287–388. Available also from: http://adsabs.harvard.edu/abs/1980FCPh....5..287T (cit. on pp. 111, 112).

TO, Chun-Hao et al., 2014. *The Astrophysical Journal*. Vol. 792, p. 139. ISSN 0004-637X. Available from DOI: 10.1088/0004-637X/792/2/139 (cit. on p. 58).

TOMCZAK, Adam R. et al., 2014. *The Astrophysical Journal*. Vol. 783, no. 2, p. 85. Available from DOI: 10.1088/0004-637X/783/2/85 (cit. on pp. 49, 52, 89).

TOMCZAK, Adam R. et al., 2016. *The Astrophysical Journal*. Vol. 817, p. 118. ISSN 0004-637X. Available from DOI: 10.3847/0004-637X/817/2/118 (cit. on p. 55).

TRUMPLER, Robert J., 1930. *Publications of the Astronomical Society of the Pacific* [online]. Vol. 42, p. 214 [visited on 2021-06-18]. ISSN 0004-6280. Available from DOI: 10.1086/124039 (cit. on p. 24).

VANZELLA, E. et al., 2007. *VizieR Online Data Catalog*. Vol. 347. Available also from: http://adsabs.harvard.edu/abs/2007yCat..34780083V (cit. on p. 100).

VANZELLA, E. et al., 2008. *Astronomy and Astrophysics*. Vol. 478, pp. 83–92. ISSN 0004-6361. Available from DOI: 10.1051/0004-6361:20078332 (cit. on p. 100).

VAZDEKIS, A. et al., 2010. *Monthly Notices of the Royal Astronomical Society*. Vol. 404, pp. 1639–1671. ISSN 0035-8711. Available from DOI: 10.1111/j.1365-2966.2010.16407.x (cit. on p. 35).

WALCHER, Jakob et al., 2011. *Astrophysics and Space Science*. Vol. 331, pp. 1–52. ISSN 0004-640X. Available from DOI: 10.1007/s10509-010-0458-z (cit. on p. 31).

WEINGARTNER, Joseph C. & DRAINE, B. T., 2001. *The Astrophysical Journal*. Vol. 548, pp. 296–309. ISSN 0004-637X. Available from DOI: 10.1086/318651 (cit. on p. 59).

WEISZ, Daniel R. et al., 2011. *The Astrophysical Journal*. Vol. 739, p. 5. ISSN 0004-637X. Available from DOI: 10.1088/0004-637X/739/1/5 (cit. on p. 86).

WHITAKER, Katherine E. et al., 2012. *The Astrophysical Journal Letters*. Vol. 754, p. L29. ISSN 0004-637X. Available from DOI: 10.1088/2041-8205/754/2/L29 (cit. on p. 55).

WHITAKER, Katherine E. et al., 2014. *The Astrophysical Journal*. Vol. 795, no. 2, p. 104. Available from DOI: 10.1088/0004-637X/795/2/104 (cit. on pp. 67, 87).

WHITAKER, Katherine E. et al., 2017. *The Astrophysical Journal*. Vol. 850, no. 2, p. 208. ISSN 0004-637X. Available from DOI: 10.3847/1538-4357/aa94ce (cit. on pp. 74, 81, 86, 87).

WIKLIND, Tommy et al. (eds.), 2013. Berlin Heidelberg: Springer-Verlag. Astrophysics and Space Science Library. ISBN 978-3-642-32361-4. Available from DOI: 10.1007/978-3-642-32362-1 (cit. on pp. 29, 31).

WILD, Vivienne et al., 2011. *Monthly Notices of the Royal Astronomical Society*. Vol. 417, pp. 1760–1786. ISSN 0035-8711. Available from DOI: 10.1111/j.1365-2966.2011.19367.x (cit. on p. 37).

WILLIAMS, Christina C. et al., 2018. *The Astrophysical Journal Supplement Series*. Vol. 236, p. 33. ISSN 0067-0049. Available from DOI: 10.3847/1538-4365/aabcbb (cit. on p. 91).

WILLOTT, Chris J. et al., 2015. *The Astrophysical Journal*. Vol. 807, p. 180. ISSN 0004-637X. Available from DOI: 10.1088/0004-637X/807/2/180 (cit. on p. 95).

WRIGHT, A. H. et al., 2018. *Monthly Notices of the Royal Astronomical Society*. Vol. 480, no. 3, p. 3491. Available from DOI: 10.1093/mnras/sty2136 (cit. on pp. 49, 51, 89).

WU, Yanling et al., 2007. *The Astrophysical Journal*. Vol. 662, pp. 952–958. ISSN 0004-637X. Available from DOI: 10.1086/517988 (cit. on p. 88).

WYDER, Ted K. et al., 2005. *The Astrophysical Journal Letters*. Vol. 619, pp. L15–L18. ISSN 0004-637X. Available from DOI: 10.1086/424735 (cit. on pp. 54, 71).

XIAO, Ting et al., 2012. *Monthly Notices of the Royal Astronomical Society*. Vol. 421, pp. 486–501. ISSN 0035-8711. Available from DOI: 10.1111/j.1365-2966.2011.20327.x (cit. on p. 85).

XU, C. Kevin et al., 2007. *The Astrophysical Journal Supplement Series*. Vol. 173, pp. 432–440. ISSN 0067-0049. Available from DOI: 10.1086/516641 (cit. on p. 67).

YUAN, Fang-Ting et al., 2019. *Astronomy and Astrophysics*. Vol. 631, A123. ISSN 0004-6361. Available from DOI: 10.1051/0004-6361/201935975 (cit. on p. 105).

ZAROUBI, Saleem, 2013. *arXiv:1206.0267 [astro-ph]*. Vol. 396, pp. 45–101. Available from DOI: 10.1007/978-3-642-32362-1_2. arXiv: 1206.0267 (cit. on p. 31).

ZHUKOVSKA, Svitlana & HENNING, Thomas, 2014. *arXiv:1407.8489 [astro-ph]*. Available also from: http://arxiv.org/abs/1407.8489 (cit. on pp. 61, 62).

ZICK, Tom Oriyan, 2020. Available also from: https://escholarship.org/uc/item/8vb5m5p4#page=62. PhD thesis. UC Berkeley (cit. on p. 86).

APPENDIX

Monthly Notices of the ROYAL ASTRONOMICAL SOCIETY

MNRAS **496,** 5341–5349 (2020) doi:10.1093/mnras/staa1928
Advance Access publication 2020 July 8

UV dust attenuation as a function of stellar mass and its evolution with redshift

Jana Bogdanoska ★ and Denis Burgarella★

Aix-Marseille Université, CNRS, LAM (Laboratoire d'Astrophysique de Marseille) UMR 7326, F-13388 Marseille, France

Accepted 2020 June 30. Received 2020 June 30; in original form 2020 February 10

ABSTRACT

Studying the ultraviolet dust attenuation, as well as its relation to other galaxy parameters such as the stellar mass, plays an important role in multiwavelength research. This work relates the dust attenuation to the stellar mass of star-forming galaxies, and its evolution with redshift. A sample of galaxies with an estimate of the dust attenuation computed from the infrared excess was used. The dust attenuation versus stellar mass data, separated in redshift bins, was modelled by a single parameter linear function, assuming a non-zero constant apparent dust attenuation for low-mass galaxies. But the origin of this effect is still to be determined and several possibilities are explored (actual high dust content, variation of the dust-to-metal ratio, variation of the stars–dust geometry). The best-fitting parameter of this model is then used to study the redshift evolution of the cosmic dust attenuation and is found to be in agreement with results from the literature. This work also gives evidence to a redshift evolution of the dust attenuation–stellar mass relationship, as is suggested by recent works in the highest redshift range.

Key words: dust, extinction – galaxies: ISM – infrared: galaxies – submillimetre: galaxies – ultraviolet: galaxies.

1 INTRODUCTION

Galaxies are complex systems containing stars, gas, dust, and dark matter, with all of their components interacting with each other to produce a combined multiwavelength emission: the spectral energy distribution (SED). The SED is the result of the combined emission from each of these components, but it is also influenced by their position relative to each other in space, what we usually refer to as the geometry of the galaxy. In galaxies, luminous stars emit most of the ultraviolet (UV) and optical light, whilst dust influences the light we receive via the process of attenuation. Part of the UV + optical light is absorbed by dust grains and re-emitted in the infrared (IR). So, it is of utmost importance to understand the effects dust has on the multiwavelength emission of galaxies. The contribution of dust needs to be accounted for in any observations of galaxies if we are to perform a complete census of their components and the physical processes acting on these components.

Interstellar dust is created from the material that is ejected from stars or directly in the interstellar medium (ISM). Dust is built from heavy elements and compounds, such as silicates, carbonaceous materials, silicon carbides, carbonates, etc. (Draine 2003). It is especially interesting to know how the quantity of dust has evolved throughout cosmic time (Takeuchi et al. 2005; Cucciati et al. 2012; Burgarella et al. 2013; Madau & Dickinson 2014). All these works agree on a general behaviour that the average Cosmic dust attenuation in galaxies increases from $z = 0$ to ~ 1.5. This rise is followed by a decrease to $z \sim 4$ when only IR data are used. Up to now, this decrease could not be constrained by IR data at higher redshifts, but ALMA and other ground-based millimetre (mm) data now provide further constraints as we try to do in this work.

Quantifying the amount of dust is challenging. The best method available today is analysing the IR SEDs of galaxies. Most of the light emitted in the far-IR part of the SED is due to the thermal emission of dust (see, e.g. Draine & Li 2007).

However, estimating the amount of light absorbed by dust can also be achieved without far-IR data by using alternate proxy methods. Probably, the most popular one is the so-called β-slope (defined as $f_\lambda \propto \lambda^\beta$; Calzetti, Kinney & Storchi-Bergmann 1994) method (e.g. Bouwens et al. 2012, 2016) proposed by Meurer, Heckman & Calzetti (1999), from which the IR Excess (IRX; equation 1)) can be estimated. This is extremely useful when no IR data are available, which is often the case above $z \approx 4$. However, this relation has been mainly determined until redshift $z \approx 3$ for UV-dominated galaxies (Bowler et al. 2018, and references therein) and some departures are observed at higher redshift and for more IR-bright galaxies (e.g. Casey et al. 2014). Other common methods for calculating the dust attenuation include using the Balmer decrement (the ratio of the Hα line to the Hβ line), as well as the Hα line, for which some assumptions need to be made (see, e.g. the introduction of the paper by Hao et al. (2011).

The relation between IRX (or $A_{\rm FUV}$) and stellar mass (M_*) is yet another tool that allows to estimate the dust attenuation in galaxies from the stellar mass of galaxies. Because M_* mirrors the previous star formation activity of galaxies, which, in turn, is responsible for producing dust particles, the stellar mass may be a good, and easy to estimate, tracer of the dust content in galaxies.

The relationship between the stellar mass and attenuation has been the focus of numerous studies as early as (e.g. Martin et al. 2007; Xu et al. 2007; Buat et al. 2009, and references therein). Most works seem to suggest that there is a linear relation between IRX and

★ E-mail: jana.bogdanoska@lam.fr (JB); denis.burgarella@lam.fr (DB)

stellar mass over quite a large mass range ($9 \leq log\ M_* \leq 12$; Heinis et al. 2014; Pannella et al. 2015; Álvarez-Márquez et al. 2016, etc.) that is dubbed the 'consensus $z \sim 2$–3 relationship' by Bouwens et al. (2016). However, in this same paper, Bouwens et al. (2016) suggest either an evolution of the dust temperature or an evolution of the relationship at large redshift. The latter might be confirmed in the most recent works. For instance, Fudamoto et al. (2017, 2020) observe an evolution of the IRX–$M_{\rm star}$ relationship between $z \sim 3$ and ~ 6 by about 0.24 dex.

This paper is organized as follows. First, we present the possible biases that might affect our analysis in Section 2. After this, the data we have used to obtain our results are presented in Section 3. In Section 4, we present a detailed explanation of the methods implemented in this project and the main results obtained, and we present our findings concerning the relationship of the dust attenuation with stellar mass $A_{\rm FUV}$ –M_* (Section 4.1), and then we use these findings to study the dust attenuation as a function of redshift $A_{\rm FUV}(z)$ (Section 4.2). In Section 5, we discuss our estimate of the cosmic dust attenuation and compare it to the values found in the literature. The possible implications of our results are discussed in Section 6. We use a Salpeter (1955) initial mass function (IMF) for the stellar masses used throughout our work, as well as a Lambda cold dark matter cosmology with $(H_0, \Omega_{\rm m}, \Omega_\Lambda) = (70, 0.3, 0.7)$, where H_0 has the units of km s^{-1} Mpc^{-1}.

2 BIASES INTRODUCED DUE TO THE NATURE OF OBSERVATIONS

For this work, we compile a lot of data over quite large redshift and stellar mass ranges. We are aware that our approach is not fully complete as the information we can collect on the IR emission of galaxies at all redshifts can hardly be exhaustive and we follow the statistical approaches presented in several papers. The relative performance in UV + optical + near-IR is more favourable than that in far-IR + submillimeter. Thus, the detection limits are better for UV-dominated galaxies than for IR-dominated ones. We estimate that we have the following biases:

(i) In terms of the redshift:

(a) At high redshift ($z > 2$–3), a significant part of the less massive galaxies are not detected at all, whilst in the far-IR, only the dustier objects can be detected. So, it is likely that our high-redshift samples will be biased against low-IRX objects. This would mean that our high-redshift trend might only be seen as upper limits.

(b) In the local Universe, we are limited by the studied volume that is likely biased against rare objects; IR-bright galaxies are rarer than UV-bright galaxies. But given that both galaxy types are rare, we assume that this bias should not dramatically impact our results.

(ii) Concerning the stellar mass:

(a) Similarly, very massive galaxies are rare and this makes it hard to study their properties. But, like for the previous point, our results should not be strongly impacted. This is confirmed by attempting to modify the upper stellar mass cut-off without changing the global characteristics.

(b) In contrast, low-mass galaxies are numerous, and usually very faint, so the completeness decreases. It was usually thought that low-mass galaxies suffer from a very low dust attenuation or might even be dust-free. But recent results seem to suggest that this could be too fast of a conclusion: Dusty galaxies might appear smaller than they are in reality in the UV because the IR part of the SED is not detected (Takeuchi et al. 2005; Whitaker et al. 2017; Álvarez Márquez et al. 2019). This effect has an important impact on the global redshift evolution of the average dust attenuation because we expect a large number of such objects.

In conclusion, we understand that this work is probably not the final word about the redshift evolution of the IRX–M_* relation. But we need to move beyond the simple linear and constant view about this relationship that was consensual, as more and more results at low and high redshifts suggest that this is not true. The simple fact that this IRX–M_* needs to produce results consistent with the redshift evolution of the average galaxy attenuation presented in the literature (Cucciati et al. 2012; Burgarella et al. 2013; Madau & Dickinson 2014, etc.) means that we have to understand it better. One place to start is to use an approach checking that the assumptions are in agreement with the evolution of the dust evolution at cosmological scales.

3 THE DATA USED

We select data from the literature to build our final sample. The selection criteria are that the IRX values have been estimated either from a direct IR-to-UV ratio or by SED fitting. We do not keep samples where IRX is estimated from the UV slope-β. Although we think β could be a useful dust tracer, it has problems for dusty galaxies that are known not to follow the Meurer et al. (1999) relation (Burgarella, Buat & Iglesias-Páramo 2005; Casey et al. 2014). The reason for this departure is not studied here. We do not use surveys using the Balmer decrements because galaxies selected from emission lines are generally younger and this might impact on our statistics. Since, IRX is the ratio of $L_{\rm IR}$ to $L_{\rm UV}$, only the galaxies with measured $L_{\rm IR}$ and $L_{\rm UV}$ are usable for our study. We also assume that the IRX estimated from SED fitting is close to $L_{\rm IR}/L_{\rm UV}$ (e.g. Malek et al. 2018). More precisely, we use the following definition, with the IR luminosity, $L_{\rm IR}$, being the total integrated luminosity in the IR, and the UV luminosity, $L_{\rm FUV}$, derived from flux measured with a filter, such as, for e.g. *GALEX*:

$$\mathrm{IRX} = \log\left(\frac{L_{\rm IR}}{L_{\rm FUV}}\right). \tag{1}$$

In this paper, we call 'dust attenuation' the amount of UV energy reprocessed by dust grains, i.e. the net effect caused by the dust grains distributed within the galaxy in a complex geometry. The UV dust attenuation, $A_{\rm FUV}$, is a quantity that tells us by how much the light from the galaxies has been obscured by dust. Practically, for energy-balance based SED fitting, $A_{\rm FUV}$ is the parameter that contains the information of how much of the UV flux has been 'converted' into IR radiation. We introduce a relationship between IRX and $A_{\rm FUV}$. In this work, we use the parametrization suggested by Hao et al. (2011), which has the following form:

$$A_{\rm FUV} = 2.5 \log\left(1 + a_{\rm FUV} \times 10^{\rm IRX}\right), \tag{2}$$

with the calibration $a_{\rm FUV} = 0.46 \pm 0.12$. The difference between this conversion and other similar ones (e.g. Buat et al. 2005) is negligible, this one having the advantage of avoiding giving unphysical negative values for the dust attenuation.

The data included in this work contains the galaxies from the GALEX-SDSS-WISE Legacy Catalog (GSWLC; Salim et al. 2016; Salim, Boquien & Lee 2018), the GOODS-N field (Pannella et al. 2015), the Cosmic Evolution Survey (COSMOS) field (Álvarez-

Table 1. Summary of the literature used to obtain the data, and values of the redshift bins from each reference.

Reference	Galaxy Count	z
Salim et al. (2016, 2018)	≈400 000	<0.3
Pannella et al. (2015)	≈50 000, stacked	0.7, 1, 1.3, 1.7, 2.3, 3.3
Heinis et al. (2014)	≈40 000, stacked	1.5, 3, 4
Álvarez-Márquez et al. (2016)	≈22 000, stacked	3
Fudamoto et al. (2017)	39	3.2
Schaerer et al. (2015)	5	6.5−7.5
Fudamoto et al. (2020)	23	4−5
Bouwens et al. (2016)	78	4−10
Burgarella et al. (2020)	18	5−10

Notes. For Salim et al. (2016, 2018), the redshift is taken to be $z = 0.1$, which is the mean value of the redshifts of all the galaxies in the sample. A range is given for the Bouwens et al. (2016) because individual galaxies are used, and the separation of the bins is performed specifically for this work.

Márquez et al. 2016), as well as the COSMOS field combined with data from the Herschel MultiTiered Extragalactic Survey (HerMES) program and the Visible and Infrared Survey Telescope for Astronomy (VISTA; Heinis et al. 2014), the Hubble Ultra Deep Field (HUDF; Bouwens et al. 2016), as well as some other high-redshift sources (Schaerer et al. 2015; Burgarella et al. 2020; Fudamoto et al. 2020). A summary of the publications used in this work is given in Table 1.

The samples in these surveys have been selected by using different criteria. The GSWLC is based on the Main Galaxy Sample (MGS) of the SDSS, and it is magnitude-limited. We only include the objects that belong to the MGS, and with SDSS photometry, and with UV data from *GALEX*. Additionally, we include only the star-forming galaxies, as defined by the $SFR-M_*-Z$ relation proposed by Speagle et al. (2014) (their equation 28), and assume a dispersion of 0.3 dex around this relation according to Peng et al. (2010), outside of which all galaxies are excluded. The different IMFs chosen by the different authors have been taken into account.

Heinis et al. (2014) use a UV-selected sample from the COSMOS field for the three different redshifts presented in their work. Furthermore, Álvarez-Márquez et al. (2016) use Lyman-break galaxies (LBGs) from the COSMOS field, selected by the classical U-dropout method at redshift $z \approx 3$. The HUDF studied by Bouwens et al. (2016) also contains a UV-selected sample of LBGs. Fudamoto et al. (2017) include UV-selected massive star-forming galaxies from the COSMOS field. Fudamoto et al. (2020) use the ALPINE sample (Le Févre et al. 2019; Bethermin et al. 2020; Faisst et al. 2020). The GSWLC contains nearby galaxies. For most of them, the spectra have been measured. They have redshifts $z < 0.3$, and a mean redshift of $z = 0.1$. The other authors use various techniques to determine the redshifts of the galaxies within their sample; Pannella et al. (2015) and Bouwens et al. (2012) use the software EAZY, whilst Heinis et al. (2014) and Álvarez-Márquez et al. (2016) use an *i*-band-selected COSMOS catalogue produced with the software LEPHARE (Ilbert et al. 2009). For the objects studied by Schaerer et al. (2015), Burgarella et al. (2020), and Fudamoto et al. (2020), the redshifts have been spectroscopically determined.

The stellar masses of the galaxies included in our final sample have been calculated by similar, but not identical methods by the different groups. Most of the authors have used the method of SED fitting (e.g. Walcher et al. 2011), by assuming a different IMF. Pannella et al. (2015) and Bouwens et al. (2016) use a Salpeter (1955) IMF, while Salim et al. (2016), Salim et al. (2018), Heinis et al. (2014), Álvarez-Márquez et al. (2016), Fudamoto et al. (2017), Burgarella et al. (2020), and Fudamoto et al. (2020) use a Chabrier (2003) IMF. They all implement the Bruzual & Charlot (2003) single stellar populations, as well as an exponentially declining star formation history (SFH), except Salim et al. (2016, 2018), who use a two-component exponential SFH, and Fudamoto et al. (2020) who use a constant SFH (Faisst et al. 2020). Some of the authors do test other SFHs in their work, concluding that its impact is negligible on the results. Schaerer et al. (2015) use a different calibration for the stellar masses, obtained by the same authors in another work (cited as Schaerer et al., in preparation, and private communication).

To account for the different IMF used, a correction has been applied so that all of the data matches a Salpeter (1955) IMF. The conversion from Chabrier (2003) to Salpeter (1955) IMF is a multiplicative factor in terms of the mass, or an additive constant when the mass is presented in logarithmic units. The correction we apply is the one given in equation (12) by Longhetti & Saracco (2009):

$$\log M_{*[\text{Salpeter}]} = \log M_{*[\text{Chabrier}]} + 0.26\,\text{dex}. \quad (3)$$

Two different types of data are included in this work: data of individual galaxies (Schaerer et al. 2015; Salim et al. 2016, 2018; Fudamoto et al. 2017; Burgarella et al. 2020; Fudamoto et al. 2020), and stacked data (Heinis et al. 2014; Pannella et al. 2015; Álvarez-Márquez et al. 2016). The data in the paper of Bouwens et al. (2016) have been stacked, but in this work, we use the photometric data of the individual galaxies directly and we perform an SED fitting on individual galaxies by using CIGALE (Burgarella et al. 2005; Noll et al. 2009; Boquien et al. 2019) (Table 1).

4 EVOLUTION OF THE DUST ATTENUATION

This section is dedicated to studying the relationship between the stellar mass of star-forming galaxies and their average dust attenuation in the FUV, as estimated by the IRX of the galaxies' SEDs. We intend to extend our study to the evolution of this relationship with cosmic times, as well as estimate the average (cosmic) dust attenuation.

We start by dividing the data in redshift bins. In the case where the data have been already divided into redshift bins these bins are kept. In the case of different authors using the same redshift, separate bins are assigned. This means that, for example, for redshift $z = 3$, we have two bins, one from Heinis et al. (2014) and another from Álvarez-Márquez et al. (2016). The data that are given for individual galaxies are divided in two bins for Bouwens et al. (2016) and Burgarella et al. (2020), and kept as a single bin for Salim et al. (2018) and Schaerer et al. (2015). The data and the best-fitting function are given in Fig. 1. Each panel shows the data given by the different authors, separated in redshift bins where appropriate.

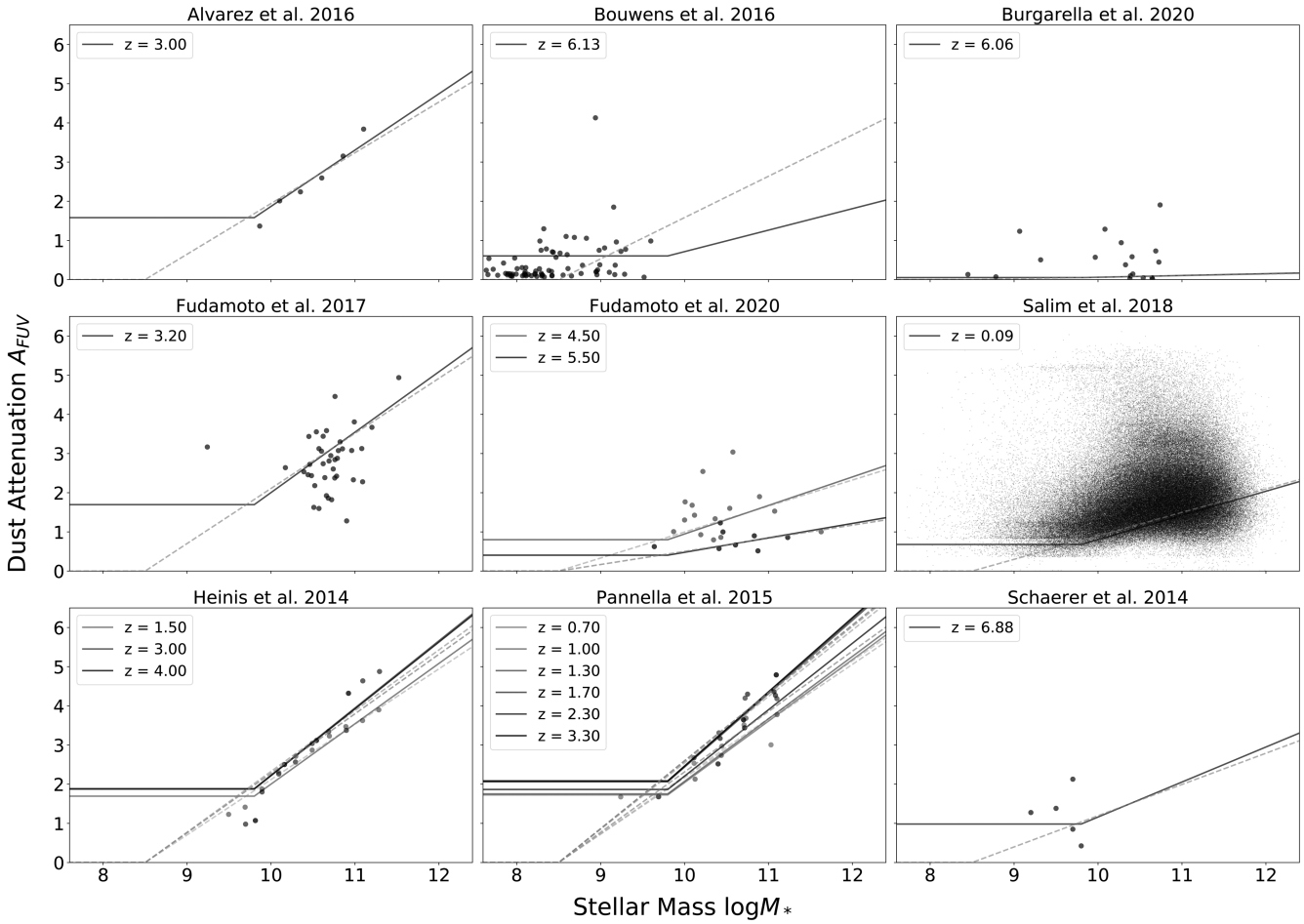

Figure 1. The dependence of the UV dust attenuation on stellar mass, showing the data from several references, along with the best-fitting model for the same redshift. Each panel represents the data from a different paper, with multiple different lines within one panel are models for different redshift bins. The dashed lines represent the model proposed in equation (4), while the full lines show the model of equation (6).

We fit the dust attenuation with a function that depends on two parameters, stellar mass and redshift, i.e. $A_{\rm FUV}(M_*, z)$, and we express it as a product of two independent functions, each of which has only one variable, namely $A_{\rm FUV} = f(M_*) \times a(z)$.

4.1 Evolution of the dust attenuation with stellar mass

The stellar mass dependence $f(M_*)$ has been studied before (e.g. Heinis et al. 2014; Pannella et al. 2015; Álvarez-Márquez et al. 2016; Bouwens et al. 2016; McLure et al. 2018), and is usually assumed to be linear either in IRX or directly in $A_{\rm FUV}$. Because we adopt a more global approach, we eventually modify this dependence and assume a broken line by using a function that is linear until a certain value for the stellar mass, and constant below. The justification for this shape is explained in detail in Section 5.1. The function has the same shape for any redshift; however, the scaling factor a is not. This constant affects both the value for the function where it is constant and the slope for the linear part. The function is as follows:

$$A_{\rm FUV}(\log M_*) = a(\log M_* - 8.5). \quad (4)$$

As mentioned before, the fitting of the data, shown in Fig. 1, is done by setting only a as a free parameter. However, the other parameter that is the x-intercept of the function, namely the value 8.5 is kept constant. This value also comes from the fitting of the data; once the best-fitting value for a was found, the χ^2 of the fit is computed for each redshift bin. For different values of the intercept, the values of the χ^2 were compared. The final values given in equation (4) are the ones giving the lowest χ^2 on average between all redshift bins. This is done, opposed to directly fitting both parameters in each redshift bins, in order to keep the redshift dependence only in a, and have one single value for the intercept.

Our goal is to find a function that describes the dependence of $A_{\rm FUV}$ on both stellar mass and redshift, and in this section, we explore separately the dependence only on stellar mass. We propose to fit the $A_{\rm FUV}$–M_* relationship with a linear function, multiplied by a factor a. This relatively simple function allows us to advance easily to the $A_{\rm FUV}$–z relationship presented in Section 4.2. However, we will explore in the following section (Section 5.1) the possibility of modifying this function.

4.2 Evolution of the dust attenuation with redshift

In this section, we will study the shape of $a(z)$, which comes from the fitting parameter of the $A_{\rm FUV}$–M_* relation, with the difference that this time it is not a simple constant a, but a function of redshift, i.e. $a(z)$.

We show in Fig. 2 the evolution in redshift of the parameter a that has been obtained from the best-fitting function of the data, as

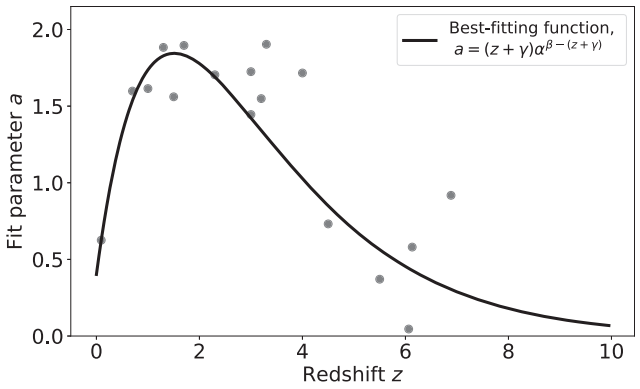

Figure 2. Fitting the parameter a from the $A_{\rm FUV}$–M_* relationship in each redshift. Each point has been obtained by fitting the available data in that redshift. The black line represents the fit of these points, as fitted with the function of equation (5).

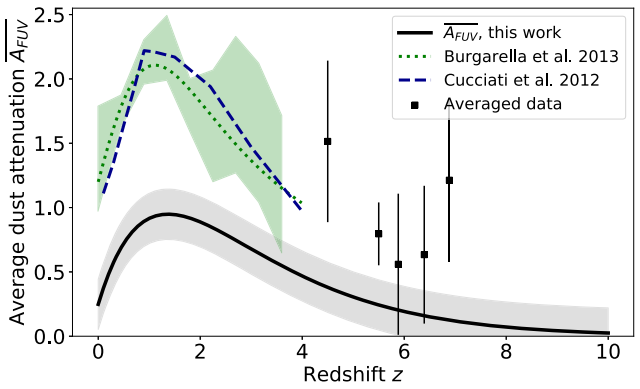

Figure 3. The evolution of the dust attenuation in the FUV with redshift. The full black line represents the integrated average dust attenuation, calculated using equation (A1), with the model of equations (4) and (5) (details of the calculations in Appendix A). Only data with $\log M_* > 9$ have been included in the computations, and, consequently, $\overline{A_{\rm FUV}}$ has been computed estimating the integrals of equation (A1) within the limits of $9 < \log M_* < 14$. The shaded area around the full black line corresponds to the total estimated 1σ uncertainty of the parameters of equation (4), namely the uncertainty of the intercept of the function estimated with the χ^2 described in Section 4.1, alongside the errors of the fitting for the coefficients of equation (5). The points represent the mean value of the data we included in our work (Fig. 1) for $z > 4$, with the error bars representing the 1σ dispersion around the mean value. The dotted green line and the shaded green area surrounding it come from the work of Burgarella et al. (2013), the line shows the best-fitting model, and the shaded area shows the error bars. The dashed dark blue line shows the results of Cucciati et al. (2012).

presented in Section 4.1, and described by equation (4). Next, we use the points shown in Fig. 2 to find a functional form for $a(z)$, by fitting these coefficients. The black line represented in Fig. 2 is the best-fitting function, described as

$$a(z) = (z+\gamma)\,\alpha^{(\beta-(z+\gamma))}, \tag{5}$$

the coefficients have the following values: $\alpha = 1.84 \pm 0.12$, $\beta = 1.59 \pm 0.12$, and $\gamma = 0.17 \pm 0.04$. We propose this function as it has a similar shape to the one used by Madau & Dickinson (2014) and Burgarella et al. (2013), but giving a better fit.

5 COMPARISON WITH THE COSMIC DUST ATTENUATION

We compare Fig. 2 to the available results in the literature. This work assumes that the $A_{\rm FUV}$–$M*$ relation is able to represent the dust attenuation of all star-forming galaxies, given their stellar mass. According to this, if we wish to compute the average dust attenuation, i.e. the cosmic dust attenuation, we need to include *all* of the star-forming galaxies. This is why we compute the weighted average of the dust attenuation, the weights being the mass function (MF) for star-forming galaxies. The details of this computation are given in Appendix A.

At any redshift data for galaxies with $\log M* < 9$ are scarce. So, in this section, we start by using only galaxies with masses in the range $9 < \log M_* < 14$ (Fig. 3), and later we include all of the objects (Section 5.1). From Fig. 3, it appears that the absolute level of $A_{\rm FUV}$ as a function of the redshift is too low, as compared to the literature (Cucciati et al. 2012; Burgarella et al. 2013; Madau & Dickinson 2014). The reason for this can be found in the way we compute $\overline{A_{\rm FUV}}$, more precisely in the shape of the mass function. Let us take as an example the MF proposed by Wright, Driver & Robotham (2018) in their fig. 1. We can see that for low-mass galaxies, such as $\log M_* = 7$ for the first three redshift bins (for $z < 0.2$), the number is as high as 10^{-1} galaxies per unit volume, whilst in the higher stellar mass range, for e.g. for $\log M = 11$ the number is two orders of magnitude lower, so it is roughly 10^{-3} galaxies per unit volume. Modelling the MF with a Schechter function means that when including galaxies with down to $\log M \sim 6$, our computation will be heavily influenced by this large number of low-mass objects. However, by defining the function that describes $A_{\rm FUV}-M_*$ with equation (4), we have set $A_{\rm FUV}$ to be zero for galaxies with $\log M_* < 8.5$, i.e. where the single-line models gives $A_{\rm FUV} < 0$, we set $A_{\rm FUV} = 0$.

5.1 Modification of the function for $A_{\rm FUV}-M*$

As it is obvious from Fig. 3, there seems to be a problem with fitting the $A_{\rm FUV}-M_*$ relationship with equation (4). We suspect that the problem lies within the different numbers of galaxies with low stellar mass versus galaxies with higher stellar mass, which dictates that the apparent average cosmic value of the dust attenuation will be shifted towards the values attributed to the low-mass galaxies. Possible physical explanations for this discrepancy will be detailed in the discussion (Section 6). But, here we explore the possibility of modifying the $A_{\rm FUV}-M_*$ relation in such a way that when comparing to the literature for the evolution of $\overline{A_{\rm FUV}}$ with cosmic time, we get results that are of similar values.

The amount of data for low-mass galaxies, especially at higher redshift, is quite low to date. Consequently, determining the shape of the $A_{\rm FUV}-M_*$ function solely from data is virtually impossible in this stellar mass range. We propose to test the simplest possible form as a first approximation: a constant. We wish to keep the function continuous, as well as to choose the parameters presented in Section 4.1 that fit the data as well as possible. Thus, we modify equation (4) to have the following form:

$$A_{\rm FUV}(\log M_*) = a \begin{cases} 1.1, & \log M_* < 9.8 \\ \log M_* - 8.7, & \log M_* \geq 9.8 \end{cases}. \tag{6}$$

This function now has two parameters that determine its shape: the break where the function changes from constant to linear (in equation (6), this parameter is equal to $\log M_* = 9.8 \pm 0.1$) and the x-intercept of the linear part (equal to 8.7 ± 0.1 in equation (6), and equal to 8.5

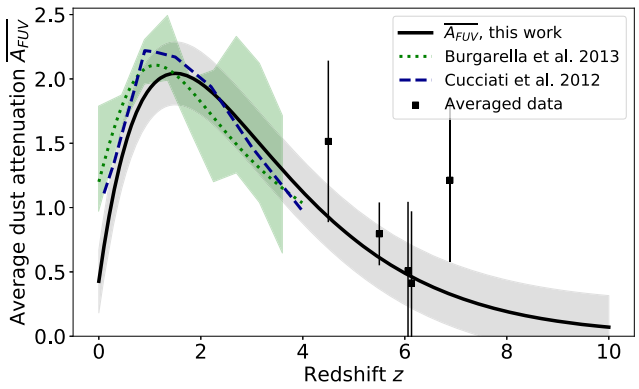

Figure 4. The evolution of the dust attenuation in the FUV with redshift. The full black line represents the integrated average dust attenuation, calculated using equation (A1), with the model of equations (5) and (6). In this case, $\overline{A_{\rm FUV}}$ has been computed using the limits of $6 < \log M_* < 14$, analogous to the limits of integration used in the work of Burgarella et al. (2013). The shaded area around the full black line corresponds to the total estimated 1σ uncertainty of the parameters of equation (6), namely the uncertainty of the intercept of the function and the position of the break estimated with the χ^2 described in Section 5.1, alongside the errors of the fitting for the coefficients of equation (5). We note, however, that the uncertainties might be underevaluated at low redshift. The origin of this underevaluation is not clear but maybe it is due to a relatively well fitting of equation (5) for $z = 0$. Similarly to Fig. 3, the points represent the mean value of the used data for $z > 4$; however, they have slightly different values than those of Fig. 3 due to the objects with $\log M_* < 9$ that were included in computing the mean. The dotted green line, the shaded green area surrounding it, and the dashed dark blue are the same as in Fig. 3.

in equation (4), also expressed in units of $\log M_*$). The value of the constant part is the value of the linear part computed for $\log M_* = 9.8$, to ensure continuity of the function. These two parameters, the break and the intercept, were determined by finding the lowest χ^2 produced by both parameters simultaneously.

The coefficient a is the same as described in Section 4.2. The redshift dependence of the cosmic dust attenuation, computed using equation (6) is presented in Fig. 4. It should be noted that replacing the function of equation (4) with that of equation (6) produces a difference in the best-fitting values of the parameters of equation (5); thus, in this case, we give the following values: $\alpha = 1.84 \pm 0.11$, $\beta = 1.84 \pm 0.12$, and $\gamma = 0.14 \pm 0.04$.

6 DISCUSSION

Understanding in its entirety the processes of formation and evolution of galaxies requires knowledge on the subject of cosmic dust. This work makes use of the fact that the scientific community is apt at and confident about estimating the stellar mass M_* of a galaxy. We are striving towards developing a model which would be able to estimate the FUV dust attenuation of a galaxy from its stellar mass and redshift. This would, in turn, enable us to better estimate the star formation rate (SFR) of a galaxy, and give us insight into the overall evolution of distant galaxies.

Some of the recently published work argues against this approach, as the evolution of the $A_{\rm FUV}-M_*$ relation has been doubted (Heinis et al. 2014; Bouwens et al. 2016; Whitaker et al. 2017). One of the goals of this work is to review this question with a larger set of data covering a large redshift range from $z = 0$ to the highest redshift galaxies. On the other hand, Bernhard et al. (2014) suggest that there is some evolution, only limited to $z < 1$. They use the relation from Heinis et al. (2014) as the basis, and for $z < 1$, they vary the normalization as $IRX'_0 = IRX_0 - 0.5 \times (1 - z)$. We attempted to add this relation to Fig. 4, but as the Heinis et al. (2014) relation is only defined for $\log M_* > 9.5$, we encountered the same problem as using equation (4) instead of equation (6).

To assess the validity of our work, we compare to the relevant literature (Cucciati et al. 2012; Burgarella et al. 2013; Madau & Dickinson 2014) until redshift $z < 4$. We can see in Fig. 4 that the values obtained by our models (equation (6), combined with equation (5)) do indeed follow a similar trend as those found in the literature, even with results obtained by using a completely different method to estimate the dust attenuation. The green dotted line shows the best-fitting model proposed by Burgarella et al. (2013), with the green shaded area showing their uncertainties. The work of Burgarella et al. (2013) is based on the study of IR and UV luminosity functions; the IRX in this work is computed as the ratio of the IR luminosity density to the UV luminosity density, estimated at different redshifts. We also compare our results to the work of Cucciati et al. (2012), who use a different method of estimating the same parameter; they estimate the intrinsic colour excess $E(B - V)$ and by using the starburst reddening curve given by Calzetti et al. (2000), they estimate the dust attenuation in the FUV. Their results are shown by the dashed dark blue line in Fig. 4.

To compare our work to that of Burgarella et al. (2013), we must compute the average value of the dust attenuation using the same stellar mass range, meaning, perform the integration within the same limits, as explained in Appendix A. Burgarella et al. (2013) state that the LFs are integrated within the range $\log_{10}(L[L_\odot]) = [7, 14]$. The corresponding range, converted into units of stellar mass by the use of the $\log M_*$–$M_{\rm UV}$ relation, where $M_{\rm UV}$, the absolute UV magnitude, given by Song et al. (2016), is $\log_{10}(M[{\rm M}_\odot]) = [6, 14]$. Cucciati et al. (2012) do not include a mass or luminosity range in their computations, so we cannot compare in an analogous way.

6.1 The apparent dust attenuation of low-mass galaxies

Using our method described in Section 4, we implicitly make the assumption that the shape of the function of the $A_{\rm FUV}$–M_* relation is the same throughout all redshifts. We can see, for example, in the data from Salim et al. (2016, 2018) (Fig. 1), a clear flattening towards the lower mass end. This sample includes galaxies with stellar masses as low as $\log M_* \approx 7$, who have a large dispersion in the $A_{\rm FUV}$, with the values of the dust attenuation being as low as $A_{\rm FUV} = 0.25$, and with some objects having a value as high as $A_{\rm FUV} = 5$. We can conclude from these data that the low-mass galaxies have a large scatter in their FUV dust attenuation and a mean significantly different from zero. We believe this justifies approximating this part of the $A_{\rm FUV}$–M_* dependence with a non-zero constant average value.

On the theoretical side, the work of Cousin et al. (2019), where they use the semi-analytical models called GAS, predicts the dust attenuation of galaxies by computing the IRX. We can see in their fig. 9 a flattening for lower stellar masses similar to the one we find using our parametrization. For reference, $\log {\rm IRX} = 0.25$ corresponds to $A_{\rm FUV} = 0.97$, according to the relation of Hao et al. (2011). Additionally, they show in fig. 11 an evolution of the IRX–mass relation.

A flattening and an increased scatter of the $A_{\rm FUV}$–M_* relation for galaxies with low stellar masses ($\log M_* < 8$) can equally be seen in simulations, such as the high-resolution cosmological zoom-in simulation FIRE-2 (Ma et al. 2019). They compute galaxy SEDs and mock images using a radiative transfer code adopting a Small

Magellanic Cloud (SMC)-type dust grain size distribution, which is preferred for galaxies at higher redshift. In Ma et al. (2019), one of the important parameters is the dust-to-metal ratio ($M_{\rm dust} = f_{\rm dust} M_{\rm metal}$). In their simulations, $f_{\rm dust}$ includes all the processes in the dust cycle (dust production, growth, and destruction), and is taken to be constant for a given model. Multiple values are tested (see their fig. 14) and it is suggested that $f_{\rm dust}$ could be observationally constrained. They find that for low-mass galaxies, there is a larger scatter and possible flattening, regardless of the value of $f_{\rm dust}$ and independently of the redshift. However, two main parameters (the opacity $\kappa_{\rm dust}$ and $f_{\rm dust}$) can impact on the absorption coefficient $\alpha \propto \kappa_{\rm dust}\, f_{\rm dust}$ that enters the radiative transfer equation and sets the dust temperature and emissivity, which sets a degeneracy. So the unexplained behaviour at low stellar mass can have different origins linked to an intrinsic dust attenuation with a surprising large amount of dust in these low-mass galaxies but other origins are possible like a more clumpy geometry where young stars would be included in dense dusty shells, or a more 'bursty' nature of the star formation or, finally, a modification of $f_{\rm dust}$ with the metallicity.

On the observational side, we now see more and more evidence that the simple low-mass low-$A_{\rm FUV}$ assumption might not be fully valid.

A scatter is suggested in fig. 2 of Whitaker et al. (2017), which shows that for stellar masses around $\log M_* = 9$, the dust attenuation can be in the range $0.5 < A_{\rm FUV} < 2.5$. This is in agreement with our results [outliers in the top left-hand corner of the same figure; the value of $f_{\rm obscured} = 0.55$ corresponds to $A_{\rm FUV} = 0.5$ and the value of $f_{\rm obscured} = 0.95$ corresponds to $A_{\rm FUV} = 2.5$, after first converting $f_{\rm obscured}$ into IRX, and then using the Hao et al. (2011) relation to get $A_{\rm FUV}$].

We can also notice the objects reported in the work of Takeuchi et al. (2010, their Fig. 16), where we see galaxies with stellar masses as low as $7 < \log M_* < 8$, which have $A_{\rm FUV}$ values in the range $0.3 < A_{\rm FUV} < 4.1$. Indeed, to be completely certain that low-mass galaxies have a higher average dust attenuation than is predicted by previous work, we would need more statistics for fainter galaxies. The next steps of this work would include taking into account the scatter around the average value proposed by our model, so instead of proposing one average value for all low-mass galaxies, we could give a range of possible values. This is, however, beyond the scope of this paper.

The behaviour of this $A_{\rm FUV}$ *versus* $\log M_*$ law at low mass is puzzling but is required if we wish to match both the data from (Salim et al. 2016), other less complete studies at low redshift cited above but also IZw18 or SBS 0335−052 (Cannon et al. 2002; Hunt, Thuan & Izotov 2003; Wu et al. 2007; Reines, Johnson & Hunt 2008; Rémy-Ruyer et al. 2015; Cormier et al. 2017; Lebouteiller 2019). This is also required to match the $A_{\rm FUV}(z)$ shape, consistently obtained using a large variety of methods as illustrated in, e.g. Madau & Dickinson (2014).

We do not have any strong explanation yet, but we could speculate that dust is building very fast in low-mass objects (see, e.g. Burgarella et al. 2020) and could quickly reach a minimum (statistical) threshold close to the value found here, qualitatively speaking, because dust builds from metals, in a way similar to the pop.III–pop.II critical metallicity (see, e.g. Bromm et al. 2001; Schneider et al. 2002; Jaacks et al. 2018). If so, we could observe a flattening of the relation between dust attenuation and metallicity. It is very difficult to confirm this but such a flattening of the dust attenuation as a function of the metallicity is not excluded by Garn & Best (2010), Xiao et al. (2012), Koyama et al. (2015), and Qin et al. (2019). This means that the present relation does not remain infinitely flat but should present a sharp rise at some low stellar mass.

6.2 The evolution of the $A_{\rm FUV}$–$M*$ relation with the redshift

At high redshift, we also have more and more evidence from objects extracted from deep ALMA maps that the 'consensus' law is not valid anymore. Fudamoto et al. (2017, 2020) suggest that there is a significant redshift evolution of the IRX–$M_{\rm star}$ relation between $z \sim 3$ and ~ 6 by about 0.24 dex. This hypothesis is also supported by the rest of the data at $z > 4-5$ presented in this paper.

In short, the low stellar mass galaxies at low redshift exhibit a large scatter in $A_{\rm FUV}$, which can be fitted by a constant function. Based on this, we make the assumption that the $A_{\rm FUV}-M_*$ relation is constant in this mass range for all redshifts. We do leave the option of the value of the constant to vary with redshift, through the fitting of the parameter a in equation (4). Considering that for higher redshifts, we do not have low-mass galaxy data, we attempt to make up for this by assuming that the evolution of the average $A_{\rm FUV}$ follows the function proposed by Burgarella et al. (2013). We then attempt to find such a parametrization for $A_{\rm FUV}-M_*$ that would give similar values for the $A_{\rm FUV}-z$ relationship to those of Burgarella et al. (2013), when weighted by the MF and integrated to compute the mean $A_{\rm FUV}$. So, fitting the literature data (from Table 1) assures we have a function that reproduces the data well in the higher mass range, while comparing to Burgarella et al. (2013) compensates for the lack of data in the low-mass range, and gives us a prediction on which values we could expect for the $A_{\rm FUV}$ of such objects.

We are interested in gaining as much knowledge about the early Universe as possible, and understanding the dust attenuation far back in cosmic time is no exception. As can be seen in Table 1, we have included some galaxies with high redshift; however, it is only a small number of objects and only until redshift $z < 8$. So, until more observations are carried out and more advanced telescopes are used, we can only make predictions about how the dust attenuation behaves farther into the history of the Universe, at redshift $z \sim 10$. We give equation (B1) as a recipe for predicting the dust attenuation of galaxies, given their redshift and stellar mass. This can be further used to give an estimate of the dust attenuation where no data are available, as well as to make predictions and simulations to further push the limits of the knowledge of this field.

7 CONCLUSIONS

In this work, we estimate the evolution with redshift of the dust attenuation in the FUV by first exploring the evolution of the relationship between the dust attenuation and the stellar mass throughout cosmic times. The evolution of the $A_{\rm FUV}-M_*$ relationship has been debated in the literature. However, this paper strongly suggests that we need to assume that the $A_{\rm FUV}-M_*$ relationship does evolve with redshift, and we base our further studies upon this hypothesis.

An additional interesting point is that predictions can be made using the prescriptions presented in this paper. These predictions can be tested using data and the *James Webb Space Telescope* and new deep submillimetre and millimetre facilities in a relatively near future.

We can summarize this work with the following conclusions:

(i) The $A_{\rm FUV}-M_*$ relationship needs to be described with a more complicated function as opposed to the consensus linear (in terms of $\log M_*$) relationship, such as the one proposed in equation (6). Such a function needs to be able to incorporate the influence of the low-mass galaxies on the global average of the dust attenuation.

(ii) Assuming the $A_{\rm FUV}-M_*$ relationship does not evolve with redshift is not consistent with other studies concerning the evolution of the dust attenuation. On the other hand, starting from the assumption that this relation is not the same at all cosmic times

gives results similar to the ones found by groups studying the same phenomenon by the use of different methods.

(iii) The $A_{\rm FUV}-M_*$ relationship for lower stellar masses has a large scatter, with an average value that is likely to be larger than zero throughout most of the cosmic times. The physical origin of this offset cannot be derived from the present data. However, some works listed in Section 6 suggest various possible origins for the flattening at low stellar mass: it could simply be that these low-mass galaxies have a relatively high dust content but it might also be due to the stars-dust geometry and/or the dust-to-metal ratio.

ACKNOWLEDGEMENTS

The authors would like to thank Xiangcheng Ma, Christopher Hayward, and Ambra Nanni for their helpful comments and discussion. JB is also grateful for the advice and suggestions given by Junais. Finally, we thank the anonymous referee for the constructive criticism that helped bring out the best of our work.

DATA AVAILABILITY

No new data were generated or analysed in support of this research.

REFERENCES

Álvarez Márquez J., Burgarella D., Buat V., Ilbert O., Pérez-González P. G., 2019, A&A, 630, A153
Álvarez-Márquez J. et al., 2016, A&A, 587, 122
Bernhard E., Béthermin M., Sargent M., Buat V., Mullaney J. R., Pannella M., Heinis S., Daddi E., 2014, MNRAS, 442, 509
Bethermin M. et al., 2020, preprint (arXiv:2002.00962)
Boquien M., Burgarella D., Roehlly Y., Buat V., Ciesla L., Corre D., Inoue A. K., Salas H., 2019, A&A, 622, A103
Bouwens R. J. et al., 2012, ApJ, 754, 83
Bouwens R. J. et al., 2016, ApJ, 833, 72
Bowler R. a. A., Bourne N., Dunlop J. S., McLure R. J., McLeod D. J., 2018, MNRAS, 481, 1631
Bromm V., Ferrara A., Coppi P. S., Larson R. B., 2001, MNRAS, 328, 969
Bruzual G., Charlot S., 2003, MNRAS, 344, 1000
Buat V. et al., 2005, ApJ, 619, L51
Buat V., Takeuchi T. T., Burgarella D., Giovannoli E., Murata K. L., 2009, A&A, 507, 693
Burgarella D. et al., 2013, A&A, 554, A70
Burgarella D., Buat V., Iglesias-Páramo J., 2005, MNRAS, 360, 1413
Burgarella D., Nanni A., Hirashita H., Theulé P., Inoue A., Takeuchi T. T., 2020, A&A, 235, 459.02
Calzetti D., Kinney A. L., Storchi-Bergmann T., 1994, ApJ, 429, 582
Calzetti D., Armus L., Bohlin R. C., Kinney A. L., Koornneef J., Storchi-Bergmann T., 2000, ApJ, 533, 682
Cannon J. M., Skillman E. D., Garnett D. R., Dufour R. J., 2002, ApJ, 565, 931
Casey C. M. et al., 2014, ApJ, 796, 95
Chabrier G., 2003, PASP, 115, 763
Cormier D. et al., 2017, MNRAS, 468, L87
Cousin M., Buat V., Lagache G., Bethermin M., 2019, A&A, 627, A132
Cucciati O. et al., 2012, A&A, 539, A31
Draine B. T., 2003, ARA&A, 41, 241
Draine B. T., Li A., 2007, ApJ, 657, 810
Faisst A. L. et al., 2020, ApJS, 247, 61
Fudamoto Y. et al., 2017, MNRAS, 472, 483
Fudamoto Y. et al., 2020, preprint (arXiv:2004.10760)
Garn T., Best P. N., 2010, MNRAS, 409, 421
Grazian A. et al., 2015, A&A, 575, A96
Hao C.-N., Kennicutt R. C., Johnson B. D., Calzetti D., Dale D. A., Moustakas J., 2011, ApJ, 741, 124
Heinis S. et al., 2014, MNRAS, 437, 1268
Hunt L. K., Thuan T. X., Izotov Y. I., 2003, ApJ, 588, 281
Ilbert O. et al., 2009, ApJ, 690, 1236
Jaacks J., Thompson R., Finkelstein S. L., Bromm V., 2018, MNRAS, 475, 4396
Koyama Y. et al., 2015, MNRAS, 453, 879
Lebouteiller V., 2019, MNRAS, 344, 259
Le Févre O., Béthermin M., Faisst A., Capak P., Cassata P., Silverman J. D., Schaerer D., Yan L., 2019, preprint (arXiv:1910.09517)
Longhetti M., Saracco P., 2009, MNRAS, 394, 774
Ma X. et al., 2019, MNRAS, 487, 1844
Madau P., Dickinson M., 2014, ARA&A, 52, 415
Malek K. et al., 2018, A&A, 620, A50
Martin D. C. et al., 2007, ApJS, 173, 415
McLure R. J. et al., 2018, MNRAS, 476, 3991
Meurer G. R., Heckman T. M., Calzetti D., 1999, ApJ, 521, 64
Mortlock A. et al., 2015, MNRAS, 447, 2
Noll S., Burgarella D., Giovannoli E., Buat V., Marcillac D., Muñoz-Mateos J. C., 2009, A&A, 507, 1793
Pannella M. et al., 2015, ApJ, 807, 141
Peng Y.-j. et al., 2010, ApJ, 721, 193
Qin J., Zheng X. Z., Wuyts S., Pan Z., Ren J., 2019, MNRAS, 485, 5733
Reines A. E., Johnson K. E., Hunt L. K., 2008, AJ, 136, 1415
Rémy-Ruyer A. et al., 2015, A&A, 582, A121
Salim S. et al., 2016, ApJS, 227, 2
Salim S., Boquien M., Lee J. C., 2018, ApJ, 859, 11
Salpeter E. E., 1955, ApJ, 121, 161
Schaerer D., Boone F., Zamojski M., Staguhn J., Dessauges-Zavadsky M., Finkelstein S., Combes F., 2015, A&A, 574, A19
Schechter P., 1976, ApJ, 203, 297
Schneider R., Ferrara A., Natarajan P., Omukai K., 2002, ApJ, 571, 30
Song M. et al., 2016, ApJ, 825, 5
Speagle J. S., Steinhardt C. L., Capak P. L., Silverman J. D., 2014, ApJS, 214, 15
Takeuchi T. T., Ishii T. T., Nozawa T., Kozasa T., Hirashita H., 2005, MNRAS, 362, 592
Takeuchi T. T., Buat V., Heinis S., Giovannoli E., Yuan F.-T., Iglesias-Páramo J., Murata K. L., Burgarella D., 2010, A&A, 514, A4
Tomczak A. R. et al., 2014, ApJ, 783, 85
Walcher J., Groves B., Budavàri T., Dale D., 2011, Ap&SS, 331, 1
Whitaker K. E., Pope A., Cybulski R., Casey C. M., Popping G., Yun M. S., 2017, ApJ, 850, 208
Wright A. H., Driver S. P., Robotham A. S. G., 2018, MNRAS, 480, 3491
Wu Y. et al., 2007, ApJ, 662, 952
Xiao T., Wang T., Wang H., Zhou H., Lu H., Dong X., 2012, MNRAS, 421, 486
Xu C. K. et al., 2007, ApJS, 173, 432

APPENDIX A: COMPUTATION OF THE AVERAGE DUST ATTENUATION

Fig. 2 indirectly provides an information on the evolution of the dust attenuation with redshift. This makes it difficult to compare to the literature. We proceed by computing the average dust attenuation for all of the stellar masses, and in this section, we present the recipe that we followed to do that.

By definition, if the dust attenuation of a galaxy is a function of its stellar mass $A_{\rm FUV}(M_*)$, then the mean of this function would be

$$\overline{A_{\rm FUV}} = \frac{\int_{M*_{\rm min}}^{M*_{\rm max}} A_{FUV}(M_*)\phi(M_*){\rm d}M_*}{\int_{M*_{\rm min}}^{M*_{\rm max}} \phi(M_*){\rm d}M_*}. \quad \text{(A1)}$$

Here, $\phi(M_*)$ is the mass function (MF), which, in this case, acts as a normalization. We use the functional form of Schechter (1976), with ϕ_*, $\mathcal{M}^*$, and α the Schechter parameters:

$$\phi{\rm d}M = \phi^* 10^{(1+\alpha)(\log M_* - \log \mathcal{M}^*)} \exp[-10^{(\log M_* - \log \mathcal{M}^*)}]{\rm d}M. \quad \text{(A2)}$$

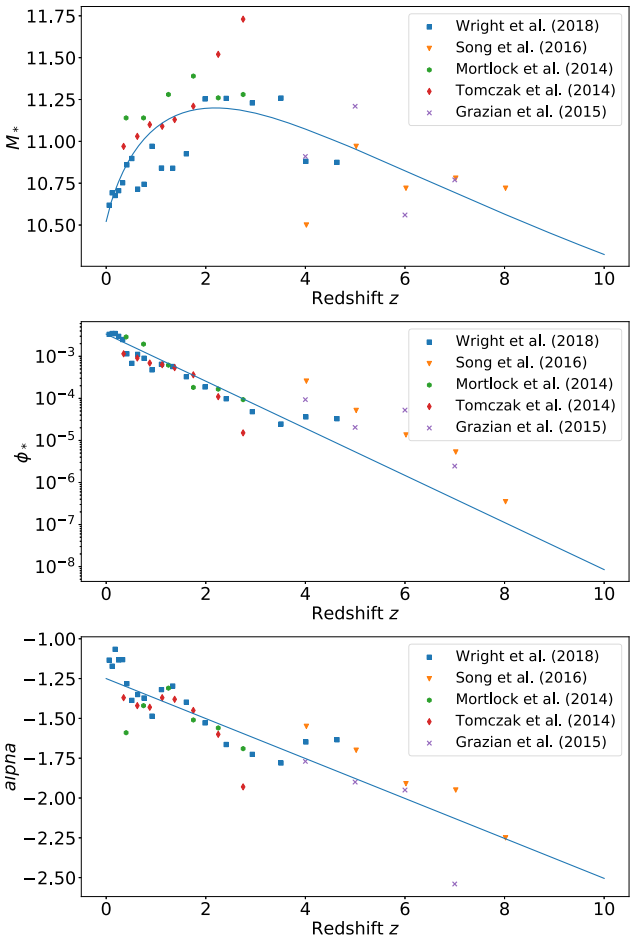

Figure A1. The fitting of the Schechter parameters. The functions used are $\mathcal{M}^* = (k_1 + k_2 z)/(1 + (z/k_3)^{k_4})$, where $k_1 = 10.52$, $k_2 = 2.38$, $k_3 = 4.80$, and $k_4 = 1.15$; $\log \phi_* = (l_1 - 0.56z)$, with $l_1 = -2.47$; $\alpha = m_1 + m_2 z$, with parameters $m_1 = -1.25$ and $m_2 = -0.13$.

The evolution of the dust attenuation–stellar mass relationship can now be expressed through the evolution of the average dust attenuation with redshift. Studying the evolution of the average dust attenuation requires an estimation of the value of equation (A1) for each redshift. This, in turn, requires the knowledge of the evolution of the MFs, for which we used the MFs of Tomczak et al. (2014), Grazian et al. (2015), Mortlock et al. (2015), Song et al. (2016), and Wright et al. (2018). We fit the values of the Schechter (1976) parameters given in these papers to be able to retrieve their value at any given redshift (Fig. A1); the values for the $\mathcal{M}^*$ parameter are fitted with the function $\mathcal{M}^* = (k_1 + k_2 z)/(1 + (z/k_3)^{k_4})$, and the best fitting is for $k_1 = 10.52$, $k_2 = 2.38$, $k_3 = 4.80$, and $k_4 = 1.15$; for ϕ_*, we have $\log \phi_* = (l_1 - 0.56z)$, with $l_1 = -2.47$ giving the best fitting; and for α, the function is a line $\alpha = m_1 + m_2 z$, with parameters $m_1 = -1.25$ and $m_2 = -0.13$.

We set up a grid of redshifts, and for each value z_i, we calculate the dust attenuation using the model we have chosen for the $\overline{A_{\rm FUV}}$–z relationship, with the corresponding value of the coefficient $a(z_i)$. For the same z_i, we estimate the Schechter (1976) parameters, and compute the corresponding MF. We then use the MF as the weight for calculating the average dust attenuation $\overline{A_{\rm FUV}}$, according to equation (A1). The results of this computation are represented in Section 4.2.

APPENDIX B: DUST ATTENUATION AS A FUNCTION OF BOTH REDSHIFT AND STELLAR MASS

The work presented in this paper strives to combine the dependence of the dust attenuation on stellar mass and its evolution with redshift. The result of this unification is a three-dimensional model for the dust attenuation as a function of both stellar mass and redshift, $A_{\rm FUV}(z, M_*)$, which is a surface in a 3D space. The stellar mass and the redshift are independent variables, while the dust attenuation depends on both of these values. This gives us the ability to estimate the dust attenuation of any galaxy from knowing its stellar mass and redshift.

We already have a functional form of both the dependences we require, $A_{\rm FUV}(M_*)$ and $A_{\rm FUV}(z)$, by fitting the parameter $a(z)$ and we can directly replace it in equation (4). Thus, we obtain the relation for $A_{\rm FUV}(z, M_*)$ if we put together equations (4) and (5) to obtain

$$A_{FUV} = (z + \gamma)\,\alpha^{(\beta-(z+\gamma))} \begin{cases} 1.1, & \log M_* < 9.8 \\ \log M_* - 8.7, & \log M_* > 9.8 \end{cases}. \quad \text{(B1)}$$

The parameters of this function are the same ones that are determined with the models discussed in Section 5.1, and, thus, their values remain the same. The 3D plot of this relation is shown in Fig. B1.

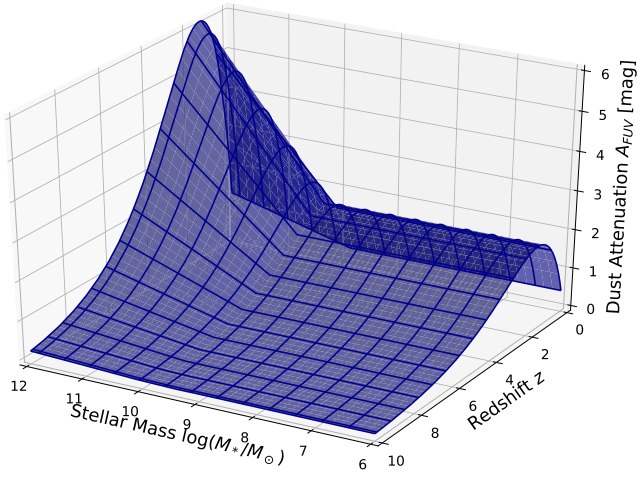

Figure B1. The dependence of the dust attenuation in the UV on stellar mass and redshift. The surface represents the model shown in equation (B1). If we take, for example, any value $\log M_* = \text{const.}$, we retrieve the dependence given by equation (5), shown in Fig. 2. Similarly, for any value of the redshift, we retrieve the models of equation (6), shown in Fig. 1.

This paper has been typeset from a TEX/LATEX file prepared by the author.